Development of PVDF micro and nanostructures for cell culture studies

Kévin Lhoste

Université Paris Descartes

Ecole doctorale Frontières du Vivant (ED474)

ENS Département Chimie / Groupe Microfluidique, organisation chimique et nanotechnologie

Development of PVDF micro and nanostructures for cell culture studies

Par Kevin LHOSTE

Thèse de doctorat de Biotechnologies, Nanotechnologies et interfaces

Dirigée par Pr. Yong CHEN

Présentée et soutenue publiquement le 30 Novembre 2012

Devant un jury composé de :

M. Yong CHEN.....Directeur de thèse
M. Juan KEYMER.....Rapporteur
M. Tarik BOUROUINA.....Rapporteur
M. Abdel EL ABED.....Examinateur
Mme Anne-Marie HAGHIRI-GOSNET.....Examinateur

Development of PVDF micro and nanostructures for cell culture studies

Abstract

Tissue engineering aims at repairing damaged tissues and recovering the lost or degraded biological functions with artificial scaffolds. In order to meet the requirement for more complex functionality such as peripheral nerve reconstruction, new types of scaffold materials are needed. In this work, we developed several micro- and nanofabrication techniques to pattern polyvinylidene fluoride (PVDF), a highly non-reactive, piezoelectric, thermoplastic fluoropolymer, which can serve as new constituents for advanced tissue engineering. We first studied the feasibility of PVDF patterning using conventional photolithography, soft lithography and microcontact printing. The fabricated patterns were systematically characterized by surface analysis techniques (FTIR, XRD) and used for cell culture studies. Then, we developed a study on electrospinning of PVDF nanofibers. Our results showed that the fabricated PVDF nanofibers were compatible with cell-based assays. Finally, we doped electrospun PVDF nanofibers with magnetic nanoparticles, which should make them excitable with a remote magnetic field.

Key words: PVDF, microfabrication, nanofibers, cell culture

Résumé

L'ingénierie tissulaire vise à réparer les tissus endommagés et à récupérer les fonctions biologiques correspondantes. Afin de restaurer un tissu endommagé tel que le système nerveux, la conception et la fabrication de nouveaux types d'échafaudages tissulaires sont nécessaires. Dans ce travail, nous avons développé plusieurs techniques de microfabrication pour le polyfluorure de vinylidène (PVDF), un fluoropolymère thermoplastique, non réactif et piézoélectrique, qui peut être utilisé pour la culture cellulaire et l'ingénierie tissulaire. Nous avons tout d'abord étudié l'adhésion et la croissance cellulaire sur des substrats en PVDF avec des motifs micro et nanométriques en utilisant différentes techniques de fabrication telles que la micro-photolithographie, la lithographie douce, l'impression par microcontact, etc. L'influence de la micro-structuration sur les activités piézo-électriques du PVDF a été caractérisée par différentes méthodes d'analyses de surface (FTIR, XRD). Par la suite, nous avons effectué une étude systématique sur la fabrication de nanofibres de PVDF et leur compatibilité avec la culture cellulaire. Enfin, nous avons démontré la possibilité de doper ces nanofibres avec des nanoparticules magnétiques ce qui les rends excitables à distance par un champ magnétique.

Mots clés: PVDF, micropatterns, nanofibres, culture cellulaire, ingénierie tissulaire

Acknowledgments

I am indebted to many people for making the time working on my PhD an unforgettable experience.

Firstly, I would like to give my deepest gratitude to my supervisor Prof. Yong Chen, who welcomed me in his group 5 years ago during my master. He helped me to get a PhD funding and gave me all what I needed to do my PhD in good conditions. His scientific advice and suggestions have been very helpful for the fulfillment of this work.

Secondly, I would like to express my gratitude to my advisors : Dr. Bruno Lepioufle from ENS Cachan and Dr. Juan Keymer from TU Delft from their valuable inputs and support.

My sincere thanks also go to the committee members who kindly accepted to evaluate this thesis work: Prof. Tarik Bourouina from ESIEE, Dr. Abdel El-abed from University Paris-descartes, Dr. Pascal Hersen from UPMC and Dr. Anne-Marie Haghiri-Gosnet from LPN CNRS.

I would like to thank professors, colleagues and friends from ENS for their instant encouragements, useful discussions and kind helps. They are: Prof. Damien Baigl, Dr. Jacques Fattaccioli, Dr. Jian Shi, Dr. Jinghua Tian, Dr. Xiongtu Zhou, Dr. Li Wang, Fan Zhang, Li Xin, Jie Hu, Jun Liu, Lianmei Jiang, Junjun Li, Jiaji Liu, Sisi Li, Zhitao Han, Hao Li, Dr. Malika Lounaci, Dr. Ayako Yamada, Dr. Antoine Diguet, Dr. Ian Broadwell, Naresh Kumar mani, Philippe Bouaziz, Yohan Farouz, Kalthoum Ben m'barek, Geraldine Hallais, Frédéric Bataille, Anne Halloppe and Dominique Ho tin noe. Special thanks to Lili Wang from the Biology department of ENS for providing the neurons I used for my experiments and to Dr. Pierre Barré and Damien Deldicque from the Geology department of ENS for the XRD measurements.

In addition I would also like to thank Prof. Helen Chan for welcoming me in her lab in the Hong-Kong Polytechnic University for 8 month during my PhD. Special thank to Pierre Allain who did his master thesis in Prof Chan's lab, working on PVDF and he is the one who introduced me to this amazing material.

Furthermore, I would like to thank Prof. François Taddei for welcoming me in his doctoral school which allowed me to meet so many interesting people to collaborate with and share the passion of crazy scientific projects. I would also like to thank the FDV doctoral school in its whole for providing such an ideal environment for students.

Special thanks to my doctoral school friends from the IVAI (In Vitro Artificial Intelligence) club: Jeremy Sibille, Quentin Perrenoud, Maéva Vignes, Renaud Renault and Mélanie Strauss for the quality of the scientific discussions, for their biological advices on my work and for the fun on the still ongoing projects of the club.

Finally, I would like to express my gratitude to Prof. Francis Rousseaux for putting me in the good tracks of research, for his always insightful advices and for his support.

This thesis has been supported for the first 3 years by the Fondation pour la Recherche Médicale (FRM). Their support is gratefully acknowledged.

Table of contents

List of Abbreviations

Polymers

PAA	poly(acrylic acid)
PAM	poly(acrylamide)
PCL	poly(ε-caprolactone)
PDMS	poly(dimethylsiloxane)
PEO	poly (ethylene oxide)
PEG	Polyethylene Glycol (PEG)
PET	poly(ethylene terephthalate)
PGA	poly(glycolic acid)
PLA	poly(lactic acid)
PLGA	poly(lactic-*co*-glycolic acid)
PMMA	poly(methyl methacrylate)
PTFE	poly(tetrafluoroethylene)
PU	poly(urethane)
PVA	poly(vinyl alcohol)
PVDF	poly(vinylidene fluoride)
PVDF-TrFE	poly(vinylidene fluoride-trifluoroethylene)

Microfabrication

FTIR	fourier transform infrared
NFES	near field electrospinning
NGC	nerve guidance channels
NIL	nanoimprint lithography
PFM	piezoresponse force microscopy
SAM	self assembled monolayer
SEM	scanning electron microscopy
TMCS	trimethylchlorosilane
XRD	x-ray diffraction

Proteins

PLL	poly-l-lysine
FN	fibronectin
LN	laminin
RGD	arginine-glycine-aspartic acid

Cells and tissues

BHK	baby hamster kidney
BMSC	bone marrow-derived stem cell
CNS	central nervous system
DRG	dorsal root ganglia
ECM	extracellular matrix
EC	endothelial cell
ESC	embryonic stem cell
MSC	mesenchymal stem cell
NSC	neural stem cell

Cell culture

DMEM	dulbecco's modified eagle's medium
FCS(BFS)	fetal calf serum (bovine fetus serum)
MEM	minimal essential medium
PBS	phosphate buffered solution

Outline

Tissue engineering aims at repairing damaged tissues and recovering the lost or degraded biological functions. The development of tissue engineering is based on cell culture and tissue formation in biomaterial scaffolds. Therefore, the proposed biomaterial should not only be non-cytotoxic but also manageable using appropriate processing technologies. Indeed, the proposed scaffolds should have designed shapes and suitable mechanical stiffness, wettability, porosity, biodegradability, etc. Ideally, the proposed scaffold should also allow mimicking of the natural cell microenvironment in order to produce a tissue with the same biological functions as found in a body. For this purpose, new design rules have to be worked out and new biomaterials have to be found. From this point of view, micro and nanofabrication technologies hold high potentials for bio-material processing that can be used for advanced tissue engineering. The future is promising but much has to be done.

One of the challenges now facing tissue engineering is the need of scaffolds for more complex functionality such as nerve reconstruction. In the world, several millions of new patients suffer from central nervous system injuries and those pathologies affect considerably their life. It is known that nervous system injuries do not heal themselves and that conventional surgical treatments are also limited in success rate. One solution is to use artificial scaffolds which are suited for nerve reconstruction. Among many important issues toward this end, the scaffold material has to be more functional, has to possess biomechanical stability, should be manageable by processing, and eventually excitable under control.

The purpose of this study is to develop a new approach for scaffold processing that can be used for neural tissue engineering. We have chosen polyvinylidene fluoride (PVDF), a highly non-reactive, piezoelectric, thermoplastic fluoropolymer, for this purpose since it can be actuated both electrically and mechanically. Accordingly, we developed a systematic investigation on the processing ability of PVDF and their applicability in cell culture and enhanced outgrowth of neurites.

This thesis is organized in five chapters:

In chapter 1, we firstly introduce the biological background which is required for this work. We describe cells and cell interaction with its microenvironment. Then, different methods including conventional photolithography, soft lithography and microcontact printing, are overviewed for the fabrication of topographical and biochemical cues which serve as extracellular matrix for cell culture and tissue engineering.

In chapter 2, we present the fabrication of micropatterns of PVDF. We begin with a brief description of the physical and chemical characteristics of PVDF. Then, we show the results obtained by using different microfabrication techniques. To this regard, we demonstrate that photolithography is not suited for PVDF processing and that conventional hot embossing does not allow producing clear patterns of PVDF due to the presence of important quantity of PVDF residuals in the recessed areas. Instead, a capillary assisted hot embossing is applicable to achieve high quality PVDF micropatterns. Finally, we show the effects of surface modification of PVDF by using air plasma and reactive ion etch (RIE) techniques. In particular, we demonstrate that microcontact printing allows creating well-defined protein patterns on a flat PVDF surface.

In chapter 3, we study the effects of PVDF micropatterns on cell adhesion and spreading. First, we review different strategies for cell adhesion and growth on PVDF surfaces. Then, we show that both air plasma and oxygen containing RIE are efficient to enhance cell adhesion whereas the SF_6 containing RIE is efficient to prevent cell adhesion. Our results of cell culture on patterned PVDF show that not well-defined fibrous-like cell clusters are formed on the pattern of conventionally hot embossing but well-defined cell sheets are formed on the pattern of capillary assisted hot embossing. More interestingly, cells grow with a good selectively on fibronectin patterns defined by microcontact printing. These results are highly promising considering the fact that PVDF is natively cytophobic but not cytotoxic.

In chapter 4, we present the fabrication of aligned PVDF-TrFE nanofibers by using electrospinning techniques. To achieve a precise deposition of the fibers, we first evaluate the applicability of near field electrospinning techniques. It turns out that only large size and flat PVDF fibers are obtainable because of the difficulty in short distance solvent evaporation. Then, patterned electrodes are used, showing good results in terms of fiber diameter and alignment quality. In addition to scanning electron microscopy, X-Ray Diffraction(XRD) and Fourier Transform Infrared Spectroscopy (FTIR) are both used for characterization, showing an enhanced piezoelectric crystalline β-phase in produced PVDF nanofibers after annealing and ice quenching. Finally, we study the neuronal culture on aligned nanofibers and show an enhanced control of outgrowth of the neurites.

In the last chapter, we describe the inclusion of magnetic nanoparticles in electrospun PVDF nanofibers. The purpose of this study is to achieve a remote mechanic activation of the piezoelectric nanofibers with a magnetic field. We first present the fabrication of PVDF-TrFE nanofibers with embedded Fe_3O_4 nanoparticles. The fabricated nanofibers are observed by scanning electron microscopy as well as XRD and FTIR to show that the inclusion of magnetic nanoparticles does not affect the crystalline phase of the fibers. Finally, the fabricated nanofibers are used for cell culture test, showing no cytotoxicity.

In appendix of this manuscript, we present two studies performed or completed during this work. The first one concerns capillary and template assisted assembly of gold nanoparticles and the observation of surface plasmon resonance that can be used for high sensitivity biosensors. The second study concerns the initial stage of a research project on microfluidic patch clamps, which could not be continued due to several technical difficulties.

CHAPTER 1

Introduction

In this chapter, we review the fundamental notions of cells, cellular microenvironment, and microfabrication techniques for the production of artificial extracellular matrix. Firstly, we introduce the concept of extracellular matrices and discuss how they can be fabricated for in vitro cell culture studies, in 2 dimensions as well as in 3 dimensions. Secondly, we introduce the piezoelectric properties of PVDF and the means to measure it. Then, we present lithography based microfabrication techniques including photolithography and soft lithography, which will be used in Chapter 2 to define PVDF patterns. Finally, we describe electrospinning techniques which will be used in Chapter 4 to produce PVDF nanofibers.

1.1 Cell microenvironment

The cell is the basic unit of life. The inside of eukaryotic cells is organized in several organelles (**Fig. 1.1**) which ensure the machinery of the cell and the nucleus which contains its genetic material. The inside of the cell is separated from the outside by the plasma membrane which is porous, permitting interactions with cellular environment.

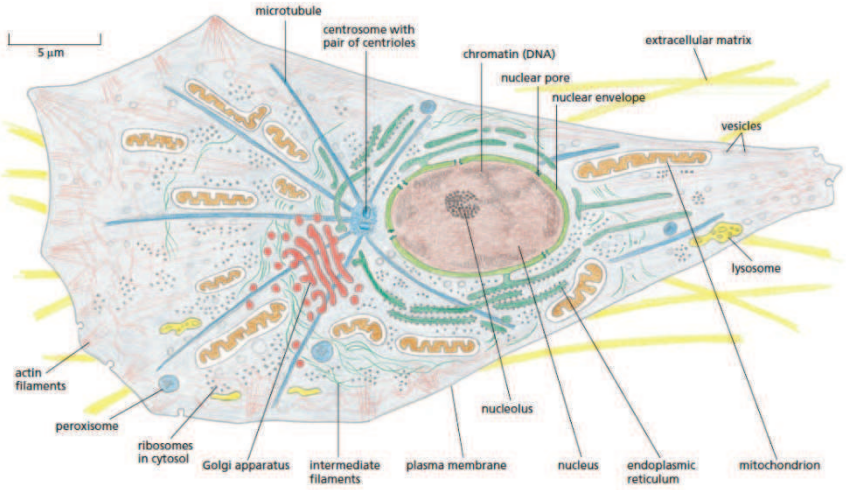

Figure 1.1 Schematics of a eukaryotic cell. (From [**1**])

The cytoskeleton provides physical support of the cell. It is composed of a network of 3 filamentous structures: actin microfilaments, intermediate filaments and microtubules (**Fig. 1.2**). Whereas microtubules and actin microfilaments are common to all type of cells, intermediate filaments vary with the function of the cell type. The cytoskeleton is useful not only to support physically cells but it is also involved in major cellular functions: movement of the cells, division and intracellular trafficking and endocytosis.

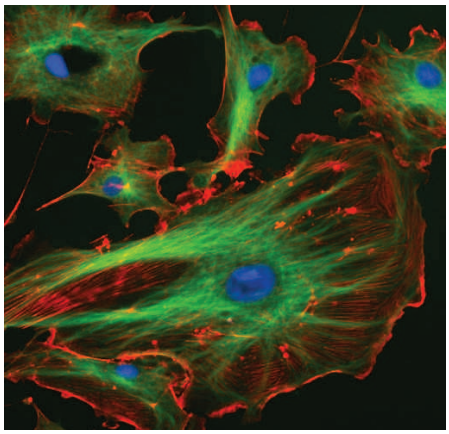

Figure 1.2 Confocal image of the eukaryotic cytoskeleton. Actin filaments are stained in red, microtubules in green and nuclei in blue. (From [**2**])

Most cells of multicellular organisms are organized in clearly defined tissues in which cells maintain strong interaction between themselves and the extracellular material. Cells can attach together through cell-cell junctions or bind to the extracellular materials they secreted.

Cellular functions are regulated by both genetic materials and cellular microenvironment, including extracellular matrix, soluble factors and cell-cell interaction. As illustrated on **Fig. 1.3**, vertebrate cells are organized in two main types of tissues. In **epithelial tissue**, cells are organized in sheets attached to the basal lamina (a form of extracellular matrix) where cells bond together tightly. On the opposite, in **connective tissues**, cells are anchored in the extracellular matrix. Accordingly, the cellular microenvironments of these two tissue types are significantly different. For example, they differ from each other in both topographical organizations and mechanical properties due to their different cellular functions.

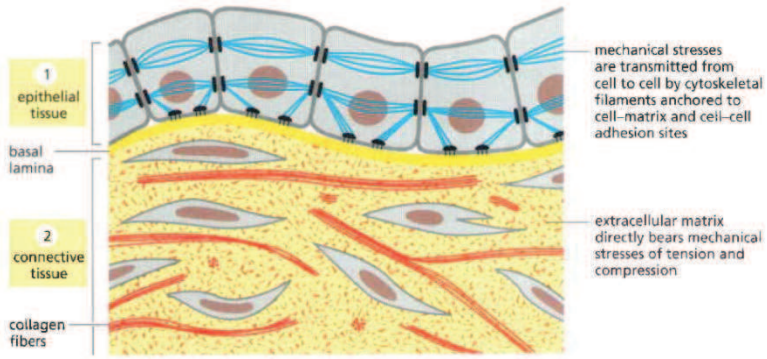

Figure 1.3 Schematics of the organization of cells in 2 types of tissues: connective tissue and epithelial tissue. (From [**1**])

1.1.1 Cell Junctions

As shown in **Fig 1.4,** four types of cell junctions can be distinguished:

a- Anchoring junctions: Anchoring junctions happen between 2 cells or between a cell and the ECM. Their main role is the structural support as those junctions are linked to the cytoskeleton of cells. Two families of trans-membrane proteins are responsible of anchoring junctions.

- ***Adherent junctions:*** Cadherins are mainly responsible for cell-cell junctions. They are homophilic which means they can only bind to the same type of receptor on the neighboring cell. Classical cadherin binds to actin filaments of the cytoskeleton, forming adherent junctions. Adherent junctions coordinate the actin based motility of adjacent cells.
- ***Desmosome junctions:*** Cell adhesion proteins such as desmoglein and desmocollin, a sub-family of cadherins which are also homophilic. However, the desmosome junctions are different from cytoskeleton anchoring sites since they are linked to the intermediate filaments of the neighboring cells. Desmosome junctions give mechanical strength.
- ***Integrins****:* Integrins link the cytoskeleton of cells (actin filaments) to the ECM which includes for example fibronectin.
- ***Hemidesmosomes:*** They are protein complex which attach the keratin of the cytoskeleton to the ECM [**4**].

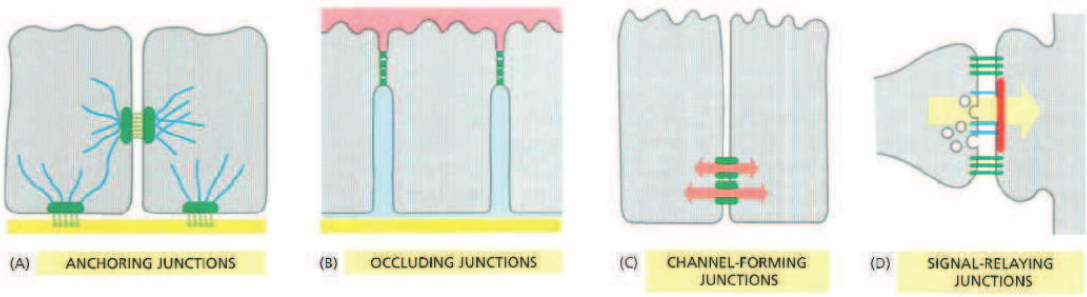

Figure 1.4 Schematics of the 4 types of junctions. (From [**1**])

b- Occulting Junctions: Tight junctions (in vertebrates) are the result of particular trans-membrane proteins that make an impermeable barrier between 2 sheets of epithelial cells. This kind of junction is often seen when the intracellular transport has to be favored with

respect to the trans-cellular transport. For example, in the gut lumen it lets the nutrients passing from the gut lumen to the bloodstream (**Fig 1.4b**).

c- Channel Forming Junction: Gap junction (in animals) provides a links directly the cytoplasm of adjacent cells letting ions and small molecules pass freely from cell to cell. Gap junctions are present in most cells of vertebrate. Each gap-junction is made of 6 trans-membrane connecting subunits. Gap junctions provides electrical coupling for heart cells and neurons (electrical synapse).

d- Signal relaying junctions: Electrochemical synapses are signal relaying junctions. Many types of cell adhesion molecules act in parallel to create a synapse.

1.1.2 The extracellular matrix (ECM)

The extracellular matrix is composed of a mesh of proteins and molecules secreted by cells [**5**]. The ECM provides structural support to cells but also act as a local storage for growth factors (**Fig. 1.5**). The deposited proteins are mainly as follows

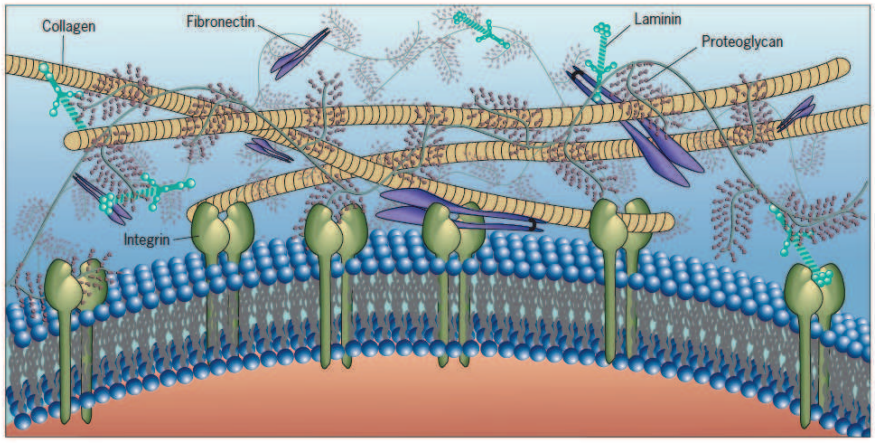

Figure 1.5 Schematic of the macromolecular organization of the ECM. (From [**3**])

a- Structural fibrous proteins

These proteins, including both collagens and elastins, are secreted by the cells and auto-assembled into 3D fibrous meshes.

- ***Collagens*** are the most abundant protein in the human body (25% of all proteins) and in most animals. Collagens are the molecules that contribute the most to the ECM structural support as collagens have a high tensile strength. Collagens are mostly

secreted by fibroblasts in the form of procollagen. After 2 transformation, troprocollagen aggregates in fibrils for most types of collagens (**Fig. 1.6**). To date 28, types of collagens have been identified [**3, 6**].

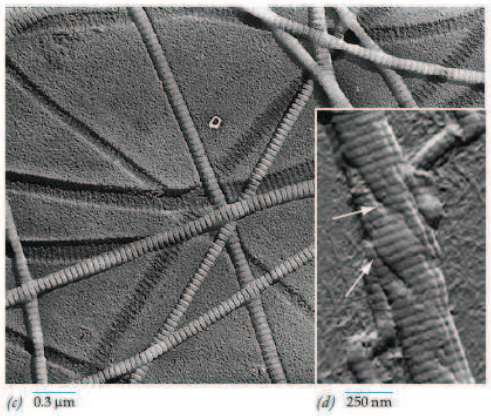

Figure 1.6 Structure of collagen: (**a**) SEM picture of human collagen fibrils, (**b**) AFM picture of a single fibril showing that its subcomponent are twisted. (From [**3**])

- ***Elastins*** are the main component of elastic fibers. They give the elasticity to the ECM as many tissues are strong but elastic (e.g.: skin, blood vessels). Elastins are strongly hydrophobic and are secreted by fibroblasts and muscle cells in the form of tropoelastin and are assembled into elastic fibers. Elastic fibers are composed of elastin covered with micro-fibrils serving as scaffolds. Elastic fibers are at least 5 times more extensible than a rubber band of the same cross-sectional area [**1**]. Elastins represent 58 to 75% of the dry weight of dog arteries [**7**] as shown on **Fig. 1.7**.

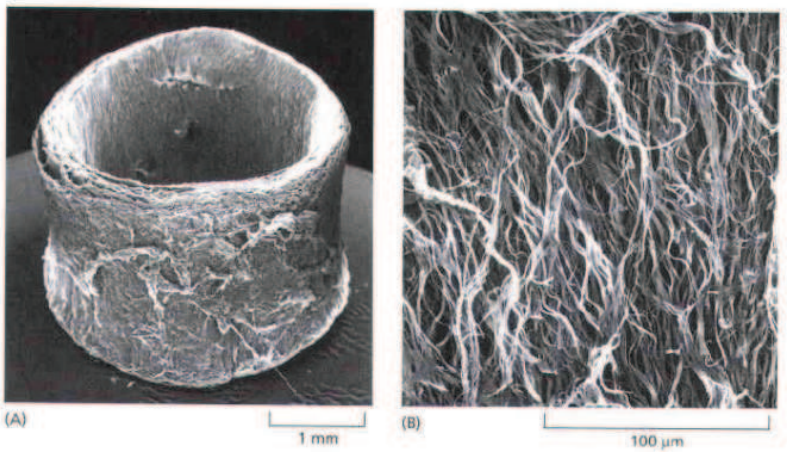

Figure 1.7 SEM picture of dog's aorta after digestion of all ECM components except elastin: (**a**) low magnification, (**b**) high magnification showing individual elastin fibers. (From [**1**])

b- Adhesion proteins

- ***Fibronectin*** is a protein that binds to integrins receptor of cells. Fibronectin adhere also to collagen, fibrin and heparansulfate proteoglycans. Each fibronectin molecule is composed of 2 polypeptides chains containing each 5-6 domains divided into structural modules. There are 30 structural modules that can be combined. For example it contains the RGB structural module (**Fig 1.8**) that binds specifically to integrins.

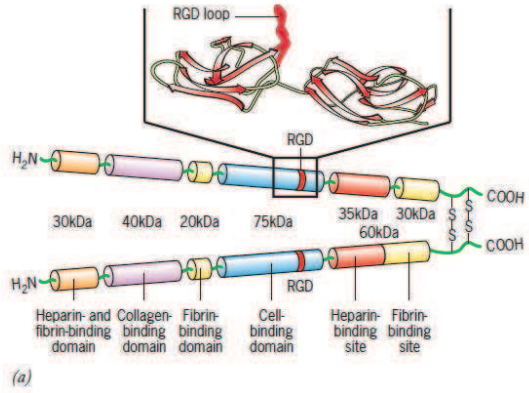

Figure 1.8 Schematics of fibronectin molecule. (From [**3**])

- ***Laminins*** are the main components of basal lamina. In vitro it organizes itself in network but to be organized as sheet it requires intervention of cells. Laminins are organized in 3 subunits α-chain (α-chain, β-chain and γ-chain) with genetic variants for each. Combination of those variants makes a total of 15 types of laminins. For example Laminins 111 is involved in neuron outgrowth. Laminins can bind to other ECM such as collagens, nidogens, and integrins as they have the required attachment sites (**Fig 1.9**).

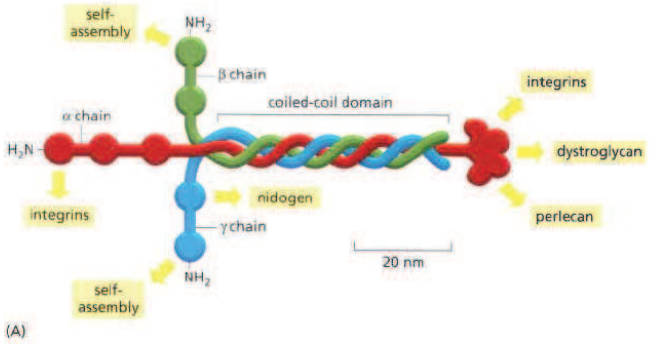

Figure 1.9 Structure of the laminin molecule. (From [**1**])

c- Proteoglycans and glycosaminoglycans (GAGs)

Proteoglycans are composed of a core protein molecule with 2 glycosaminoglycans (GAGs) covalently attached. As proteoglycans are negatively charged, they attract sodium ions in solution which attract water molecule by osmosis forming an highly hydrated gel that help the ECM to maintain its hydratation and that help collagen in its structural support role. The principal proteoglycans are: heparan sulfate, chondroitin sulfate and keratan sulfate.

Hyaluronic acid is a GAGs that is not found as a proteoglycan. It is also extracellular filler but plays an important role in different processes (embryonic development, healing process, inflammation, tumor development) as it interacts with the CD44 transmembrane receptor [**3, 5**].

1.2 Engineering of microenvironment

Constant progress in microfabrication techniques allows researchers to engineer microenvironments with smaller and smaller features. Nowadays it is possible to fabricate substrate on a whole range of scales from the μm scales to access single cells to few nanometers which is the size of a few DNA base pairs. Moreover, microfluidics which is the technology to control liquids at the micro-scale and beyond [**8-9**], is particularly interesting for biological studies and for bioengineering as most biological process happen in liquid phase.

This opens the doors to many applications in biomedical engineering and especially for regenerative medicine. The principle is to use microfabrication techniques to mimic natural microenvironments in order to foster regeneration of injured tissue as some tissues such as neural cells do not have the ability to recover their normal functions after an injury. Axons of neurons in humans can be very long (up to one meter for sciatic nerve axons) [**10**] and their function depends of their tight connectivity with other neurons. During morphogenesis, neurons receive constant chemical and electrical cues that guide the axon growth cone to find their target which is possible due to the proximity cells at this stage of development. However if the CNS (Central Nervous System) of an adult is injured and axons are cut, most of the time it will not be able to regrow because the chemical cues of its target are out of reach. The neuron in absence of electrical stimulation will degenerate and die. So finding ways to guide

axons grow and more generally cellular growth is very important and has immediate clinical application.

1.2.1 Microscale control of biomolecular cues

Cell behavior is partially regulated by a multitude of biomolecular cues present in the ECM. Those biomolecular cues can be secreted by cells in immediate proximity (autocrine, juxtacrine and paracrine signaling) or by distant cells (endocrine signaling). Some of these molecules bound to cells directly, other bound to the extracellular matrix. [**11-12**]. For many biomolecules, cell response is modulated by the molecular concentration in the form of gradients. Gradients can be steep if a cell is exposed to different biomolecular concentrations or shallow if a cell is exposed to a single concentration.

a- Microfluidic generation of gradients

Microfluidics can be used to generate concentration gradients with size on the order of biological cells (10-100μm) [**13-14, 17-18**]. *Jeon et al.* have been the first group to use microfluidics to generate complex concentration gradient with different concentration profiles [**13-14**]. Gradient generation is achieved by sequentially splitting, mixing and merging. **Figure 1.10a** shows a general view of the chip. The inlet (on top) is composed of 3 input connected to 3 solutions of different colors: green dye (left), red dye (right) and a 1:1 mix of red and green (middle). The output (bottom) is a large channel (900μm) where we can see the gradient of colors from green (left) to red (right) which correspond to a gradient of dye concentration.

The splitting process can be understood with an electronic analogy between electrical resistance and fluidic resistance (**Fig. 1.10b**).

The resistance R_H of the vertical channels is considered negligible compared to the resistance R_v of the horizontal channels because the vertical channels are 20 times longer than horizontal channels. This approximation can be done because Poiseuille's law [**15**] shows that in the case of laminar flow, fluidic resistance is linearly proportional to the length of the channel.

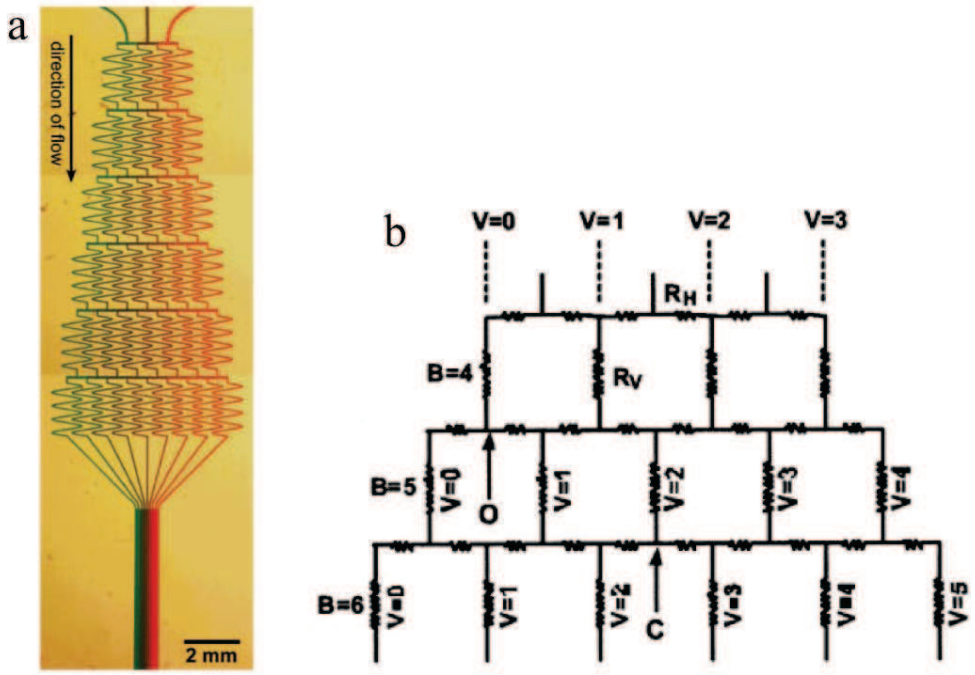

Figure 1.10 Microfluidic gradient generation: (**a**) overview (From [**14**]), (**b**) schematics of the gradient generation process (From [**13**]).

The splitting ratio will be influenced by the addition of the fluidic resistances. For each splitting point of the circuit the relative portion of the flow going to the left (F_{left}) is calculated using formulae (**1**) and the relative portion of the flow going to the right is calculated using formulae (**2**) :

$$F_{Left} = \frac{(B-V)}{B+1} \quad (1)$$

$$F_{right} = \frac{(V+1)}{(B+1)} \quad (2)$$

For example on the point C (**Fig. 1.10b**), the fluidic resistance is equal on the left and on the right, thus the splitting ratio will be 1/2 which verifies the Formulae (**1**) and (**2**):

$$F_{Left} = F_{right} = \frac{(B-V)}{(B+1)} = \frac{5-2}{6} = \frac{1}{2}$$

At the point 0: $F_{Left} = \frac{(B-V)}{(B+1)} = \frac{4-0}{4+1} = \frac{4}{5}$ and $F_{right} = \frac{(V+1)}{(B+1)} = \frac{0+1}{5} = \frac{1}{5}$

The mixing is realized in the serpentine channels (**Fig.1.10a**) it is based on the diffusion mixing principle [**16**]. When the flow is laminar the 2 flows are separated but the in the interface between the 2 flows there is an interdiffusion region where the faster diffusing analyte diffuses into the slower diffusing one (**Fig 1.11**).

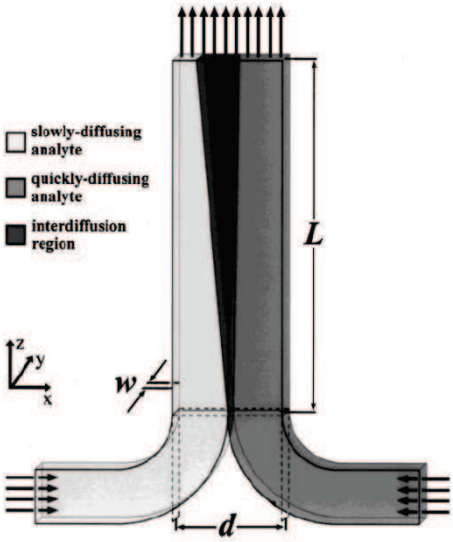

Figure 1.11 Illustration of the diffusion in microchannels. (From [**16**])

As the diffusion is proportional to the time the two liquids are in contact, the role of the serpentine after each T-junction (**Fig 1.10a**) is to increase this time in order to obtain diffusive mixing. Finally the liquids are merged together at the bottom of the chip. *Dertinger et al.* [**14**] managed to obtain complex gradient profile (**Fig 1.12**).

Concentration gradient have been used to study many biological process: basic cellular function [**19-21**], cell chemotaxis [**27-29**] and specially its implications in cancer treatments [**22-26**], drug treatments and toxicity studies [**30-32**] as well as neuronal growth [**33-37**].

Some cells such as neurons are sensitive to shear flow and in this case conventional fluidic gradient generation is not well adapted. In order to solve these problems, an alternative technique has been developed [**38-40**] where the fluidic gradient generator is used to adsorb biomolecules on a surface with a gradient. The fluidic channels are removed and cells can be cultivated on this substrate.

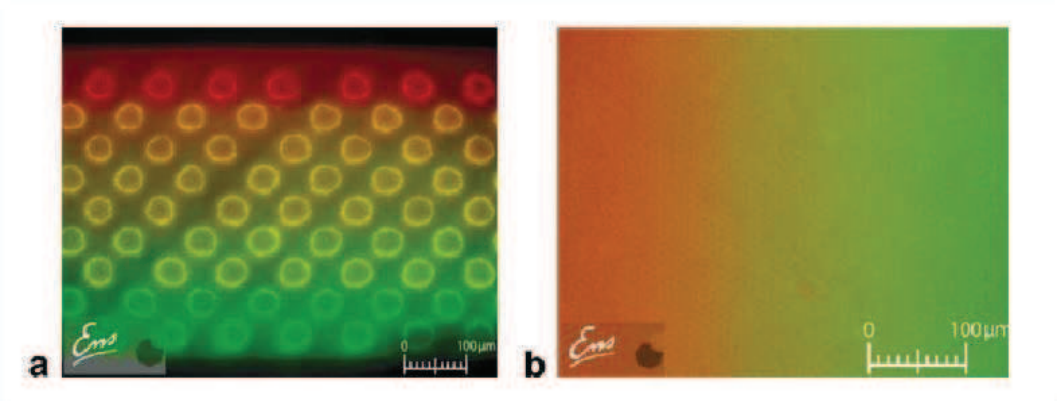

Figure 1.12 Surface functionalized (PDMS stamps) with a gradient of protein. (BSA-FITC in green, BSA-Cy3 in red, the other colors are a mix of different proportions of both). The stamp comprises micropillars (**a**) 40 µm of diameter, (**b**) 5 µm of diameter. (From [**41**])

b- Imprinting of protein patterns by microcontact printing

Microcontact printing was initially developed by *Whitesides et al.* as one of the soft-lithography techniques. Those techniques are called "soft lithography" as they do not use photolithography but use a micropatterned elastomer (PDMS: PolyDiMethylSiloxane) to generate micropatterns [**42**]. The particular application of microcontact printing was to pattern surfaces with SAMs (Self-Assembled Monolayers) [**43-45**] which can be used as mask [**46**]. Rapidly after, it has been used to pattern proteins [**47-48**] and mammalian cells [**49-51**].

Technical aspects of those techniques will be developed more in details in the paragraph 1.5 of this chapter. Briefly, the principle of microcontact printing is the following: a solution is incubated on a PDMS micropatterned stamp in order to adsorb molecules on the surface of the stamp. Then the stamp is placed in contact with the surface in order to transfer the patterns of molecules.

Microcontact printing is now widely used in biology and bioengineering particularly to create patterns of cell-adhesive ECM proteins (Fibronectin, Laminin). New process use second step of PEG or PEG-PLL backfilling is used to passivate areas without protein [**52-53**]. It is also possible to pattern multiple layer of protein in order to make more complex structures (**Fig. 1.13**) [**54**] and to bond covalently protein to the substrate to provide long term adhesion [**55**].

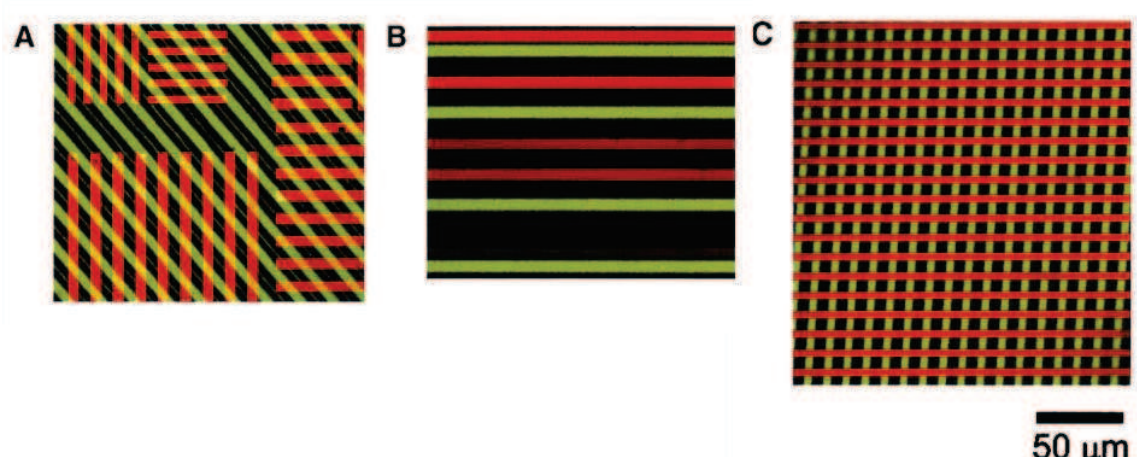

Figure 1.13 Different patterns of proteins imprinted on a surface by multilayer microcontact printing: (**a**) 2 different proteins, (**b**) 16 different proteins imprinted. Adsorption protein has been achieved through a fluidic network. (**c**) 3 different proteins printed simultaneously with a single stamp. (From [**54**])

Due to the strong adhesion of the cells on proteins, microimprinted patterns can be used to deform cell at the single cell level. This new tool is very useful as allows researchers to study biophysics of cells and the links with cellular functions. Physical constraints are believed to play important part in critical physiological process such as morphogenesis, cell division, metastasis of cancer, etc…

Chen et al. [**56**] used "adhesion islands" of proteins of different size (5µm-40µm) surrounded by anti-adhesive polymer. They showed that proliferation of cells increase with adhesion islands areas and that a decrease of adhesion area triggers cell apoptosis (programmed cell death).

Théry et al. [**57**] used patterns of adhesive proteins of different shapes to study influence of the ECM on the cell division and particularly on the orientation of the mitotic spindle. **Fig. 1.14** shows fluorescent images of the fibronectin patterns (**Fig. 1.14a**) and confocal images assembled of different layers with cortactin and ezrin tagged to show localization of the mitotic spindle. They showed that the shape of the ECM determines mitotic spindle orientation (**Fig. 1.14c**). This method present interests to study morphogenesis [**58**].

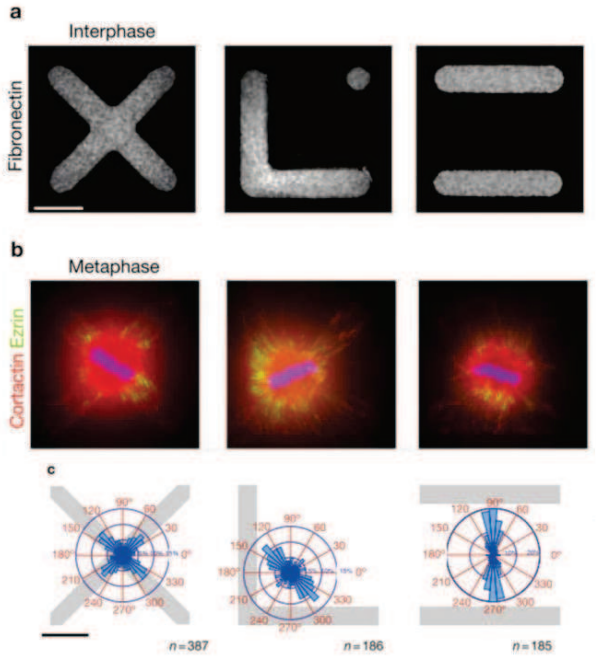

Figure 1.14 Study of the influence of ECM on the orientation of the mitotic spindle: (**a**) fibronectin patterns, (**b**) confocal fluorescent images (z-stack) with cortactin and ezrin tagged, (**c**) measurement of the mitotic spindle distribution. (From [**57**])

Recently, *Tseng et al.* [**60**] used this method of control of cell shape in addition with a control of substrate (poly-acrylamide gel) stiffness to control cell microenvironment and to measure cell contraction levels. They showed that cancer cells are more contracted that normal cells and that contraction levels varies in function of tumorigenic signals.

Another interesting application of microcontact is the engineering of neuronal networks. [**61-73**]. Connectivity of neurons is more important than the neuronal cells alone and so ability to control neuron patterning and influence its connectivity is of primary interest [**61**] as it can have many applications in brain machine interfaces, in regenerative medicine of the central nervous system and more globally in the understanding of brain by reverse engineering approaches

Kam et al. [**63**] used microimprinted Poly-L-lysine conjugated laminin to make neurons 'rat hippocampus neurons) adhere and grow on the surface and they showed that the laminin is responsible of the specific neuronal adhesion and axon outgrowth (**Fig. 1.15a**).

Wyart et al. [**64**] used microimprinted patterns of PLL to create neuronal network with different topologies (**Fig 1.15b**). They observed by voltage clamp that the physiology of the neurons is normal and the presence of inhibitory and excitatory synapse which validate this approach for studying neuronal process and especially synaptic connectivity.

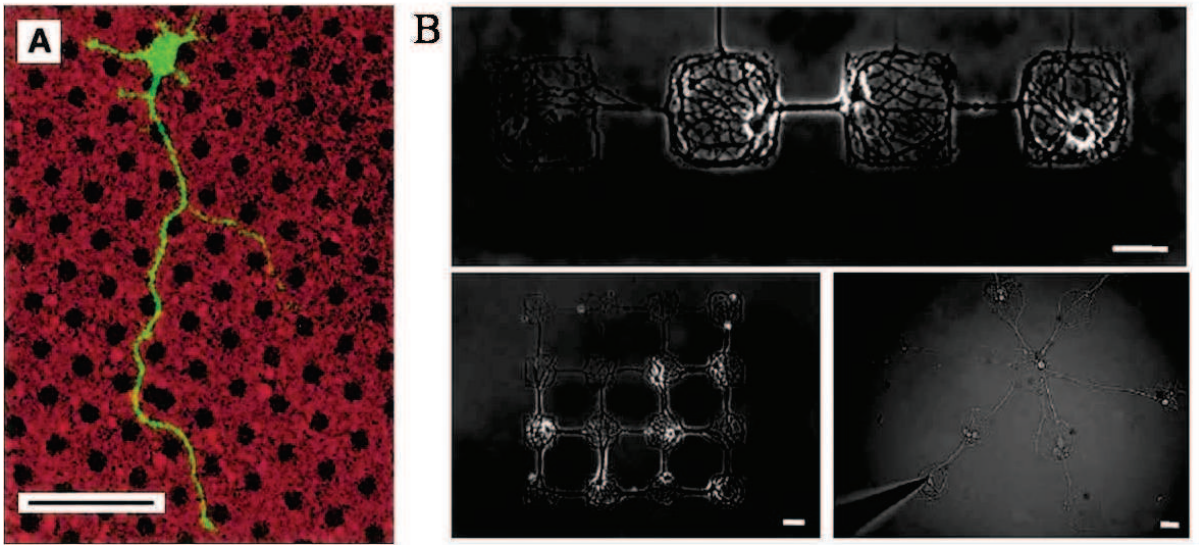

Figure 1.15 (**a**) Rat hippocampus neuron cultured on PLL microimprinted pattern after 1 day. The scale bar is 50 µm. (From [**63**]) (**b**) Neurons cultured on PLL patterns with different topologies: linear network, 4x4 matrix and star. (From [**64**])

1.2.2 Topographical control of cell

Overview of the effects of surface topography

Effects of surface topography on cells in vitro has been observed since 1911 [**74]** and contact guidance which is the orientation of cells on grooves and lines has been observed since 1945 [**75-79**] however, experimental techniques available at this time could not explain the biomolecular mechanism behind this phenomenon.

Progress in the semi-conductor industries allowed the researchers in the 1990's to fabricate routinely substrate with features on the order of cells (few µm) and to observe the effects of engineered microstructures on cell behavior [**80-85**]. *Clark et al.* **[81]** showed early that cells are affected by discontinuities. They cultured BHK (Baby Hamster Kidney) cells on steps with different height (1, 3, 5, 10, 18µm) and they observed alignment of cells on the edge of the step (**Fig. 1.16a**) and that higher steps provide higher alignment. They also observed that probability of crossing the step is the same in both directions (descent or ascent).

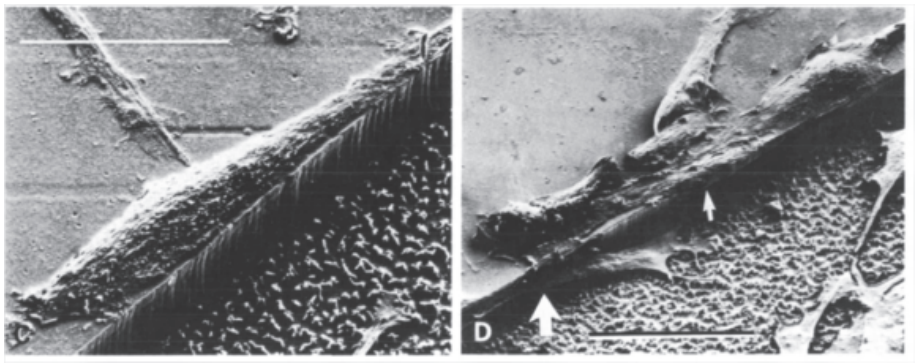

Figure 1.16 (**a-b**) BHK Cells cultured on different micropatterned substrates with 10 µm steps. (**a**) Cell aligned along the edge of the step. (**b**) Cell is aligned both on top and bottom surface. (From [**81**])

Later experiments (**Fig 1.17**) by *Clark et al.* **[82]** on micropatterned grooved substrates (4-24 µm pitch, 0.2-1.9 µm depth) confirmed previous results and showed that a decrease of pitch increase cell alignment (Pitch = groove + ridge).Cells on grooves with 12 µm pitch with 2 µm depth (**Fig 1.17b**) are aligned across several lines whereas cells on grooves with 6 µm pitch with same depth are perfectly aligned (**Fig 1.17d**). They also found that groove depth is more important parameter for cell alignment than pitch: On 6 µm pitch with 0.3 µm depth (**Fig 1.17c**), cells present no alignment compared to the cells on the same pitch substrate but with 2 µm groove depth which are perfectly aligned (**Fig 1.17d**).

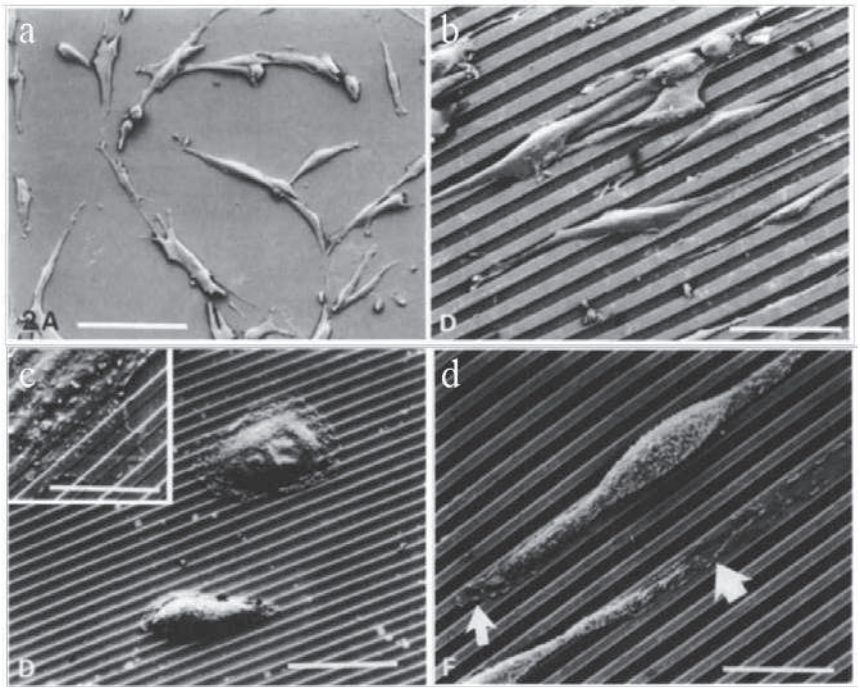

Figure 1.17 (**a-b**) BHK Cells cultured on different micropatterned substrates: (**a**) planar substrate, (**b**) 12µm pitch, 2µm deep grooves, (**c**) MDCK cells on 6µm pitch, 0.3µm groove, (**d**) MDCK cells on 6µm pitch, 2µm deep grooves. Scales bar are (**a**) 120µm, (**b**) 54 µm, (**c**) 60µm and (**d**) 30µm. (From [**82**])

Influence of topography on cell alignment has also been demonstrated at the nanoscale: *Teixeira et al.* [**84**] found that cells (Human corneal epithelial cells) are sensitive to topographies as small as 70 nm patterns in silicon. They confirmed that showed that when the pitch of the lines is reduced to 400 nm (**Fig. 1.18**) cells present a higher degree of alignment than cells on lines with 4000 nm pitch (**Fig. 1.19**).

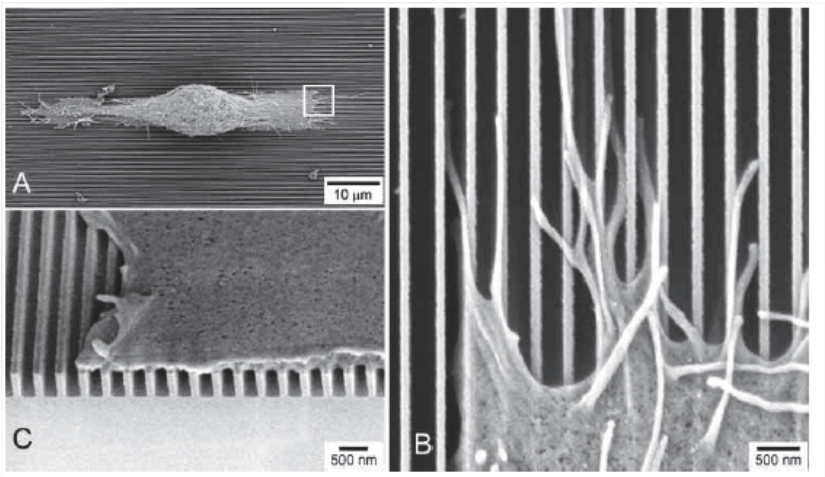

Figure 1.18 SEM images of cells cultured on patterns with 400 nm pitch 600nm depth. (**a**) Cell aligned along nanostructured substrate. (**c**) Cross-sectional image of cell patterned substrate. (**b**) Filopodia are oriented by topography. (From [**84**])

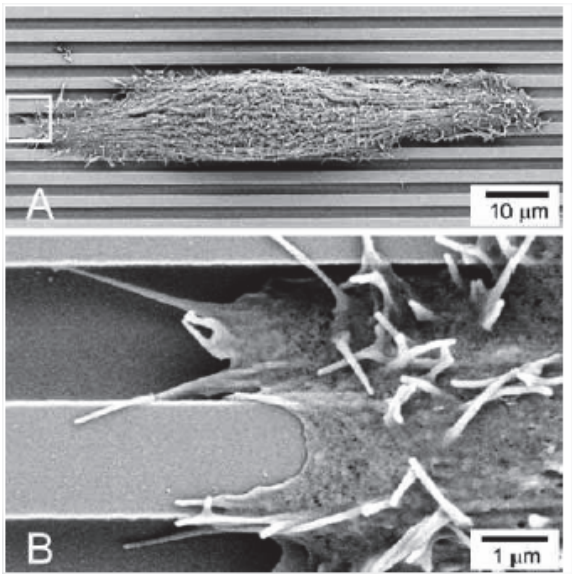

Figure 1.19 SEM images of cells cultured on patterns with 4000 nm pitch with 600nm depth. (**a**) Cell aligned along microstructured substrate. (**b**) Lamellipodia were able to adhere to the floor of the grooves on 2100 nm wide grooves. (From [**84**])

When the pitch is reduced to 400 nm, Filipodia are aligned along the patterns (**Fig 1.18b**) and lamellipodia do not touch the bottom of the grooves (**Fig 1.18c**). However when the pitch is increased, the lamellipodia where able to adhere to the bottom of the grooves and filipodia where oriented perpendicularly to the patterns as well as along the patterns (**Fig. 1.19b**).They also confirmed that pattern depth is more important than the pitch as cells cultured on 150nm grooves presented the same degree of alignment independently of the pitch.

Experiments have been also conducted on isotropic topographies such as micropillars, nanopits and nanopots. *Craighead et al.* [**83**] observed that cells attach and grow preferably on the top of the pillars that on the silicon surface. **Fig. 1.20** shows astrocytes cultured on 0.5 µm micropillars with staining of focal contact in green (with vinculin). We can see that focal contact points are located on top of the pillars and that the cell membrane does not touch the silicon surface. They also showed that this effect is independent of the micropillars height and pitch.

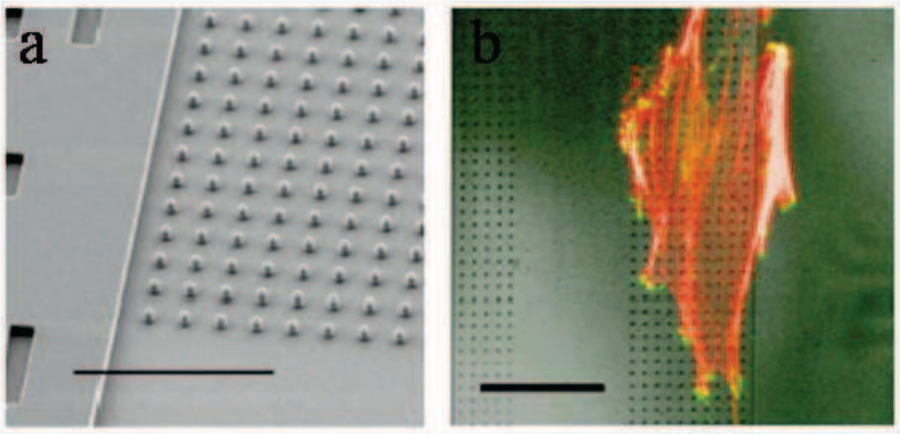

Figure 1.20 (a) SEM picture of 0.5 µm silicon micropillars spaced by 2 µm. **(b)** Primary cortical astrocytes stained for vinculin (focal contacts) (shown in green) and actin filaments (shown in red). Scales bar are **(a)** 20µm, **(b)** 50µm. (From [**83**])

Pan et al. [**86**] studied the effects of different height of pillars on cells. Similarly to *Craighead,* they observed that cells adhere on the top of the pillar but unless Craighead, *Pan et al ,* observed that the cell membrane is deformed by the micropillars and that this deformation increase with micropillars height (**Fig. 1.21**). We can also see that the cells on 5 µm high micropillars are more spread (**Fig 1.21c**) and that the cytoskeleton (in red) is disorganized. *Dickinson et al.* [**88**] obtained comparable results but they showed that cell spreading on micropillars is highly dependent to the cell line as different cell lines have different cytoskeleton properties.

In their case they showed that cancerous cells (MG-63 and SaOs-2) presented a deformation of cytoskeleton and nuclei on micropatterns whereas healthy HOP (Human OsteoProgenitor) cells were not affected by the micropillars.

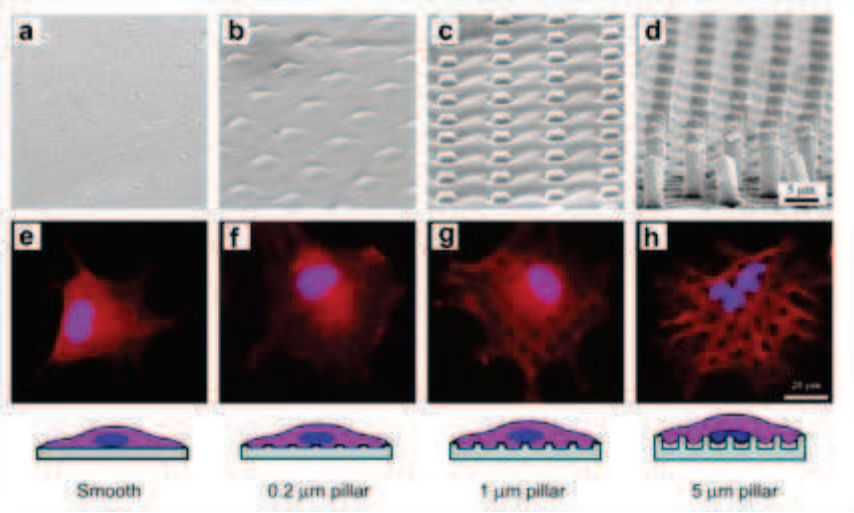

Figure 1.21 BMSCs cells cultured on PLGA micropillars (3 µm width, 6 µm spacing) **(a)** Control smooth surface. (**b**) 0.2 µm height micropillars. (**c**) 5 µm height micropillars. (From [**86**])

The 5 µm height micropillars interact also with the organelles of the cells and specifically the cell nucleus. We can see clearly on (**Fig. 1.21c**) that the cell nucleus is elongated and constrained by the micropillars behind it. To demonstrate this hypothesis they fabricated special micropillar patterns aiming at changing the cell nucleus shape by constraining it (**Fig 1.22).**

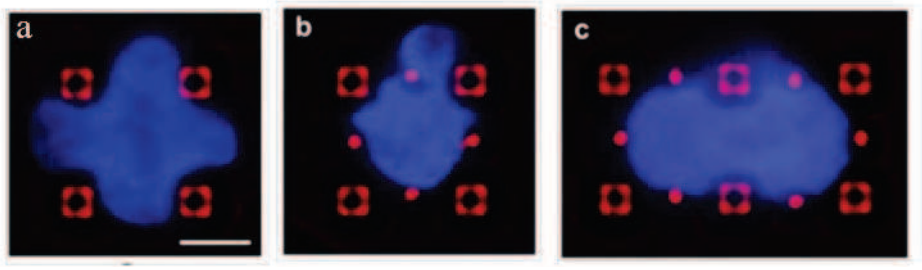

Figure 1.22 (a-b-c) BMSCs cells cultured on PLGA micropillars arranged to induce cell nucleus constraint. (From [**86**])

Davidson et al. [**87**] showed that cells are still viable after nucleus deformation caused by the micropillars. However it is strongly believed that this topographical constraint of the nucleus impede or slow down some cellular functions such as proliferation.

Nikkhah et al. [**90**] used micropillars of different height to cultivate MSCs on microenvironment of different stiffness. They showed that Human MSCs grown on the more rigid substrate with shorter micropillars (0.97μm) spread normally and present enhanced ostreogenic markers whereas MSCs on the taller micropillars (12.9μm) which have the lowest stiffness present a rounded shape. More recent studies [**91-92**] confirmed the major role of substrate stiffness in the cell differentiation.

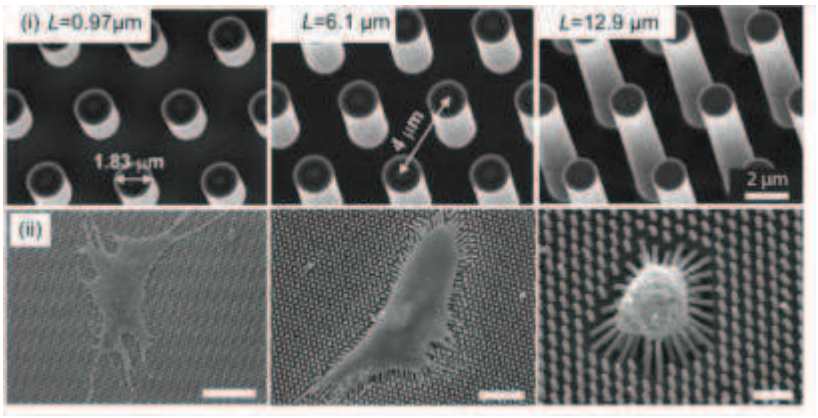

Figure 1.23 The effect of stiffness on MSC morphology and differentiation using PDMS micropillars of varying heights. Scale bars, 50 μm (bottom left), 30 μm (bottom middle), 10 μm (bottom right). (From [**89-90**])

Neuronal growth on microstructures has been studied extensively as way to influence neurite outgrowth and localization [**93-96**]. *Craighead et al.* [**83**] showed that neuron soma adhere preferably on micropillars rather than on bare silicon (**Fig. 1.24**).

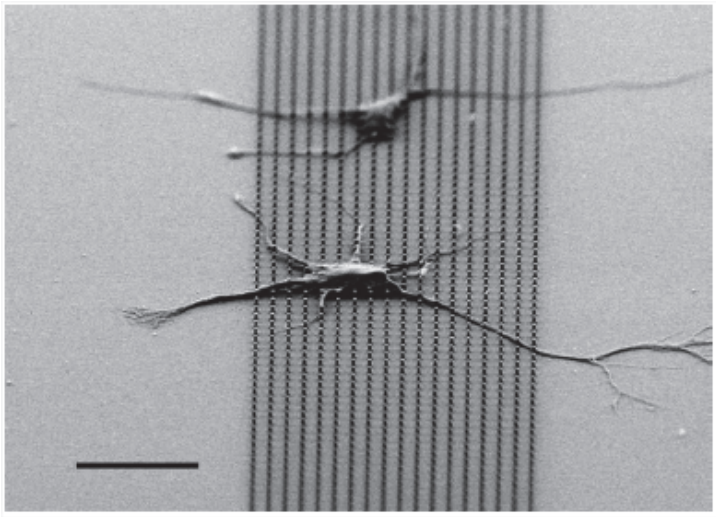

Figure 1.24 An SEM of rat hippocampal neurons cultured for 24 h on silicon micropillars (0.5 μm silicon micropillars spaced by 2 μm) coated with poly-L-lysine (scale bar=20 μm). (From [**83**])

Rajnicek et al. [**93-94**] cultured neurons (embryonic xenopus spinal cord neurons and rat hippocampal neurons) on microgrooved quartz (14nm-1100nm depth and 1µm-4µm width). They found that behavior of neural cells is dependant of cell type and groove dimensions. Xenopus spinal cord neurons exhibited classical topographical guidance by growing parallel to grooves (**Fig 1.25a4, b1**). In contrast, rat hippocampal neurons grew perpendicular to shallow, narrow grooves (**Fig 1.25a2**) and parallel to deep wide ones. **Fig 1.25b2** shows a rat hippocampal neuron whose soma is on flat quartz and his neurite grow parallel to cell body and turn abruptly perpendicular when it encounter the 140nm deep and 1µm wide grooves. They also found that microstructure induce neurite outgrowth. **Fig 1.25c** shows xenopus neurons at the frontier of the micropatterns. Neurite which grew on the microgrooves are straighter and longer than those which grew on the flat quartz.

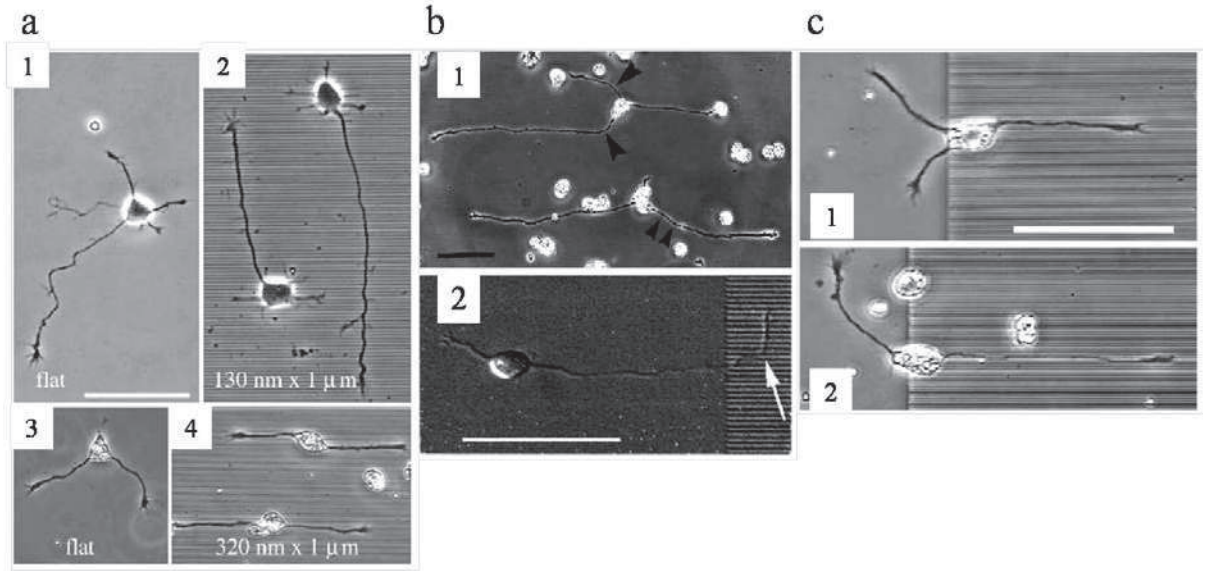

Figure 1.25 (a) Rat hippocampal neurons (***1-2***) and Xenopus spinal cord neurons (***3-4***) cultured on flat (***1-3***) and microgrooved (***2-4***) quartz substrate. (**b**) (***1***) Xenopus neuron on microgrooves (1 µm wide and 14nm deep) (**2**) Rat hippocampal neuron at the frontier between flat quartz and microgrooves (1µm wide and 140nm deep). (**c**) Xenopus neurons at the frontier between flat quartz and microgrooves (***1***) 1 µm wide and 320nm deep (***2***) 1 µm wide and 520nm deep. (From [**93**])

Cellular consequences of the microfabricated environments

Several articles and review address extensively this problematic regrouping cell type, substrates types, features size and their biological effect on cells [**97-105**]. Based on the review by *Bettinger et al.* [**97**] we choose here to draw a general overview of the biological parameters that can be affected by surface topography.

Morphology: As we have seen in the last paragraph topography affects particularly cells morphology. Patterns of lines (micro and nano) induce alignment and elongation of cells along the edge of the patterns (contact guidance). Stronger response has been observed on substrate with lower pitch and higher groove depth. Contact guidance has been observed on many cell types. Micropillars decrease cell spreading compared to flat surface. However this effect can be balanced by reducing stiffness of the micropillars by using PDMS for example [**89-90**].

Attachment and adhesion: Patterns of lines and especially at the nanoscale enhance cell attachment as it mimic proteins of the ECM such as collagen. Micropillars generally reduce cell attachment as cells cannot form big focal adhesion points on micropillars. For adhesion, the nature of the substrate is important (hydrophilic or hydrophobic) as it will determine is adhesion protein secreted by the cells can attach to the surface.

Proliferation: Micro and naopatterns seems to induce slower proliferation rate than on flat surfaces.

Migration: Micropatterns and nanopatterns of lines induce a biased migration of cells in the direction of the lines and increase of migration velocities for many cell types (endothelial cells , epithelial, osteoblasts, C6 glioma cells). Micropillars seem to have no impact on cell migration.

Genotypic Alteration*:* *Wójciak-Stothard et al.* [**99**] observed that cells (macrophage) activity (tyrosine phosphorilation) was stimulated by discontinuities and so cells were more active in phagocytosis. *Chou et al.* [**100**] demonstrated this activation at the genotypic level by showing that expression of m-RNA for fibronectin is stimulated. Recent studies showed that fibroblast cultured on nanopits presented an alteration of many genes links to apoptotic initiation, DNA repair and transcription regulation [**101**].

Differentiation: Some groups used topography as a way to induce differentiation. *Yim et al.* [**102**] showed that hMSCs (Human Mesenchymal stem Cells) can be differentiated in neurons using nanopits arrays

Link between physical cues and chemical cues

As we have seen before, cells are sensitive to very small topographies (70nm lines) and chemical cues may have also a topographical component depending on the size of the adsorbed molecules. It is very common to combine microfabricated topographies cues and chemical cues [**106-107**]. Chemical cues tend to desorbate into the culture medium after some time and the addition of topographical features can make the patterning more stable in time. Chemical and topographic patterning can be associated to make different effects. For example, *Taylor et al.* (Jeon's group) [**108**] developed a compartmented microfluidics platform for neuron culture. One compartment is for soma of neurons (on black on **Fig. 1.26a**) and the other one for the axon projection (in yellow). Somal compartment is patterned with proteins (poly-l-lysine) to make the soma of neuron adhere and microgrooves separate this compartment from the other one. Axons are guided to grow in the microgrooves.

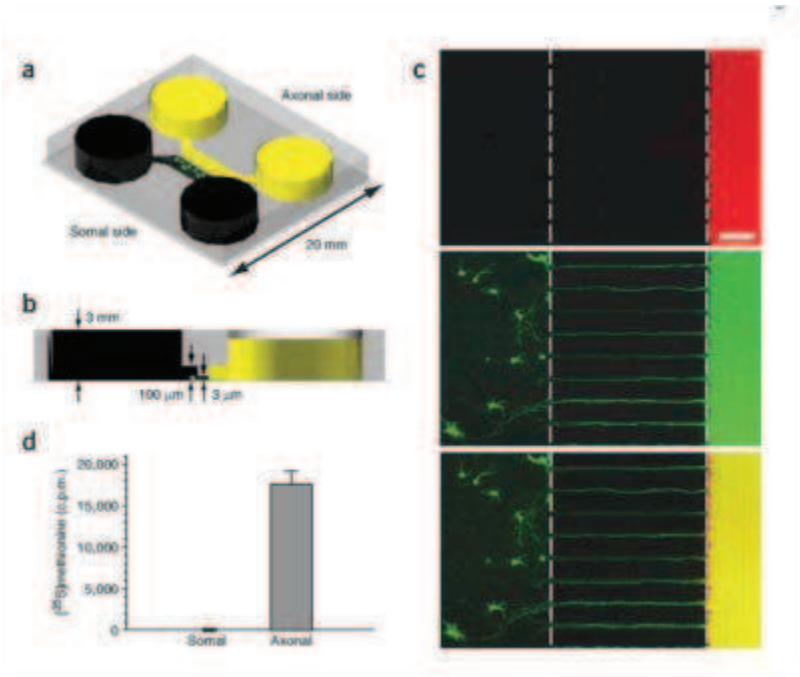

Figure 1.26 (a) Overview of the microfluidic chip. (**b**) Side view. (**c**) Fluorescent images to show that the two compartments are fluidicly isolated. (**d**) Counts of radioactivity in samples from somal and axonal compartments after [^{35}S]methionine was localized to the axonal compartment for over 20 h. (From [**108**])

1.3 3D Scaffolds

As we have seen in the last paragraph microstructure can influence cells on different aspects. However this influence is limited in height: surface topography will strongly influence the few cell layer immediately on top of it and have less and less influence when more cell layer are present. In order to be able to fabricate not only cell sheets (endothelial tissue) but complex cell structures and one day organs, it is necessary to be able to control cells in 3 dimensions. It can be achieved with 3D scaffolds. Scaffolds are structures that aim at mimicking the extracellular matrix (ECM) by providing mechanical support to the cells. [**109-110**]. The material of the scaffold as well as the method of fabrication is important for scaffold functionality. This paragraph aims at giving an overview on the challenges of making 3D scaffold with a particular focus on nanofibers based scaffold as this matter will be discussed later in this manuscript.

1.3.1 Scaffold Materials

Choice of the material is important as different materials have different mechanical properties and interactions with cells. Scaffolds can be bioresorbable or not.

a- Natural polymers

Natural polymers present advantages as they are bioresorbable and are recognizable by cells. However their mechanical strength is limited. Natural polymers are generally soluble in water they have to be made water insoluble during the scaffold fabrication process. Natural polymers are constituted of 3 classes of molecules:

Proteins: Proteins used for tissue engineering are generally extracted from bovine or porcine tissue. Most common used proteins are: Collagen, gelatin, fibrin and silk fibroin.

Polysaccharides: In general polysaccharides lack cell-adhesive sites. They need to be functionalized to trigger cell adhesion. Principal polysaccharides used are: Hyaluronic acid, alginate, chondroitin sulfate, chitosan and chitin.

***Decellularized-ECM*:** New protocols allow to remove completely cells from an ECM while conserving ECM integrity [**111**]. ECMs from different organs have different properties.

b- Synthetic Polymers

Prion disease's outbreaks in year 1990's shone the light on the danger of natural materials for implants: it is very difficult to guarantee that the purified extract is totally free form pathogen agents (e.g.: prions). However synthetic polymers need to be functionalized to promote cell adhesion. Four main families of polymers are used in tissue engineering:

Non degradable polymers: They have long history of biomedical use: Silicone, PET, PTFE, PMMA and PVDF.

Poly(α-hydroxyacid)s**:** PLGA or poly(lactic-*co*-glycolic acid), polycaprolactone (PCL), polyglycolide (PGA), polylactic acid (PLA), poly-3-hydroxybutyrate (PHB)

Hydrogels: Hydogels are mostly constituted by water. They are made by cross linking water soluble polymer chains such as Polyethylene Glycol (PEG), Polyethylene oxide (PEO), Polyvinyl Alcohol (PVA), Polyacrylic Acid (PAA). Hydrogels can be crosslinked by UV and their structure is very comparable to those of ECM.

Others**:** Polyurethanes (PU) are elastomers; they are mechanically resistant but provide elasticity.

c- Inorgorganic materials :

Hydroxyl apatite (HAp) is the biological form of calcium apatite. It can be found in the body in bones and teeth and is bioactive. Coral has been used in tissue engineering as its calcium carbonate is bioactive. Porous material made from corals is optimal for bone regeneration.

d- Composite materials :

Composite materials are made of a combination of organic and inorganic materials. Polymeric scaffold coated with apatite will be more bioactive and promote cell adhesion.

1.3.2 Techniques of fabrication

Microfabrication techniques are very adapted to make patterns with high resolution. However those techniques are not adapted for doing 3D patterning of biomaterials as it requires a layer by layer fabrication process. On the opposite, solvent evaporation and phase separation based techniques are very efficient at creating pores and making 3D structures. However control over the scaffold structure is very limited and control of pore size is difficult. Between those 2 families of fabrication techniques electrospinning is a very interesting technique as it creates easily fibrous 3D structures while providing relative control over the scaffold structure. This paragraph aims at giving a brief overview of the different 3D fabrication techniques.

a- Membrane creation techniques

Solvent casting/Porogen leaching: Solvent casting consists of dissolving a polymer in a volatile solvent and casting it on a solution that will provide support to the polymer while the solvent is evaporating. The structure of the resulting scaffold will depends on several parameters: concentration of polymer, nature of solvent, casting substrate, casting temperature, drying process. Porogen agent such sodium chloride, ammonium bicarbonate and glucose can be introduced to create pores in the resulting scaffold. Injection of high pressure CO_2 can also create pores.

***Phase separation*:** The general principle is to dissolve polymer in a solvent and to extract the solvent by liquid-liquid demixing (phase inversion) or solid-liquid demixing (freeze drying). Phase inversion use usually 2 non-miscible solvent to create 2 phase solution with a polymer-rich phase and a polymer-poor phase. In certain conditions (viscosity, density, interfacial tension and agitation speed) the phases interchange by diffusion. Freeze drying use controlled temperature and pressure conditions to sublimate solvent. It is a very common technique to create pore in biomaterials as it offer control over pore size interconnectivity and porous distribution. It can create materials with 90% porosity such as hydrogels.

b- Rapid Prototyping techniques

Rapid prototyping techniques are the techniques that allow use computer numerical control (CNC) machines to fabricate 3D objects. Recent advances on the resolution achievable by those techniques make them attractive for the fabrication of 3D scaffold [**112-115**] due to the control over the structure of the resulting scaffold. Those technique can be subtractive (micromachining, laser ablation) if the fabrication begin from a bulk material and removes material or additive (3D printing) if material is deposited through the process. There are 3 families of 3D printing based on the way to bring material to the surface [**116**].

Molten polymer Deposition: Common 3D printing use extruding of thermoplastics (ABS, PLA, HDPE) to manufacture objects layer by layer. This process is called *Fused Deposition Modeling* (FDM). The polymer is melted and deposited on the surface. This technique is very cheap and now open source 3D printer (reprap, makerbot) can be build under 1000$ (**Fig. 1.27a**) [**117**]. The printing material is very cheap (HDPE 17€/kg) and the conception of the printer is quite simple and modulable. However the resolution is limited: the minimum feature size is 500 µm-2 mm and minimum layer thickness is 300 µm [**118**] and some limitations exist in the shapes achievable due to the displacement of the melted polymer. **Fig. 1.27b** shows an example of scaffold that can be fabricated using this technique.

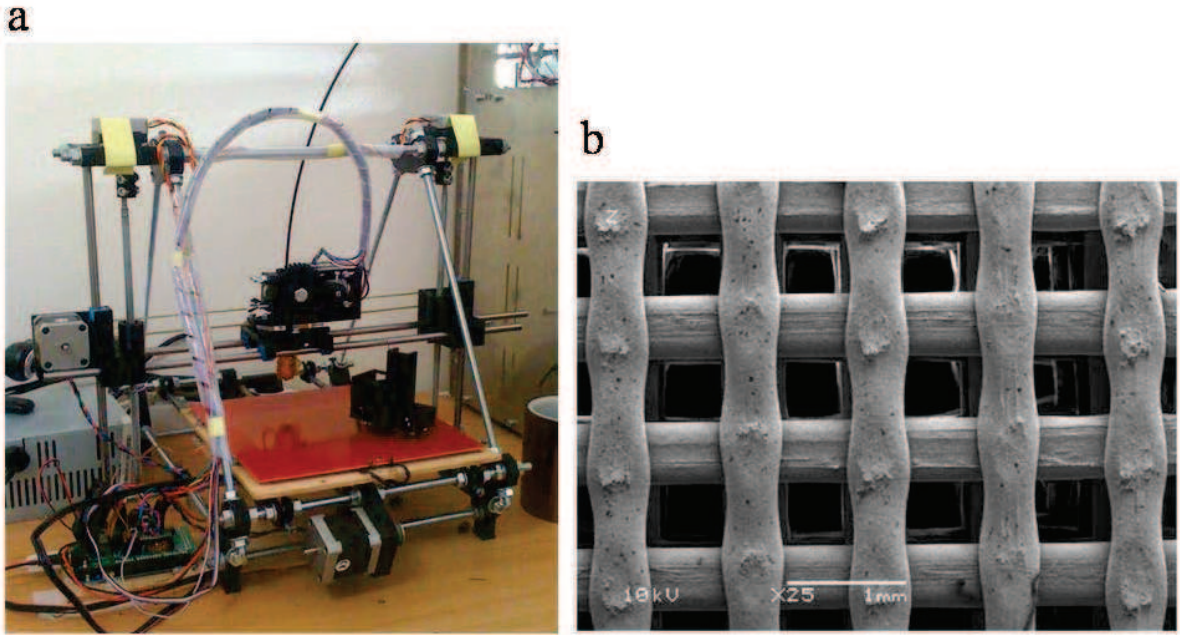

Figure 1.27 (a) Overview of a reprap open source 3D printer. (From [**117**]) (**b**) Scaffold fabricated using fused deposition modeling. (From [**111**])

Granular material binding: Selective laser sintering (SLS) and Powder bed / inkjet head 3D printing, deposit a layer of powder for each layer and bind selectively the powder [**118-119**]. SLA use laser for this purpose and common powder bed 3d printer use a liquid binding agent [**120**]. **Fig 1.28** is a schematic of the powder bed 3D printing. This technique has high resolution object with minimum feature size of 100 µm and minimum layer thickness of ~100 µm [**122**] but the powder residues can be very hard to remove in holes which is a problem for biocompatibility. **Fig 1.28b** shows an example of complex geometries that can be printed using this technique.

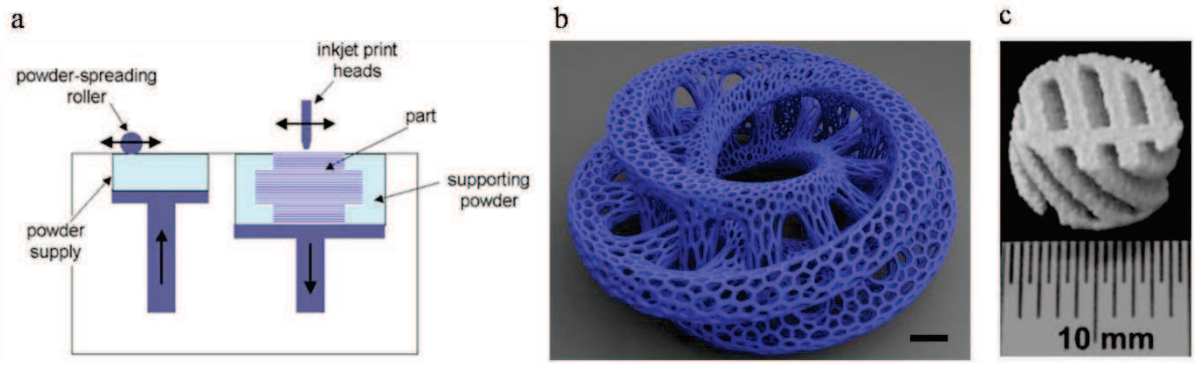

Figure 1.28 (a) Schematic of the inkjet head 3D printing. (From [**120**]) (**b**) Example of object that can be printed using this technique. Scale bar is 1cm (From [**121**]) (**c**) Hydroxylapatite scaffold. (From [**113**])

A wide range of material can be printed using this method and printing materials are relatively cheap. *Leukers et al.* [**113**] used this technique to fabricate 3D ceramic scaffold in Hydroxylapatite (HAp) for cell culture

Photopolymerisation: it is the technique that has the best theoretical resolution. However, as in photolithography, it needs special polymers that are UV sensitive and are very expensive. Inkjet head photopolymer 3D printer deposit photopolymer in the form of microdroplets which are polymerized by UV [**123**] this technique has an excellent resolution as each layer is 16 µm thick. Recent progress in stereolithography with the use of 2-photon laser to polymerize the resist in 3 dimension offer maximum resolution in 3D [**124-127**]. Very complex 3 dimensional structures can be achieved as shown on **Fig. 1.29**.

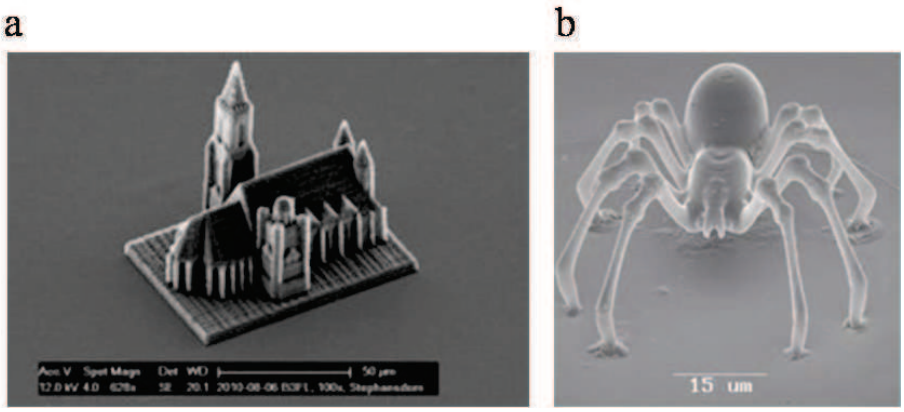

Figure 1.29 (a-b) Example of complex 3D structures that can be achieved using 2 photon stereolithography. (**a**) (From [**124**]) (**b**) (From [**127**]).

c- Electrospinning

Electrospinning will be presented more in details in paragraph 1.6. The general idea is to dissolve polymer in a fast evaporating solvent. The polymer solution is placed in a syringe and high voltage (>10Kv) is applied between the syringe tip and a grounded collector. The strong electric field ejects the polymer solution and the solvent evaporates during "flight" of the polymer to the collector. It is possible to produce random nanofibers as well as aligned nanofibers with controlled diameter (from 100nm).

1.3.3 Nanofibers scaffolds

a- Advantages of electrospinning over other method of scaffold fabrication

Electrospinning is a very versatile method as with relatively limited equipment (a syringe pusher and a high voltage source), it can make nanofibers with diameter ranging from 3nm to 5µm [**128**]. This size range is ideal to interact with cells as it ECM is also constituted of molecules of the same range of size. Nanofibers can be made from different polymers (natural, synthetic, composite) and can be functionalized which make them ideal candidates for tissue engineering applications [**129-132**]. Moreover, by changing the electrospinning setup it is possible to obtain fibers with very different morphologies that can be used for different applications. For example co-axial two capillary spinneret (**Fig 1.30a)** allow formation of hollow nanofibers (**Fig 1.30b)** whereas rotating drums allow formation of highly aligned nanofibers (**Fig 1.30d)**.

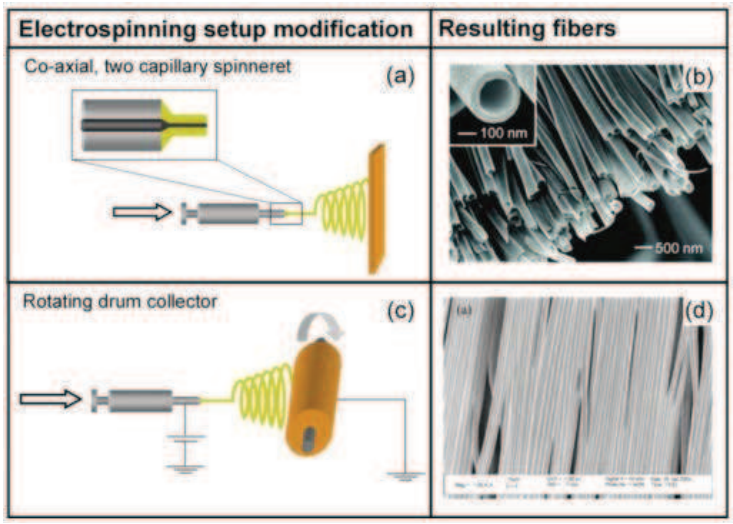

Figure 1.30 (a) Co-axial two capillary spinneret setup for producing hollow nanofibers. (**b**) SEM of produced hollow nanofibers. (**c**) Rotating drum setup for producing highly aligned nanofibers. (**d**) SEM of produced aligned nanofibers. (From [**129**])

Nanofibers scaffold have high surface to volume ratio and can be highly microporous which favors cell adhesion, proliferation, and differentiation [**130**]. Hence nanofibers scaffolds are very good candidate to mimic ECM.

b- Nanofibers composition

Nanofibers can be made from a wide range of polymers [**128,130**]:

***Natural polymers*:** Collagen, elastin, fibrinogen, silk fibroin, chitosan, dextran, gelatin, hyaluronic acid. Natural polymer are often more difficult to electrospin end the solvent has to be chosen in order not to damage structure of biomolecules. Electrospun collagen has been used extensively as collagen is the main component of ECM. Natural polymers can also be mixed with synthetic polymers before electrospinning in order to enhance biocompatibility of the resulting scaffolds.

***Synthetic polymers*:** PLA, PET, PCL, PLLA-CL, PLGA, PLGA-PEG. PLGA is one of the most used electrospun polymer as PLGA electrospun mats can have a porosity greater than 90% which induce high percentage of cell attachment.

Composite scaffold can be fabricated by sequentially electrospinning different polymer on the same substrate. For example collagen type I and III can be electrospun sequentially to make their ratio similar to the one in natural ECM.

c- Nanofiber scaffold applications for tissue engineering

Nanofibers scaffold have been used for different biomedical applications: drug delivery, wound dressing, cardiac graft and engineering of many type of tissues: cartilage, ligament, skeletal, skin, blood vessel, neural. We choose to focus this short review on the neural tissue engineering and the effects induced by nanofibers on neuron growth and differentiation [**133-134**].

Stem cell neural differentiation and alignment: It has been found that culture of stem cells on nanofibers induce neural differentiation. *Yang et al.* [**135-136**] cultured Neural Stem Cells (NSCs) on Poly-L-Lactic-Acid (PLLA) nanofibers (150-350nm) randomly deposited and aligned. They showed that randomly aligned nanofibers promote NSCs adhesion and differentiation and that neurite outgrew in the direction of nanofibers for the aligned nanofibers scaffold. *Xie et al.* confirmed those results on Embryonic Stem Cells (ESCs) on poly(ε-caprolactone) (PCL) nanofibers (250nm diameter) [**137**]. Undifferentiated ESs were induced to form EBs (Embryonic Bodies) containing neural progenitor cells using retinoic acid treatment protocol. They demonstrated that Embryonic stem Cells (ESCs) on aligned and random PCL nanofibers differentiate into neural lineages (neurons, oligodendrocytes, and astrocytes). On the control experiments (ESCs and EBs in petri dish) neural lineage markers could not be found which validates specific effect of nanofibers. They also found that aligned nanofibers enhance differentiation and induce neurite alignment and outgrow in the direction of nanofibers.

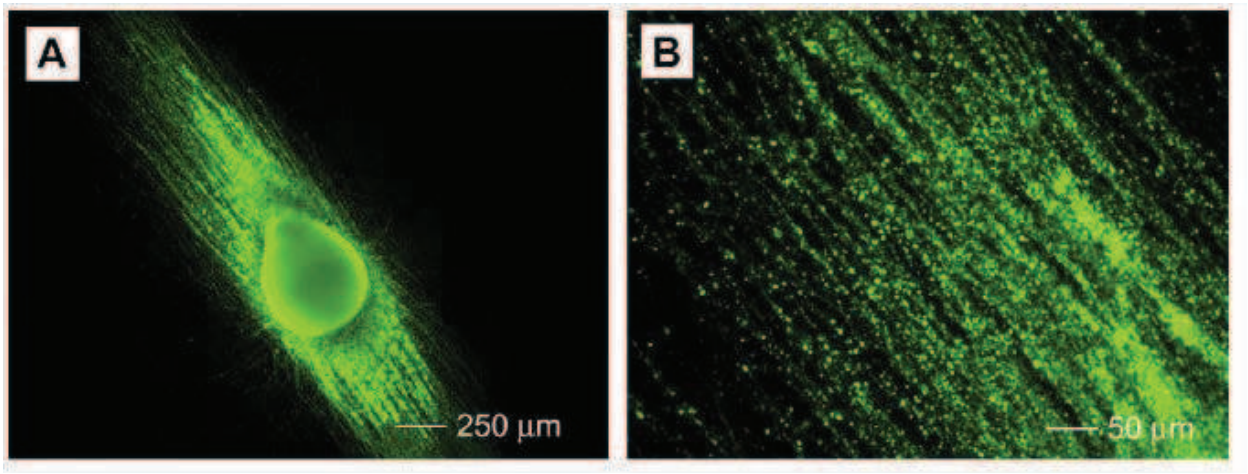

Figure 1.31 (a-b) Fluorescent images of ESs cells after 14 days of culture on PCL aligned nanofibers and tagged with Tuj1(for neuron). (From [**137**])

Christopherson et al. [**138**] studied the influence of the diameter of nanofibers on the neural stem cell differentiation and proliferation. They fabricated randomly distributed Poly(ethersulfone) (PES) of diameters ranging from 283 nm to 1452 nm. Scaffolds and control experiments on petri dish and spin coated PES were coated with laminin to promote neuron adhesion. They tested scaffold in 2 experimental conditions: a differentiation assay (presence of retinoic acid and fetal bovine serum) and a proliferation assay (in the presence of FGF-2). They found that for the proliferation assay, as fiber diameter increases, rNSCs show reduced migration, spreading and proliferation. Under the differentiation condition rNSCs spread and assume glial cell shape and preferentially differentiate into oligodendrocytes, whereas they elongate and differentiate into neuronal lineage on 749-nm and 1452-nm fibers.

***Neurite outgrowth alignment and promotion*:** Similarly to contact guidance, neurite guidance has been verified by many groups [**139-141]** *Corey et al.* [**139**] demonstrated that explanted rat Dorsal Root ganglia (DRG) neurite cultured on PLLA nanofibers (average diameter= 524nm) oriented along fibers even without protein coatings. They observed an augmentation of ~25% of neurite growth length on highly aligned nanofibers and that neurite alignment is directly proportional to the nanofibers alignment. *Wang et al.* showed that neurite alignment is also proportional to nanofibers density [**140**].

***Neurite Guidance conduits (NGC's)*:** The principle of neurite guidance channels is to guide nerve growth through a conduit. Each end of the conduit is attached to one nerve stump (**Fig. 1.32**). Until now NGC used clinically are made in bulk polymers such as Teflon and their efficiency is very limited. Recently researchers used different means of structuring nanofibers into NGCs in order to enhance nerve regrowth through nanofiber topographic guidance [**142-146**].

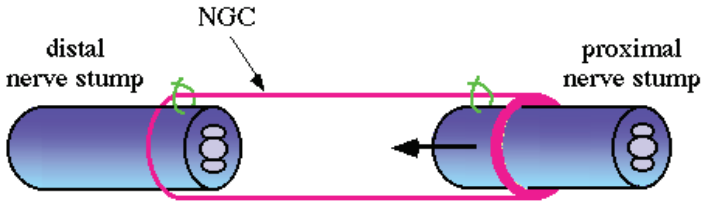

Figure 1.32 Nerve guidance channel. (From [**142**])

Panseri et al. [**144**] fabricated porous NGCs made with randomly electrospun PLGA/PCL nanofibers (**Figure 1.33a-b)** and they tested the efficiency of the conduits on rats after sciatic nerve section (**Figure 1.33a-c).** The advantage of PLGA/PCL is its degradability so no other surgery to remove the conduit is needed.

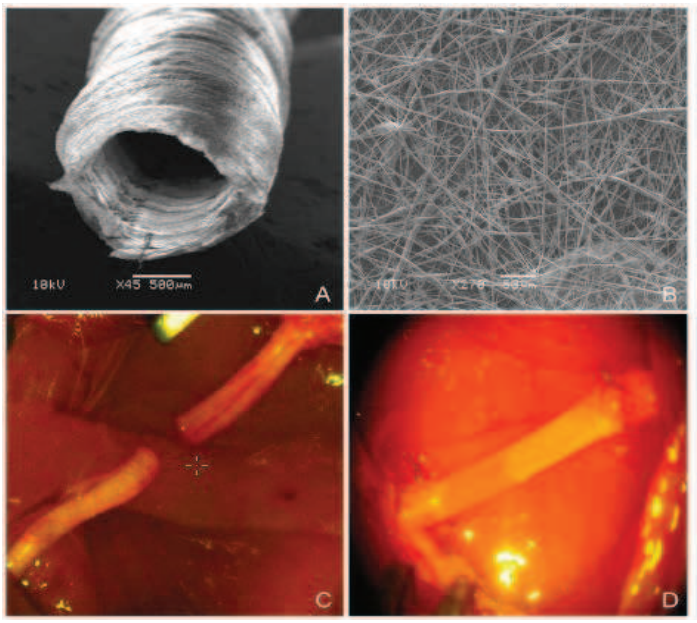

Figure 1.33 (**a**) Overview of the Nerve guidance conduit. (**b**) Detailed view of the random electrospun nanofibers constituting it. (**c**) Rat Sciatic nerve section. (**d**) Sciatic nerve with the neural guidance conduit. (From [**144**])

They showed that regeneration of the sciatic nerve after 4 month of implantation was better in those conduits made from nanofibers than in normal silicone tubes.

Researches are still in progress to fabricate NGC with more complex structures. For example *Zhang et al.* [**146**] used electrospinning of ultrafine fibers on a patterned collector to make fibrous Polycaprolactone (PCL) and poly-DL-lactide (PDLLA) tube with micropatterns. They managed to make NGCs with aligned nanofibers in the inner layer and random nanofibers in the outer layer: the inner layer is for topographical guidance and the outer layer is to improve mechanical resistance of the NGC.

1.3.4 Towards Active bioscaffolds

As we have seen along the last chapters, topography and chemical cues can influence cell functions which can be used for tissue regeneration. However those cues are rather passive: once the scaffold has been seeded with cells, there is no way to modify its functions. A scaffold that could be active would open the way to more complex interactions with cells. An active scaffold could play 2 main roles: Sensor for monitoring the activities of cells during their development and actuator regulating activity of cells from the exterior.

a- Electro Active scaffolds made from electro active polymers

Neural cells communicate with electric pulse (action potentials) as their membrane has voltage gated ion channels that are activated by changes in electrical potential difference near the channel. Neurons that are not stimulated by other neurons degenerates and dies and so, many researches have been done on the electric stimulation of neuron growth as it mimics neuron-neuron communication. It is well known that an electric field (1V/cm) applied at the culture level can effectively enhance and orientate neurite outgrowth [**147**] Hence many studies focus on trying to use this effect combined with topographical and chemical guidance on scaffold [**148-151**]. The idea is to fabricate a scaffold in a polymer that is electrically conductive such as polypyrrole (PPy), polythiophene (PT), polyaniline (PANI), poly(3,4-ethylenedioxythiophene) (PEDOT) and to apply an electric field to stimulate neurons.

For example, *Yow et al.* [**149**] fabricated a collagen-based 3D fiber scaffold containing Polypyrrole and showed that hMSCs (human MSCs) cultured on these fibers expressed markers that are characteristic of neural lineage. They also demonstrated that cellular function can be influenced (early expression of MAP2 and upregulation of synaptophysin) by applying an external electrical field and that prolonged stimulation of the culture system is detrimental.

Electrical stimulation of conductive polymers has also been used to achieve controlled drug release [**150-151**] through different mechanism (gel deswelling, PH change,). One way to accomplish this is to fabricate a pH-sensitive polymer and use the presence of an electric current to change the local pH, initiating erosion of the polymer and the release of any drug contained within the polymer [**152**].

b- Potential of piezoelectric scaffolds.

Piezoelectric materials have the ability to generate charges in response to a mechanical stimulation (direct piezoelectric effect) and reversibly they can be deformed by an electric stimulation (reverse piezoelectric effect). Due to this properties, piezoelectric materials are commonly used as sensors (e.g.: echography), actuators (e.g.: inkjet printer head) and can be used for energy generation (e.g.: lighter igniter). Thus, the incorporation of these properties in bioscaffolds could be a way to obtain active bioscaffolds.

In addition some biological materials such as collagen, bone or tendon exhibits some piezoelectric properties. In particular bone regeneration seems to be linked with bone piezoelectric properties and osteoblast ability to sense this cues to induce bone regeneration [**153**]. Thus a piezoelectric scaffold would mimic the natural microenvironment of osteoblasts. As piezoelectric polymers can induce a transient change in surface charge without requiring external energy sources or electrodes they could be also use to mimic neural microenvironment.

Most common piezoelectric materials are natural crystals (quartz, Rochelle salt), artificial crystals (Gallium orthophosphate, Langasite), synthetic ceramics (ZNO, PZT, Barium titanate). Those materials are not easy to pattern and ceramics have biocompatibility problems due to the presence of lead and so they are not adapted for making bioscaffolds. PVDF (PolyVinyliDene Fluoride) is the only synthetic polymer that exhibit strong piezoelectric properties [**146**]. PVDF is a thermoplastic which has strong chemical resistance, is biocompatible and optically transparent. Hence, PVDF is an excellent candidate for making bioscaffolds with piezoelectric properties.

Until now few studies has been conducted on the subject compared to the number of studies conducted on conductive polymer. *Valentini et al.,* in the 80's confirmed the PVDF biocompatibility and showed that piezoelectric bulk PVDF enhance neurite outgrowth in vivo and in vitro [**154-156].** Later, *Gallego et al.* proposed new micropatterning methods for PVDF and showed that cells could be cultured on PVDF micropillars. However they did not study the specific effects of PVDF piezoelectricity on cells [**157-158**]. Finally, *Xie et al.* [**134**] cultured cells on aligned PVDF and PVDF-TrFE nanofibers. They demonstrated the potential of aligned PVDF–TrFE scaffolds in supporting neuronal cell growth and neurite extension for neural applications.

In conclusion PVDF has many potential applications but still little is known on its specific effects on cells and it is why we choose this material as our subject of studies.

1.4 Piezoelectric properties of PVDF and PVDF-TrFE

Many materials exhibit piezoelectricity: natural crystals (quartz, Rochelle salt), artificial crystals (Gallium orthophosphate, Langasite), synthetic ceramics (ZNO, PZT, Barium titanate). Biological materials exhibit also some piezoelectric properties: bone, Tendon, Silk, Wood, Enamel, Dentin, and DNA. PVDF (PolyvVinyliDene Fluoride) is the only synthetic polymer that exhibit strong piezoelectric properties [**159**]. PVDF piezoelectric properties are much more important than the natural crystal with the highest piezoelectric properties which is quartz (**Table 1.1**). Piezoelectric properties are less important than those of ceramics (BaTio3, PZT) because PVDF is maximum 60-70% crystalline which limits the maximum piezoelectric properties.

Material	Piezo constant (pC/N)
BaTiO3	191
Quartz	2.3
PZT-4	289
PVDF	-33

Table 1.1 Piezoelectric constants of different materials. (From [**155**])

Piezoelectric properties of PVDF have been discovered by *Kawai et al.* [**160**] in 1969. In 1997 *Omote et al.* discovered that the Polyvinyl-trifluoroethylene copolymer (PVDF-TrFE) exhibit enhanced piezoelectric properties [**161**]. PVDF and its copolymer are semi-crystalline: They are made of ordered regions of monomer units (crystallites) surrounded by an amorphous regions. Piezoelectric response is linked with its crystalline phases are only 3 of its phases are piezoelectric. In order to get a piezoelectric response, PVDF needs to have the proper piezoelectric phase (*β-phase)* to create dipoles and need also to be poled to orientate those dipoles. PVDF piezoelectric properties are still not completely understood and are still an active area of research. This paragraph review what is known on PVDF piezoelectric properties and the different means of measuring it.

1.4.1 PVDF crystalline properties

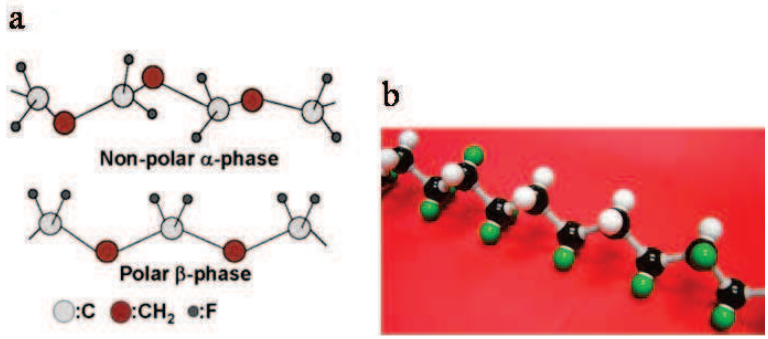

Figure 1.34 (a) Schematic of the non polar α phase and the polar piezoelectric β phase. (From [**162**]) (**b**) 3D model of PVDF-TrFE. (From [**163**])

PVDF has 4 main crystalline phases [**204-205**]: α, β, γ and δ which correspond to different molecule conformations.

Phase I: *β-phase* piezoelectric

This phase is the main piezoelectric polar phase. The chain conformation is all Trans (TTT) oriented with Fluor atom on the same side of the polymer chain (**Fig. 1.34**). This conformation gives the maximum dipole which generates the piezoelectric properties. β-phase can be obtained drying films cast from highly polar solvent HexaMethylPhosphorAmide (HMPA) at temperatures between 60°C and 140°C [**164**]. β-phase can also be obtained by drying at 100°C PVDF/DMF (DiMethylFormamide) solution with addition of Mg(NO3)2,6H2O [**165]**. Stretching *α-phase* PVDF produce *β-phase* due to the asymmetry generated by the physical stress [**165**]. PVDF-TrFE exhibit naturally β-phase due to the asymmetry introduced (**Figure 1.34b**).

Phase II: *α-phase* non piezoelectric.

This form is the most common. The chain conformation is trans-gauche trans-gauche (TG^+TG^-) with no dipole moment. Recrystallization at T below 160°C [**165,167**]

Phase III: γ-phase

This phase has almost the same conformation as the β-phase. Its conformation is ($TTTG^+$ $TTTG^-$).cast from DMAc 65° γ. casting from DMSO or DMF [**165, 168**]

Phase IV: δ phase

This phase has also trans-gauche trans-gauche conformation (TG^+TG^-) but C-F bonds are aligned in one direction resulting in a dipole moment.

Choice of solvent is important in the determination of the crystalline phase that will appear: generally the more polar the solvent is, the more polar the crystalline phase will be. Rate of evaporation seems also to influence phase of the polymer: slow evaporation solvent such as will results in β-phase whereas fast evaporation solvent will result in α-phase. Intermediate solvent will result in a mix between both.

Different crystalline phase have different microscopic aspects. **Fig. 1.35** shows a SEM picture of 2 PVDF films from the same solution (10% wgt in DMF/Acetone) and spin-coated with the same conditions. The film dried at 140°C is optically very transparent. SEM picture (**Fig. 1.35b)** shows that there is no crystals, the surface is very smooth. It is characteristic of the amorphous α-phase. In comparison, the film dried at room temperature has a white aspect and is not optically transparent. At the microscale it presents big spherulites (**Fig. 1.35a)** which shows the presence of a crystalline phase. Experiment detailed later shown that this phase is γ-phase.

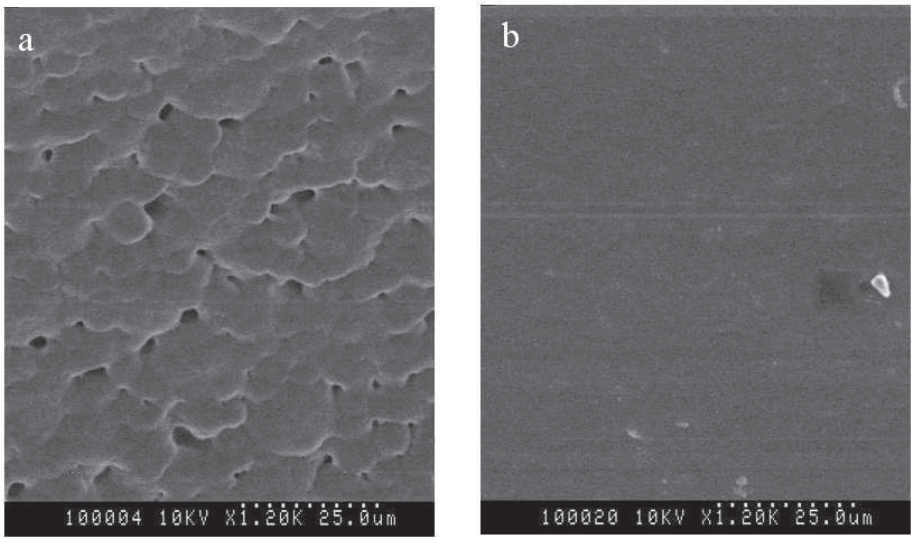

Figure 1.35 SEM picture of PVDF film : (**a**) dried at 30°C: γ-phase, (**b**) dried at 140°C *α-phase.*

Crystal forms can be transformed by different means generally it involved temperature and/or electric field as those parameters affect molecules movement and polarity. Most studied PVDF phase transformations are the following:

***α-phase to* β-phase conversion:** stretching (stretched 6 times its size) at 90°C [**165**]

β-phase to γ *-phase conversion* annealing at 181°C [**165**]

γ-phase to β-phase annealing at 90°C 5h [**165**]

Fig 1.36 shows the interconnections between the different phases of PVDF and the different means of changing one phase into another. This diagram is given as a reference as it comes from an article of 1982 and new findings have not been added.

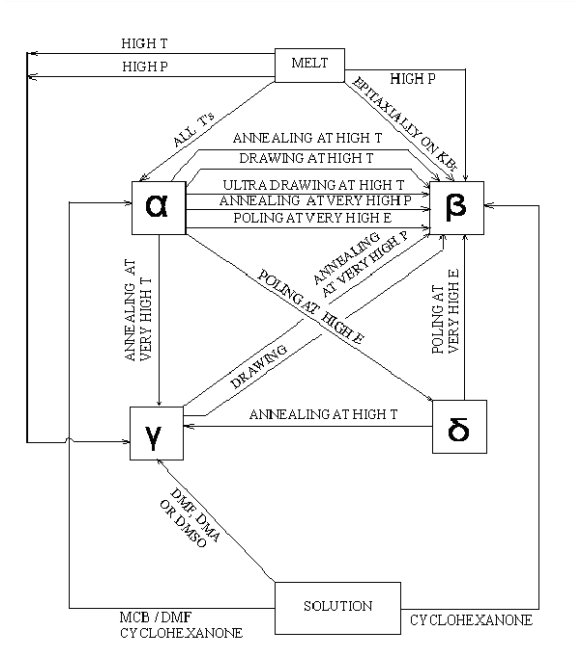

Figure 1.36 Schematic illustrations of the interconnections of the different phases. (From [**166, 169**])

Fig. 1.37 shows the actual phase transformations we verified experimentally. We found that the use of acetone in DMF (DMF/Acetone ratio = 4:5 wgt) does not prevent the formation of γ-phase. However we found that the temperature of drying is the most important parameter for the formation of γ-phase.

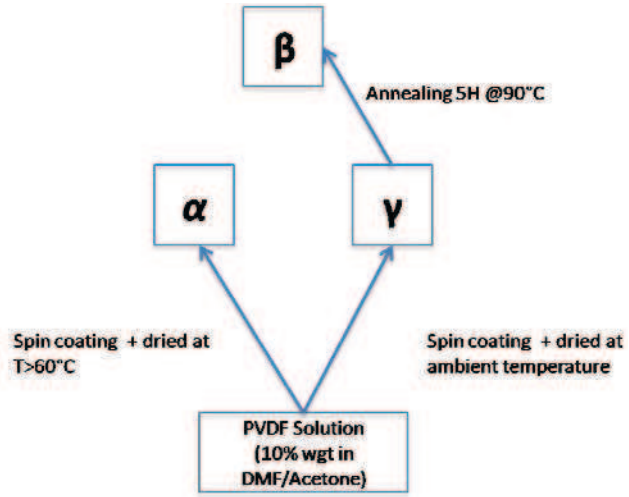

Figure 1.37 Schematic illustrations of the interconnections of the different phases found experimentally.

1.4.2 PVDF and PVDF-TrFE poling

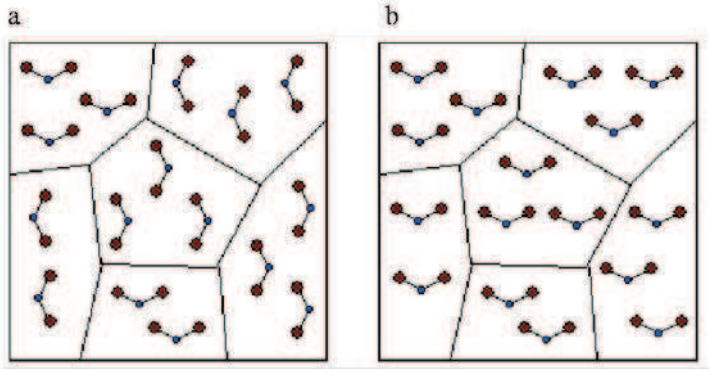

Figure 1.38 Schematic illustrations of the effect of poling on the dipoles: (**a**) unpoled, (**b**) poled. (From [**170**])

Poling is necessary to align the dipoles in the same direction. Electric poling consists at applying a very high voltage to orientate the dipoles along this electric field. Without poling, the local piezo effect will be annealed at the macroscale (**Fig. 1.38**). It is possible to do direct poling of the α-phase without transforming to the γ-phase or β-phase, however as the γ-phase is polar and very similar, the field needed to orientate all the dipoles will be less important that the one needed from the α-phase. Poling of the PVDF-TrFE copolymer is also need for the same reasons.

Relaxation temperature of the PVDF is 50°C for the α-phase and 90°C for the β-phase [**165**]. Hence, poling should be conducted at 50°C < T_{poling} < 90°C in order to allow relaxation of the α-phase while preventing annealing of the β-phase. **Fig 1.39** shows a schematic illustration of the 2 main techniques available for poling: Corona discharge and in situ poling.

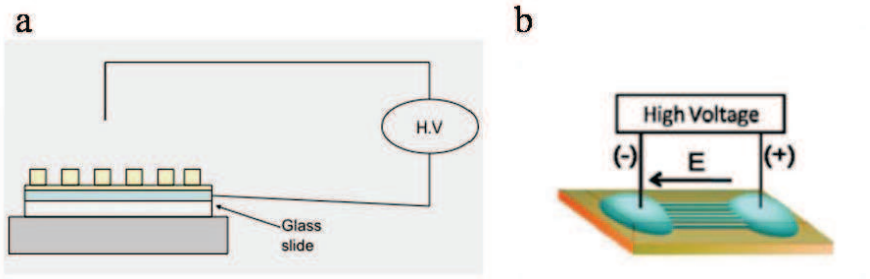

Figure 1.39 Schematic illustrations of the apparatus used to realize poling of PVDF and PVDF-TrFE: (**a**) corona discharge, (**b**) in situ poling. (From [**171**])

***Corona discharge*:** A high voltage is applied between a tip electrode and the grounded substrate (~20MV/m^{-1}). The tip electrode is use to make straight electric field lines which yield better dipole alignment.

***In situ poling*:** *Hansen el al.* [**171**] used this technique to realize poling of electrospun PVDF nanofibers. They applied the high voltage between the 2 electrodes that will serve later as measurement electrodes. The poling voltage is also (~20MV/m^{-1}). To insure electrical isolation between the 2 electrodes, they coated the device in PDMS and immerged it in a bath of insulating silicone oil.

Poling time are generally around 5 hours. Poling is realized at T<90°C and at the end, the high voltage is kept on while the setup is cooling so the crystals will keep their polarity during cooling down.

1.4.3 Measurement of piezoelectric activity

a- Direct Measurements of piezoelectric constants *(d_{33} meter and PFM)*:

Piezoelectric constants:

Piezoelectricity is the combined effect of the electrical behavior of the material and stress applied on it [**159**]:

$$D = \varepsilon E$$

$$S = sT \text{ (Hooke's law)}$$

where D is the electric charge density displacement, ε is permittivity and E is electric field, S is strain, s is compliance and T is stress. They can be combined

$$\{S\} = \left[s^E\right]\{T\} + [d^t]\{E\}$$

$$\{D\} = [d]\{T\} + \left[\varepsilon^T\right]\{E\}$$

The second equation is used to describe the direct piezoelectric effect :

$$\{D\} = [d]\{T\} + \left[\varepsilon^T\right]\{E\}$$

Where {D} is the electric charge density displacement, T is the stress vector, ε is the permittivity matrix and E is the electric field vector. [d] is the matrix for the direct piezoelectric effect which contains the piezoelectric constants:

$$\begin{bmatrix} 0 & 0 & 0 & 0 & d_{15} & 0 \\ 0 & 0 & 0 & d_{24} & 0 & 0 \\ d_{31} & d_{32} & d_{33} & 0 & 0 & 0 \end{bmatrix}$$

Explanation of the unusual coefficient notation can be found here [**172**].

The piezoelectric materials are generally characterized through their d_{33}. For information the PVDF piezoelectric constants can be found in **Table 1.2**.

Piezoelectric strain (pC/N)	d_{31}=21	d_{32}=2.3	d_{33}=-26	d_{24}=-27	d_{15}=-23

Table 1.2 PVDF piezoelectric constants. (From [**170**])

d_{33} meter:

d_{33} can be measured with a dedicated machine called a d_{33} meter (**Fig. 1.40**) which applies a known force . As d_{33} is measured through the direct piezoelectric effect, an electrical contact is needed on top and bottom of the sample which make it impossible to use for substrate such as nanofibers.

Figure 1.40 d_{33} meter. (From [**173**])

Piezoresponse Force Microscopy (PFM):

PFM is a special mode of AFM where the tip is used to measure the piezoelectric response of a substrate. This method can be use even on bare polymers without top electrode as the tip of AFM serve as the electrode. The only requirement is that the ground of AFM and the back of the substrate has to be connected. The tip of AFM imposes a voltage and the deformation of the substrate is measured [**174**]. **Fig 1.41** shows an example of PFM measurement from [**175**]. The measured phase is the polarity of the d_{33} (**Fig 1.41c**) while the measured amplitude is the magnitude of the d_{33}. It is also possible to superpose those measurements with 3D topographical map of the AFM mode (**Fig 1.41a-b**).

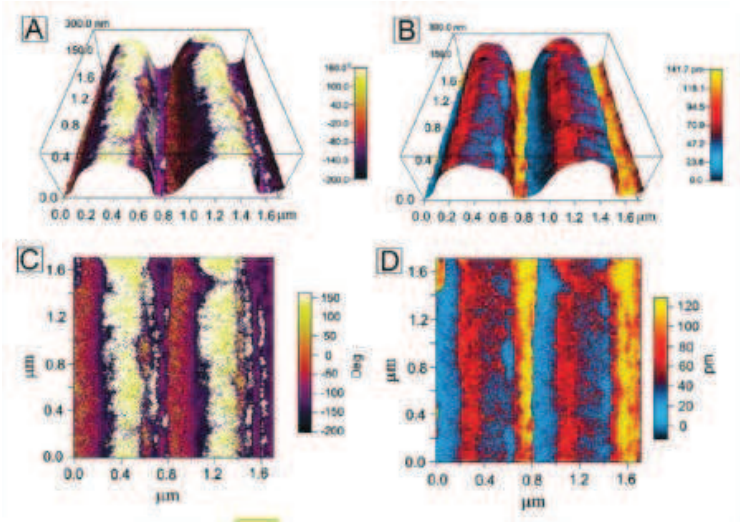

Figure 1.41 PFM measurement of micropatterned PVDF-TrFE: (**a**) phase superposed with topography, (**b**) amplitude superposed with topography, (**c**) 2D phase and (**d**) 2D topography. (From [**175**])

For ferroelectric materials such as PVDF its polarity can be switched by applying a sequence of dc bias imposed on top of the ac driving voltage, and the piezoresponse can be measured as a function of dc bias [**175**].

b- Measurement of output voltage:

Piezoelectric properties can be evaluated by measuring the open loop voltage. *Hansen et al.* [**171**] used a dc motor to apply a fixed strain (0.05%) during different durations (0.06, 0.04, and 0.03 s) to aligned PVDF nanofibers. They obtained output voltages in the range of 15-20 mV. They used a voltage preamplifier to condition the voltage.

We build a voltage preamplifier based on an instrumentation operational amplifier (Analog Device AD622 [**176**]) as it is low-cost and has an input impedance of 15Gohms . The preamplifier runs on batteries in order to remove noise coming from mains. **Fig. 1.42** shows the preamplifier we build and the schematic circuit. The input (Yellow) is plugged to the electrodes with the nanofiber between and the output (black and white) is plugged to a digital multimeter plugged to a computer via USB. By default the amplifier has a unit gain but gain can be set up by changing a single resistor.

The circuit used is a differential voltage amplifier where the amplifier amplifies the difference between the 2 input wires.

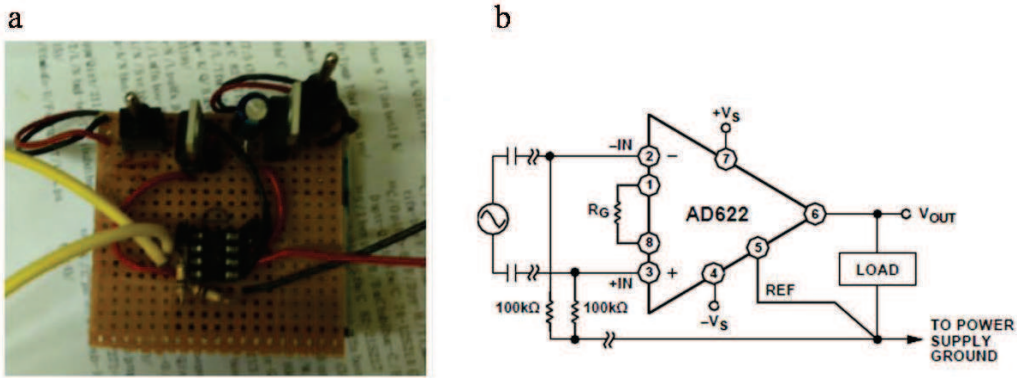

Figure 1.42 (**a**) Electronic circuit with the instrumentation amplifier. (**b**) Schematic of the circuit. (From [**176**])

This method presents some limitations: the substrate needs to be flexible in order to be able to exert a force and the way the force is applied should be reproducible. Device fabrication take many steps from casting polymer, patterning, poling etc… This method of measurement can only give an estimation of the final performance of the device but cannot be used alone as it does not give feedback of the fabrication steps that can be improved.

c- Indirect measurements of piezoelectric properties

As we have seen before, the piezoelectric properties are strongly linked with crystal phases of the polymer. Hence by measuring the relative % of crystalline phase we can have an approximation of the final piezoelectric activities of a device. We used 2 methods that are very common in material science: FTIR spectroscopy (Fourier Transform InfraRed) and XRD (X-Ray Diffraction). Other techniques such as DSC (Differential Scanning Calorimetry) and Raman spectroscopy can be used for the same purposes. This part is not intended as describing the measurement technique which would be too long. We will give the discriminant characteristics of the different crystalline phases of PVDF and PVDF-TrFE that we compiled from multiple sources [**164-170,177-183**].

Fourier Transform Infrared spectroscopy (FTIR)

FTIR can be used to identify crystalline phases as different phases absorb infrared differently. For PVDF phase measurements, FTIR is used in ATR (Attenatuated Total reflection Mode). Infrared light is sent to the sample at different wavelength and the absorbance of the material

is calculated. Data that can be found in literature usually present FTIR absorbance spectra that can be converted easily in the other type of spectra (% transmittance). The localization of the peaks are not changed by the type of spectra used. **Fig. 1.43** Shows FTIR spectra of pure components of PVDF. We put in black the most significant peaks and in red the part of those peaks that allows fast identification of the crystalline phases.

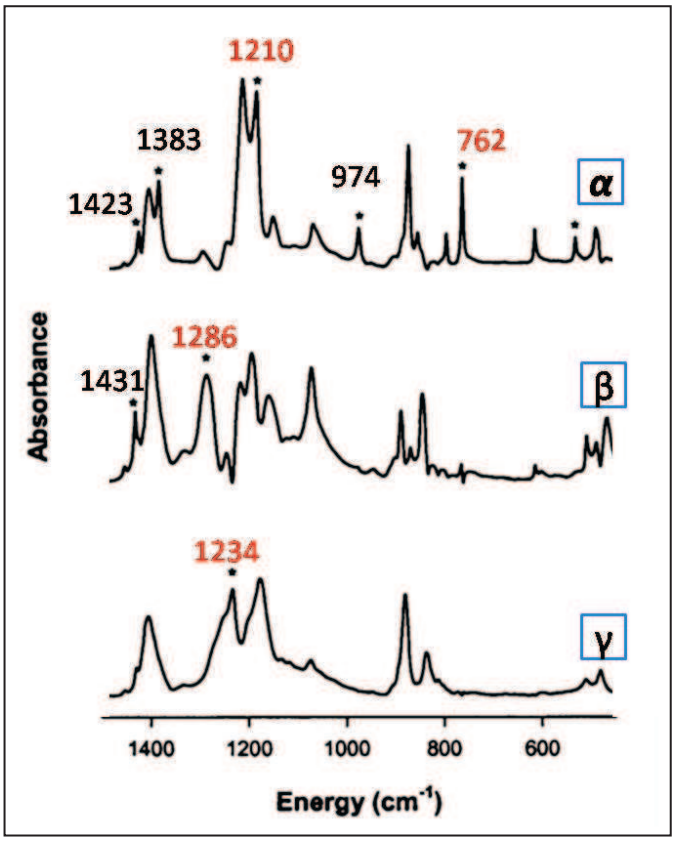

Figure 1.43 FTIR spectra of the pure components of PVDF. Adapted from [**177**].

PVDF-TrFE piezoelectric properties come from the β phase of the PVDF and so the peaks that allow identification of the β phase in PVDF-TrFE are the same as in PVDF (1286-1431 cm^{-1}). **Fig. 1.44** Shows FTIR spectra of PVDF-TrFE powder. As we can see the β phase is present because of the peak at 1286 cm^{-1}. However the peak at 1431 is less obvious. The spectra of PVDF-TrFE in any conditions as less peaks than the PVDF because the dominant phase in this copolymer is the β phase.

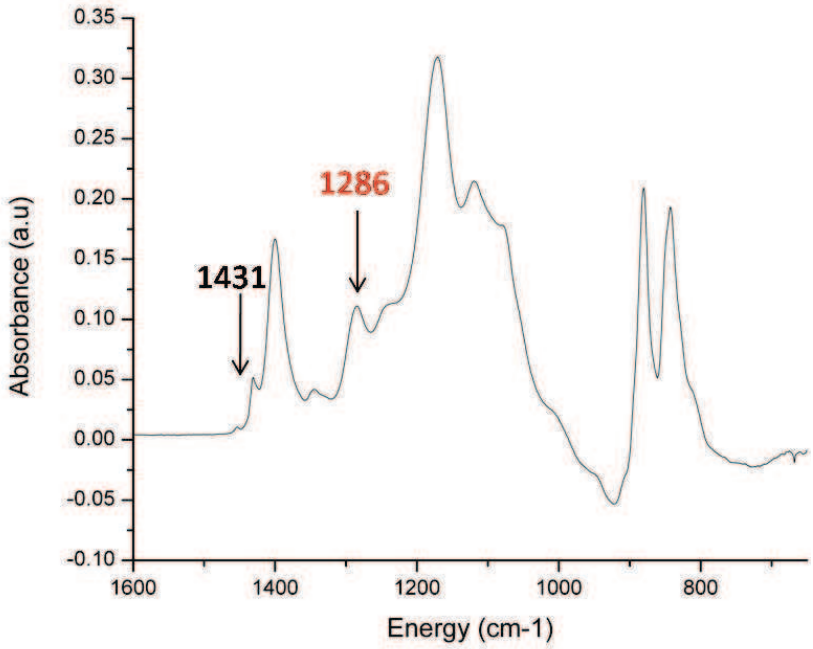

Figure 1.44 FTIR spectra PVDF-TrFE powder.

X-Ray Diffraction (XRD)

X-ray diffraction use an X-ray source that rotate around the sample and measure scattering in function of the angle. This allows identification of crystalline plans. XRD technique used for identifying crystal plane in PVDF and PVDF-TrFE crystal phases is called 2θ XRD analysis. **Table 1.3** regroups the information on the localizations of the 2 theta peaks of the different crystal phases of PVDF and PVDF-TrFE. We can see that many crystal planes have 2 theta peaks located around 20°. Thus, it is not easy to identify properly the different phases. X-ray diffraction should be used with other techniques such as FTIR.

Alpha	
x-tal plane	2 theta (°)
100	17.7
020	18.4
021	19.9
111	27.8
200	35.7
002	39
022	57.4

Beta	
x-tal plane	2 theta (°)
110	20.8
200	20.7
020	36.6
101	36.6
221	56.1

Gamma	
x-tal plane	2 theta (°)
020	18.5
002	19.2
110	20.1
101	20.3
022	26.8
200	36.2
211	38.7

Table 1.3 Crystal planes of PVDF's crystal phases and their corresponding 2 theta peaks. (From [**170**])

Fig 1.45 shows XRD diffractograms of the different phases of PVDF.

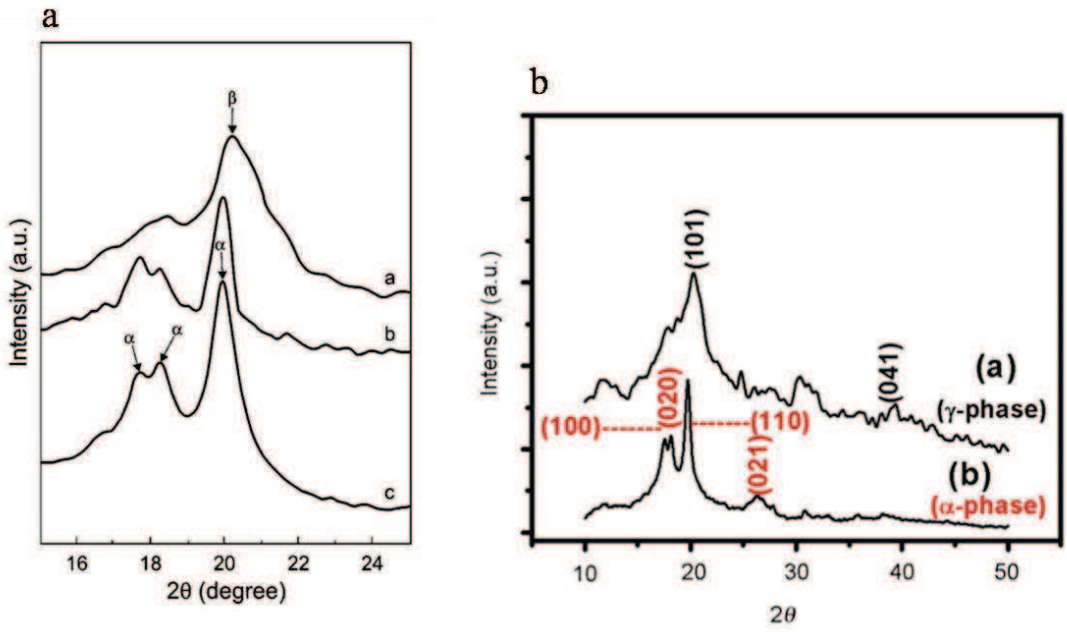

Fig. 1.45 XRD diffractograms of the different crystalline phases of PVDF (**a**) β phase compared to α-phase. (From [**167**]) (**b**) α-phase compared to γ-phase. (From [**165**])

1.5 Microlithography techniques

1.5.1 UV Photolithography

UV photolithography is the most common microfabrication technique. This technique has been developed by semiconductor industry and now is widely used in research laboratories. In general, a thin layer of photoresist which is UV-sensitive is spin coated on the surface a substrate. When exposed to a UV light through a photomask, the expose portion of the resist becomes insoluble or soluble in the photoresist developer, depending on the tone of the photoresist (positive photoresist becomes soluble and negative photoresist becomes insoluble in developer, respectively). After development, the replica of the mask pattern is transferred into the substrate by different pattern transfer methods. Whereas step-and-repeat projection photolithography is generally used by semiconductor industry to ensure a high throughput and a sub-micrometer resolution, contact or proximity photolithography is used in research laboratories to produce patterns over large surface with a feature size down to 1 μm (**Fig. 1.46**).

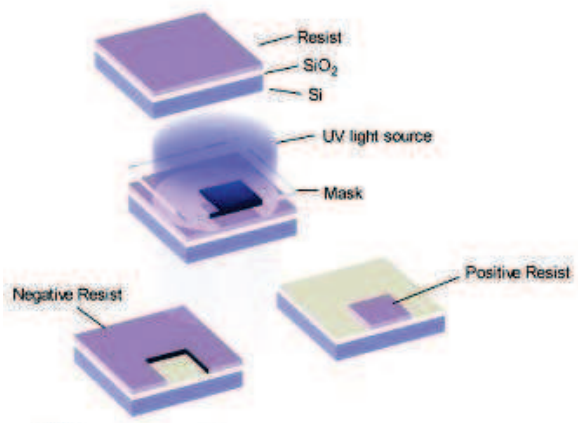

Figure 1.46 Schematics of the photolithography process with positive and negative tone photoresist. (From [**184**])

Both controls of the exposure (for a give UV light source) and the development time (for a given developer composition) are important to achieve a good resist profile. Theoretically, the profile of the exposure dose and the development can be calculated based on diffraction theory and molecular reaction dynamics but in most cases the experimental parameters are determined empirically. In practice, the thickness of the photoresist (e.g. AZ5214E) for lift-off, doping and etching is about 1.5μm, whereas the thickness of the photoresist (e.g. SU-8) for other applications (MEMS, microfluidics) varies between a few to a few hundred micrometers. AZ5214E is a particular photoresist which can be used as either positive or negative resists. When used as positive resist, the well-developed profile of AZ5214E can be vertical or sloped because of the UV absorption of the photoactive compounds that limit the light penetrating to the bottom of the patterns (**Fig. 1.47b**). When used as negative photoresist, it can result in a undercut resist profile which is favorable to lift-off.

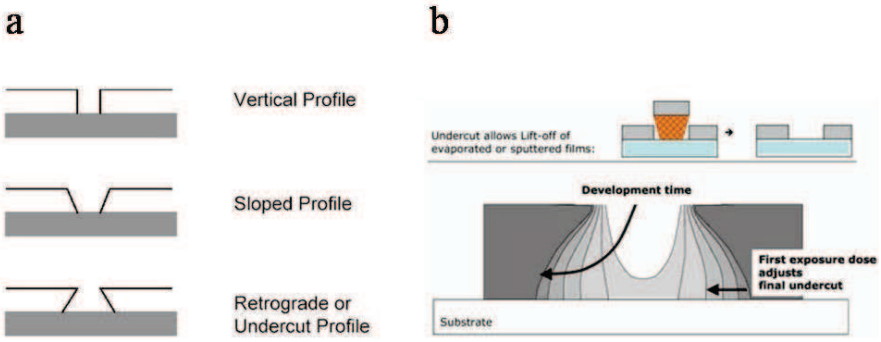

Figure 1.47 (**a**) Three types of photoresist profiles. (From [**185**]) (**b**) Profile of the AZ5214 resist after reversal. (From [**186**])

a- Fabrication of the photomask

Before all, a mask pattern has to be designed and produced. In our work, the mask design can be done using commercial software (Tanner EDA) which results in patterns in different formats.

For masks with only large features (> 20µm), printed transparencies can be used which are convenient and low cost (**Fig. 1.48a**). They are printed by high resolution laser printers laser (3600 dpi) on transparent films.

For masks with smaller feature sizes, standard photo-masks have to be prepared. Now, patterned generated in GDSII format by Tanner EDA is transformed into DXF format with a freeware (Layout, Caltech) and then loaded in to the computer of a micro-pattern generator (µPG101, Heidelberg Instruments). This pattern generator allows producing patterns of feature sizes down to ~1µm. It uses a focused laser beam to print the pattern (from a digital file of the design) on photoresist-coated chromium/soda lime substrate. After exposure and development, the chromium layer is selectively etched by a chemical solution and the remaining photoresist is removed with acetone.

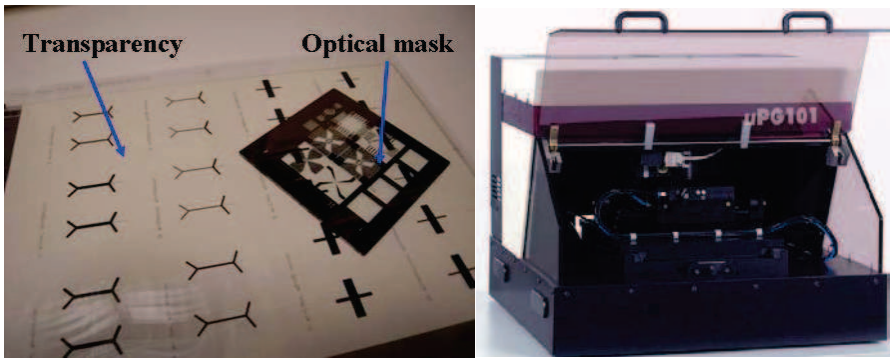

Figure 1.48 (**a**) Transparency mask and optical mask. (**b**) µPG 101 direct laser writer (Heidelberg Instruments [**187**]) installed in the ENS laboratory.

b- Main steps of the photolithography

Cleaning of the substrate: The cleaning process depends of the substrate: Silicon (Si) is generally already cleaned which needs less care than glass. Glass is hydrophilic and often contains inorganic particles or organic residues resulted from glass fabrication or transport. A pre-cleaning step using piranha can then be required prior to classic cleaning. Glass slides are immersed in piranha solution (H2SO4: H2O2=3:1) for 30 min in order to remove organic

residue by oxidation. Afterward, cleaning is done in an ultrasonic bath of acetone and then in isopropanol.

Surface treatment: In order to enhance the adhesion or the spreading of the resist on the substrate, an additional surface treatment may be required. Depending on the type of the substrate and the material to be deposited, the surface of the substrate can be treated by oxygen plasma (to create OH groups and make the surface hydrophilic) or silanization (to make the surface hydrophobic).

Surface pre-coating: Omnicoat (Microchem) solution is recommended as a pre-coating layer for SU8 photoresist, which enhances the adhesion of the resist to the substrate and allows easy stripping using the SU-8 remover [**188**].

Spin-coating: Normally, the spin coating of SU-8 photoresist has 2 steps: the first step allows the photoresist spreading at low rotation speed (500rpm) and low acceleration during 5-10 sec. The second step allows the evaporation of the solvent in the resist at higher rotation speed (1000 - 4000 rpm) during 30 sec. Photoresist manufacturers usually provides curves of spin coating speed versus thickness.

Pre-exposure bake: This step is used to further evaporate the solvent of the photoresist.

Exposure: The right amount of energy has to be delivered to the surface. The photoresist datasheets provided by the manufacturers describe the exposure dose or energy per surface unit (mJ/cm^2) needed for optimal exposure. The exposure time has to be calculated after measuring the intensity of the UV source. The distance between the mask and the photoresist layer is determinant for photolithography quality. Ideally, a perfect contact without air gap is required to achieve the highest resolution or the smallest feature size. If the contact is not good, the diffraction effect will blur the edge of the patterns. In order to enhance contact between the mask and the photoresist, the edge of the spin coated SU-8 photoresist (which has a larger thickness that the other part) should be removed. As can be understood, this optional step called edge removal is important for large thickness depositions. The exposure of photoresist can also be realized without mask by using directly the μ PG101.

Post Exposure Bake (SU8**):** For SU-8 resist, this PEB step is needed for the crosslinking of the resist [**189**].

Reversal bake (AZ5214 negative): This step is critical for the inversion process. It is use to crosslink exposed part of the resist reversing the tone of the photoresist.

Flood exposure (AZ5214 negative): this step is realized without any mask. The goal is to make unexposed portion of the photoresist soluble in the developer.

Development: Substrate are immerged in the developer corresponding to the photoresist used (MIF726 for AZ5214E and SU8 developer for SU8)

Hard bake (SU8)**:** This step is optional, it is used to reinforce adherence of SU8 with the substrate.

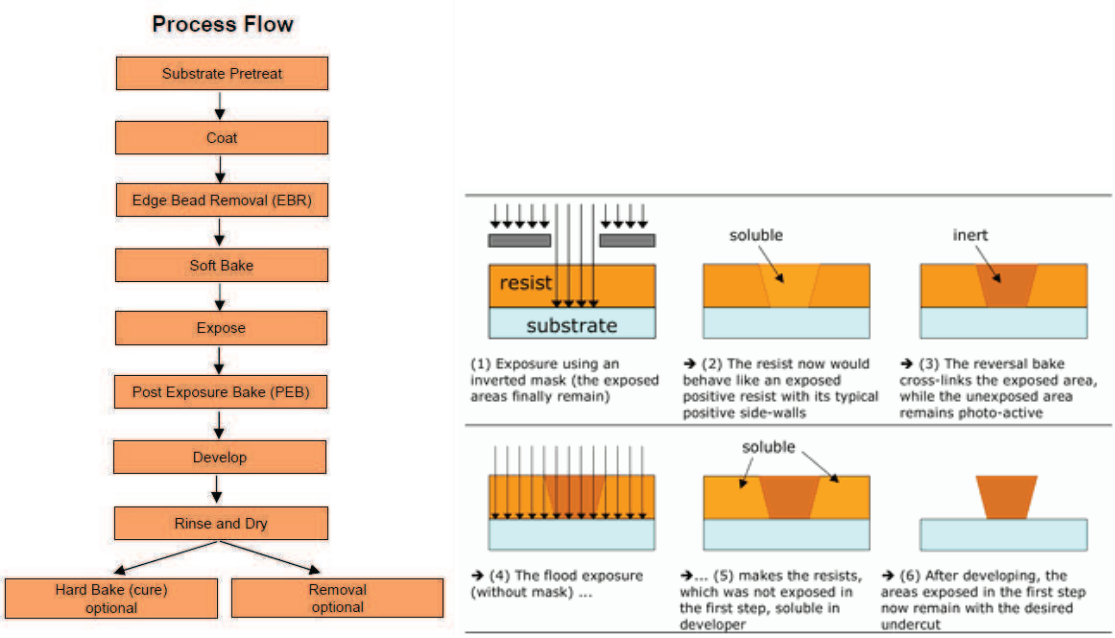

Figure 1.49 Process flow of photolithography: (**a**) with SU8 photoresist (From [**189**]), (**b**) with AZ5214 photoresist (From [**186**]).

c) Metal deposition and lift-off

In research laboratories, lift-off is often used to transfer the photolithography-defined patterns in features of a metallic thin film which can then be used as masks for reactive ion tech or microelectrodes. A thin film of gold, Ni, Cr, or other types of metals is deposited by electron-beam or thermal evaporation on the patterned resist layer. Then, the resist is dissolved in acetone with or without ultrasonic agitation, resulting in metallic features on the surface of the substrate (**Fig. 1.50**). Such a process is called lift-off, which is obviously easier with an undercut resist profile.

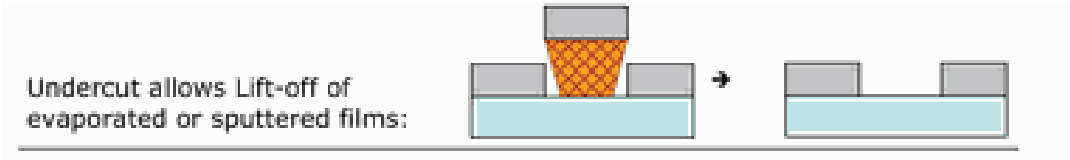

Figure 1.50 Illustration of metal deposition. (From [**186**])

1.5.2 Soft lithography

Photolithography and the associated pattern transfer techniques (etching, deposition etc...) came from the semiconductor industry which generally requires expensive equipment and may not be fully suitable or sufficient for chemical and biological applications.

As alternative and complement to conventional microfabrication techniques, *Xia and Whitesides* [**191**] proposed a soft lithography which is based on the use of polydimethylsiloxane (PDMS) mold or stamp. PDMS is an elastomeric material which can be easily casted on a master pattern and the replicated features can then be used for microcontact printing or device fabrication. Since then, soft lithography techniques were widely spread in research laboratories and are now routinely used in different research fields.

a- The PDMS

PDMS is a polymer belonging to the group of organosilicon (**Fig. 1.51**) [**192**]. The pre-polymer PDMS is a liquid, prepared by mixing part A (vinyl groups) and B (hydrosiloxanes groups+ catalyst) at different ratios. It can then be used for cross-linking at various temperatures which leads to solidified PDMS layer of different stiffness. The common ratio used is 10:1 (wt Part A vs Part B). The higher the mixture ratio, the softer the resulted PDMS layer will be.

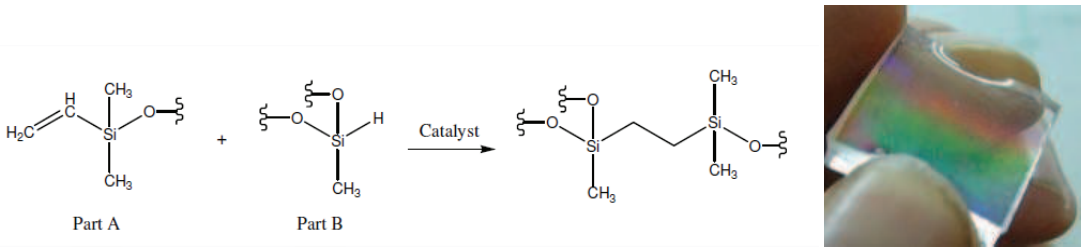

Figure 1.51 (**a**) PDMS crosslinking. (from [**193**]) (**b**) A PDMS block. (From [**194**])

PDMS has many interest properties for both processing and applications:

- It is mechanically and chemically stable,
- It is transparent over a large spectral range,
- It is cheap and easy to process,
- It is biocompatible,
- It can be easily bond to glass or silicon,
- Its surface can be modified by silanization,
- It is elastic with an adjustable Young's module,
- It has a low surface energy.

b- Fabrication of PDMS stamps

PDMS stamps are on the basis of all soft lithography. As shown in **Fig. 1.52**, the master patterns (mold) are first made by photolithography on silicon. After deposition of TMCS (tetramethylchlorosilane) to prevent PDMS sticking on the mold, the liquid PDMS is poured over the mold and then cured at a typical temperature of 80°C for 30 min. After the mold release, the solidified PDMS layer can be cut into individual stamps.

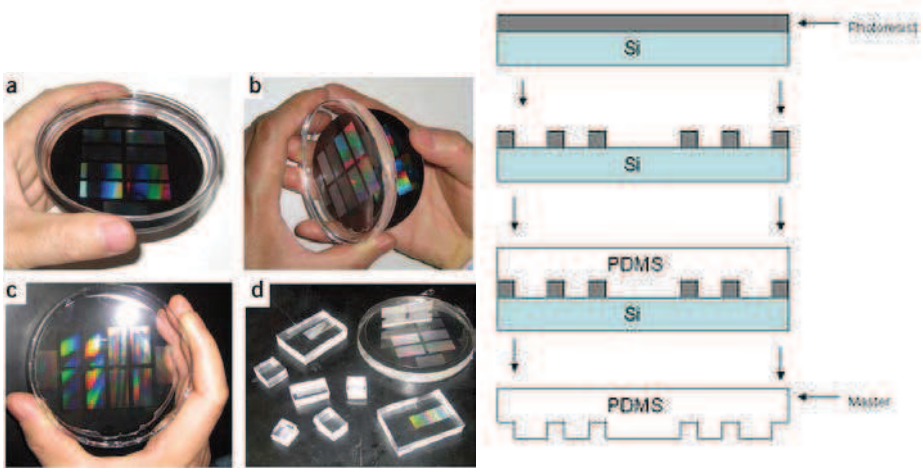

Figure 1.52 (**a**) PDMS stamp fabrication. (From [**195**]) (**b**) Schematic of the process view from the side. (From [**196**])

c- Microcontact printing

A solution of biomolecules is incubated on the surface of the PDMS stamp (inking). After evaporation, the stamp is brought into contact on the surface of the substrate to be functionalized (printing) (**Fig 1.53).** The surface treatment of PDMS by using atmospheric plasma for example can decrease temporarily the hydrophobicity of PDMS so that it can be used to enhance the spreading of the solution on the stamp for an improved printing [**195**].

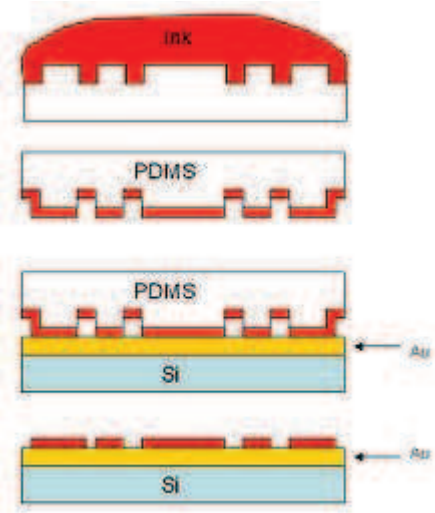

Figure 1.53 Schematic of microcontact printing. (From [**196**])

1.6 Electrospinning

The above described methods allow producing micro patterns with defined geometry or layout, which are required for device fabrication as well as fundamental research. These methods are essentially lithography. In general, non-lithography methods such as chemical organization, aluminum anodic oxidation, electrospinning, self-assembling, etc. cannot be applied to define patterns of arbitrary geometry but they are lower cost and higher throughput with respect to well-known lithography methods. Electrospinning, in particular, is attractive for the manufacturing of a large variety of nanofibers. These nanofibers have nanoscale diameters, high surface-to-volume ratio, and unique physicochemical properties for different applications. In this study, we were also interested in using the electrospinning method in order to fabricate nanofibers which can be actuated electrically.

Electrospinning is an easy method which only needs a syringe pump, a high-voltage power supply and a collector (**Fig. 1.54**). During the electrospinning, a polymer solution is injected at a constant flow rate from the nozzle of the syringe which forms a Taylor cone when the syringe is positive powered and the collector is negative powered. The collector is electrically conductive such as silicon wafer, aluminum foil, conductive paper, and other metal structures. The distance between the two electrodes is in the range of 10~25 cm and the applied electrical voltage in the range of 0.5–30 kV, depending on the solution property. When the electrical force is larger than the surface tension, a polymer jet is formed, the solvent is rapidly evaporated, and dry fibrous mats are fabricated on the collector. In general, nanofibers are deposited on a solid surface but it can also be suspended in a metal frame or over a large surface.

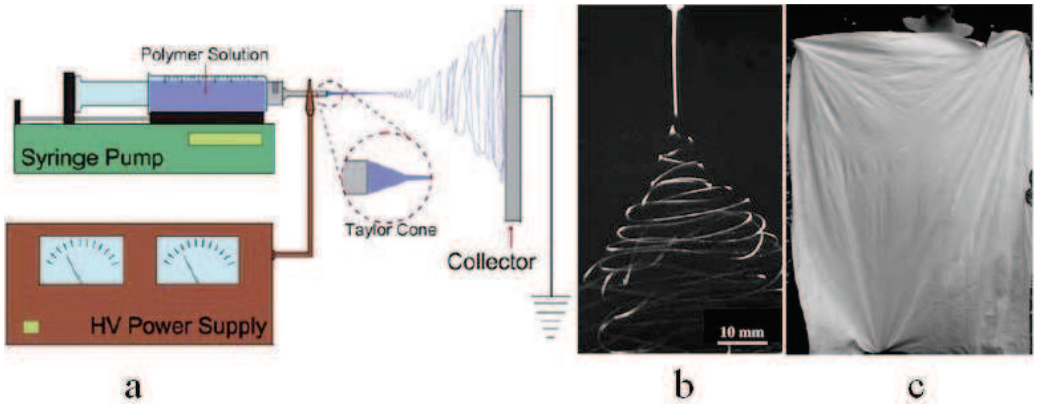

Figure 1.54 (**a**) Typical set-up for electrospinning. (**b**) Nanofibers jetting out from the Taylor cone by high velocity CCD. (**c**) An optical image of the large area nanofiber mats. (From [**197**])

Nanofibers are important for fundamental research and a number of applications. Although the process of the electrospinning is simple, a few important parameters have to be adjusted to control the quality of the deposition.

On one hand, the property of the polymer solution including viscosity, concentration, polymer molecular weight, solvent, surface tension, charge, and temperature have to be controlled. The solution viscosity should be high enough to keep the fiber structure against breaking by the strong electrical field and to avoid the formation of beads. However, a too high viscosity will prevent the jet formation or result in too large fiber diameters. The

viscosity of the solution is related to the concentration of the solution and the molecular weight of the polymer. In a diluted solution, the polymers are separated each other and homogenous distributed in the solution without interaction. Only beads or beads included fibers can be obtained. In a semi concentrated solution (contact concentration), fibers can be correctly obtained. In a highly concentrated solution (entanglement concentration), large diameter fibers can be produced. The molecular weight of the polymer affects the solution viscosity so the fiber diameter. Polymer solutions of large molecular weight but a relatively low concentration could be suited for electrospinning. Otherwise, if the polymer's molecular weight is too small, no fiber can be produced even with quite high concentration. To choose a good solvent, the dissolved ability and the boiling point should be considered. It is necessary that the solvent can evaporate completely when the fibers reach the collector, otherwise, the fibers will be connected together. Therefore, it is better to use the solvent with low boiling point. However, too low boiling point solvent will evaporate quickly and result in easy aggregation of the polymer at the tip of the nozzle, which inhibits the feeding of the polymer solution out of the syringe. In general, the water is used for the hydrophilic solvent and $CHCl_3$, CH_2Cl_2, DMF, THF, ethanol and other organic or the mixture of the solvent are chosen for the hydrophobic polymer. Besides the above consideration, the solvent may affect the structure of the fibers. For example, smooth polystyrene fibers with several hundreds of nanometer diameter could be obtained with the concentration of 12.5% in DMF. Using the mixture solvent of DMF and THF will easily produce the fibers with many pores, which has been used for the treatment of contaminants and other molecular absorption. In addition, the surface tension, composition and charge of the solution can also affect the fiber structures. Salts and some charged surfactant are generally added into the solution to eliminate the beads on the fiber, which is attributed to the increased charge of the solution by the additive regents. However, it was stated that additive of salts to increase conductivity as well caused the increase of mass flow rate that resulted in thicker fibers formation, since the conductivity needs to be controlled at a proper regime of 10^{-6}~10^{-8} (Ωm^{-1}) in order for the jet to maintain a stable stream status. The average diameter of the electrospun nanofibers are normally in the order of several hundred nanometers. When materials with large size exist in the solution, some novel structures could be obtained such as the necklace structure by doping the SiO_2 microsphere in the PVA solution. The surface tension of the solution ensures that the sphere was encapsulated inside the fibers.

On the other hand, the operation parameters including voltage, distance, flow rate, the structure and design of the nozzle and collectors have to be optimized. Only after attainment of a threshold voltage, fiber formation occurs, which induces the necessary charges on the solution along with electric field and initiates the electrospinning process. Above the critical value, the voltage may affect the Taylor cone, fiber diameter, fiber quantity and so on. For example, there is a greater probability of beads formation at a too high voltage. The distance between the tip and the collector has to be optimized to give the fibers sufficient time to dry before reaching the collector. Otherwise, flat fibers can be produced if the distance is not sufficiently large and a too large distance requires a much high electric voltage. The flow rate of the polymer from the syringe is also an important parameter. A lower feed rate is more desirable as the solvent will get enough time for evaporation. High flow rates result in beaded fibers due to unavailability of proper drying time prior to reaching the collector. The form, the size and the movement of the collector are all important parameters for the fiber distribution. Since the electrospun process is mainly driven by the electrical field, and fibers would preferentially deposit to the conductive part of the collector. Thus the fiber deposition can be manipulated by regulating the distribution of the electrical field, which could be realized by the design of collectors with different types. To produce the patterned, alignment or more complex structure fibers, researched have come up with sophisticated design of the collector and use such as rotating drum. When the drum rotates at high speed (1000-4000 rpm) it creates a linear velocity vector that drags the fibers on the drum with alignment.

Electrospinning of polymers offers unique opportunities for the preparation of nearly every soluble or melt polymer. Composites can be prepared simply by addition of a composite component to the electrospinning solution. Thereby, composite fibers, functional fiber, and fibers with complex structure can be prepared by electrospinning of polymers with additional compounds. Up to date, many natural polymers have been reported by electrospinning to produce the nanofibers, including cellulose, alginate, gelatin, chitin, hyaluronic acid, collagen, chitosan and silk. Because most of these polymers are biocompatible and water soluble, and some of them are the important component existed in the organism, the resulted nanofibers have been widely used for the biosensor, cell culture, proliferation and other applications. However, these materials often lack the desired physical mechanical properties or are difficult to electrospin on their own. In comparison with the natural polymer, the synthetic polymer has good chemical stability and mechanical performance. And the structure and property could be changed via organic synthesis according to the requirement. The popular polymer for

the electrospinning includes PVA, PVA, PVP, PCL, PVDF, PEO, PEI and PUA. In order to obtain good property both of the biocompatible and mechanical, development of hybrid materials consisting of a blend of synthetic and natural materials were usually prepared. Apart from the polymer, some organic molecules have been encapsulated into the nanofiber for the application of sensors and organic electronic study.

1.7 Research objectives of this work

Tissue engineering aims at repairing damaged tissues and recovering the corresponding biological functions. In order to restore the damaged tissue of higher functions such neural systems, design and manufacturing of new types of cell culture platform are needed. In this work, we developed several micro-fabrication techniques for polyvinylidene fluoride (PVDF), a highly non-reactive, piezoelectric, thermoplastic fluoropolymer, which can be used for cell culture and tissue engineering. We first studied the cell adhesion and growth on PVDF substrates patterned using different fabrication techniques, including micro-photolithography, soft lithography, microcontact printing. The influence of micro-patterning on PVDF piezoelectric activities were characterized using different surface analysis methods (FTIR, XRD). Then, we developed a systematic study on the fabrication of PVDF nanofibers and their compatibility to cell culture investigations. Finally, we show the feasibility of doping the electrospun PVDF nanofibers with magnetic nanoparticles which makes the nanofibers excitable with a remote magnetic field.

References

[1] Alberts, B., Johnson, A., Lewis, J., Raff, M., Roberts, K., & Walter, P. (2007). Molecular Biology of the Cell. Garland Science.

[2] http://en.wikipedia.org/wiki/Cytoskeleton

[3] Karp, G. (2009). Cell and Molecular Biology: Concepts and Experiments. Wiley.

[4] Borradori, L., & Sonnenberg, a. (1999). Structure and function of hemidesmosomes: more than simple adhesion complexes. The Journal of investigative dermatology, 112(4), 411–8. doi:10.1046/j.1523-1747.1999.00546.x

[5] http://en.wikipedia.org/wiki/Extracellular_matrix

[6] http://en.wikipedia.org/wiki/Collagen

[7] http://en.wikipedia.org/wiki/Elastin

[8] http://en.wikipedia.org/wiki/Axon

[9] http://en.wikipedia.org/wiki/Microfluidics

[10] Tabeling, P. (2010). Introduction to Microfluidics. Oxford University Press. doi:978-0-19-856864-3

[11] Cooper, G. (2000). *The Cell: A Molecular Approach. 2nd edition.* Sinauer Associates. Retrieved from http://www.ncbi.nlm.nih.gov/books/NBK9839/

[12] Gallego-perez, D. (2011). MICRO/NANOSCALE ENGINEERING OF THE CELL MICROENVIRONMENT.)

[13] Jeon, N. L., Dertinger, S. K. W., Chiu, D. T., Choi, I. S., Stroock, A. D., & Whitesides, G. M. (2000). Generation of Solution and Surface Gradients Using Microfluidic Systems. *Langmuir*, *16*(22), 8311–8316. doi:10.1021/la000600b

[14] Dertinger, S. K. W., Chiu, D. T., Jeon, N. L., & Whitesides, G. M. (2001). Generation of Gradients Having Complex Shapes Using Microfluidic Networks. *Analytical Chemistry*, *73*(6), 1240–1246. doi:10.1021/ac001132d

[15] http://hyperphysics.phy-astr.gsu.edu/hbase/ppois.html

[16] Kamholz, A. E., Weigl, B. H., Finlayson, B. A., & Yager, P. (1999). Quantitative Analysis of Molecular Interaction in a Microfluidic Channel: The T-Sensor. *Analytical Chemistry*, *71*(23), 5340–5347. doi:10.1021/ac990504j

[17] Kim, S., Kim, H. J., & Jeon, N. L. (2010). Biological applications of microfluidic gradient devices. *Integrative biology:quantitative biosciences from nano to macro*, *2*(11-12), 584–603. doi:10.1039/c0ib00055h

[18] Wu, H., Huang, B., & Zare, R. N. (2006). Generation of complex, static solution gradients in microfluidic channels. *Journal of the American Chemical Society*, *128*(13), 4194–5. doi:10.1021/ja058530o

[19] Yang, M., Li, C.-W., & Yang, J. (2002). Cell Docking and On-Chip Monitoring of Cellular Reactions with a Controlled Concentration Gradient on a Microfluidic Device. *Analytical Chemistry*, *74*(16), 3991–4001. doi:10.1021/ac025536c

[20] Zaari, N., Rajagopalan, P., Kim, S. K., Engler, A. J., & Wong, J. Y. (2004). Photopolymerization in Microfluidic Gradient Generators: Microscale Control of Substrate Compliance to Manipulate Cell Response. *Advanced Materials*, *16*(23-24), 2133–2137. doi:10.1002/adma.200400883

[21] Chung, B. G., & Choo, J. (2010). Microfluidic gradient platforms for controlling cellular behavior. *Electrophoresis*, *31*(18), 3014–27. doi:10.1002/elps.201000137

[22] Lin, F., Saadi, W., Rhee, S. W., Wang, S.-J., Mittal, S., & Jeon, N. L. (2004). Generation of dynamic temporal and spatial concentration gradients using microfluidic devices. *Lab on a chip*, *4*(3), 164–7. doi:10.1039/b313600k

[23] Irimia, D., Geba, D. A., & Toner, M. (2006). Universal microfluidic gradient generator. *Analytical chemistry*, *78*(10), 3472–7. doi:10.1021/ac0518710

[24] Irimia, D., Liu, S.-Y., Tharp, W. G., Samadani, A., Toner, M., & Poznansky, M. C. (2006). Microfluidic system for measuring neutrophil migratory responses to fast switches of chemical gradients. *Lab on a chip*, *6*(2), 191–8. doi:10.1039/b511877h

[25] Lin, F., Nguyen, C. M.-C., Wang, S.-J., Saadi, W., Gross, S. P., & Jeon, N. L. (2005). Neutrophil Migration in Opposing Chemoattractant Gradients Using Microfluidic Chemotaxis Devices. Annals of Biomedical Engineering, 33(4), 475–482. doi:10.1007/s10439-005-2503-6

[26] Atencia, J., Morrow, J., & Locascio, L. E. (2009). The microfluidic palette: a diffusive gradient generator with spatio-temporal control. Lab on a chip, 9(18), 2707–14. doi:10.1039/b902113b

[27] Saadi, W., Wang, S.-J., Lin, F., & Jeon, N. L. (2006). A parallel-gradient microfluidic chamber for quantitative analysis of breast cancer cell chemotaxis. Biomedical microdevices, 8(2), 109–18. doi:10.1007/s10544-006-7706-6

[28] Walsh, C. L., Babin, B. M., Kasinskas, R. W., Foster, J. A., McGarry, M. J., & Forbes, N. S. (2009). A multipurpose microfluidic device designed to mimic microenvironment gradients and develop targeted cancer therapeutics. Lab on a chip, 9(4), 545–54. doi:10.1039/b810571e

[29] Siyan, W., Feng, Y., Lichuan, Z., Jiarui, W., Yingyan, W., Li, J., Bingcheng, L., et al. (2009). Application of microfluidic gradient chip in the analysis of lung cancer chemotherapy resistance. Journal of pharmaceutical and biomedical analysis, 49(3), 806–10. doi:10.1016/j.jpba.2008.12.021

[30] Pihl, J., Sinclair, J., Sahlin, E., Karlsson, M., Petterson, F., Olofsson, J., & Orwar, O. (2005). Microfluidic gradient-generating device for pharmacological profiling. Analytical chemistry, 77(13), 3897–903. doi:10.1021/ac050218+

[31] Zhu, X., Yi Chu, L., Chueh, B., Shen, M., Hazarika, B., Phadke, N., & Takayama, S. (2004). Arrays of horizontally-oriented mini-reservoirs generate steady microfluidic flows for continuous perfusion cell culture and gradient generation. The Analyst, 129(11), 1026–31. doi:10.1039/b407623k

[32] Du, Y., Shim, J., Vidula, M., Hancock, M. J., Lo, E., Chung, B. G., Borenstein, J. T., et al. (2009). Rapid generation of spatially and temporally controllable long-range concentration gradients in a microfluidic device. Lab on a chip, 9(6), 761–7. doi:10.1039/b815990d

[33] Chung, B. G., Flanagan, L. A., Rhee, S. W., Schwartz, P. H., Lee, A. P., Monuki, E. S., & Jeon, N. L. (2005). Human neural stem cell growth and differentiation in a gradient-generating microfluidic device. Lab on a chip, 5(4), 401–6. doi:10.1039/b417651k

[34] Millet, L. J., Stewart, M. E., Nuzzo, R. G., & Gillette, M. U. (2010). Guiding neuron development with planar surface gradients of substrate cues deposited using microfluidic devices. Lab on a chip, 10(12), 1525–35. doi:10.1039/c001552k

[35] Walsh, C. L., Babin, B. M., Kasinskas, R. W., Foster, J. A., McGarry, M. J., & Forbes, N. S. (2009). A multipurpose microfluidic device designed to mimic microenvironment gradients and develop targeted cancer therapeutics. Lab on a chip, 9(4), 545–54. doi:10.1039/b810571e

[36] Kothapalli, C. R., van Veen, E., de Valence, S., Chung, S., Zervantonakis, I. K., Gertler, F. B., & Kamm, R. D. (2011). A high-throughput microfluidic assay to study neurite response to growth factor gradients. Lab on a chip, 11(3), 497–507. doi:10.1039/c0lc00240b

[37] Bhattacharjee, N., Li, N., Keenan, T. M., & Folch, A. (2010). A neuron-benign microfluidic gradient generator for studying the response of mammalian neurons towards axon guidance factors. Integrative biology: quantitative biosciences from nano to macro, 2(11-12), 669–79. doi:10.1039/c0ib00038h

[38] Jiang, X., Xu, Q., Dertinger, S. K. W., Stroock, A. D., Fu, T.-M., & Whitesides, G. M. (2005). A general method for patterning gradients of biomolecules on surfaces using microfluidic networks. *Analytical chemistry*, *77*(8), 2338–47. doi:10.1021/ac048440m

[39] Caelen, I., Bernard, A., Juncker, D., Michel, B., Heinzelmann, H., & Delamarche, E. (2000). Formation of Gradients of Proteins on Surfaces with Microfluidic Networks. *Langmuir*, *16*(24), 9125–9130. doi:10.1021/la000851k

[40] Fosser, K. A., & Nuzzo, R. G. (2003). Fabrication of patterned multicomponent protein gradients and gradient arrays using microfluidic depletion. *Analytical chemistry*, *75*(21), 5775–82. doi:10.1021/ac034634a

[41] Crozatier, C., Berre, M. L., & Chen, Y. (2006). Multi-colour micro-contact printing based on microfluidic network inking. *Microelectronic Engineering*, *83*(4-9), 910–913. doi:10.1016/j.mee.2006.01.015

[42] Qin, D., Xia, Y., & Whitesides, G. M. (2010). Soft lithography for micro- and nanoscale patterning. Nature protocols, 5(3), 491–502. doi:10.1038/nprot.2009.234

[43] Kumar, A., Biebuyck, H. A., & Whitesides, G. M. (1994). Patterning Self-Assembled Monolayers: Applications in Materials Science. *Langmuir*, *10*(5), 1498–1511. doi:10.1021/la00017a030

[44] Hidber, P. C., Helbig, W., Kim, E., & Whitesides, G. M. (1996). Microcontact Printing of Palladium Colloids: Micron-Scale Patterning by Electroless Deposition of Copper. *Langmuir*, *12*(5), 1375–1380. doi:10.1021/la9507500

[45] Kumar, A., & Whitesides, G. M. (1993). Features of gold having micrometer to centimeter dimensions can be formed through a combination of stamping with an elastomeric stamp and an alkanethiol "'ink'" followed by chemical etching. *Applied Physics Letters*, *63*(14), 2002. doi:10.1063/1.110628

[46] Alom Ruiz, S., & Chen, C. S. (2007). Microcontact printing: A tool to pattern. *Soft Matter*, *3*(2), 168. doi:10.1039/b613349e

[47] Bernard, A., Delamarche, E., Schmid, H., Michel, B., Bosshard, H. R., & Biebuyck, H. (1998). Printing Patterns of Proteins. *Langmuir*, *14*(9), 2225–2229. doi:10.1021/la980037l

[48] James, C. D., Davis, R. C., Kam, L., Craighead, H. G., Isaacson, M., Turner, J. N., & Shain, W. (1998). Patterned Protein Layers on Solid Substrates by Thin Stamp Microcontact Printing. *Langmuir*, *14*(4), 741–744. doi:10.1021/la9710482

[49] Mrksich, M., Dike, L. E., Tien, J., Ingber, D. E., & Whitesides, G. M. (1997). Using microcontact printing to pattern the attachment of mammalian cells to self-assembled monolayers of alkanethiolates on transparent films of gold and silver. *Experimental cell research*, *235*(2), 305–13. doi:10.1006/excr.1997.3668

[50] Singhvi, R., Kumar, A., Lopez, G., Stephanopoulos, G., Wang, D., Whitesides, G., & Ingber, D. (1994). Engineering cell shape and function. *Science*, *264*(5159), 696–698. doi:10.1126/science.8171320

[51] Kane, R. (1999). Patterning proteins and cells using soft lithography. *Biomaterials*, *20*(23-24), 2363–2376. doi:10.1016/S0142-9612(99)00165-9

[52] Théry, M., & Piel, M. (2009). Adhesive micropatterns for cells: a microcontact printing protocol. *Cold Spring Harbor protocols*, *2009*(7), pdb.prot5255. doi:10.1101/pdb.prot5255

[53] Ammar, A., Damien, C., Jenny, F., Matthieu, P., & Nicolas, C. (2011). Micropatterning on silicon elastomer (PDMS) with deep UVs. Retrieved from http://dx.doi.org/10.1038/protex.2011.239

[54] Bernard, A., Renault, J. P., Michel, B., Bosshard, H. R., & Delamarche, E. (2000). Microcontact Printing of Proteins. *Advanced Materials*, *12*(14), 1067–1070. doi:10.1002/1521-4095(200007)12:14<1067::AID-ADMA1067>3.0.CO;2-M

[55] Rozkiewicz, D. I., Kraan, Y., Werten, M. W. T., de Wolf, F. A., Subramaniam, V., Ravoo, B. J., & Reinhoudt, D. N. (2006). Covalent microcontact printing of proteins for cell patterning. *Chemistry (Weinheim an der Bergstrasse, Germany)*, *12*(24), 6290–7. doi:10.1002/chem.200501554

[56] Chen, C. S. (1997). Geometric Control of Cell Life and Death. Science, 276(5317), 1425–1428. doi:10.1126/science.276.5317.1425

[57] Théry, M., Racine, V., Pépin, A., Piel, M., Chen, Y., Sibarita, J.-B., & Bornens, M. (2005). The extracellular matrix guides the orientation of the cell division axis. Nature cell biology, 7(10), 947–53. doi:10.1038/ncb1307

[58] Tseng, Q., Duchemin-Pelletier, E., Deshiere, A., Balland, M., Guillou, H., Filhol, O., & Théry, M. (2012). Spatial organization of the extracellular matrix regulates cell-cell junction positioning. *Proceedings of the National Academy of Sciences of the United States of America*, *109*(5), 1506–11. doi:10.1073/pnas.1106377109

[59] Théry, M. (2010). Micropatterning as a tool to decipher cell morphogenesis and functions. *Journal of cell science*, *123*(Pt 24), 4201–13. doi:10.1242/jcs.075150

[60] Tseng, Q., Wang, I., Duchemin-Pelletier, E., Azioune, A., Carpi, N., Gao, J., Filhol, O., et al. (2011). A new micropatterning method of soft substrates reveals that different tumorigenic signals can promote or reduce cell contraction levels. *Lab on a chip*, *11*(13), 2231–40. doi:10.1039/c0lc00641f

[61] Offenhausser, A., B?cker-Meffert, S., Decker, T., Helpenstein, R., Gasteier, P., Groll, J., M?ller, M., et al. (2007). Microcontact printing of proteins for neuronal cell guidance. *Soft Matter*, *3*(3), 290. doi:10.1039/b607615g

[62] Cornish, T., Branch, D. W., Wheeler, B. C., & Campanelli, J. T. (2002). Microcontact printing: a versatile technique for the study of synaptogenic molecules. *Molecular and cellular neurosciences*, *20*(1), 140–53. doi:10.1006/mcne.2002.1101

[63] Kam, L., Shain, W., Turner, J. N., & Bizios, R. (2001). Axonal outgrowth of hippocampal neurons on micro-scale networks of polylysine-conjugated laminin. *Biomaterials*, *22*(10), 1049–1054. doi:10.1016/S0142-9612(00)00352-5

[64] Wyart, C., Ybert, C., Bourdieu, L., Herr, C., Prinz, C., & Chatenay, D. (2002). Constrained synaptic connectivity in functional mammalian neuronal networks grown on patterned surfaces. *Journal of Neuroscience Methods*, *117*(2), 123–131. doi:10.1016/S0165-0270(02)00077-8

[65] Scholl, M., Sprössler, C., Denyer, M., Krause, M., Nakajima, K., Maelicke, A., Knoll, W., et al. (2000). Ordered networks of rat hippocampal neurons attached to silicon oxide surfaces. *Journal of Neuroscience Methods*, *104*(1), 65–75. doi:10.1016/S0165-0270(00)00325-3

[66] Clark, P., Britland, S., & Connolly, P. (1993). GROWTH CONE GUIDANCE AND NEURON MORPHOLOGY ON MICROPATTERNED LAMININ SURFACES. Journal of cell science, 105, 203 – 212.

[67] Heller, D. A., Garga, V., Kelleher, K. J., Lee, T.-C., Mahbubani, S., Sigworth, L. A., Lee, T. R., et al. (2005). Patterned networks of mouse hippocampal neurons on peptide-coated gold surfaces. Biomaterials, 26(8), 883–9. doi:10.1016/j.biomaterials.2004.03.029

[68] Specht, C. G., Williams, O. A., Jackman, R. B., & Schoepfer, R. (2004). Ordered growth of neurons on diamond. Biomaterials, 25(18), 4073–8. doi:10.1016/j.biomaterials.2003.11.006

[69] Marconi, E., Nieus, T., Maccione, A., Valente, P., Simi, A., Messa, M., Dante, S., et al. (2012). Emergent functional properties of neuronal networks with controlled topology. (M. Zochowski, Ed.)PloS one, 7(4), e34648. doi:10.1371/journal.pone.0034648

[70] Kleinfeld, D., Kahler, K., & Hockberger, P. (1988). CONTROLLED OUTGROWTH OF DISSOCIATED NEURONS ON PATTERNED SUBSTRATES. The Journal of neuroscience, 8(11), 4098 – 4120.

[71] Vogt, A. K., Lauer, L., Knoll, W., & Offenhäusser, A. (2003). Micropatterned substrates for the growth of functional neuronal networks of defined geometry. Biotechnology progress, 19(5), 1562–8. doi:10.1021/bp034016f

[72] Corey, J. M., Wheeler, B. C., & Brewer, G. J. (1991). Compliance of hippocampal neurons to patterned substrate networks. *Journal of neuroscience research*, *30*(2), 300–7. doi:10.1002/jnr.490300204

[73] Boehler, M. D., Leondopulos, S. S., Wheeler, B. C., & Brewer, G. J. (2012). Hippocampal networks on reliable patterned substrates. *Journal of neuroscience methods*, *203*(2), 344–53. doi:10.1016/j.jneumeth.2011.09.020

[74] Harrison, R. G. (1911). ON THE STEREOTROPISM OF EMBRYONIC CELLS. *Science (New York, N.Y.)*, *34*(870), 279–81. doi:10.1126/science.34.870.279

[75] Weiss, P. (1958). Cell contact. *International Review of Cytology: A Survey of Cell Biology*, *7*, 391 – 423. doi:10.1016/S0074-7696(08)62692-3

[76] Weiss, P. (1945). Experiments on cell and axon orientation in vitro: The role of colloidal exudates in tissue organization. *Journal of Experimental Zoology*, *100*(3), 353–386. doi:10.1002/jez.1401000305

[77] Curtis, A., & Varde, M. (1964). CONTROL OF CELL BEHAVIOR - TOPOLOGICAL FACTORS. *Journal of the National Cancer Institute*, *33*(1).

[78] Dunn, G. A., & Heath, J. P. (1976). A new hypothesis of contact guidance in tissue cells. *Experimental Cell Research*, *101*(1), 1–14. doi:10.1016/0014-4827(76)90405-5

[79] Ohara, P. T., & Buck, R. C. (1979). Contact guidance in vitro. *Experimental Cell Research*, *121*(2), 235–249. doi:10.1016/0014-4827(79)90002-8

[80] Curtis, A., & Wilkinson, C. (1997). Topographical control of cells. *Biomaterials*, *18*(24), 1573–1583. doi:10.1016/S0142-9612(97)00144-0

[81] Clark, P., Connolly, P., Curtis, A., Dow, J., & Wilkinson, C. (1990). TOPOGRAPHICAL CONTROL OF CELL BEHAVIOR .2. MULTIPLE GROOVED SUBSTRATA. *Development*, *108*(4), 635 – 644.

[82] Clark, P., Connolly, P., Curtis, A., Dow, J., & Wilkinson, C. (1987). TOPOGRAPHICAL CONTROL OF CELL BEHAVIOR .1. SIMPLE STEP CUES. *Development*, *99*(3), 439 – 448.

[83] Craighead, H. ., James, C. ., & Turner, A. M. . (2001). Chemical and topographical patterning for directed cell attachment. *Current Opinion in Solid State and Materials Science*, *5*(2-3), 177–184. doi:10.1016/S1359-0286(01)00005-5

[84] Teixeira, A. I., Abrams, G. a, Bertics, P. J., Murphy, C. J., & Nealey, P. F. (2003). Epithelial contact guidance on well-defined micro- and nanostructured substrates. *Journal of cell science*, *116*(Pt 10), 1881–92. doi:10.1242/jcs.00383

[85] Clark, P., Connolly, P., Curtis, A. S., Dow, J. A., & Wilkinson, C. D. (1991). Cell guidance by ultrafine topography in vitro. *Journal of cell science*, *99 (Pt 1)*, 73–7. Retrieved from http://www.ncbi.nlm.nih.gov/pubmed/1757503

[86] Pan, Z., Yan, C., Peng, R., Zhao, Y., He, Y., & Ding, J. (2012). Control of cell nucleus shapes via micropillar patterns. *Biomaterials*, *33*(6), 1730–5. doi:10.1016/j.biomaterials.2011.11.023

[87] Davidson, P. M., Özçelik, H., Hasirci, V., Reiter, G., & Anselme, K. (2009). Microstructured Surfaces Cause Severe but Non-Detrimental Deformation of the Cell Nucleus. *Advanced Materials*, *21*(35), 3586–3590. doi:10.1002/adma.200900582

[88] Dickinson, L. E., Rand, D. R., Tsao, J., Eberle, W., & Gerecht, S. (2012). Endothelial cell responses to micropillar substrates of varying dimensions and stiffness. *Journal of biomedical materials research. Part A*, *100*(6), 1457–66. doi:10.1002/jbm.a.34059

[89] Nikkhah, M., Edalat, F., Manoucheri, S., & Khademhosseini, A. (2012). Engineering microscale topographies to control the cell-substrate interface. *Biomaterials*, *33*(21), 5230–46. doi:10.1016/j.biomaterials.2012.03.079

[90] Fu, J., Wang, Y.-K., Yang, M. T., Desai, R. A., Yu, X., Liu, Z., & Chen, C. S. (2010). Mechanical regulation of cell function with geometrically modulated elastomeric substrates. *Nature methods*, *7*(9), 733–6. doi:10.1038/nmeth.1487

[91] Yang, M. T., Fu, J., Wang, Y.-K., Desai, R. A., & Chen, C. S. (2011). Assaying stem cell mechanobiology on microfabricated elastomeric substrates with geometrically modulated rigidity. *Nature protocols*, *6*(2), 187–213. doi:10.1038/nprot.2010.189

[92] Discher, D. E., Janmey, P., & Wang, Y.-L. (2005). Tissue cells feel and respond to the stiffness of their substrate. *Science (New York, N.Y.)*, *310*(5751), 1139–43. doi:10.1126/science.1116995

[93] Rajnicek, A., Britland, S., & McCaig, C. (1997). Contact guidance of CNS neurites on grooved quartz: influence of groove dimensions, neuronal age and cell type. *Journal of Cell Science*, (110), 2905–2913.

[94] Rajnicek, A., & McCaig, C. (1997). Guidance of CNS growth cones by substratum grooves and ridges: effects of inhibitors of the cytoskeleton, calcium channels and signal transduction pathways. *Journal of cell science*, *110 (Pt 2*, 2915–24.

[95] Gomez, N., Lee, J. Y., Nickels, J. D., & Schmidt, C. E. (2007). Micropatterned Polypyrrole: A Combination of Electrical and Topographical Characteristics for the Stimulation of Cells. *Advanced functional materials*, *17*(10), 1645–1653. doi:10.1002/adfm.200600669

[96] Fan, Y. W., Cui, F. Z., Hou, S. P., Xu, Q. Y., Chen, L. N., & Lee, I.-S. (2002). Culture of neural cells on silicon wafers with nano-scale surface topograph. *Journal of Neuroscience Methods*, *120*(1), 17–23. doi:10.1016/S0165-0270(02)00181-4

[97] Bettinger, C. J., Langer, R., & Borenstein, J. T. (2009). Engineering substrate topography at the micro- and nanoscale to control cell function. *Angewandte Chemie (International ed. in English)*, *48*(30), 5406–15. doi:10.1002/anie.200805179

[98] Singhvi, R., Stephanopoulos, G., & Wang, D. I. (1994). Effects of substratum morphology on cell physiology. *Biotechnology and bioengineering*, *43*(8), 764–71. doi:10.1002/bit.260430811

[99] Wójciak-Stothard, B., Curtis, A., Monaghan, W., MacDonald, K., & Wilkinson, C. (1996). Guidance and activation of murine macrophages by nanometric scale topography. *Experimental cell research*, *223*(2), 426–35. doi:10.1006/excr.1996.0098

[100] Chou, L., Firth, J. D., Uitto, V. J., & Brunette, D. M. (1995). Substratum surface topography alters cell shape and regulates fibronectin mRNA level, mRNA stability, secretion and assembly in human fibroblasts. *Journal of cell science*, *108 (Pt 4*, 1563–73.

[101] Biggs, M. J. P., Richards, R. G., & Dalby, M. J. (2010). Nanotopographical modification: a regulator of cellular function through focal adhesions. *Nanomedicine : nanotechnology, biology, and medicine*, *6*(5), 619–33. doi:10.1016/j.nano.2010.01.009

[102] Yim, E. K. F., Pang, S. W., & Leong, K. W. (2007). Synthetic nanostructures inducing differentiation of human mesenchymal stem cells into neuronal lineage. *Experimental cell research*, *313*(9), 1820–9. doi:10.1016/j.yexcr.2007.02.031

[103] Curtis, A. S. ., Casey, B., Gallagher, J. ., Pasqui, D., Wood, M. ., & Wilkinson, C. D. . (2001). Substratum nanotopography and the adhesion of biological cells. Are symmetry or regularity of nanotopography important? *Biophysical Chemistry*, *94*(3), 275–283. doi:10.1016/S0301-4622(01)00247-2

[104] Diehl, K. A., Foley, J. D., Nealey, P. F., & Murphy, C. J. (2005). Nanoscale topography modulates corneal epithelial cell migration. *Journal of biomedical materials research. Part A*, *75*(3), 603–11. doi:10.1002/jbm.a.30467

[105] Yu, H., Tay, C. Y., Pal, M., Leong, W. S., Li, H., Li, H., Wen, F., et al. (2012). A Bio-inspired Platform to Modulate Myogenic Differentiation of Human Mesenchymal Stem Cells Through Focal Adhesion Regulation. *Advanced Healthcare Materials*, n/a–n/a. doi:10.1002/adhm.201200142

[106] Jung, D. R., Kapur, R., Adams, T., Giuliano, K. A., Mrksich, M., Craighead, H. G., & Taylor, D. L. (2001). Topographical and physicochemical modification of material surface to enable patterning of living cells. *Critical reviews in biotechnology*, *21*(2), 111–54. doi:10.1080/20013891081700)

[107] Charest, J. L., Eliason, M. T., García, A. J., & King, W. P. (2006). Combined microscale mechanical topography and chemical patterns on polymer cell culture substrates. *Biomaterials*, *27*(11), 2487–94. doi:10.1016/j.biomaterials.2005.11.022

[108] Taylor, A. M., Blurton-Jones, M., Rhee, S. W., Cribbs, D. H., Cotman, C. W., & Jeon, N. L. (2005). A microfluidic culture platform for CNS axonal injury, regeneration and transport. *Nature methods*, *2*(8), 599–605. doi:10.1038/nmeth777

[109] Ikada, Y. (2006). Tissue Engineering, Volume 8: Fundamentals and Applications (Interface Science and Technology) (p. 490). Academic Press.

[110] Carletti, E., Motta, A., & Migliaresi, C. (2011). Scaffolds for tissue engineering and 3D cell culture. 3D Cell Culture (pp. 17–39). Springer. doi:10.1007/978-1-60761-984-0_2

[111] Hoshiba, T., Lu, H., Kawazoe, N., & Chen, G. (2010). Decellularized matrices for tissue engineering. Expert opinion on biological therapy, 10(12), 1717–28. doi:10.1517/14712598.2010.534079

[112] Yeong, W.-Y., Chua, C.-K., Leong, K.-F., & Chandrasekaran, M. (2004). Rapid prototyping in tissue engineering: challenges and potential. Trends in biotechnology, 22(12), 643–52. doi:10.1016/j.tibtech.2004.10.004

[113] Leukers, B., Gülkan, H., Irsen, S. H., Milz, S., Tille, C., Seitz, H., & Schieker, M. (2005). Biocompatibility of ceramic scaffolds for bone replacement made by 3D printing. Materialwissenschaft und Werkstofftechnik, 36(12), 781–787. doi:10.1002/mawe.200500968

[114] Ovsianikov, A., Gruene, M., Pflaum, M., Koch, L., Maiorana, F., Wilhelmi, M., Haverich, A., et al. (2010). Laser printing of cells into 3D scaffolds. Biofabrication, 2(1), 014104. doi:10.1088/1758-5082/2/1/014104

[115] Lam, C. X. ., Mo, X. ., Teoh, S. ., & Hutmacher, D. . (2002). Scaffold development using 3D printing with a starch-based polymer. Materials Science and Engineering: C, 20(1-2), 49–56. doi:10.1016/S0928-4931(02)00012-7

[116] http://en.wikipedia.org/wiki/3D_printing

[116] http://reprap.org/wiki/Prusa

[117] http://reprap.org/wiki/Mendel

[118] http://en.wikipedia.org/wiki/Powder_bed_and_inkjet_head_3d_printing

[119] http://en.wikipedia.org/wiki/Selective_laser_sintering

[120] http://www.xpress3d.com/Zcorp3DP.aspx

[121] http://www.shapeways.com/model/237637/mobius-tori.html

[122] http://www.zcorp.com/en/Products/3D-Printers/ZPrinter-650/spage.aspx

[123] http://objet.com/knowledge-center/rapid-prototyping/technologies inkjet

[124] Jeon, S., Malyarchuk, V., Rogers, J. A., & Wiederrecht, G. P. (2006). Fabricating three-dimensional nanostructures using two photon lithography in a single exposure step. Optics Express, 14(6), 2300. doi:10.1364/OE.14.002300

[125] LEE, K.-S., KIM, R. H., PRABHAKARAN, P., YANG, D.-Y., LIM, T. W., & PARK, S. H. (2007). TWO-PHOTON STEREOLITHOGRAPHY. *Journal of Nonlinear Optical Physics & Materials*, *16*(01), 59–73. doi:10.1142/S021886350700355X

[126] Park, S.-H., Yang, D.-Y., & Lee, K.-S. (2009). Two-photon stereolithography for realizing ultraprecise three-dimensional nano/microdevices. *Laser & Photonics Review*, *3*(1-2), 1–11. doi:10.1002/lpor.200810027

[127] http://www.asdn.net/asdn/nanotools/two-photon_polymerization.shtml

[128] Pham, Q. P., Sharma, U., & Mikos, A. G. (2006). Electrospinning of polymeric nanofibers for tissue engineering applications: a review. *Tissue engineering*, *12*(5), 1197–211. doi:10.1089/ten.2006.12.1197

[129] Yoo, H. S., Kim, T. G., & Park, T. G. (2009). Surface-functionalized electrospun nanofibers for tissue engineering and drug delivery. *Advanced drug delivery reviews*, *61*(12), 1033–42. doi:10.1016/j.addr.2009.07.007

[130] Vasita, R., & Katti, D. S. (2006). Nanofibers and their applications in tissue engineering. *International Journal of Nanomedicine*, *1*(1), 15–30. doi:10.2147/nano.2006.1.1.15

[131] Nisbet, D. R., Forsythe, J. S., Shen, W., Finkelstein, D. I., & Horne, M. K. (2009). Review paper: a review of the cellular response on electrospun nanofibers for tissue engineering. *Journal of biomaterials applications*, *24*(1), 7–29. doi:10.1177/0885328208099086

[132] Boudriot, U., Goetz, B., Dersch, R., Greiner, A., & Wendorff, J.-H. (2005). Role of Electrospun Nanofibers in Stem Cell Technologies and Tissue Engineering. *Macromolecular Symposia*, *225*(1), 9–16. doi:10.1002/masy.200550702

[133] Lee, Y.-S., Collins, G., & Livingston Arinzeh, T. (2011). Neurite extension of primary neurons on electrospun piezoelectric scaffolds. Acta biomaterialia, 7(11), 3877–86. doi:10.1016/j.actbio.2011.07.013

[134] Xie, J., MacEwan, M. R., Schwartz, A. G., & Xia, Y. (2010). Electrospun nanofibers for neural tissue engineering. *Nanoscale*, *2*(1), 35–44. doi:10.1039/b9nr00243j

[135] Yang, F., Xu, C. Y., Kotaki, M., Wang, S., & Ramakrishna, S. (2004). Characterization of neural stem cells on electrospun poly(L-lactic acid) nanofibrous scaffold. *Journal of Biomaterials Science, Polymer Edition*, *15*(12), 1483–1497. doi:10.1163/1568562042459733

[136] Yang, F., Murugan, R., Wang, S., & Ramakrishna, S. (2005). Electrospinning of nano/micro scale poly(L-lactic acid) aligned fibers and their potential in neural tissue engineering. *Biomaterials*, *26*(15), 2603–10. doi:10.1016/j.biomaterials.2004.06.051

[137] Xie, J., Willerth, S. M., Li, X., Macewan, M. R., Rader, A., Sakiyama-Elbert, S. E., & Xia, Y. (2009). The differentiation of embryonic stem cells seeded on electrospun nanofibers into neural lineages. Biomaterials, 30(3), 354–62. doi:10.1016/j.biomaterials.2008.09.046

[138] Christopherson, G. T., Song, H., & Mao, H.-Q. (2009). The influence of fiber diameter of electrospun substrates on neural stem cell differentiation and proliferation. *Biomaterials*, *30*(4), 556–64. doi:10.1016/j.biomaterials.2008.10.004

[139] Corey, J. M., Lin, D. Y., Mycek, K. B., Chen, Q., Samuel, S., Feldman, E. L., & Martin, D. C. (2007). Aligned electrospun nanofibers specify the direction of dorsal root ganglia neurite growth. *Journal of biomedical materials research. Part A*, *83*(3), 636–45. doi:10.1002/jbm.a.31285

[140] Wang, H. B., Mullins, M. E., Cregg, J. M., Hurtado, A., Oudega, M., Trombley, M. T., & Gilbert, R. J. (2009). Creation of highly aligned electrospun poly-L-lactic acid fibers for nerve regeneration applications. *Journal of neural engineering*, *6*(1), 016001. doi:10.1088/1741-2560/6/1/016001

[141] Prabhakaran, M. P., Venugopal, J., Chan, C. K., & Ramakrishna, S. (2008). Surface modified electrospun nanofibrous scaffolds for nerve tissue engineering. *Nanotechnology*, *19*(45), 455102. doi:10.1088/0957-4484/19/45/455102

[142]http://biomed.brown.edu/Courses/BI108/BI108_2001_Groups/Nerve_Regeneration/Guidance_Channels/Guidance_Channels_Page_1.htm

[143] Hashi, C. K., Zhu, Y., Yang, G.-Y., Young, W. L., Hsiao, B. S., Wang, K., Chu, B., et al. (2007). Antithrombogenic property of bone marrow mesenchymal stem cells in nanofibrous vascular grafts. *Proceedings of the National Academy of Sciences of the United States of America*, *104*(29), 11915–20. doi:10.1073/pnas.0704581104

[144] Panseri, S., Cunha, C., Lowery, J., Del Carro, U., Taraballi, F., Amadio, S., Vescovi, A., et al. (2008). Electrospun micro- and nanofiber tubes for functional nervous regeneration in sciatic nerve transections. *BMC biotechnology*, *8*(1), 39. doi:10.1186/1472-6750-8-39

[145] Teo, W. E., Kotaki, M., Mo, X. M., & Ramakrishna, S. (2005). Porous tubular structures with controlled fibre orientation using a modified electrospinning method. *Nanotechnology*, *16*(6), 918–924. doi:10.1088/0957-4484/16/6/049

[146] Zhang, D., & Chang, J. (2008). Electrospinning of three-dimensional nanofibrous tubes with controllable architectures. *Nano letters*, *8*(10), 3283–7. doi:10.1021/nl801667s

[147] Patel, N., & Poo, M. (1982). ORIENTATION OF NEURITE GROWTH BY EXTRACELLULAR ELECTRIC-FIELDS. *The Journal of neuroscience*, *2*(4), 483 – 496.

[148] Subramanian, A., Krishnan, U. M., & Sethuraman, S. (2012). Axially aligned electrically conducting biodegradable nanofibers for neural regeneration. *Journal of materials science. Materials in medicine*, *23*(7), 1797–809. doi:10.1007/s10856-012-4654-y

[149] Yow, S.-Z., Lim, T. H., Yim, E. K. F., Lim, C. T., & Leong, K. W. (2011). A 3D Electroactive Polypyrrole-Collagen Fibrous Scaffold for Tissue Engineering. *Polymers*, *3*(1), 527–544. doi:10.3390/polym3010527

[150] Guimard, N. K., Gomez, N., & Schmidt, C. E. (2007). Conducting polymers in biomedical engineering. *Progress in Polymer Science*, *32*(8-9), 876–921. doi:10.1016/j.progpolymsci.2007.05.012

[151] Mozafari, M., Mehraien, M., Vashaee, D., & Tayebi, L. (n.d.). Electroconductive Nanocomposite Scaffolds: A New Strategy Into Tissue Engineering and Regenerative Medicine. *Nanocomposites - New Trends and Developments*.

[152] Li, Y., Neoh, K. G., & Kang, E. T. (2005). Controlled release of heparin from polypyrrole-poly(vinyl alcohol) assembly by electrical stimulation. *Journal of biomedical materials research. Part A*, *73*(2), 171–81. doi:10.1002/jbm.a.30286

[153] MIARA, B., ROHAN, E., ZIDI, M., & LABAT, B. (2005). Piezomaterials for bone regeneration design—homogenization approach. *Journal of the Mechanics and Physics of Solids*, *53*(11), 2529–2556. doi:10.1016/j.jmps.2005.05.006

[154] Aebischer, P., Valentini, R. F., Dario, P., Domenici, C., & Galletti, P. M. (1987). Piezoelectric guidance channels enhance regeneration in the mouse sciatic nerve after axotomy. *Brain research*, *436*(1), 165–8. Retrieved from http://www.ncbi.nlm.nih.gov/pubmed/3690349

[155] Fine, E. G., Valentini, R. F., Bellamkonda, R., & Aebischer, P. (1991). Improved nerve regeneration through piezoelectric vinylidenefluoride-trifluoroethylene copolymer guidance channels. *Biomaterials*, *12*(8), 775–780. doi:10.1016/0142-9612(91)90029-A

[156] VALENTINI, R., VARGO, T., GARDELLAJR, J., & AEBISCHER, P. (1992). Electrically charged polymeric substrates enhance nerve fibre outgrowth In vitro. *Biomaterials*, *13*(3), 183–190. doi:10.1016/0142-9612(92)90069-Z

[157] Gallego, D., Ferrell, N. J., & Hansford, D. J. (2007). Fabrication of Piezoelectric Polyvinylidene Fluoride (PVDF) Microstructures by Soft Lithography for Tissue Engineering and Cell Biology Applications. *Materials Research*, *1002*.

[158] Gallego-Perez, D., Ferrell, N. J., Higuita-Castro, N., & Hansford, D. J. (2010). Versatile methods for the fabrication of polyvinylidene fluoride microstructures. *Biomedical microdevices*, *12*(6), 1009–17. doi:10.1007/s10544-010-9455-9

[159] http://en.wikipedia.org/wiki/Piezoelectricity

[160] Kawai, H. (1969). The Piezoelectricity of Poly (vinylidene Fluoride). *Jpn. J. Appl. Phys.*, *8*(7), 975. doi:10.1143/JJAP.8.975

[161] Omote, K., Ohigashi, H., & Koga, K. (1997). Temperature dependence of elastic, dielectric, and piezoelectric properties of "single crystalline'' films of vinylidene fluoride trifluoroethylene copolymer. *Journal of Applied Physics*, *81*(6), 2760. doi:10.1063/1.364300

[162] Chang, J., Dommer, M., Chang, C., & Lin, L. (2012). Piezoelectric nanofibers for energy scavenging applications. *Nano Energy*, *1*(3), 356–371. doi:10.1016/j.nanoen.2012.02.003

[163] http://www2.fiu.edu/~zhangj/Research.html

[164] Low, Y. K. A., Meenubharathi, N., Niphadkar, N. D., Boey, F. Y. C., & Ng, K. W. (2011). α- and β-poly(vinylidene fluoride) evoke different cellular behaviours. *Journal of biomaterials science. Polymer edition*, *22*(12), 1651–67. doi:10.1163/092050610X519471

[165] Satapathy, S., Gupta, P. K., Pawar, S., & Varma, K. B. R. (n.d.). Crystallization of β-phase Poly (vinylidene fluoride) films using dimethyl sulfoxide (DMSO) solvent and at suitable annealing condition, 1–18. Retrieved from http://arxiv.org/abs/0808.0419

[166] Lovinger, A. (1982). Developments in Crystalline Polymers - Poly (vinylidene fluoride) (pp. 195–273). Applied Science Publishers Ltd.

[167] Gregorio, R., & Ueno, E. (1999). Effect of crystalline phase, orientation and temperature on the dielectric properties of poly (vinylidene fluoride) (PVDF). *JOURNAL OF MATERIALS SCIENCE*, (34), 4489– 4500.

[168] Park, Y. J., Kang, Y. S., & Park, C. (2005). Micropatterning of semicrystalline poly(vinylidene fluoride) (PVDF) solutions. *European Polymer Journal*, *41*(5), 1002–1012. doi:10.1016/j.eurpolymj.2004.11.022

[169] Chavan, H. S. (2006). *Investigation of beta-phase poly (vinylidene fluoride) films using small-angle X-ray scattering*. UNIVERSITY OF CINCINNATI.

[170] Esterly, D. M. (2002). *Manufacturing of Poly(vinylidene fluoride) and Evaluation of its Mechanical Properties*. Virginia Polytechnic Institute and State University.

[171] Hansen, B. J., Liu, Y., Yang, R., & Wang, Z. L. (2010). Hybrid nanogenerator for concurrently harvesting biomechanical and biochemical energy. *ACS nano*, *4*(7), 3647–52. doi:10.1021/nn100845b

[172] http://en.wikipedia.org/wiki/Voigt_notation

[173] https://www.kcftech.com/lab_testing_equipment/piezoelectric_d33meter.shtml

[174] http://en.wikipedia.org/wiki/Piezoresponse_Force_Microscopy

[175] Liu, Y., Weiss, D. N., & Li, J. (2010). Rapid Nanoimprinting and Excellent Piezoresponse of Polymeric Ferroelectric Nanostructures, *4*(1), 83–90.

[176] http://www.analog.com/static/imported-files/data_sheets/AD622.pdf

[177] Benz, M., Euler, W. B., & Gregory, O. J. (2002). The Role of Solution Phase Water on the Deposition of Thin Films of Poly(vinylidene fluoride). *Macromolecules*, *35*(7), 2682–2688. doi:10.1021/ma011744f

[178] Cebe, P., & Runt, J. (2004). P(VDF-TrFE)-layered silicate nanocomposites. Part 1. X-ray scattering and thermal analysis studies. *Polymer*, *45*(6), 1923–1932. doi:10.1016/j.polymer.2004.01.014

[179] Davis, G. T., McKinney, J. E., Broadhurst, M. G., & Roth, S. C. (1978). Electric-field-induced phase changes in poly(vinylidene fluoride). *Journal of Applied Physics*, *49*(10), 4998. doi:10.1063/1.324446

[180] Gregorio, Rinaldo. (2006). Determination of the α, β, and γ crystalline phases of poly(vinylidene fluoride) films prepared at different conditions. *Journal of Applied Polymer Science*, *100*(4), 3272–3279. doi:10.1002/app.23137

[181] Kobayashi, M., Tashiro, K., & Tadokoro, H. (1975). Molecular Vibrations of Three Crystal Forms of Poly(vinylidene fluoride). *Macromolecules*, *8*(2), 158–171. doi:10.1021/ma60044a013

[182] Lovinger, A. J. (1982). Annealing of poly(vinylidene fluoride) and formation of a fifth phase. *Macromolecules*, *15*(1), 40–44. doi:10.1021/ma00229a008

[183] Mandal, D., Yoon, S., & Kim, K. J. (2011). Origin of piezoelectricity in an electrospun poly(vinylidene fluoride-trifluoroethylene) nanofiber web-based nanogenerator and nano-pressure sensor. *Macromolecular rapid communications*, *32*(11), 831–7. doi:10.1002/marc.201100040

[184] http://wikis.lib.ncsu.edu/index.php/Soft_Lithography

[185] http://www.billechols.name/Religion/Finding_God_Through_Science_4.htm

[186] http://www.microchemicals.eu/photoresist/photoresist_image_reversal_resists_eng.html

[187] http://www.himt.de/en/products/muepg101.php

[188] Omnicoat datasheet : http://www. microchem.com/OMNICOAT.pdf

[189]http://www.mesacrl.utwente.nl/mis/generalinfo/downloads/equipment/Delta%2020%20SU-8/Description%20of%20SU.pdf

[190] AZ5214E datasheet http://groups.mrl.uiuc.edu/dvh/pdf/AZ5214E.pdf

[191] Xia, Y., & Whitesides, G. M. (1998). Soft Lithography. Angewandte Chemie International Edition, 37(5), 550–575. doi:10.1002/(SICI)1521-3773(19980316)37:5<550::AID-ANIE550>3.3.CO;2-7

[192] http://en.wikipedia.org/wiki/Polydimethylsiloxane

[193] www.biomemsrc.org/biomems/documents/PDMS_Protocol.pdf

[194] http://www.ws.chemie.tu-muenchen.de/groups/hydrogeo/techniques/micromodeltech/

[195] Qin, D., Xia, Y., & Whitesides, G. M. (2010). Soft lithography for micro- and nanoscale patterning. Nature protocols, 5(3), 491–502. doi:10.1038/nprot.2009.234

[196] http://en.wikipedia.org/wiki/Micro_contact_printing

[197] Ramakrishna S, Fujihara K, Teo WE, Lim TC, Ma Z.AN INTRODUCTION TO ELECTROSPINNING AND NANOFIBERS. World Scientific, Singapore (2005)

CHAPTER 2

Micropatterning of PVDF

In this chapter, we first review the state of the art of PVDF and PVDF-TrFE micro-processing and then we review the physical properties of PDVF. In a third part, we present the results obtained in this work using both conventional and nonconventional lithography techniques. Afterward, we evaluate the performance of each of these techniques in terms of pattern resolution and reproducibility. Finally, we discuss the surface modification of PVDF. The results of cell culture on PVDF patterns will be shown in the next chapter.

2.1 Introduction

Fluoropolymers are an active subject of research in bioengineering due to their biocompatibility and very physical and chemical resistance. However this resistance makes their patterning more difficult than conventional polymers. Different techniques have been used to pattern fluoropolymers. Some polymers such as PTFE (PolyTetraFluoroEthylene) and Teflon can be vapor deposited by graft-polymerization and ion beam deposition [**1-3**]. *Leclair et al.* [**1**] and *Goessl et al.* [**2**] used a combination of photolithography and plasma deposition to produce patterns of fluoropolymers. First, photolithography was used to define the patterns on glass. Then, plasma was used to deposit PTFE from C_4F_8 gas. Finally lift-off was realized to remove the fluoropolymer deposited on the photoresist. *Wang et al.* used ion-beam sputtering on a Teflon target to deposit film with the same structural properties as Teflon [**3**].

PVDF however cannot be sputtered and the most common method to deposit PVDF is the spin-coating of a solution of PVDF dissolved in a polar solvent (DMF, DMAc, DMSO). Different strategies have been developed to pattern PVDF.

Lee et al. [**4**] and *Bormashenko et al.* [**5**] used laser micromachining to pattern PVDF. *Lee et al.* used femtosecond laser to realize ablation of a layer of PVDF sandwiched between 2 Ni/Cu electrodes. The laser induced cracking and peeling of PVDF/NiCu (**Fig 2.1**) due to the thermally induced mechanical stress resulting in a poor resolution. Laser ablation of PVDF is also limited by the H_2 emission as a byproduct of ablation.

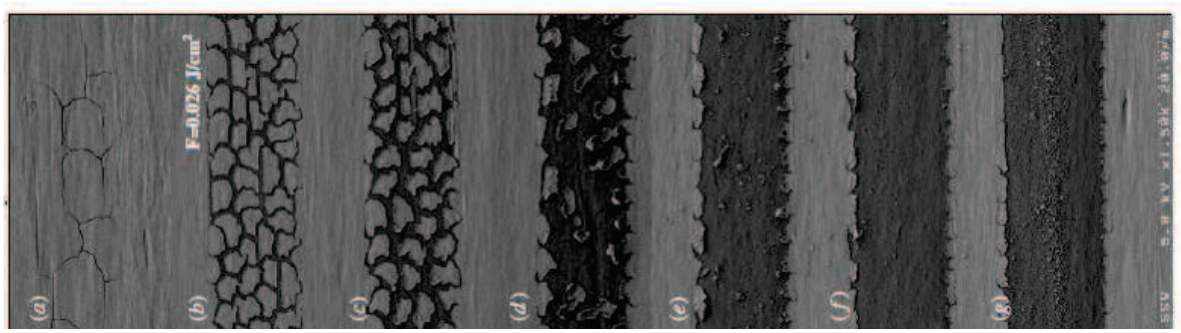

Figure 2.1 SEM micrographs showing the morphological changes of NiCu layers and PVDF film as a function of laser fluence. (From [**4**])

Bormashenko et al. [**5**] managed to deform PVDF using a CO_2 laser beam to produce spherical and pseudo micro-lens that operate in the infrared bands as a proof of principle.

Techniques from classical micro-fabrication have been used also: *Narayanan et al.* [**6**] defined pattern of resist on a PVDF film sandwiched between aluminum electrodes and used an aluminum etching solution to remove part of the film that are not protected by the photoresist. *Sharma et al.* [**7**] used O_2 dry etching to pattern PVDF-TrFE. Due to the high physical resistance of the PVDF-TrFE, the etch rate was relatively slow (150nm/min) compare to the etching rate of the photoresist (100nm/min).

Chang et al. [**8-9**] used shear force to pattern PVDF-TrFE with high crystallinity on aluminum micropatterns. The PVDf-TrFE is spin-coated to form a thin film (300nm) on the aluminum micropatterns. Then, after heating above the melting temperature and cooling to 140°C the shear process is realized by applying a PDMS flat stamp on the top of the patterns with a pressure of 10^5 Pa and applying a force of 1N laterally. The maximum lateral velocity was 1mm/h and so it took 1h to pattern a 1mm square area (**Fig. 2.2**).

In opposite of the technique evoked above which need special equipment and are low throughput some groups applied the soft lithography to pattern PVDF and PVDF-TrFE.

Park et al. [**10**] used a temperature controlled capillary micro-molding technique to make patterns of semi-crystalline PVDF. A droplet of PVDF solution was injected at the entry of the PDMS channels (**Fig 2.3a**) and after the solution has reached the outlet the temperature was adjusted to control the evaporation rate of solvent through PDMS. This process produced rapidly micro-patterns with no PVDF remaining between lines but its use is limited to patterns where the channels are connected.

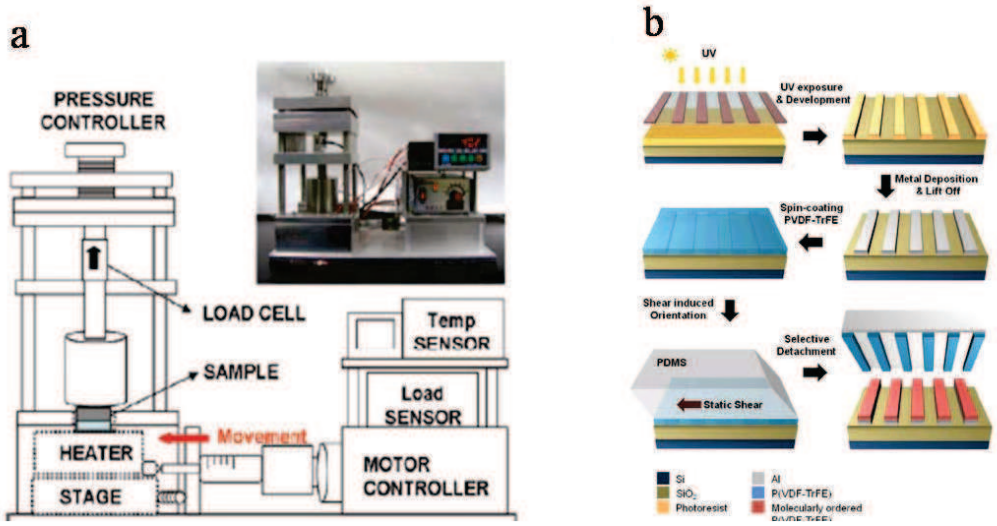

Figure 2.2 (**a**) Schematic diagram of the apparatus used to produce the static shear for patterning the PVDF-TrFE. (From [**9**]) (**b**) Schematic diagram of the micropatterning process of a thin PVDF-TrFE film by selective shear and detachment. (From [**8**])

Other groups [**11-13**] used successfully nanoimprint lithography (NIL) technique [**16-17**] to pattern PVDF and PVDF-TrFE. Thermal nanoimprinting is a simple process, yet it is able to create nanostructures as small as 5 nm. It uses a patterned mold to press against a polymer film heated above its glass transition temperature and thus transfers the pattern from the imprinting mold to the imprinted film. The other advantage of this technique is the possibility to influence crystallization of the PVDF to increase the ratio of the piezoelectric β-phase. NIL has been used previously to order phase separated domains of a copolymer [**18**].

Liu et al. [**13**] used thermal nanoimprint to imprint 2 dimension patterns (squares) and one dimension patterns (lines) of PVDF-TrFE as small as 139 nm by applying pressure (300psi) and heat (130°C-150°C) with a nanoimprint press. The imprinting time is very short 3min. The PVDF-TrFE is diluted (0.5-10%) in solvent (MEK) and spin-coated at 3000 rpm for 60s which makes PVDF-TrFE film of ~190nm. The imprinting mold is made of 200nm photoresist on silicon. The resulting imprinted patterns have a thickness of 200nm with 80-90nm remaining (**Fig 2.3c**) between the patterns. The imprinted patterns present a very good piezoelectric response without further annealing or poling. *Zhang et al.* [**11**] obtained similar results but using a much higher imprinting pressure (1800 psi) and longer imprinting duration (2h). *Hu et al.* [**12**] used the same technique to imprint patterns of PVDF with controlled crystallization of the non-piezoelectric α-phase. When the imprinting mold depth (100nm) is

inferior to the PVDF film (300nm) lamellae are formed across the sample (**Fig 2.3b**) but when the mold depth is superior to the PVDF film thickness (60nm) there is a confinement of the polymer and the lamellae are not formed.

NIL techniques are very interesting as they are high resolution and high throughput but the height and width of the patterns is limited and PVDF remains between features.

Gallego et al. [**14-15**] used soft lithography based technique to imprint continuous and discontinuous PVDF microstructures (**Fig 2.4**) from 5µm to 25µm width (pillars, lines, criss-crossed lines) with a very good aspect ratio (height 5-10µm). They used a PDMS stamp as an imprinting mold to imprint embossed features on the PVDF film (10% PVDF dissolved in DMF, 3000 rpm 1minute). They applied relatively small pressure (32psi) compared to previous nanoimprint experiments (300psi-1800psi) [**11-13**] and low temperature (90°C for 5minutes). For discontinuous pattern they spin-coated the PVDF solution on the PDMS stamp and removed the PVDF on the top of the stamp (**Fig 2.4**) leaving only PVDF in the recessed areas of the stamp. Finally the remaining PVDF inside the microstructures is transferred onto a glass slide.

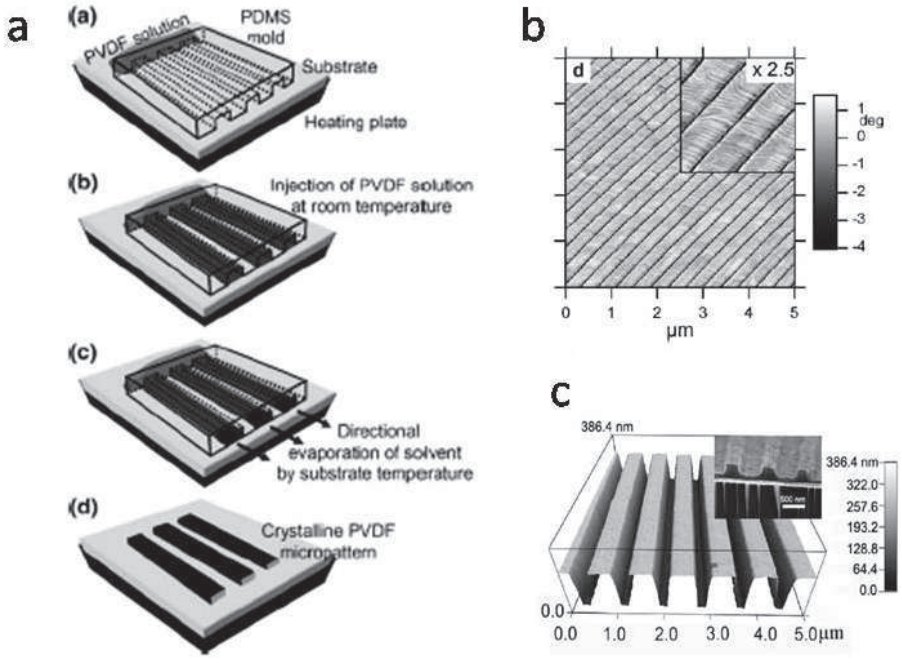

Figure 2.3 (**a**) Schematic of the capillary driven micromolding process controlled by temperature. (From [**10**]) (**b-c)** Micropatterning of PVDF and PVDF-TrFE using NIL (**b**) AFM phase images of the PVDF crystallized in the nanotrenches of the print mold, showing the morphology at the topmost part of the film. (From [**12**]) (**c**) AFM topography images of 190 nm PVDF-TrFE film patterned with a 200nm depth mold. Insert shows the cross-section SEM picture of this sample. (From [**13**])

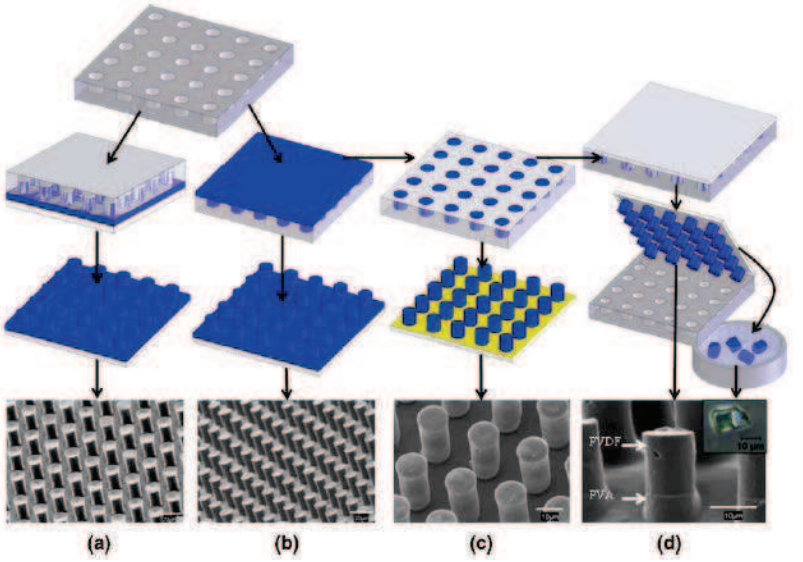

Figure 2.4 Fabrication flows for: (**a**) imprinted; (**b**) stamped continuous; (**c**) stamped discrete; and (**d**) freestanding microstructures. SEM micrographs show representative 1.5:1 aspect ratio pillar patterns fabricated using each of the techniques. (From [**15**])

2.2 Physical and chemical properties of PVDF

Polyvinylidene fluoride (PVDF) is thermoplastic and highly non-reactive polymer. It commonly used in the chemical, semiconductor, medical and defense industries. In biology, PVDF membranes are widely used for western blots for immobilization of proteins, due to its non-specific affinity for amino acids. PVDF is produced by the polymerization of vinylidene difluoride.

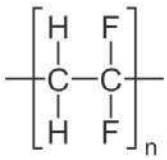

Figure 2.5 Chemical structure of PVDF (From [**24**]).

PVDF has a glass transition temperature (T_g) of about −35 °C and is typically 50–60% crystalline. Depending on the chain conformations, PVDF shows different properties. When mechanically stretched, the molecular chains of PVDF can be oriented and then poled under tension. The poled PVDF is a ferroelectric polymer, exhibiting efficient piezoelectric and pyroelectric properties [**25-46**].

Copolymers of PVDF such as P(VDF-TriFluoroEthylene) (PVDF-TrFE) and P(VDF-TetraFluoroEthylene) (PVDF-TFE) are also used in piezoelectric and electrostrictive applications. While the copolymers' unit structures are less polar than that of pure PVDF, the copolymers typically have a much higher crystallinity which may result in a larger piezoelectric response **[47-55].**

2.3 PVDF patterning

2.3.1. Spin coating

Spinning coating is commonly used in microfabrication, which allows depositing a thin layer of resist on a substrate with a thickness in the range of a few nanometers to a few hundreds of micrometers. Typically, a drop of the resist dissolved in a solvent is deposited on a substrate which can be then spread to cover the whole surface of the substrate by spinning. During the spinning, the solvent will be partially evaporated, resulting in a homogenous thin film coated on the substrate. The remaining solvent will be further evaporated by heating or used during the following patterning steps.

PVDF can be dissolved with a 5-10% concentration in polar solvents, such as listed in **Table 2.1**. Other solvent such as acetone or Methyl Ethyl Ketone (MEK) can also be used to dissolve PVDF at high temperature but it may re-crystallizes upon cooling [**20**]. To produce PVDF thin films by spin coating, PVDF is often dissolved in a mixture of 2 solvent: one with a slow rate of evaporation (DMF, DMAc or DMSO) which solutes the polymer and another one with a fast rate of evaporation (acetone) which will evaporate during the spin-coating. We used 10% PVDF dissolved in a mixture of DMF and acetone (4:5wgt). Here, DMF has been chosen as the main solvent because it causes less swelling of PDMS [**10, 21**], which is needed during the patterning process.

Prior to spin coating, the glass substrate is plasma treated during 3 minutes to improve its wettability and help the solvent to spread evenly on the surface. The spin coating is performed in 2 steps: firstly a low speed (500 rpm) spinning for 10 sec. and then a high speed (1000 – 4000 rpm) spinning for 30 sec. **Figure 2.6** shows the film thickness as a function of the speed of high speed spinning.

Solvent	Boiling Point °C	Flash Point °C
Dimethyl Formamide (DMF)	153	67
Dimethyl Acetamide (DMAc)	166	70
Tetramethyl Urea	177	65
Dimethyl Sulfoxide (DMSO)	189	35
Triethyl Phosphate	215	116
N-Methyl-2-Pyrrolidone	202	95

Table 2.1 PVDF solvents. (From [**19**])

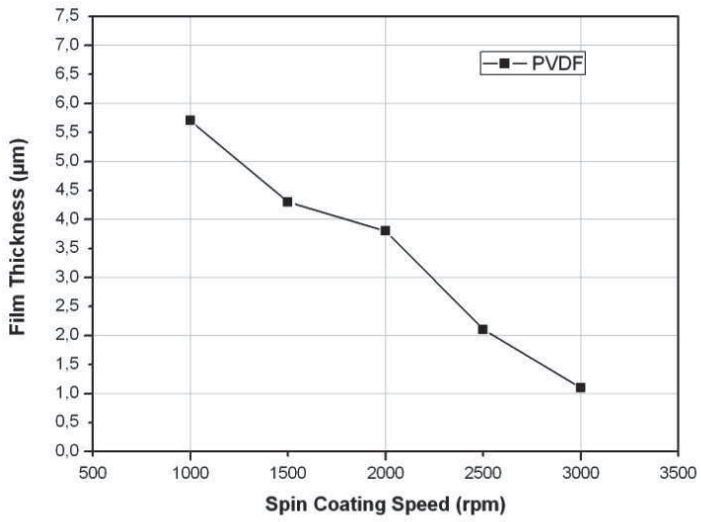

Figure 2.6 Film thickness of PVDF versus spin coating speed.

After spin coating, the main solvent will be evaporated. We found that this evaporation step is critical for the thickness homogeneity of the formed PVDF film. If the solvent evaporates slowly (<60°C), large PVDF crystals could be formed, showing a large film thickness inhomogeneity (**Fig 2.7 a**). Otherwise, if the solvent is evaporated fast (110 °C), the formed PVDF crystals are not visible and the film thickness became rather homogenous (**Fig 2.7b**). Such a difference in the thickness homogeneity of the film could be visualized by eye: The flat PVDF layer is perfectly transparent whereas the rough PVDF layer is opaque.

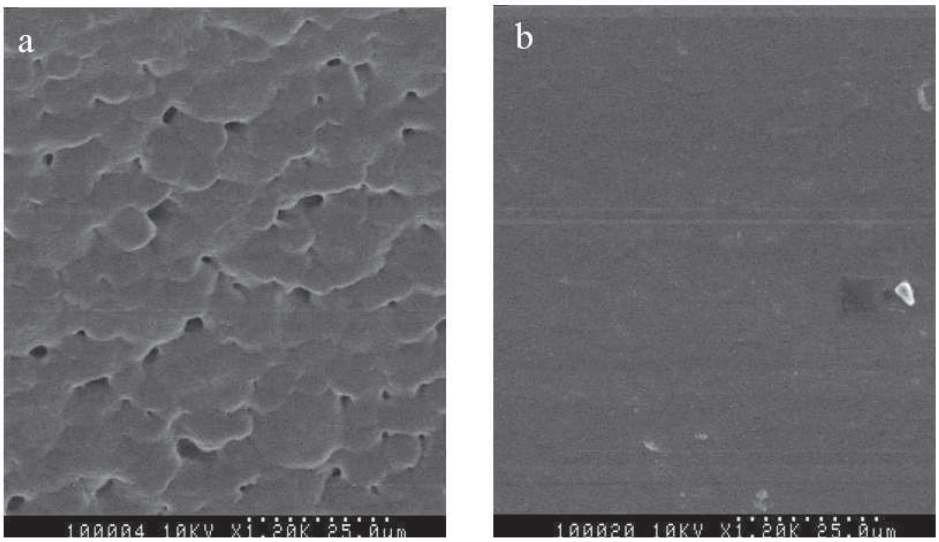

Figure 2.7 SEM pictures of PVDF layer. (**a**) Crystals are formed due to slow evaporation. (**b**) Fast evaporation leads to a very homogenous layer.

2.3.2 Reactive Ion Etching (RIE)

Reactive ion etch is commonly used to transfer a resist pattern into the substrate or other material deposited on the resist. In our work, we evaluated the etching performance of different reactive gases, i.e., O_2, SF_6, CHF_3 or their mixture for PVDF thin films. During RIE, the chemical bonds can be broken so that the unprotected part of the film can be removed or modified. PVDF has a carbon backbone linked with single C-C bonds (**Table 2.2**) which can be easily broken. However, the use of fluoride gas compounds (SF_6, CHF_3) may be more interesting to reach a high degree of the etching anisotropy. Indeed, we found that O_2 etching (35 sccm, 100w, 190 mTorr) is highly efficient, which showed an etched thickness of 3.2 μm in 7 min (**Fig. 2.8**). We noticed however that after 4 min, the surface of the etched part became rough and the residual parts are very difficult to remove.

The etch speed of PVDF with fluorine-based RIE is significantly slower than that of O_2. For example, SF_6 etching (SF_6 10 sccm, 60 w, 10mTorr) can only etch 1.1 μm for 11 min. (**Fig 2.9**). CHF_3 etching (20 sccm, 30w, 30 mTorr) with 2 sccm O_2 allows to remove PVDF at a lower rate (<100 nm/min). Here, O_2 is used with CHF3 to act as a scavenger gas to absorb F* atoms that have reacted with the surface and thus increasing F concentration on the surface. These low etch speeds can be explained by the grafting of F on the C backbone instead of the breaking of the C=C and C≡C bonds which have a much higher bond energy than the C-F bond.

Bond	Bond Energies (kj/mol)
C≡ O	1079
C≡C	835
C=O	799
C=C	602
C=S	573
C-F	495
H-C	411
C-O	358
C-C	346
S-F	284
C-S	272

Table 2.2 Bond energy of bonds in PVDF (from [**22**]).

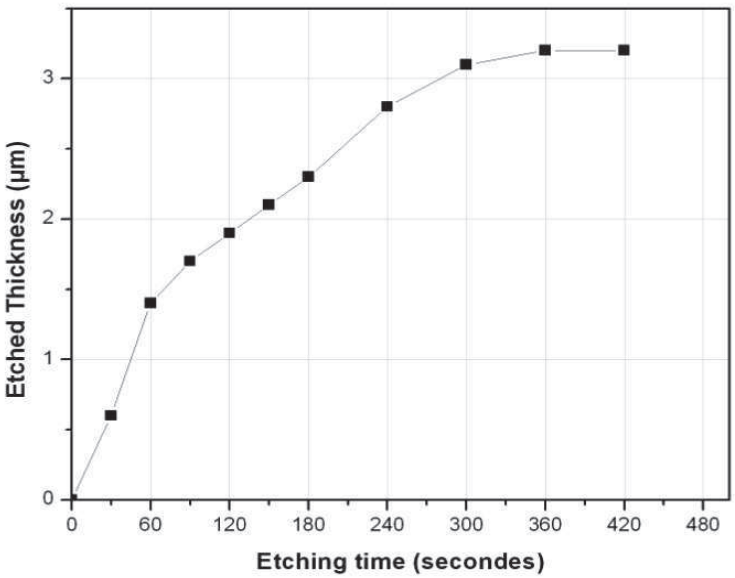

Fig. 2.8 Etched thickness of PVDF versus etching time using O_2 plasma.

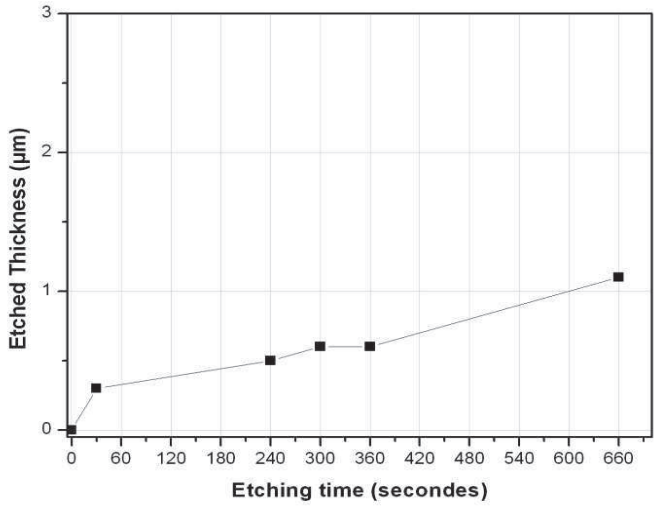

Figure 2.9 Etched thickness of PVDF versus etching time using SF_6 plasma

Two types of RIE masks were used to define PVDF patterns on a substrate. The first one consisted of a lithographically defined resist pattern using conventional photoresist SU8. SU8 (SU8 3010) was spin coated (4000 rpm = 9.2 µm) on top of the PVDF layer. After UV exposition and development, we obtained good SU8 patterns (**Fig. 2.10**). After RIE, the photoresist patterns should be removed to obtain the PVDF patterns. SU8 is generally removed in a SU8 remover solution. However, we found that this solution did also dissolve PVDF. Also, SU8 could be etched by RIE with an etching speed (7min/2.6µm) comparable to that for PVDF, making this process unsuited for our purpose. The use of other types of photoresists such as AZ5214 could not solve this problem either because of the process compatibility. In fact, acetone which is generally used to remove AZ5214 can also dissolve PVDF.

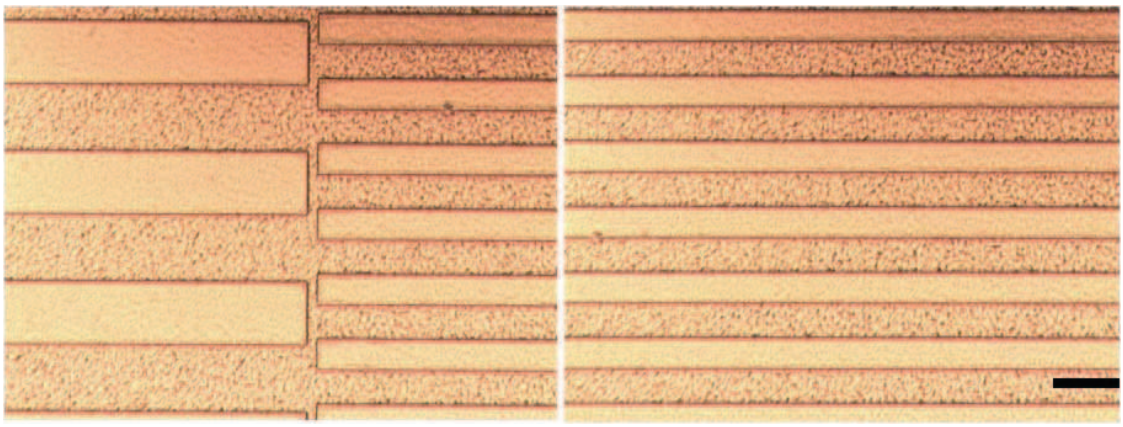

Figure 2.10 Microphotographs of SU8 patterns on a PVDF film (scale bar 30 µm).

The second type of etch mask is a shadow mask of PDMS made by soft lithography. To evaluate the feasibility of this approach, we brought a PDMS square directly into contact with the PVDF layer. After RIE and the shadow mask removal, we found that the edge of the patterns was not well defined due probably to the problems of contact: a small gap may leave between the PDMS mask and the PVDF layer which prohibits a good pattern edge definition (**Fig. 2.11**).

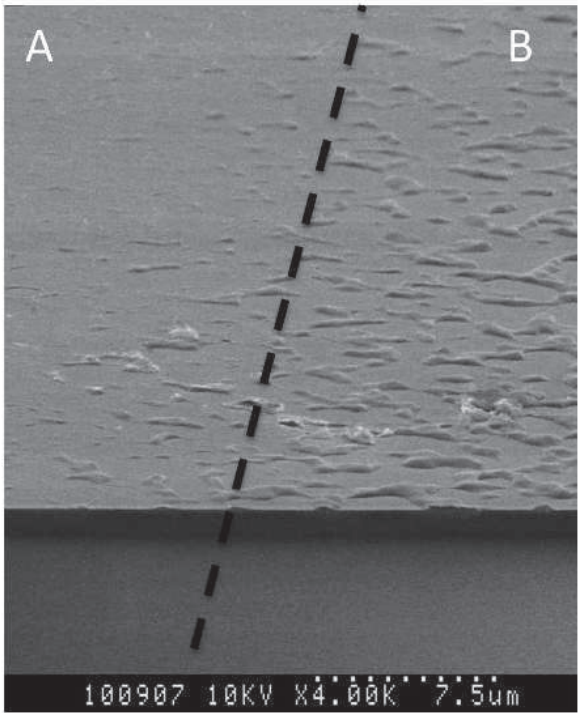

Figure 2.11 SEM image of the boundary zone between etched and non-etched PVDF. The dashed line is the approximate boundary between (**A**) etched zone and (**B**) non etched zone.

2.3.3 Soft lithography methods

We used soft lithography techniques to pattern it. The goal was to make large scale patterns easily in a reproducible way. We used a soft lithography technique called hot embossing or micro-imprinting: Patterns are transferred from a mold onto a thermoplastic polymer by heating this polymer above its glass transition temperature (T_g). When heated, the polymer is softened which can then be molded into the mold structured with the help of a pressure applied between the mold and the substrate.

The molds were realized by PDMS soft lithography: A master of resist on silicon substrate is prepared by photolithography. After the surface treatment of the master with TMCS (TriMethyl ChloroSilane) which facilitates the release of the master after molding, liquid PDMS (10:1) is poured over the master and cured in an oven overnight (80°C). By changing the type of photoresist used for the master, we could control the thickness of the patterns (1-50 μm). In this work, we fabricated master patterns of lines and pillars of different size and spacing in the range between 5 μm and 100 μm.

Two hot embossing techniques have been tested to pattern PVDF on glass: The first one was based on wetting of a PVDF solution on the surface of PDMS mold and then transferring the PVDF layer onto the glass slide; the second one is based on direct embossing of a PVDF solution deposited on a glass slide. Previously, *Gallego et al.* [**14-15**] have already shown the feasibility of patterning a PVDF thin film by using the wetting based technique. In their work, the PVDF solution is directly spin coated on the PDMS mold (1000 – 3000 rpm). Immediately after spin-coating, the PVDF film on the outside of the patterns is removed using a pre-heated glass (200°C) and applying slight pressure (<30 kPa) for few seconds and repeating the process until the only remaining PVDF is inside the recessed parts of the patterns. Finally the patterns are transferred onto the gold coated slide by applying pressure (200-310 kPa) and heat (180-200 °C) for 10 seconds. Following their work, we tried to obtain the similar patterns on a glass slide but did not reach satisfactory results. In fact, we found that with their proposed process it is very difficult to achieve the gold as PVDF solution tends to form a continuous film on top of the PDMS stamp. There seems no clear separation between the recessed parts and the top layer (**Fig. 2.12**) and the whole PVDF layer can be easily removed by the pre-heated stamped glass slide.

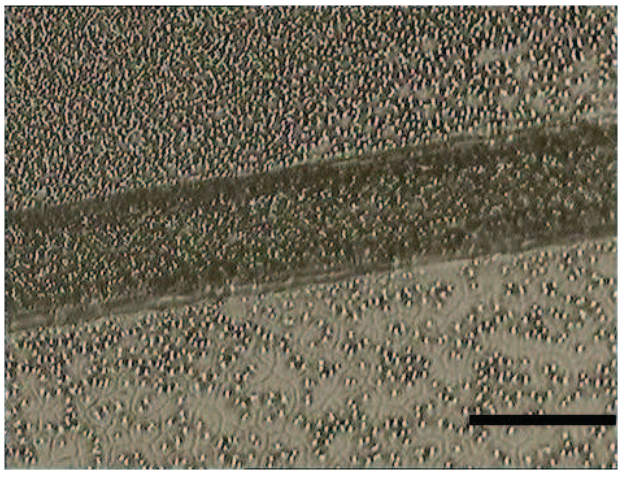

Figure 2.12 PVDF layer spin-coated on the PDMS stamp (scale bar 100 μm).

We managed to overcome this difficulty by decreasing PVDF concentration from 10% to 5%. Now, PVDF only remains in the recessed parts of the stamp (**Fig. 2.13**) and we obtained the patterned PVDF features on the glass after the pattern transfer (**Fig. 2.14**). However, the resulted PVDF patterns are not perfect, due probably to the adhesion between the PVDF features and the PDMS stamps.

As can be understood, the critical phase of this method is the removal of PVDF on the non-recessed area by stamping with the preheated glass: if it not stamped enough, PVDF will remain on top and the pattern transfer will not be good. Otherwise, if it is over stamped, PVDF in the recessed area can also be removed so that the transferred pattern will not be perfect. Anyway, this method is very dependent of the operator ability and so it should not be applicable in a reproducible manner.

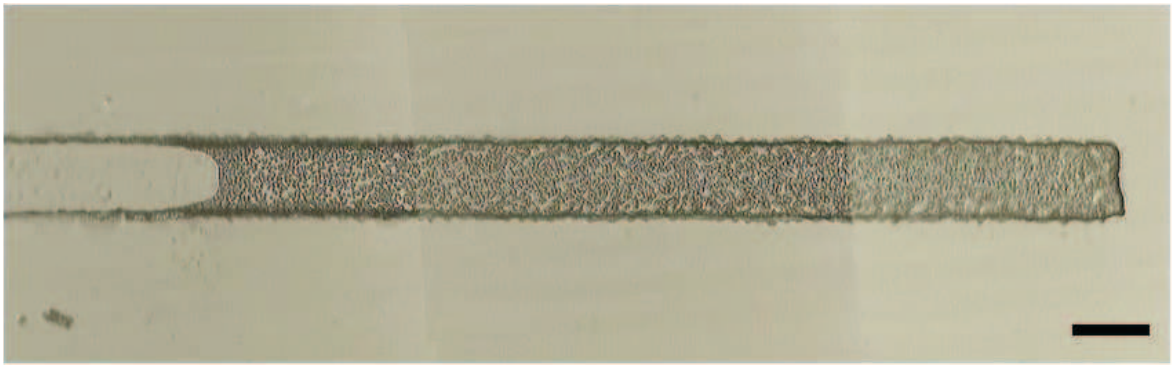

Figure 2.13 5% PVDF spin coated on PDMS stamp after the pre-heated glass stamping process to remove PVDF outside of the recessed areas.(scale bar 100 μm).

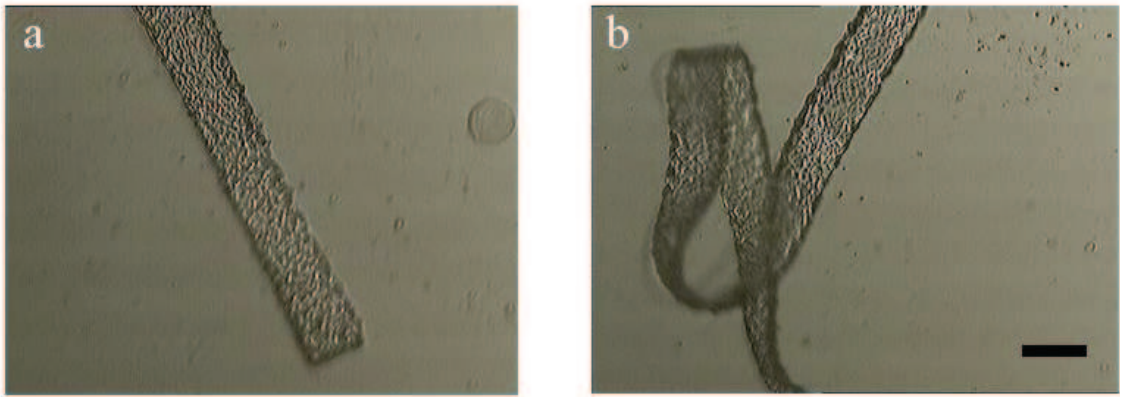

Figure 2.14 (**a-b**) PVDF patterns transferred on the glass slide (scale bar 100 μm).

The second hot embossing technique is more conventional one using a hot press (**Fig. 2.15**). Prior to spin-coating of PVDF, a glass slide was treated by O_2 plasma (3 min). A PVDF solution of 10% wgt in DMF/Acetone (4:5 wgt) was then spin coated. Different parameters have been evaluated: Mold type (silicon or PDMS), mold pattern depth, PVDF film thickness, PVDF with or without solvent, heating temperature and time, applied pressure, cooling time, etc..

Figure 2.15 Hydraulic press with a pair of hot plates used in this work.

Previously, *Liu et al.* [**13**] developed a nanoimprint process with P(VDF-TrFE) copolymer and resist mold made in photoresist on silicon. After spin-coating and evaporation of the solvent (30 min 80°C), a nanoimprinter (Nanorex NX-B100) was used to apply high pressure between the mold and the polymer layer (300 psi) while heating (3 min 130-135°C). After cooling to room temperature, the mold was released. This imprinting process is reproducible but it allows only making continuous imprinted patterns as there is always polymer remaining under the imprinted features. For example, when they used a 190nm thick film with a mold with 200 nm depth the resulting imprinted patterns is 200 nm high and the residual layer is around 70-90 nm underneath the imprinted patterns.

Following their work, we tried to pattern PVDF instead of P(VDF-TrFE) copolymer. After spin-coating on a glass slide (2000-3000 rpm for 1 min.), the sample is heated at 70°C for 1h in order to evaporate completely the solvent. The mold was made of photoresist

(AZ5214 ~1.5μm) on a silicon substrate and treated with TMCS to avoid adhesion between PVDF and the mold. Then, the mold and the PVDF sample were heated at 140°C and a pressure of 150 Psi for 5 min. After cooling upon to the room temperature, the mold is released from the substrate. We obtained imprinted patterns (**Fig. 2.16**) which are consistent with the mold.

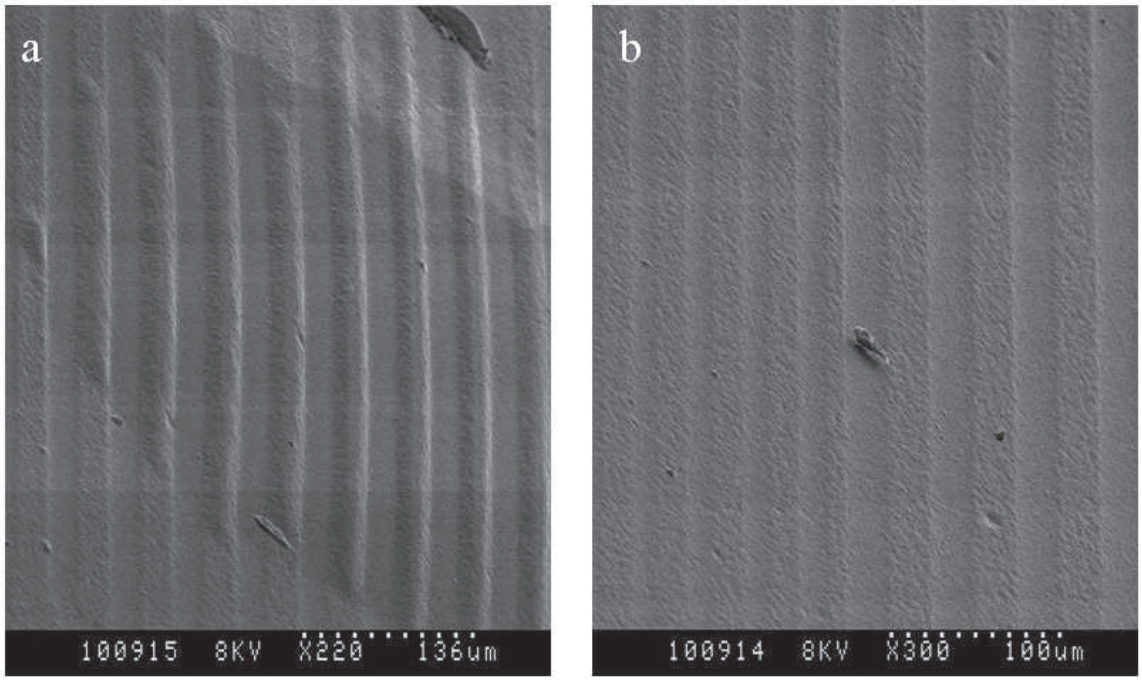

Figure 2.16 SEM images of a PVDF layer obtained after solvent evaporation and patterning with a silicon-mold using a hot press.

We also tried to use a PDMS mold instead of a silicon mold: PDMS is elastic so that is allows a more homogenous distribution of the imprinting force. The PDMS molds were prepared by soft lithography with a photoresist pattern made in AZ5214 resist (AZ5214 ~1.5μm depth) and bonded to glass slides after plasma treatment. After spin coating and solvent evaporation, the mold and the PVDF sample were heated to 165°C and a pressure of 150 psi was applied for 5 min. Here, we used a higher temperature to soften the PVDF which is still below the PVDF melting temperature (171°C) [**23-24**]. After cooling down to the room temperature and the mold release, we obtained imprinted patterns of PVDF as shown in **Fig. 2.17**. As expected, the imprinted patterns showed the replicated features of the mold (100 μm line-and-spacing and ~1μm depth) but we can clearly see the residual layer of the PVDF between each two lines as well as the rounded line edges due to the embossing induced deformation of the PDMS mold.

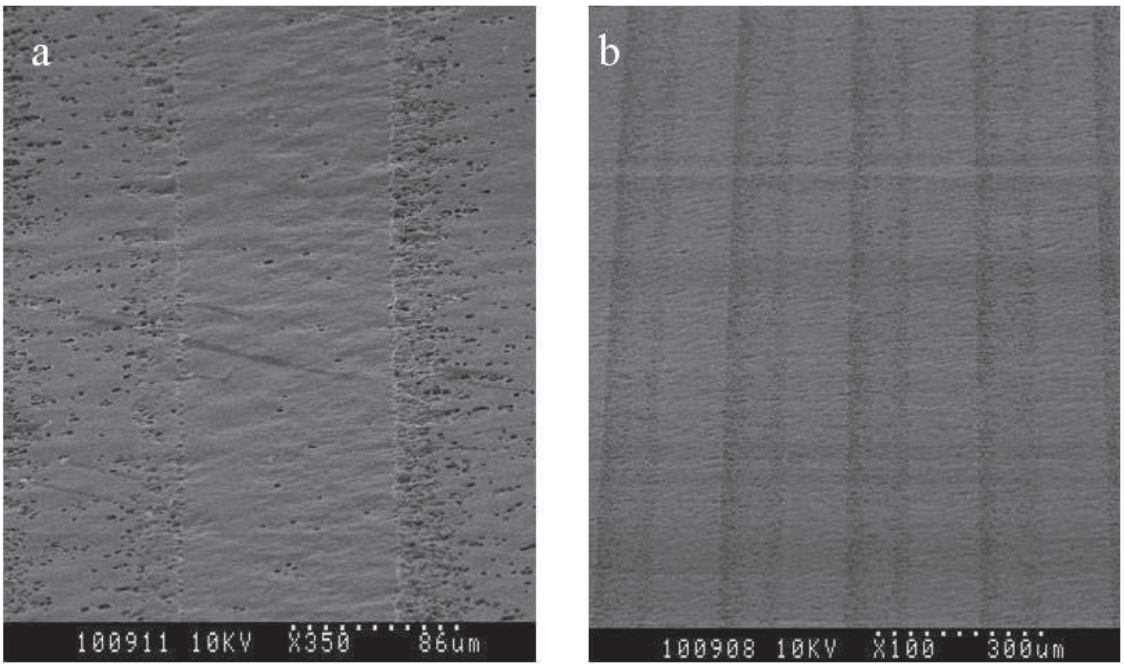

Figure 2.17 SEM images of a PVDF layer patterned by hot embossing with a PDMS mold at 165 °C for 5 min.

We observed however that the feature of the samples patterned without solvent evaporation were much better than that with solvent evaporation. A more quantitative study has then been developed by using PDMS molds with different line width (5 - 50 μm) and depth (1 - 3 μm). Spin-coating is replaced by dropping a droplet of the PVDF solution on the surface of the glass slide. The PDMS mold is brought into contact with the substrate and the ensemble is placed inside the hot press. The press is heated to 135°C and slight pressure is applied (~50 psi) for 15-20 min. Here, we used a longer imprinting time in order to remove completely the residual solvent in PVDF film prior to unmolding (The resulted PVDF structure can be swelled if any residual solvent remains). After cooling down to the room temperature, the pressure is released and the mold is removed. **Figure 2.18** shows SEM picture of two patterned PVDF structures with well-defined feature edges, illustrating a high quality replication with the PDMS mold. Here, the thickness of the pattern is ~2.4 μm which is consistent with the 3 μm depth of the PDMS mold. Clearly, there is no continuous film underneath of imprinted features but only a small area of residual PVDF between adjacent lines which can be removed by RIE.

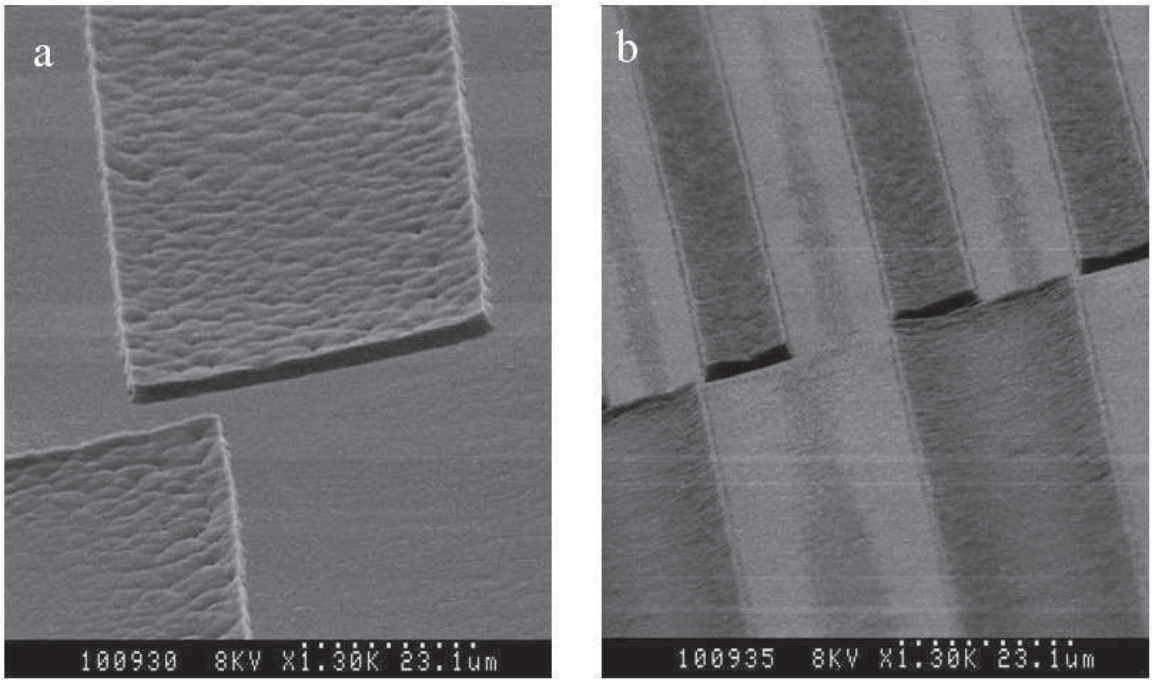

Figure 2.18 SEM images of PVDF layer patterned by hot embossing without solvent evaporation with a PDMS mold at 135°C.

Atomic Force Microscopy (AFM) has been used to characterize precisely the remaining PVDF between patterns (**Fig.2.19-2.20**). Clearly, 5 sec etching is sufficient to remove all the residual PVDF between the patterned features. It seems also that the surface the PVDF features become smoother after RIE. As discussed below, the PVDF surface modification induced by RIE may not be desired so that we choose to find another solution to remove the residual feature of PVDF.

We assumed that the success of the patterning was due to the capillary migration of the PVDF solution inside the channels of the mold, enhanced by the solvent evaporation. To verify this theory we used PDMS molds with larger depth (50 μm) to increase the capillary force and treated PDMS molds with an O_2 plasma for 3-5 min. The other parameters were kept the same as before except that silicon was now used as substrate because it is easier to see by optical microscopy the PVDF residuals. Figure 2.21 displays an imprinted pattern (50 μm line width and 100 μm spacing), showing no PVDF residuals.

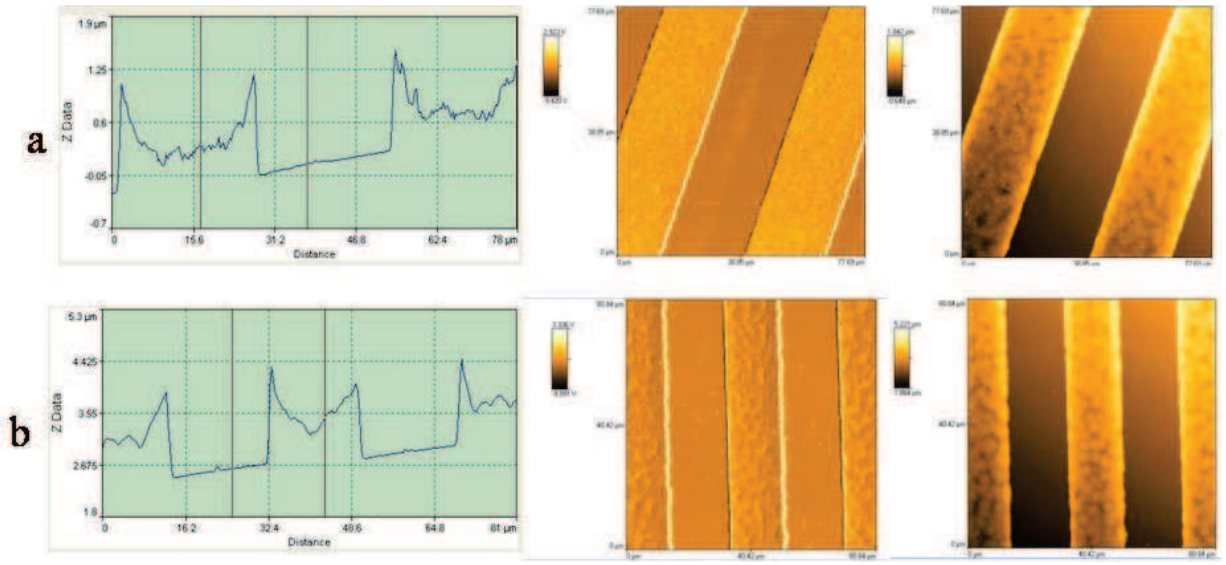

Figure 2.19 Surface topography measured by AFM: (**a**) Without RIE. (**b**) After RIE for 5 s.

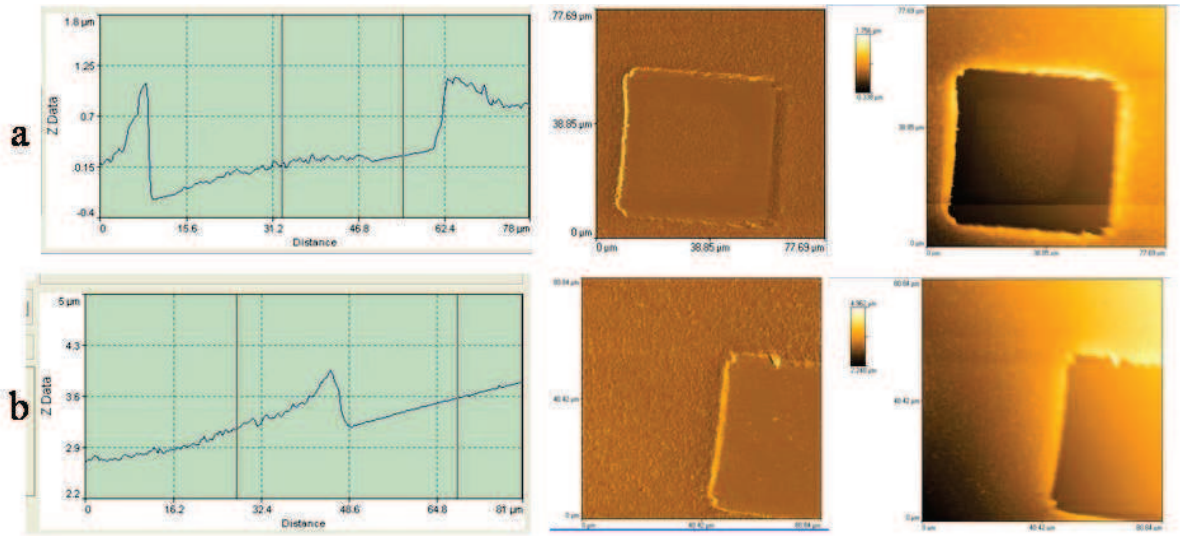

Figure 2.20 Surface topography measured by AFM: (**a**) Without RIE (**b**) After RIE for 5 s.

In general, the imprinted features of PVDF adhere better to the glass surface than the non-imprinted part and connections between the patterned area and non-patterned counter-part are sufficiently small which can be easily broken. Thus we can peel off the non-imprinted part of PVDF, leaving desired patterns on the substrate. Using this technique, we were able to produce pillar and line arrays of different sizes and spacing (**Fig 2.22**).

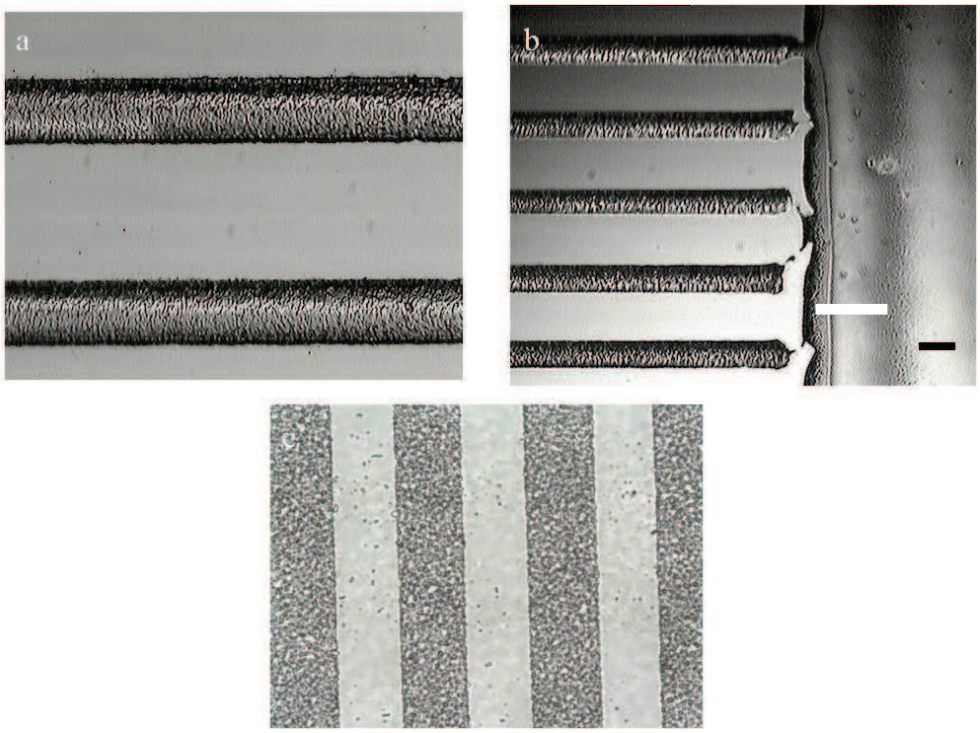

Figure 2.21 (**a-d**) Microphotograph of PVDF micropatterns on a silicon substrate realized by hot embossing (scale bars 50µm).

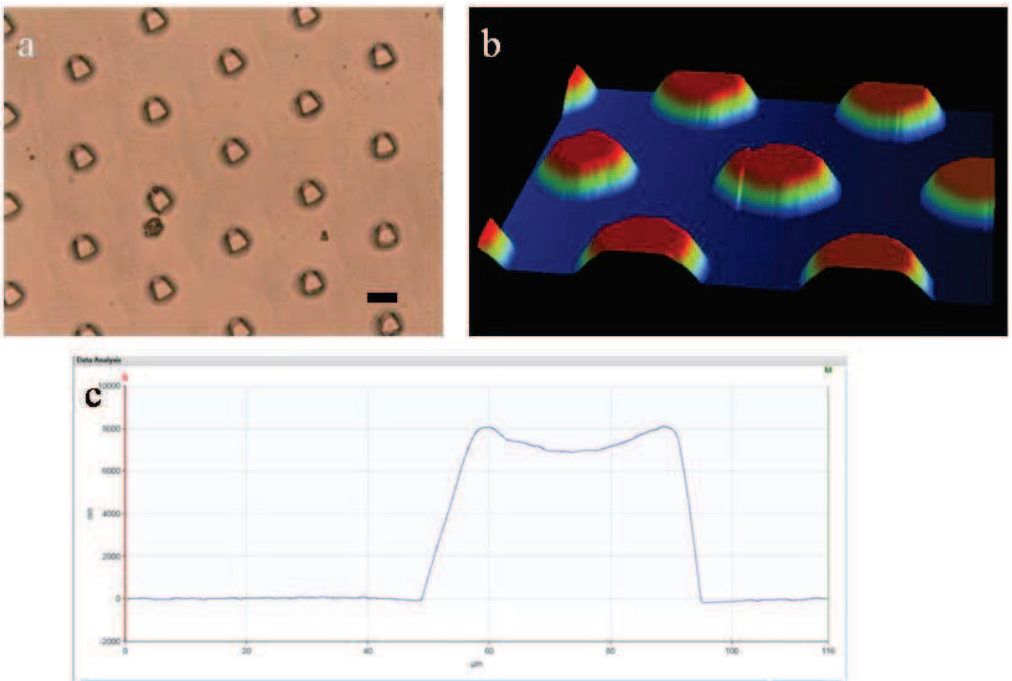

Figure 2.22 (**a-c**) Microphotograph of PVDF micropatterns on a silicon substrate realized by hot embossing (scale bars 50µm).

2.4 Surface modification of PVDF

A biomaterial should be non-toxic and provide good conditions for cell adhesion and proliferation. This is often achieved by surface modification of the biomaterial such as grafting of adhesion proteins on the surface. Adhesion of proteins on a surface relies on the surface charge and surface wetting properties.

PVDF is natively hydrophobic (contact angle >80°) due to the inclusion of fluoride atoms. In order to change its wetting properties, we studied two methods: RIE and plasma treatment. To measure the contact angle, we used a custom-made goniometer composed of an SUB microscope, a pipette to deliver 3µl water droplets, and a light source on the back (**Fig. 2.23**). The support underneath the sample is black in order to make the droplet black by reflection and thus to increase the contrast between the white background and the black droplet which is necessary to measure accurately the contact angle.

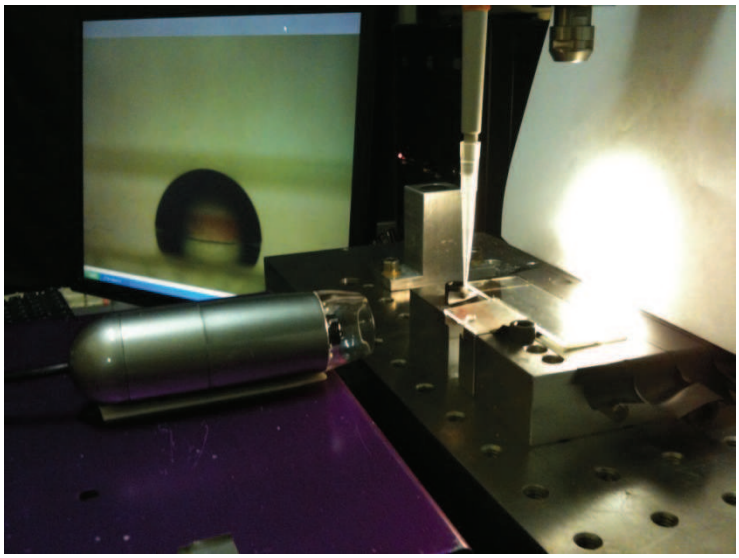

Figure 2.23 Optical setup for contact angle measurement.

RIE is used to remove materials by breaking atomic bonds and circulating ways the volatile byproducts. Physically, the surface of the material can be attacked, which may result in a rough surface morphology, depending on the type of the gas and the etch parameter (bias, power, pressure, etc.). With the increase of the surface roughness, the material wetting property can be changed. Chemically, the atomic bonds at the material surface can be broken and new bonds can be formed which modify the surface energy and its interaction with fluids.

Air plasma used in plasma cleaner operates at low power radiofrequencies (~15 mW) to generate plasma composed of nitrogen (80%) and oxygen (20%). Oxygen is the more reactive specie in this plasma, it will oxidize materials.

We used the same set of RIE parameters (gas volume, work pressure and RF power) of that used in micro-patterning, except the reaction time. As shown in **Figure 2.24**, the fluorine based treatments (CHF_3-O_2 and SF_6) allowed increasing the contact angle of the PVDF surface, whereas the SF_6 gas can even make the PVDF surface super-hydrophobic (contact angle >150°) after 5min RIE (**Fig. 2.25**). This super-hydrophobic effect can be explained by the replacement of H atoms by F atoms from SF_6 due to the fact that the C-F bond is stronger than C-H bonds. However, this cannot be the only explanation as Teflon which is similar to PVDF but with hydrogen atoms replaced by fluorine is not super-hydrophobic and has a contact angle of 110°. **Figure 2.26** shows SEM pictures of PVDF surface before and after RIE, providing a microscopic view of the surface roughness induced by SF_6 plasma.

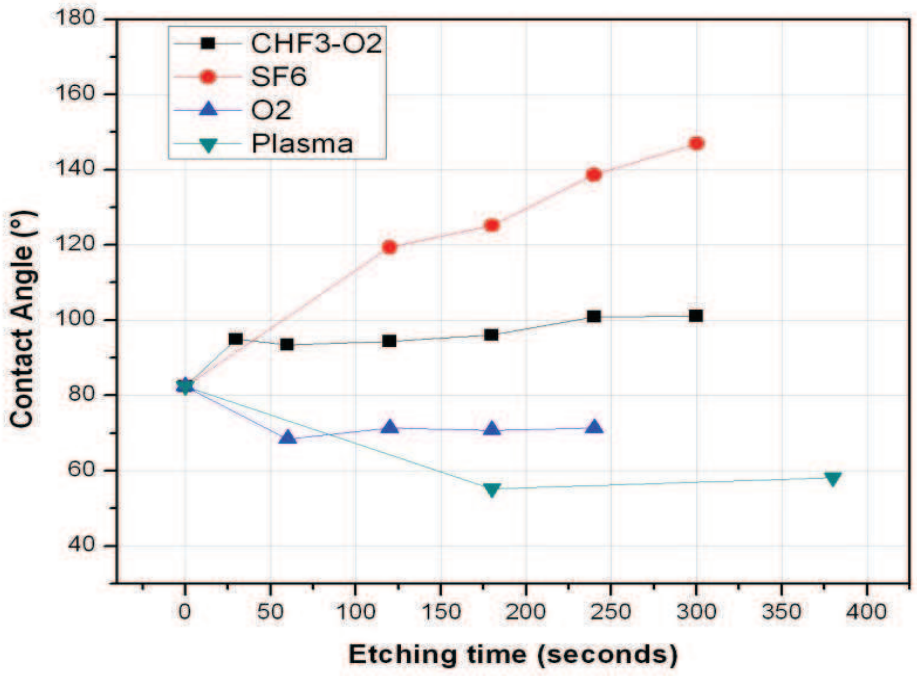

Figure 2.24 Variation of the measured contact angle as a function of etching time for different reaction gases.

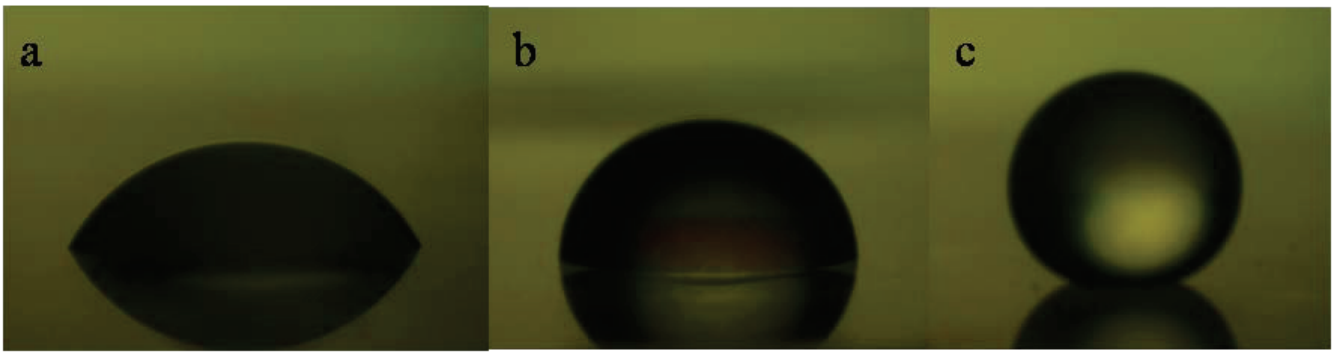

Figure 2.25 Contact angle of a water droplet on PVDF surfaces.(**a**) After 3 min in oxygen contain plasma.(**b**) Native surface.(**c**) After 6 min RIE with SF_6gas.

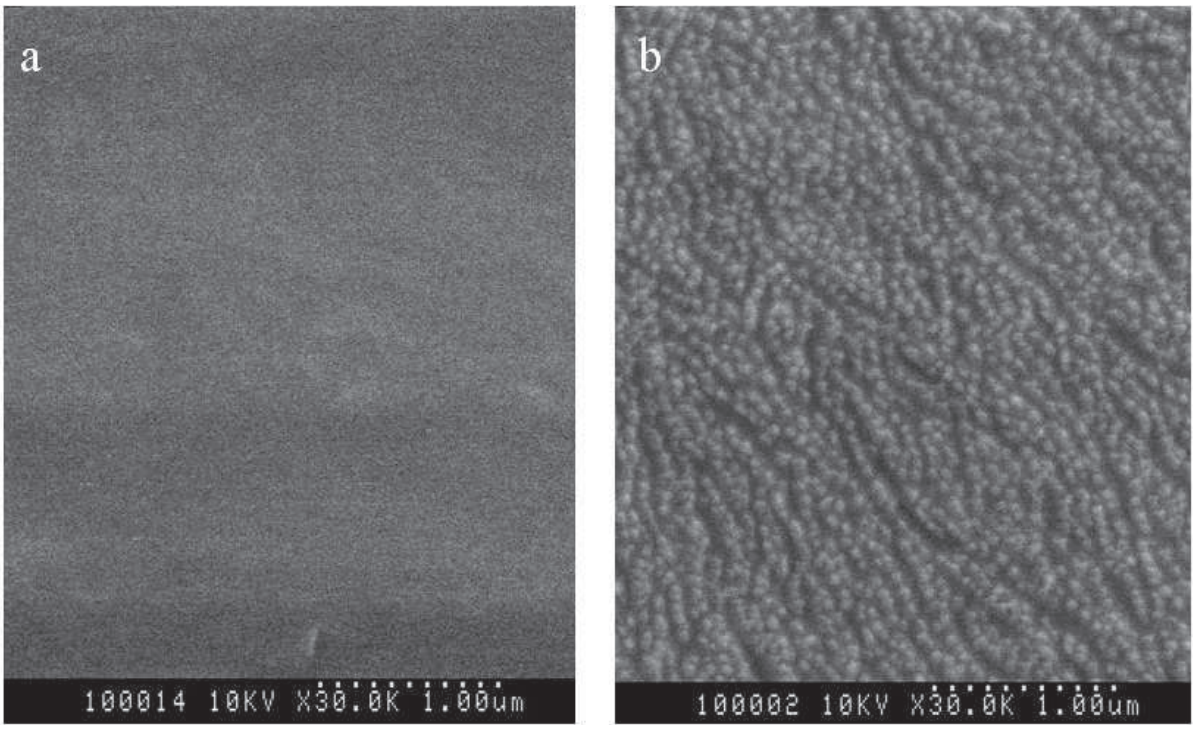

Figure 2.26 SEM pictures of PVDF surfaces. (**a**) Before RIE. (**b**) After RIE with SF_6 gas.

The wetting properties of SF_6modified PVDF surface can remain for a long time, which suggest that the RIE treated surfaces are irreversible (**Fig 2.27**).

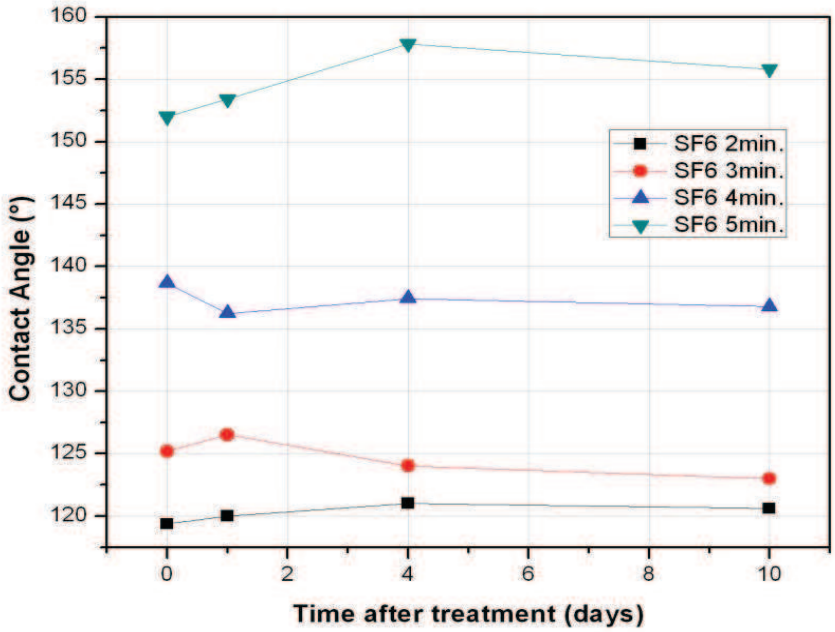

Figure 2.27 Evolution of the contact angle on SF6 etched PVDF over 10 days.

The RIE modification of PVDF surfaces using CHF_3-O_2 gas mixture or CHF_3 along results also in an increased contact angle (100° and 110° after 8 min RIE, respectively). This can be explained by both effects of fluorination and oxidization.

RIE with $O_2$is efficient to make PVDF more hydrophilic: the contact angle has been decreased from 82.4 ° to 68.40° after 1 min etching (**Fig. 2.24**). However, further etching has no significant effect to the decrease of the contact angle. The wetting properties of O_2modified PVDF surface can also remain for a long time, as showing in **Fig 2.27**.

Finally, the plasma treatment is very efficient to increase the wettability of the PVDF surface as it brings the contact angle from 82.4 ° to 55.15° in 3 min (**Fig. 2.25**). A further treatment decreases however slightly the wettability (contact angle >60°). This can be explained by the fact that a long plasma treatment may affect the stability of the elements of bulk PVDF which can then been liberated to compete with the surface OH groups. **Figure 2.28-2.29** shows the measured contact angle as a function of time, indicting a slow variation of the treated material surfaces.

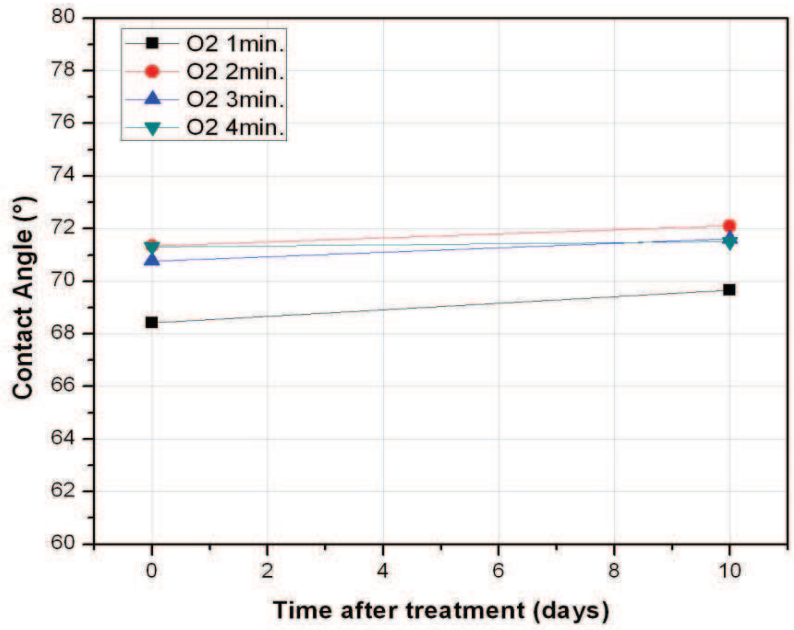

Figure 2.28 Evolution of the contact angle on O_2 etched PVDF over 10 days.

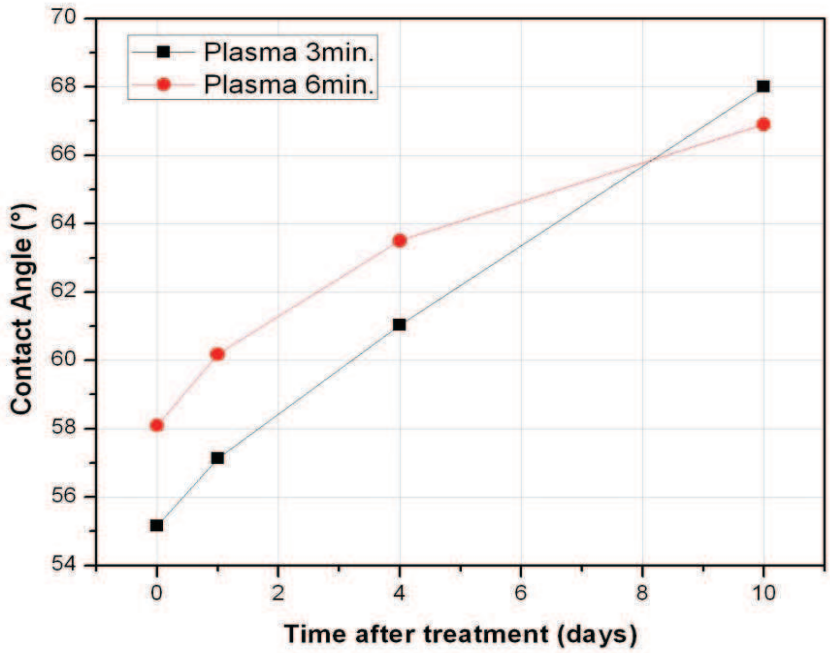

Figure 2.29 Evolution of the contact angle on SF6 etched PVDF over 10 days.

In conclusion, our study indicates that the wetting property of the PVDF surface can be directed into two directions: it can be made to be more hydrophilic by oxygen containing plasma treatment or RIE with oxygen gas (contact angle <55°) or more hydrophobic by RIE with SF_6 or CHF_3 gas (contact angle >90°). It can even become super-hydrophobic (contact angle >150°) by RIE with SF_6 for 5 min. the RIE modified PVDF surfaces are stable in time as for more than 10 days, whereas the plasma treated PVDF surface degraded slowly by time (contact angle augmented of 10° in 10 days) which should also suited for cell culture studies.

2.5 Microcontact printing of protein on PVDF

Microcontact printing has been used to pattern proteins (fibronectin) on spin-coated PVDF layer. Firstly, the PVDF solution is spin-coated on glass slides and solvent is evaporated during 2 h (cells are very sensitive to solvents so that we have to ensure that all solvent has been evaporated). A mold of SU-8 photoresist on silicon was fabricated by photolithography (**Fig. 2.30a**) with patterns of lines of different width. Then, after silanization (TMCS) to ensure unmolding, PDMS was poured over the silicon mask and cured overnight (80°C). After unmolding we obtain the PDMS stamp (**Fig. 2.30b**). Immediately before beginning of the microcontact printing process, PDMS stamps are treated with air plasma for 30 seconds to increase wettability of their surface hence improving the adsorption of the protein solution. Then, a droplet of fibronectin (Sigma Aldrich) is dropped on the PDMS stamp and left for incubation during 30 min. Afterward, the liquid is removed by aspiration and the PDMS stamp with proteins is placed on the surface of a flat PVDF layer. After slightly pressing the PDMS stamp, the stamp is left for 5 min to let proteins adsorb on the PVDF surface. Finally, the stamp is removed. The patterned PVDF samples have to be kept in PBS solution in order to avoid protein degradation.

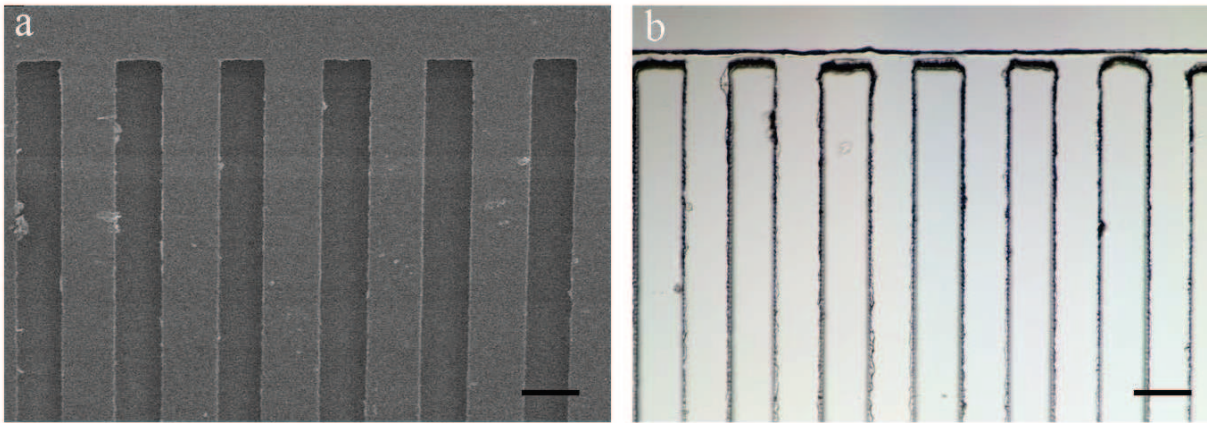

Figure 2.30 (**a**) SEM picture of the photoresist mold (**b**) Microphotography of the corresponding PDMS stamp. (Scale bars are 100µm)

As fibronectin is not fluorescent by itself we used fluorescent fibrinogen (fibrinogen-FITC) in order to assess the microcontact printing process. We can see that the pattern of protein has been perfectly imprinted on PVDF even with the smallest lines of 30 µm (**Fig 2.31**).

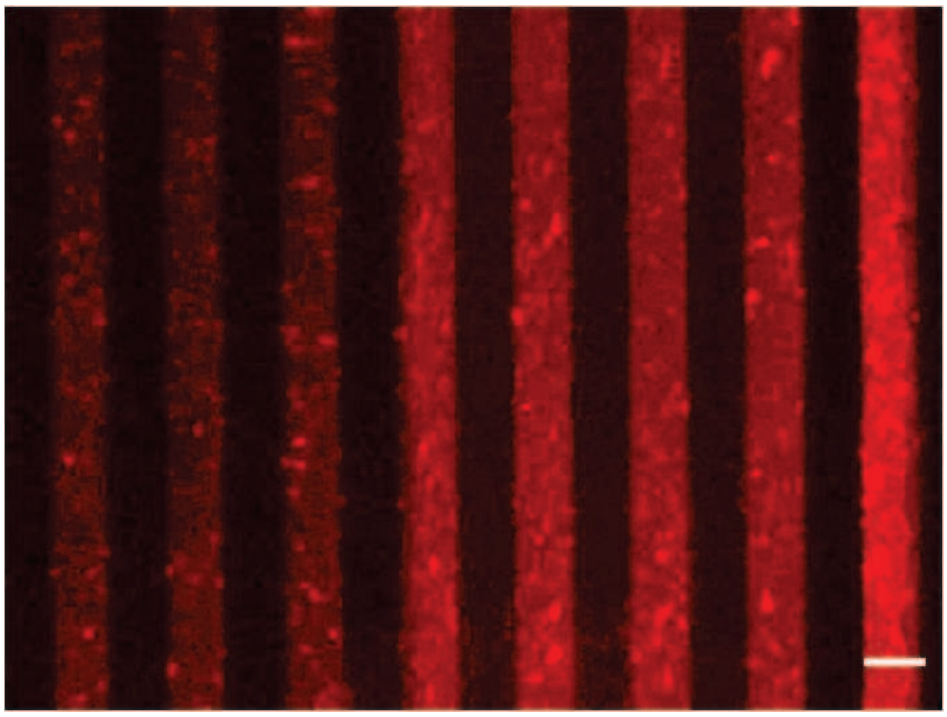

Figure 2.31 Microphotographs of Fibrinogen-FITC imprinted patterns on PVDF. (Scale bar is 30µm)

2.6 Conclusion

We developed different patterning techniques for thin layer PVDF micro-processing. Our results showed that it is rather difficult to apply conventional thin layer hot embossing to achieve a clear pattern definition without residual in the recessed area. Alternatively, capillary assisted hot embossing could be used to obtain a better microstructure patterning of PVDF. As results, we obtained 10 μm to 100 μm line-and-space gratings of 2 μm height and 100 pitch pillars of 7 μm height. Spectroscopic characterizations (XRD, FTIR) of the samples showed that PVDF after the hot embossing still have a γ phase which can be converted to piezoelectric β phase by poling. In addition, we have studied the wetting property of the PVDF thin films treated by plasma and RIE techniques. Our results showed that the PVDF surface could be tuned from hydrophobic to hydrophilic by oxygen plasma or oxygen containing RIE. However, the SF6 containing RIE turned the PVDF surface into super-hydrophobic. Finally, we applied micro-contact printing to define cytophilic areas on a flat PVDF surface. Interesting results on cell culture will be discussed in the next chapter.

References

[**1**] Leclair, A. M., Ferguson, S. S. G., & Lagugné-Labarthet, F. (2011). Surface patterning using plasma-deposited fluorocarbon thin films for single-cell positioning and neural circuit arrangement. *Biomaterials*, *32*(5), 1351–60. doi:10.1016/j.biomaterials. 2010.10. 051

[2] Goessl, A., Garrison, M. D., Lhoest, J.-B., & Hoffman, A. S. (2001). Plasma lithography — thin-film patterning of polymeric biomaterials by RF plasma polymerization I: Surface preparation and analysis. *Journal of Biomaterials Science, Polymer Edition*, *12*(7), 721–738. doi:10.1163/156856201750411620

[3] Wang, L., Li, H., He, J., He, X., Li, W., Wang, Y., & Li, H. (1997). Structure analysis of teflon-like thin films synthesized by ion beam sputtering deposition. *Materials Letters*, *33*(1-2), 77–78. doi:10.1016/S0167-577X(97)00074-8

[4] Lee, S., Bordatchev, E. V., & Zeman, M. J. F. (2008). Femtosecond laser micromachining of polyvinylidene fluoride (PVDF) based piezo films. *Journal of Micromechanics and Microengineering*, *18*(4), 045011. doi:10.1088/0960-1317/18/4/045011

[5] Bormashenko, E., Pogreb, R., Socol, Y., Itzhaq, M. H., Streltsov, V., Sutovski, S., Sheshnev, A., et al. (2004). Polyvinylidene fluoride—piezoelectric polymer for integrated infrared optics applications. *Optical Materials*, *27*(3), 429–434. doi:10.1016/j.optmat.2004.04.015

[6] Narayanan, N. B., Bonakdar, A., Dargahi, J., Packirisamy, M., & Bhat, R. (2006). Design and analysis of a micromachined piezoelectric sensor for measuring the viscoelastic properties of tissues in minimally invasive surgery. *Smart Materials and Structures*, *15*(6), 1684–1690. doi:10.1088/0964-1726/15/6/021

[7] Sharma, T., Je, S.-S., Gill, B., & Zhang, J. X. J. (2012). Patterning piezoelectric thin film PVDF–TrFE based pressure sensor for catheter application. *Sensors and Actuators A: Physical*, *177*, 87–92. doi:10.1016/j.sna.2011.08.019

[8] Chang, J., Jung, H. J., Jeong, H., Park, Y. J., Sung, J., Kang, S. J., Jung, G. Y., et al. (2011). One-step micropatterning of highly-ordered semi-crystalline poly(vinylidene fluoride-co-trifluoroethylene) films by a selective shear and detachment process. *Organic Electronics*, *12*(1), 98–107. doi:10.1016/j.orgel.2010.10.007

[9] Jung, H. J., Chang, J., Park, Y. J., Kang, S. J., Lotz, B., Huh, J., & Park, C. (2009). Shear-Induced Ordering of Ferroelectric Crystals in Spin-Coated Thin Poly(vinylidene fluoride- co -trifluoroethylene) Films. *Macromolecules*, *42*(12), 4148–4154. doi:10.1021/ma900422n

[10] Park, Y. J., Kang, Y. S., & Park, C. (2005). Micropatterning of semicrystalline poly(vinylidene fluoride) (PVDF) solutions. *European Polymer Journal*, *41*(5), 1002–1012. doi:10.1016/j.eurpolymj.2004.11.022

[11] Zhang, L., Ducharme, S., & Li, J. (2007). Microimprinting and ferroelectric properties of poly(vinylidene fluoride-trifluoroethylene) copolymer films. *Applied Physics Letters*, *91*(17), 172906. doi:10.1063/1.2800803

[12] Hu, Z., Baralia, G., Bayot, V., Gohy, J.-F., & Jonas, A. M. (2005). Nanoscale control of polymer crystallization by nanoimprint lithography. *Nano letters*, *5*(9), 1738–43. doi:10.1021/nl051097w

[13] Liu, Y., Weiss, D. N., & Li, J. (2010). Rapid nanoimprinting and excellent piezoresponse of polymeric ferroelectric nanostructures. *ACS nano*, *4*(1), 83–90. doi:10.1021/nn901397r

[14] Gallego, D., Ferrell, N. J., & Hansford, D. J. (2007). Fabrication of Piezoelectric Polyvinylidene Fluoride (PVDF) Microstructures by Soft Lithography for Tissue Engineering and Cell Biology Applications. *Materials Research*, *1002*.

[15] Gallego-Perez, D., Ferrell, N. J., Higuita-Castro, N., & Hansford, D. J. (2010). Versatile methods for the fabrication of polyvinylidene fluoride microstructures. *Biomedical microdevices*, *12*(6), 1009–17. doi:10.1007/s10544-010-9455-9

[16] Chou, S. Y., Krauss, P. R., & Renstrom, P. J. (1995). Imprint of sub-25 nm vias and trenches in polymers. *Applied Physics Letters*, *67*(21), 3114. doi:10.1063/1.114851

[17] Chou, S. Y., Krauss, P. R., & Renstrom, P. J. (1996). Imprint Lithography with 25-Nanometer Resolution. *Science*, *272*(5258), 85–87. doi:10.1126/science.272.5258.85

[18] Li, H.-W., & Huck, W. T. S. (2004). Ordered Block-Copolymer Assembly Using Nanoimprint Lithography. *Nano Letters*, *4*(9), 1633–1636. doi:10.1021/nl049209r

[19] Arkema PVDF Datasheet http://www.arkema-inc.com/kynar/page.cfm?pag=1159

[20] Arkema PVDF Datasheethttp://www.arkema-inc.com/kynar/page.cfm?pag=1160

[21] Lee, J. N., Park, C., & Whitesides, G. M. (2003). Solvent compatibility of poly(dimethylsiloxane)-based microfluidic devices. *Analytical chemistry*, *75*(23), 6544-54. doi:10.1021/ac0346712

[22] http://www.wiredchemist.com/chemistry/data/bond-energies-lengths

[23] http://www.sigmaaldrich.com/catalog/product/aldrich/182702?lang=fr&region=FR

[24] http://en.wikipedia.org/wiki/Polyvinylidene_fluoride

[25] Kawai, H. (1969). The Piezoelectricity of Poly (vinylidene Fluoride). *Jpn. J. Appl. Phys.*, *8*(7), 975. doi:10.1143/JJAP.8.975

[26] Fukada, E., & Takashit.S. (1969). Piezoelectric Effect in Polarized Poly (vinylidene Fluoride). *Jpn. J. Appl. Phys.*, *8*(7), 960. doi:10.1143/JJAP.8.960

[27] Nakamura, K., & Wada, Y. (1971). Piezoelectricity, pyroelectricity, and the electrostriction constant of poly(vinylidene fluoride). *Journal of Polymer Science Part A-2: Polymer Physics*, *9*(1), 161–173. doi:10.1002/pol.1971.160090111

[28] Tamura, M. (1974). Piezoelectricity in uniaxially stretched poly(vinylidene fluoride). *Journal of Applied Physics*, *45*(9), 3768. doi:10.1063/1.1663857

[29] Oshiki, M., & Fukada, E. (1975). Inverse piezoelectric effect and electrostrictive effect in polarized poly(vinylidene fluoride) films. *Journal of Materials Science*, *10*(1), 1–6. doi:10.1007/BF00541025

[30] Tamura, M., Ogasawara, K., & Yoshimi, T. (1976). Piezoelectricity in uniaxially stretched poly(vinylidene fluoride) films and its applications. *Ferroelectrics*, *10*(1), 125–127. doi:10.1080/00150197608241962

[31] Tasaka, S., & Miyata, S. (1981). The origin of piezoelectricity in poly(vinylidene fluoride). *Ferroelectrics*, *32*(1), 17–23. doi:10.1080/00150198108238668

[32] Johnson, G. E., Blyler, L. L., Crane, G. R., & Gieniewski, C. (1981). Thermal piezoelectric stability of poled uniaxially-and biaxially-oriented poly(vinylidene fluoride. *Ferroelectrics*, *32*(1), 43–47. doi:10.1080/00150198108238672

[33] Tashiro, K., Tadokoro, H., & Kobayashi, M. (1981). Structure and piezoelectricity of poly(vinylidene fluoride). *Ferroelectrics*, *32*(1), 167–175. doi:10.1080/00150198108238688

[34] Fukada, E., Date, M., Neumann, H. E., & Wendorff, J. H. (1988). Nonlinear piezoelectricity in poly(vinylidene fluoride). *Journal of Applied Physics*, *63*(5), 1701. doi:10.1063/1.339905

[35] Harnischfeger, P., & Jungnickel, B.-J. (1990). Features and origin of the dynamic and the nonlinear piezoelectricity in poly (vinylidene fluoride). *Ferroelectrics*, *109*(1), 279–284. doi:10.1080/00150199008211426

[36] Scheinbeim, J. I., Yoon, C. H., Pae, K. D., & Newman, B. A. (1980). Ferroelectric hysteresis effects in poly(vinylidene fluoride) films. *Journal of Applied Physics*, *51*(10), 5156. doi:10.1063/1.327462

[37] Herchenröder, P., Segui, Y., Horne, D., & Yoon, D. (1980). Ferroelectricity of Poly(Vinylidene Fluoride): Transition Temperature. *Physical Review Letters*, *45*(26), 2135–2137. doi:10.1103/PhysRevLett.45.2135

[38] Scheinbeim, J. I., Yoon, C. H., Pae, K. D., & Newman, B. a. (1980). Ferroelectric hysteresis effects in poly(vinylidene fluoride) films. *Journal of Applied Physics*, *51*(10), 5156. doi:10.1063/1.327462

[39] Herchenröder, P., Segui, Y., Horne, D., & Yoon, D. Y. (1980). Ferroelectricity of Poly(Vinylidene Fluoride): Transition Temperature. *Phys. Rev. Lett.*, *45*(26), 2135–2138.

[40] Lee, H., Salomon, R. E., & Labes, M. M. (1978). Pyroelectricity in Polymer Blends of Poly(vinylidene fluoride). *Macromolecules*, *11*(1), 171–175. doi:10.1021/ma60061a030

[41] McKinney, J. E., Davis, G. T., & Broadhurst, M. G. (1980). Plasma poling of poly(vinylidene fluoride): Piezo- and pyroelectric response. *Journal of Applied Physics*, *51*(3), 1676. doi:10.1063/1.327775

[42] Wada, Y., & Hayakawa, R. (1981). A model theory of piezo- and pyroelectricity of poly(vinylidene fluoride) electret. *Ferroelectrics*, *32*(1), 115–118. doi:10.1080 /00150198108238681

[43] Newman, B. A., Chung, K. T., Pae, K. D., & Scheinbeim, J. I. (1981). Piezoelectric and pyroelectric properties of poly(vinylidene fluoride) films at high hydrostatic pressure. *Ferroelectrics*, *32*(1), 135–140. doi:10.1080/00150198108238684

[44] Takemura, T. (1984). Piezo- and pyroelectric properties of poly(vinylidene fluoride) under high pressure. *Ferroelectrics*, *57*(1), 243–248. doi:10.1080/00150198408012766

[45] Al-Jishi, R., & Taylor, P. L. (1985). Equilibrium polarization and piezoelectric and pyroelectric coefficients in poly(vinylidene fluoride). *Journal of Applied Physics*, *57*(3), 902. doi:10.1063/1.334690

[46] Gerhard-Multhauptab, R. (1987). Poly(vinylidene fluoride): A piezo-, pyro- and ferroelectric polymer and its poling behaviour. *Ferroelectrics*, *75*(1), 385–396. doi:10.1080/00150198708008991

[47] Stack, G. M., & Ting, R. Y. (1989). Piezoelectric properties and temperature stability of poly(vinylidene fluoride-trifluorethylene) copolymers. *IEEE transactions on ultrasonics, ferroelectrics, and frequency control*, *36*(4), 417–23. doi:10.1109/58.3177

[48] Wang, H., Zhang, Q. M., Cross, L. E., & Sykes, a. O. (1993). Piezoelectric, dielectric, and elastic properties of poly(vinylidene fluoride/trifluoroethylene). *Journal of Applied Physics*, *74*(5), 3394. doi:10.1063/1.354566

[49] Kochervinski, V. V. (2003). Piezoelectricity in crystallizing ferroelectric polymers: Poly(vinylidene fluoride) and its copolymers (A review), *48*(4), 649–675.

[50] Hicks, J. C., Jones, T. E., & Logan, J. C. (1978). Ferroelectric properties of poly(vinylidene fluoride-tetrafluoroethylene). *Journal of Applied Physics*, *49*(12), 6092. doi:10.1063/1.324528

[51] Jayasuriya, A. C., & Scheinbeim, J. I. (2001). Ferroelectric behavior in solvent cast poly (vinylidene fluoride/hexafluoropropylene) copolymer films, *176*, 386–390.

[52] Xu, H. (2001). Dielectric properties and ferroelectric behavior of poly(vinylidene fluoride-trifluoroethylene) 50/50 copolymer ultrathin films. *Journal of Applied Polymer Science*, *80*(12), 2259–2266. doi:10.1002/app.1330

[53] Mai, M., Martin, B., & Kliem, H. (2011). Ferroelectric switching in Langmuir-Blodgett and spin-coated thin films of poly(vinylidene fluoride/trifluoroethylene) copolymers. *Journal of Applied Physics*, *110*(6), 064101. doi:10.1063/1.3636397

[54] Takahashi, Y., Nakagawa, Y., Miyaji, H., & Asai, K. (1987). Direct evidence for ferroelectric switching in poly(vinylidene fluoride) and poly(vinylidene fluoride-trifluoroethylene) crystals. *Journal of Polymer Science Part C: Polymer Letters*, *25*(4), 153–159. doi:10.1002/pol.1987.140250402

[55] Christie, M. C., Scheinbeim, J. I., & Newman, B. A. (1997). Ferroelectric and piezoelectric properties of a quenched poly(vinylidene fluoride-trifluoroethylene) copolymer. *Journal of Polymer Science Part B: Polymer Physics*, *35*(16), 2671–2679. doi:10.1002/(SICI)1099-0488(19971130)35:16<2671::AID-POLB10>3.0.CO;2-6

CHAPTER 3

Cells on patterned PVDF

In this chapter, we present the results of cell culture on a variety of PVDF patterns. Firstly, the results of cell culture on flat surface of PVDF with and without surface modification are discussed in comparison to that of conventional substrates (glass, polystyrene Petri dish). Secondly, the results of cell culture on topographic patterns of PVDF are shown. Effects of patterning residuals, surface coating and plasma treatment are studied in order to provide a more clear assessment. Finally, the results of fibronectin micro-contact printing on a flat PVDF surface are presented. .

3.1 Background and motivation

A biomaterial is defined as a material which interacts with biological systems. Natively, fluoropolymers such as PTFE, PCTFE, FEP, and PVDF do not interact with cells because of their high degree of hydrophobicity. Consequently, the most of fluoropolymers are used in applications where no cell should be attached on (e.g., PTFE vein grafts [**1-2**]). In contrast, hydrogels (e.g., PEG, alginate, chitosan) interact strongly with cells as they are mostly water containing so that they are widely studied as artificial extracellular matrix (ECM) [**3**]. Indeed, hydrogels are often used in applications in such as wound healing applications or 3D scaffolding.

PVDF is hydrophobic and not favorable to cell adhesion. With the help of adhesion molecules such as fibronectin, however, cell adhesion can be improved on the surface of PVDF [**4-5**]. *Klee et al*. [**4**] used graft polymerization and chemical vapor deposition (CVD) polymerization to bond permanently fibronectin to PVDF. *Ribeiro et al.* [**5**] studied the influence of the surface charge of PVDF at different crystalline phases (beta poled, beta unpoled, alpha; etc.) on the adsorption of fibronectin and the adhesion and proliferation of cells. As topographic features also influence the cell adhesion [**6**], the effect of cell adhesion has also been used with patterned PVDF surfaces. *Lensen et al.* **[7]** observed that although cells did not adhere on a PFPE film they could adhere on a patterned PFPE surface where cells were subjected to contact guidance in the same way as on conventional biomaterials [**8-9**]. Finally, *Gallego et al.* [**10**] showed similar effects with PVDF. In this work, we developed a more systematic study on cell-PVDF interaction by using PVDF micropatterns fabricated by different methods as discussed in Chapter 2.

3.2 Cell culture protocol and culture on flat surfaces

3.2.1 Cell culture protocol

NIH 3T3 cells (fibroblasts) were cultured in an incubator at 37°C with 5 % CO2 in Dulbecco's-modified Eagle's medium (DMEM, Sigma, France) supplemented with 10 % FBS (Bioscience, Japan), 1 %L-glutamine, 1% Penicillin/Streptomycin (P/S) (Invitrogen, France) until confluence. To maintain cells in the exponential growth phase (~1°-10^6cells mL^{-1}), they were diluted at a ratio of 1:5-1:10 every 2 days. After dissociation in a 0.25 % Trypsin-EDTA (Invitrogen, France) solution and centrifugation, cells were re-suspended at a density of 1 - 10^6cellsmL^{-1}. Before cell seeding, samples were sterilized under UV exposure or immersed in ethanol 70%.

3.2.2 Cell culture on flat surfaces with surface modification

In general, cells adhere more easily to surfaces with higher surface energy (hydrophilic) but the most commonly used surfaces for cell culture are glass slides (naturally hydrophilic) and polystyrene petri dishes (naturally hydrophobic). To make the polystyrene suited for cell culture, the surfaces of the polystyrene culture Petri dishes are modified by the manufacturer to improve cell adhesion. In order to have a close comparison of the cell adhesion performance between different substrates, we observed the morphology of NIH 3T3 cells after 2 hours culture on glass slides, polystyrene Petri dish (nunclon surface), and native and surface modified PVDF (the surface modification of PVDF has already been detailed in chapter 2).

On glass (without protein coating), most of NIH 3T3 cells after 2 hours of culture begin to spread on the culture surface (**Fig 3.1 a**) and they adopt an elongated morphology (**Fig 3.1 b**). Some cells are not attached, showing a sphere-shaped morphology (**Fig 3.1c**). On the surface of a culture Petri dish, more cells are attached, showing a very elongated morphology (**Fig 3.1d**). Clearly, NIH 3T3 cells cultured on the surface of the polystyrene Petri dish behavior more likely as fibroblasts due to a strong cell-material interaction.

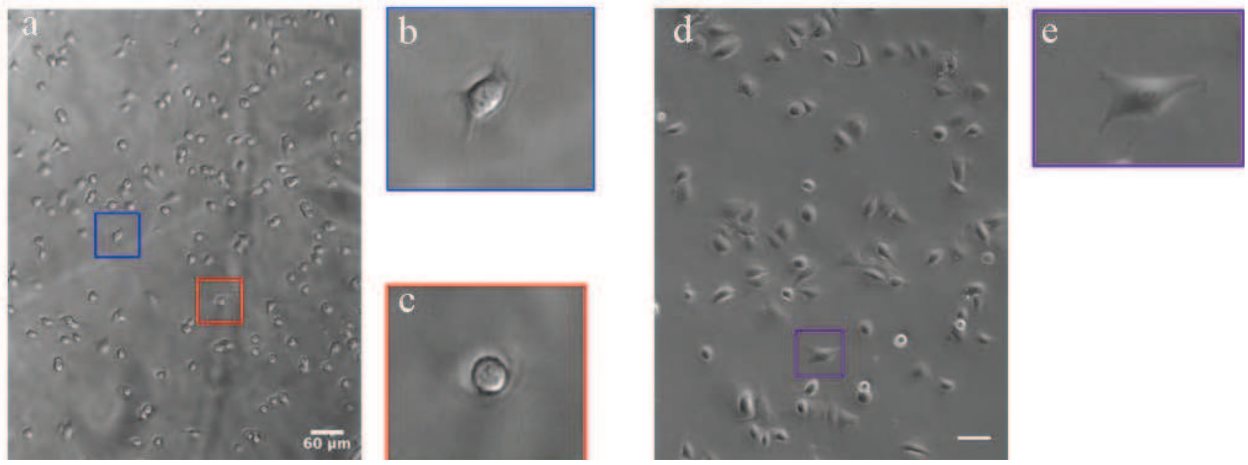

Figure 3.1(**a**) Microphotograph of NIH 3T3 cells cultured on a glass slide after 2 h. (**b**) An enlarged view of a cell adhered to the surface. (**c**) An enlarged view of a cell not attached on the surface. (**d**) Microphotograph of NIH 3T3 cells cultured on the surface of a Petri dish after 2 h. (**e**) An enlarged view of a cell which adheres to the surface. Scale bar is 50 µm.

On a flat surface of PVDF, cells are not attached after 2 hours of culture (Fig. 3.2a). This result was expected as the surface of PVDF is hydrophobic which is not favorable for cell adhesion. The plasma treatment was very efficient to increase the surface energy of PVDF so that cells adhered and spread very well after 2 hours of culture (Fig. 3.2b). Indeed, cells showed a typical morphology of fibroblasts, which is similar to that cultured on the surface of a culture Petri dish (Fig. 3.1d). On the surface of PVDF modified by O_2 etching (Fig 3.2c), only half of the cells are attached. On the surface of PVDF modified by SF_6 etching, no cell is attached, which was expected for the cell culture on a super-hydrophobic surface (Fig. 3.2d). These results are in consistent with the observation shown in chapter 2.

3.3 Cell culture on patterned surfaces with topographic features

3.3.1 Cell culture on conventionally patterned surface

Cell culture on patterned substrates has been extensively studied using different materials and fabrication techniques. In order to compare the results obtained with PVDF patterns, we first show cells cultured on patterned SU8 resists on a glass substrate, with the same geometric parameters (lines 15-100 µm).

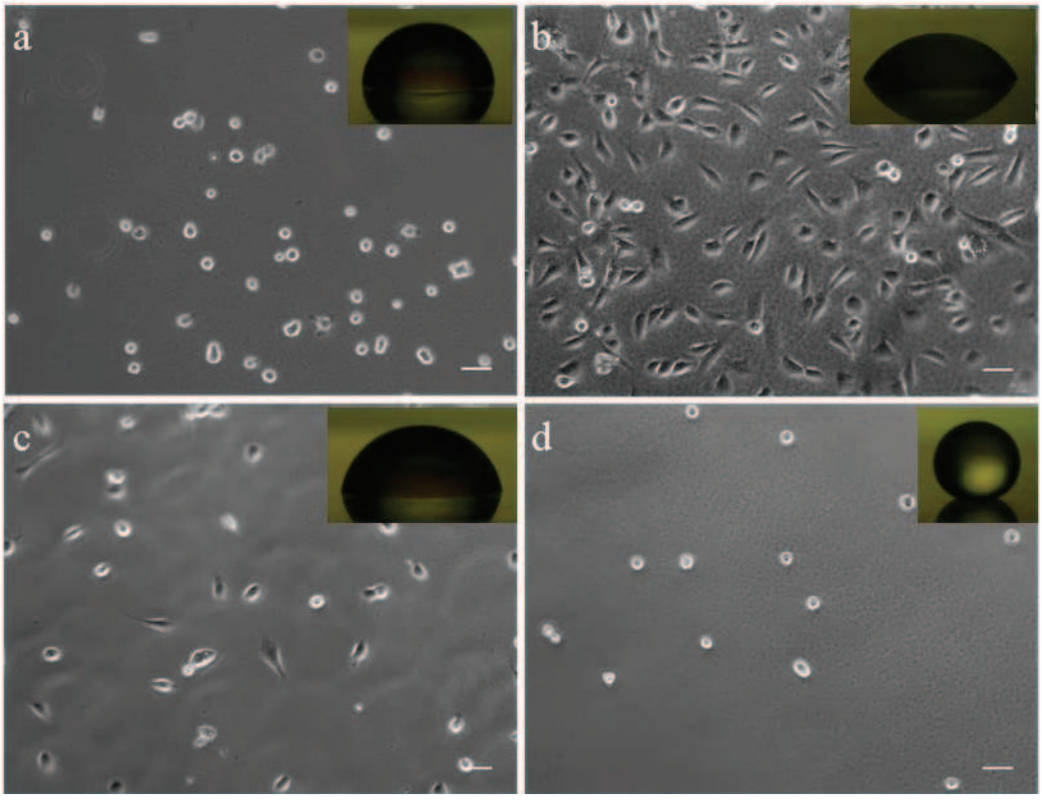

Figure 3.2 Microphotographs of NIH 3T3 cells cultured on a flat surface of PVDF after 2 h. (**a**) Without surface modification. (**b**) After plasma treatment. (**c**) After reactive ion etch with O_2 gas. (**d**) After reactive ion etch with SF_6 gas (scale bar = 50 μm). Insets are microphotographs of water droplets on the corresponding substrates.

SU8 is a biocompatible photoresist commonly used in bio-MEMS. It is a chemically amplified epoxy based negative resist which was originally developed for the fabrication of advanced semiconductor devices. However, this resist has several attributes which make it suitable for micromachining applications. Because of the highly cross-linked matrix, SU8 is both thermally and chemically stable after development, making it well suited for many applications. For cell based assays, SU8 must be baked at 150° for more than 72 hours before cell seeding [**1**], which leads to evaporation of residual solvent so that the material toxicity can be reduced.

We first coated SU8 3005 on a glass slide at a speed of 3000 rpm for 30 s to achieve a thickness of approximately 10 μm. The resist was then soft-baked on a 65 °C hot plate for 5 min and on a 95 °C hot plate for 25 min. Afterward, SU-8 was exposed using 365 nm UV at 13 mW. After a post-exposure bake on a 65 °C hot plate for 5 min and on a 95 °C hot plate for 10 min, the resist was developed for 10 min at room temperature and rinsed with isopropanol. Finally, the SU8 patterns were hard baked at 150 °C for 72 h. When cells are

cultured on SU8 micropatterns, they attach on glass as well as on SU8 lines. After 48 hours, there are as many cells on the top of the lines as between lines (**Fig. 3.3 c-e**).

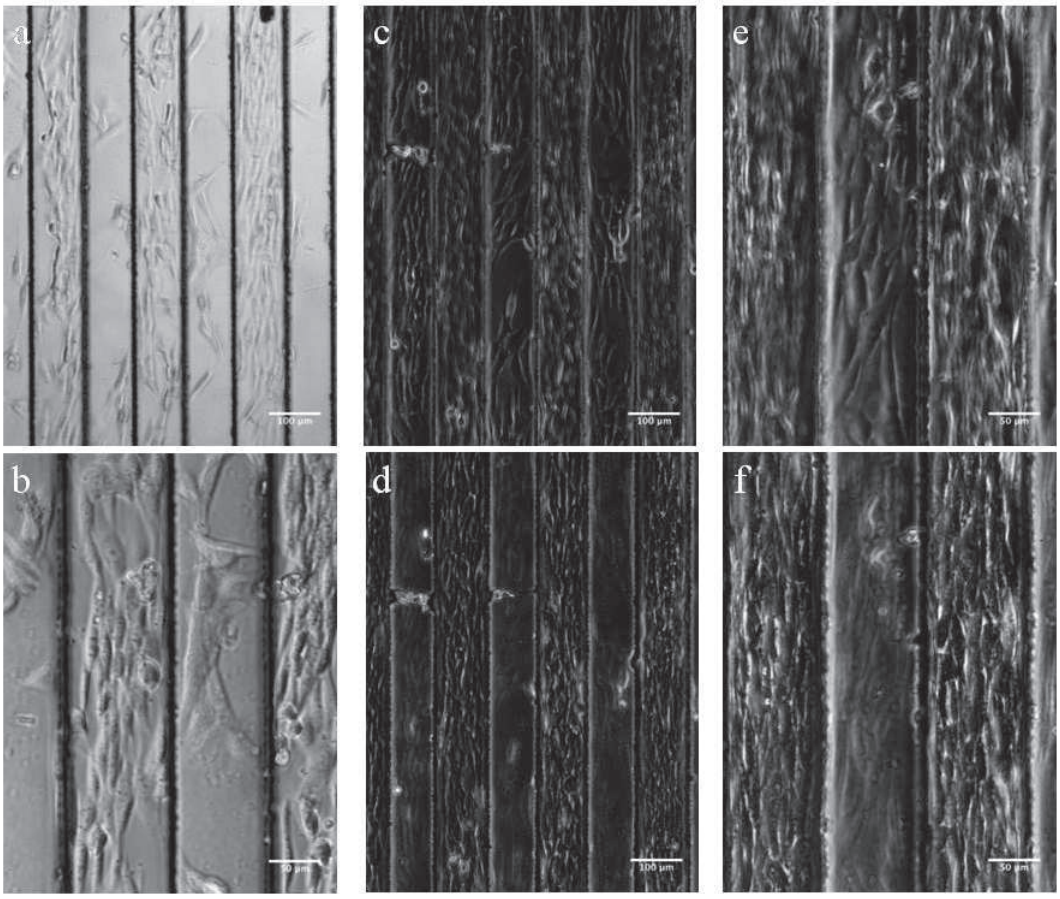

Figure 3.3 Microphotographs of cells cultured on SU8 micropatterns: (**a-b**) after 24h, (**c-f**) after 48h. Focus is made on patterns for c-e and on the glass for d-f**.**

3.3.2 Cell culture on PVDF patterned surfaces

We discussed in chapter 2, PVDF could be patterned by different techniques and the surface of the patterned PVDF could be also modified by the different methods. Consequently, the morphology as well as the physicochemical properties of the resulted patterns could be different.

Figure 3.4 shows the cell culture results obtained with PVDF patterns without residuals in the recession areas. As can be seen, after 1 day culture cells could be attached on glass between PVDF lines (**Fig. 3.4 a-b**). At this stage, the cell density is still low and the cell alignment cannot be clearly observed. After 48 h, cell density comes sufficiently high to all recession areas (**Fig. 3.4 c-f**). However, no cell is attached on the top of the PVDF features.

Cell alignment can now be clearly seen, which is even more pronounced when the distance between the two lines is small (100μm).

Immediately, we can have several important remarks. Firstly, PVDF is not toxic since cells can fairly grew along the edge of PVDF features and the cellular distribution after 2 days of culture could still be homogenous (**Fig. 3.4f**). Secondly, without surface modification cells cannot adhere on PVDF since there is no single cell observed on the PVDF surface. Consequently, a PVDF pattern on glass can have an extremely high adhesion contrast of cells. Thirdly, the PVDF patterns are stable in time, which is necessary for long term culture studies.

The above observations also let us suggest the following cell alignment kinetics: At the beginning cells are evenly seeded on a PVDF patterned surface, they only adhered on the area of exposed glass substrate but did not show a clear alignment. With the increase of the cell density by growth, cells near the edge of the PVDF features became aligned (**Fig 3.4a**). Consequently, other cells in contact with these aligned cells will also be aligned. The increase of the cell seeding density would shorten the time required to reach the cell confluence.

As already discussed in chapter 2, it was not easy to achieve a perfect PVDF patterning with some of the techniques. One of the common feature defects is the remaining residuals of PVDF in the recessed area between PVDF lines. These residuals have clearly effects on cell patterning. In fact, the residual features of PVDF have the same effects to prohibit cell adhesion, although their morphologies are less well defined. **Figure 3.5a** shows a microphotograph of cells cultured on such a pattern after 2 hours of culture. Clearly, cells are all immobilized clear to the edge of the PVDF patterns and they were forced to elongate in the area of where the PVDF has been completely removed. This effect could not be changed with the increase of the incubation time. Indeed, cell adhesion area did not increase with due to limited space of exposed glass and with the increase of the incubation time cells trend to aggregate in the area of exposed glass but not extend to the PVDF area.

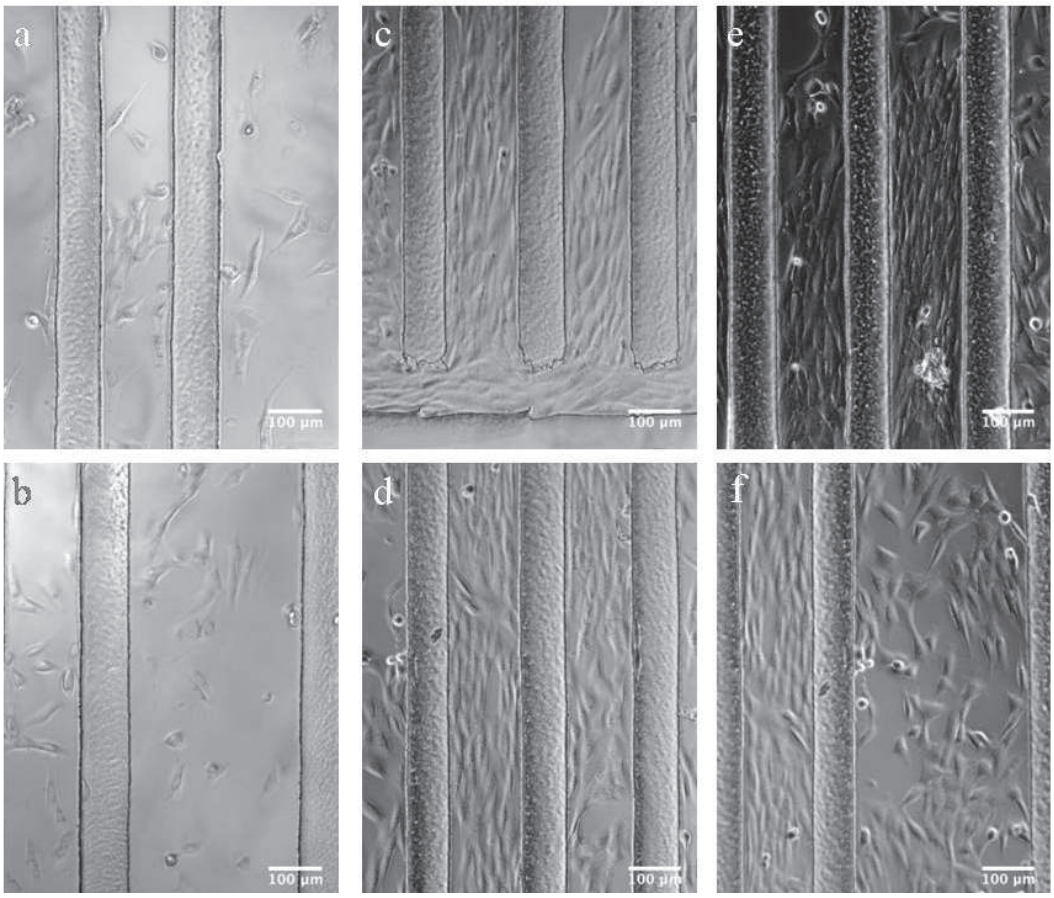

Figure 3.4 Microphotographs of cells cultured on micropatterned PVDF without remaining PVDF between lines: (**a-b**) after 24 h, (**c-f**) after 48 h.

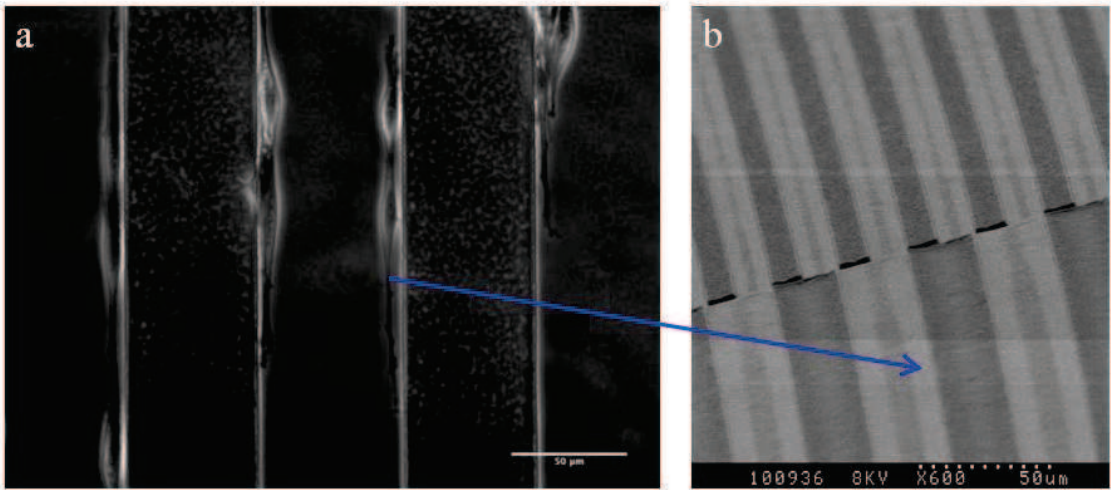

Figure 3.5 (**a**) Microphotograph of cells cultured on PVDF micropatterns after 2 h. (**b**) SEM picture of the PVDF pattern before cell culture.

Figure 3.6 shows the results obtained with a PVDF pattern with square holes after 24 hours of culture. Clearly, cell clusters were formed in the recessed areas. Some clusters could even be formed between two squares but their roots were still in the recessed areas. Moreover, the morphology of the PVDF pattern measured by AFM shows the existence of residuals in the recessed square areas (**Figure 3.6b**), which explains the attachment of the single cell to the four corners of a square (**Figure 3.6c**). Here, the main body of the cell might be in suspension above the residual feature of PVDF, due to high selectivity of cell adhesion.

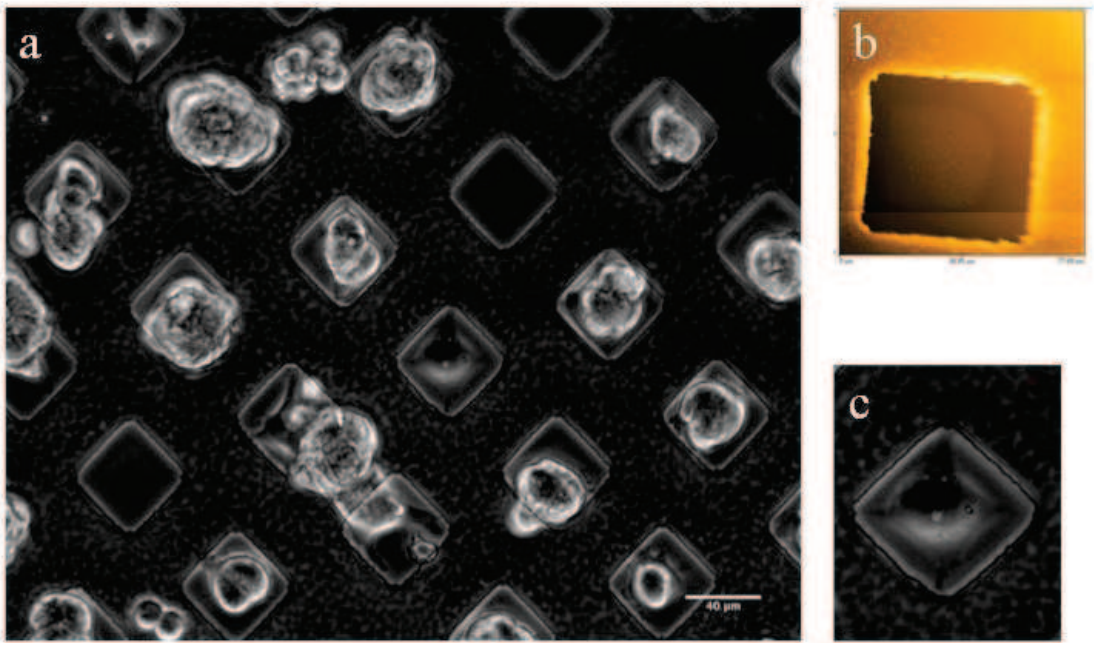

Figure 3.6 (**a**) Microphotograph of cells cultured on PVDF micropatterns after 24 h. (**b**) AFM topographic image of a single square before cell seeding. (**c**) Detail of a cell inside a square.

When cells are placed on PVDF line patterns of much reduced spacing, cells are strongly elongated but it seems difficult to achieve a homogenous distribution. **Figure 3.7a** and **3.7b** show microphotographs of cells patterned on 20 µm line-and-spacing arrays. As can be seen, cell clusters could also be found due to aggregation but others died. **Figure 3.7c**and **3.7d** show microphotographs of cells patterned on 50 µm line-and-spacing arrays. Now, continuous cell stripes could be formed which looked like fibrous bundles. Here, the cell-cell adhesion force might be more important than that between cell and substrate, due probably to the narrow spacing and the residual PVDF between two lines.

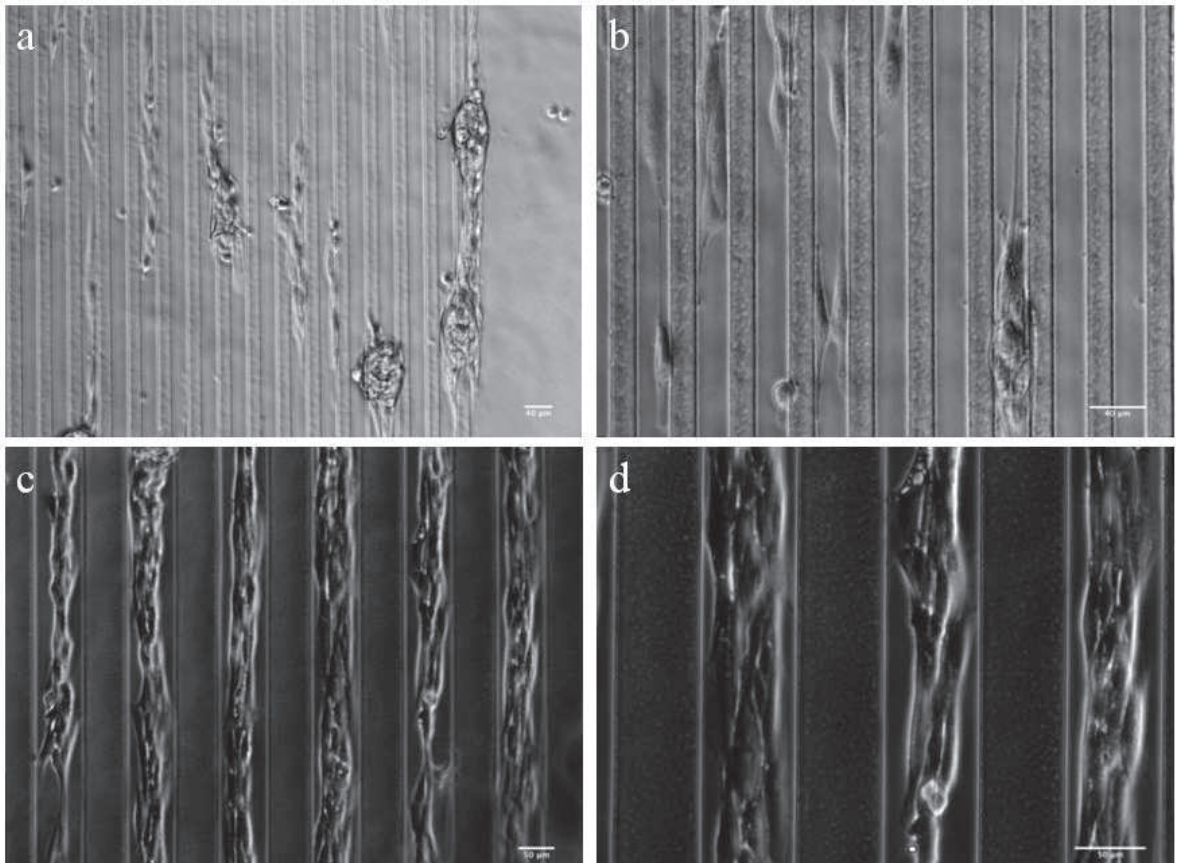

Figure 3.7 Microphotographs of cells cultured on PVDF micropatterns after 24 h: (**a-b**) 20 µm lines spaced by 20 µm, (**c-d**) 50µm spaced by 50 µm.

3.3.3 Effects of protein coating

The above results were obtained with PVDF patterns without protein coating. The same experiments have been done with PVDF patterns after fibronectin coating. A droplet of fibronectin solution is incubated on each sample during 15 min before cell seeding. Then, the remaining solution is aspired with a tissue and samples are kept in a sterile hood for 15 min. to let the fibronectin dry and be adsorbed on the PVDF surface. After cell seeding and incubation in a cell culture medium, cell images are taken to show the adhesion and proliferation of cells on the PVDF patterns.

Figure 3.8 shows microphotographs of cells cultured on PVDF line and square structures. After 2h incubation, cells patterned on PVDF line structures could be attached on the surface of the recessed area as well as on the top surface of PVDF pattern area (**Fig. 3.8a**). After 24 h incubation, the cell number increased in both areas but they all aligned in the direction of the micropatterns (**Fig. 3.8a**). On squares, the material selectivity of the cell

adhesion can be clearly seen. After 2 h incubation, cells all remained outside the PVDF features (**Fig. 3.8c**). After 24h incubation, the cell number also increased but they were still mainly localized outside the square feature of PVDF, showing a clear effect of contact guidance (**Fig. 3.8d**).

These observations confirm that fibronectin is well adsorbed on the surface of PVDF which enhances the cell adhesion as well as the cell spreading. In such a way, the hydrophobicity of the PVDF can be much reduced. The observed adhesion selectivity on micro-square patterns is due probably the size effect, i.e., when the square size is comparable to that of the cell, the cell preferentially stays at the lower level of the pattern.

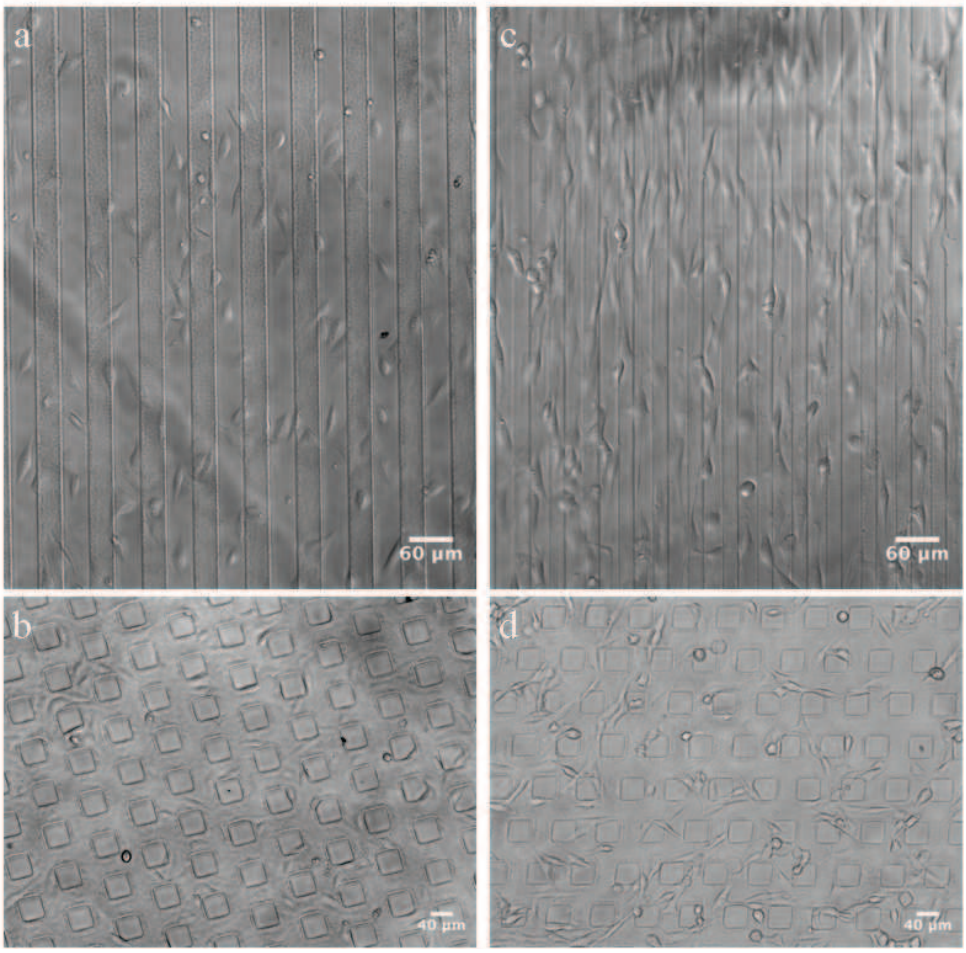

Figure 3.8 Microphotographs of cells cultured on PVDF micropatterns after 24 h: (**a-b**) 20 µm lines spaced by 20 µm, (**c-d**) 50 µm spaced by 50 µm.

3.3.4 Effects of plasma treatment

The PVDF patterns were treated in a plasma chamber for 3 min. before cell seeding. After 2h incubation, many cells could be attached to the sample surface, including both patterned and non-patterned areas (**Fig. 3.9a**). As discussed in chapter 2, the plasma treatment tunes the PVDF surface into hydrophilic so that cells could easily attached on. Compared to the micropatterns coated with fibronectin (**Fig. 3.8a**), the cell attachment seems to be easier on the plasma treated PVDF surface, showing a similar cell morphology of that cultured on the surface of a culture Petri dish. After 24 h incubation, some small cellular networks were formed on the PVDF patterned areas whereas cells reached a confluent stage in the non-pattern area (**Fig. 3.8b**). Obviously, the cell alignment was now less efficient comparing to that one the fibronectin coated PVDF pattern. On the sample coated with fibronectin, the effect of cell-surface interaction is more important than that of cell-cell coupling so that the cell growth was guided by the surface topography, showing the observed cell alignment. On the sample treated by plasma, the effect of cell-surface interaction is less important comparing to the cell-cell coupling so that cells can more easily form random cellular networks, showing no alignment effect.

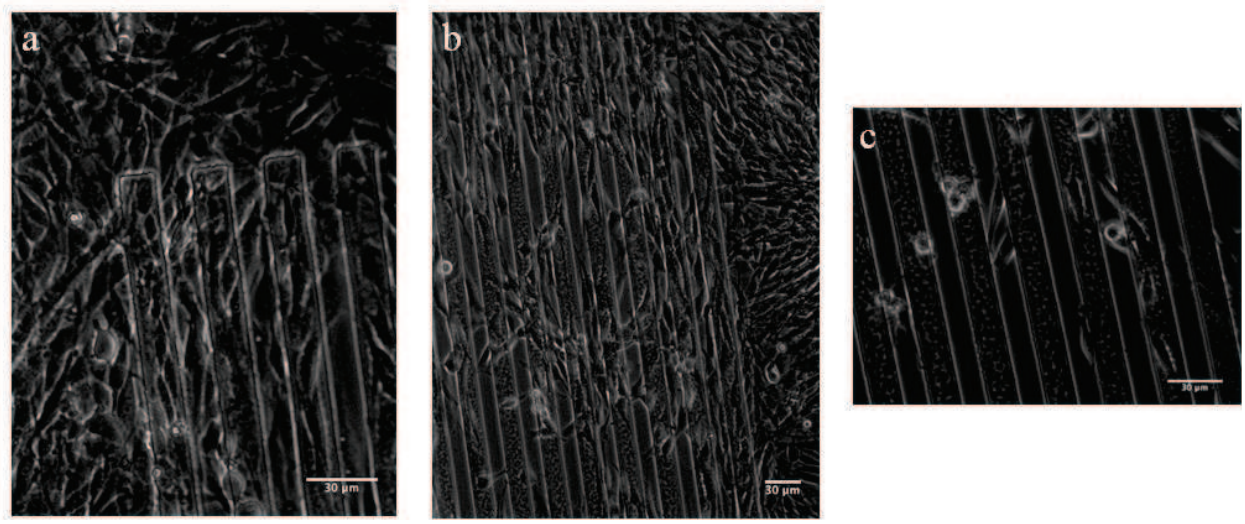

Figure 3.9 Microphotographs of cell cultured on plasma treated PVDF micropatterns: (**a**) after 2 h, (**b-c**) after 24 h.

3.4. Cell cultured on flat PVDF surfaces with protein patterns

Protein patterns can be also easily produced on PVDF flat surface. PDMS stamps with periodic line arrays of different line width and spacing have been used to define fibronectin patterns on the thin layers of PVDF coated on glass slides according to the protocol described in chapter 2. After protein patterning, NIH 3T3 cells were cultured and both phase contrast and immunofluorescence images were taken for the performance assessment.

Figure 3.10 shows phase contrast images of cells cultured for 48 h on a flat surface of PVDF patterned with fibronectin by micro-contact printing. Without going into details, several observations can be made. Firstly, cells form cell stripes defined by the fibronectin or the PDMS stamp. Apart from some irregularity, the most of cells remain in the patterned area due to strong cell-surface interaction. Secondly, no dead cell can be found. Since after seeding cells are evenly distributed on the surface of the substrate, the absence of dead cell on the surface means that cells migrated from the bare PVDF are to the protein coated areas. Third, the cells immobilized in the cell stripe areas are aligned due to the contact guidance effect.

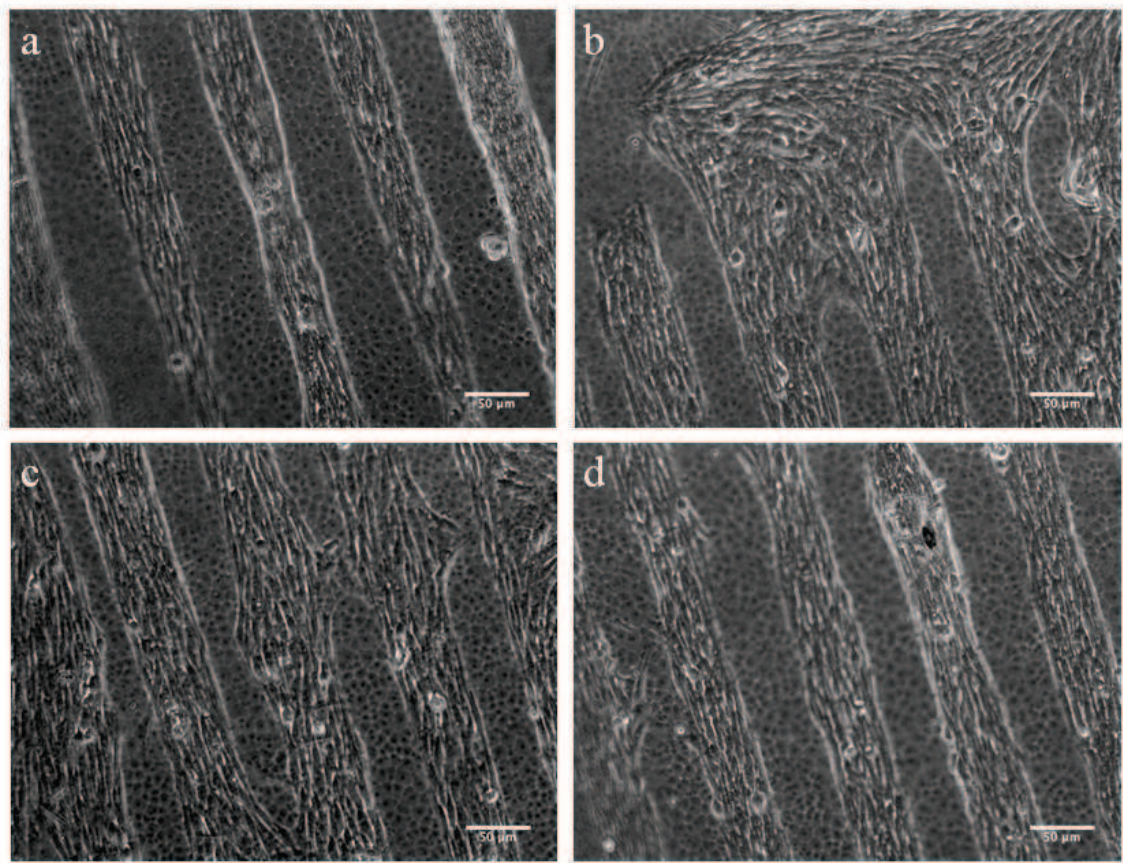

Figure 3.10 (**a-d**) Microphotographs of cells cultured for 48 h on a PVDF substrate with protein (fibronectin) stripes defined by micro-contact printing.

Cell immunostaining has been done according to the protocol of Annex 3. We were mostly interested in imaging of actin filaments and cell nuclei. Actin filaments were tagged using fluorescent-dye attached phalloidin (protocol in annex 3) whereas nuclei were tagged using DAPI.

Figure 3.11 and 3.12 show phase contract and immunofluorescence images of cells cultured on protein line patterns defined by microcontact printing. **Figure 3.11a** and **b** show respectively a phase contrast image and a merged image (phase contrast super-imposed with nuclei image tagged with DAPI in blue). **Figure 3.11c and d** show respectively a phase contrast image and an immunofluorescence image of actin filaments tagged with phalloidin (green) and nuclei tagged with DAPI (blue). Here, the immunofluorescence image of the cell nuclei shows that the imaged cells are not on a single focal plan (some of blue dots are out of focus), suggesting that the cell stripes are formed in multiple layers. A more detailed observation (**Figure 3.13d**) revealed that the actin filaments are all aligned in the same direction of the cell stripes or the protein patterns underneath. More detailed investigations will be needed a more clear assessment of the stripe morphology which is out of the scope of the present study.

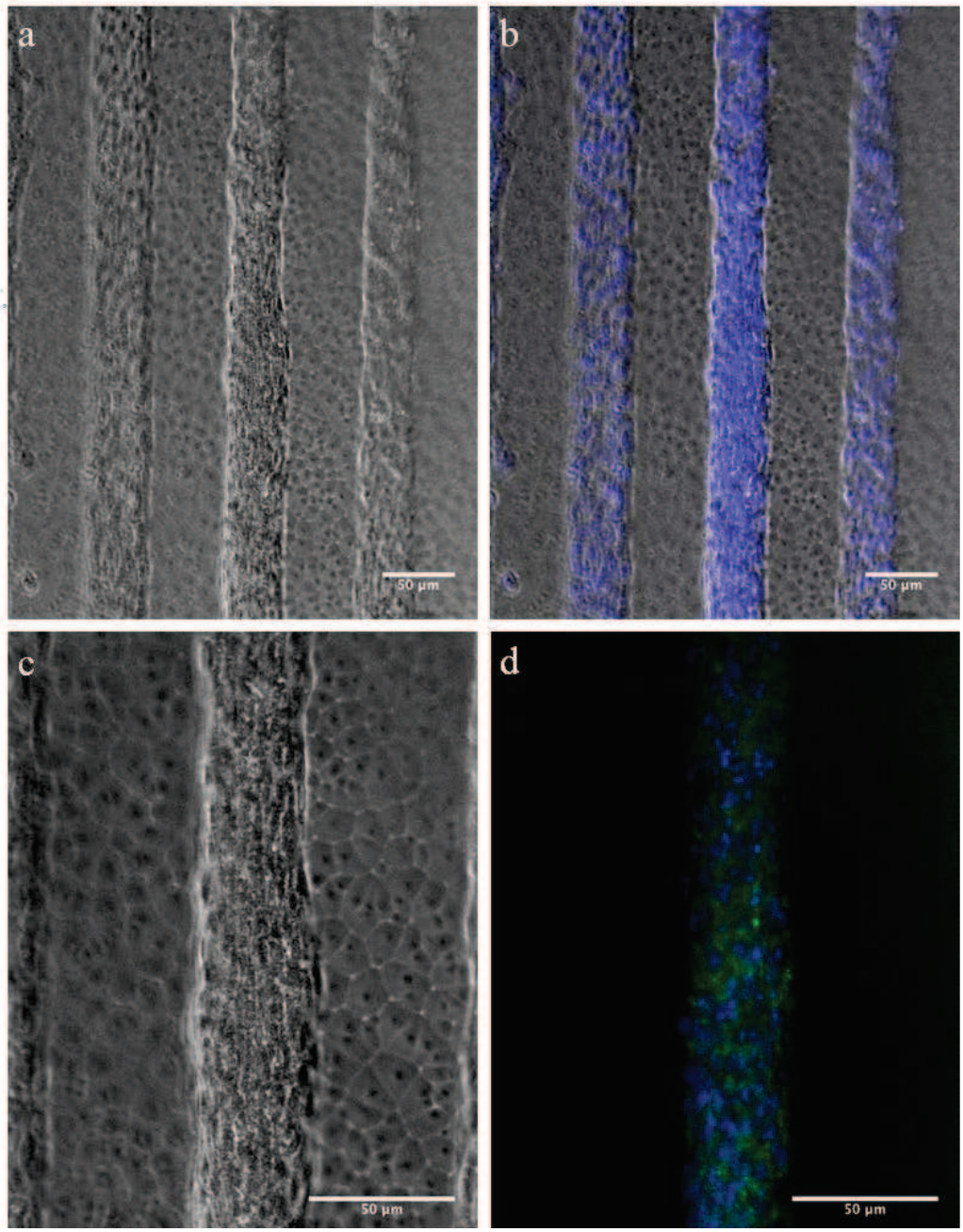

Figure 3.11 Cells cultured on protein stripes patterned by microcontact printing: (**a**) Bright field image (**b**) Superposition of bright field and fluorescent microphotograph with cell nucleus tagged with DAPI (blue). (**c**) Bright field image. (**d**) Fluorescent image with actin tagged with phalloidin (green) and nucleus tagged with DAPI (blue).

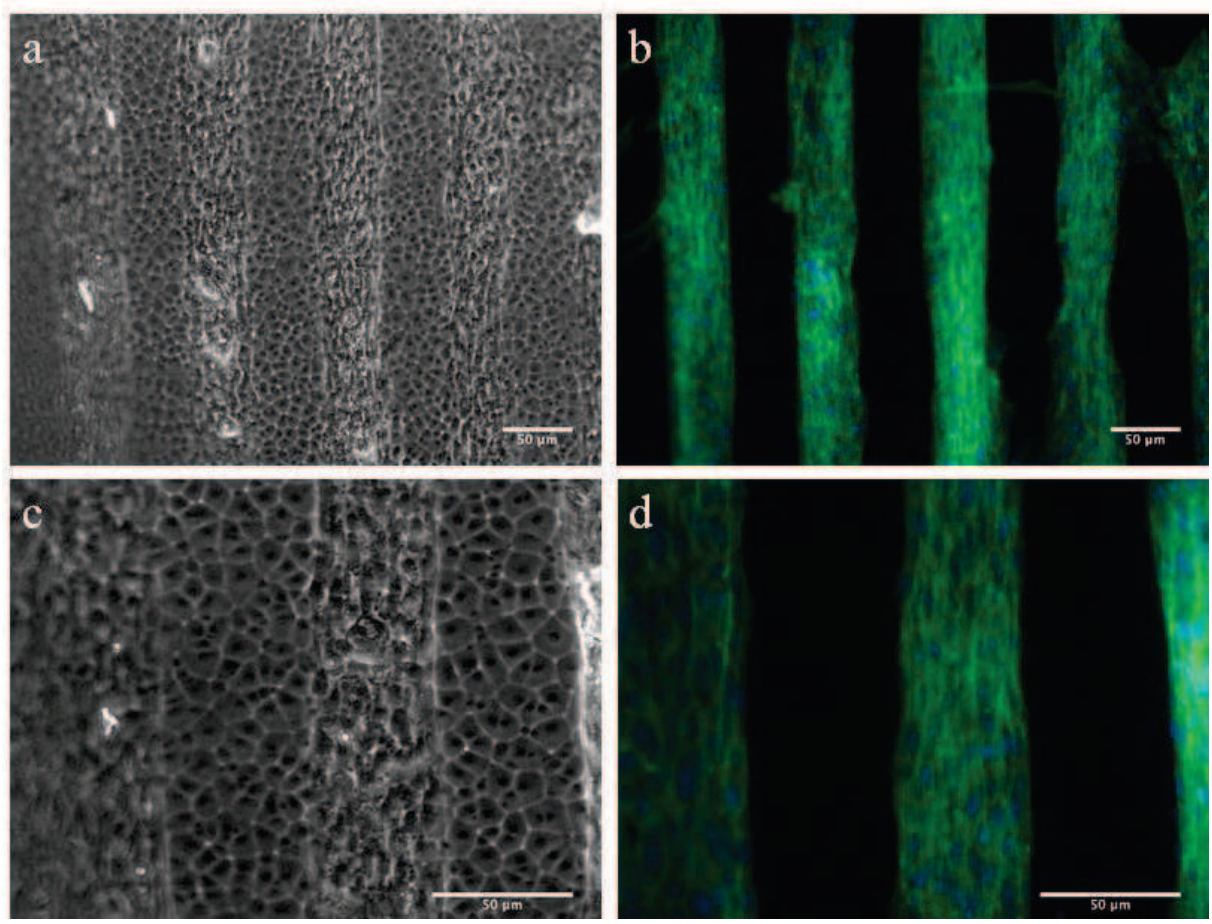

Figure 3.12 Cells cultured on protein stripes patterned by microcontact printing: (**a-b**) bright field images, (**c-d**) fluorescence images with actin tagged with phalloidin (green) and nucleus tagged with DAPI (blue).

3.5. Conclusion

PVDF micropatterns or protein patterned flat PVDF surfaces can be used to demonstrate the high selectivity and high stability of cell adhesion. With surface modification, cells preferentially adhere in the non-patterned area (glass) between PVDF lines. When spacing between two PVDF lines is sufficiently large (in the order of 100μm), well-defined cell stripes can be formed, showing also a cell alignment effect along cell lines. With the decrease of the spacing between two PVDF lines, the quality of the cell stripe decreases but the edge effect persists. Moreover, the pattern residuals of PVDF largely influence the cell adhesion and spreading. Homogenous surface coating of fibronectin makes cells attachable on PDVF due to increased cell-substrate interaction. Accordingly, cells can be more homogeneously adhered on both PVDF patterned and non-patterned area, where topography induced effects become dominant. Homogenous surface treatment by plasma exposure makes the PVDF hydrophilic so that cells can also be easily attached. However, the pattern topography has less important effect on the cell adhesion because of relative week cell-substrate interaction comparing to the cell-cell coupling. Microcontact printing defined protein patterns on a flat PVDF surface are remarkably efficient to guide cell adhesion and spreading. Well-defined cell stripes can be obtained, showing clearly cell alignment as well as multiple layer cell aggregates. Comparing to other types of materials currently used in cell patterning, PVDF is certainly interesting because of its high selectivity and high stability in cell adhesion. Unlike PEG, PVDF does not swell when polymerized and it can be easily processed. PVDF is not cytotoxic so that no special treatment is needed prior to cell culture. Finally, PVDF is transparent which makes it compatible with conventional cell culture and imaging techniques.

References

[1] Bastounis, E., Georgopoulos, S., Maltezos, C., Alexiou, D., Chiotopoulos, D., & Bramis, J. (1999). PTFE-vein composite grafts for critical limb ischaemia: a valuable alternative to all-autogenous infrageniculate reconstructions. *European journal of vascular and endovascular Surgery*, *18*(2), 127–32. doi:10.1053/ejvs.1999.0880

[2] Panayiotopoulos, Y. P., & Taylor, P. R. (1997). A paper for debate: vein versus PTFE for critical limb ischaemia--an unfair comparison? *European journal of vascular and endovascular surgery: the official journal of the European Society for Vascular Surgery*, *14*(3), 191–4. Retrieved from http://www.ncbi.nlm.nih.gov/pubmed/9345238

[3] Ottenbrite, Raphael M;Park, Kinam; Okano, T. (Ed.). (2010). *Biomedical applications of hydrogels handbook*. Springer. Retrieved from http://www.springer.com/materials /biomaterials/book/978-1-4419-5918-8

[4] Klee, D., Ademovic, Z., Bosserhoff, A., Hoecker, H., Maziolis, G., & Erli, H.-J. (2003). Surface modification of poly(vinylidenefluoride) to improve the osteoblast adhesion. *Biomaterials*, *24*(21), 3663–3670. doi:10.1016/S0142-9612(03)00235-7

[5] Ribeiro, C., Panadero, J. a, Sencadas, V., Lanceros-Méndez, S., Tamaño, M. N., Moratal, D., Salmerón-Sánchez, M., et al. (2012). Fibronectin adsorption and cell response on electroactive poly(vinylidene fluoride) films. *Biomedical materials (Bristol, England)*, *7*(3), 035004. doi:10.1088/1748-6041/7/3/035004

[6] Curtis, a, & Wilkinson, C. (1997). Topographical control of cells. *Biomaterials*, *18*(24), 1573–83. Retrieved from http://www.ncbi.nlm.nih.gov/pubmed/9613804

[7] Lensen, M. C., Schulte, V. a., Salber, J., Diez, M., Menges, F., & Möller, M. (2008). Cellular responses to novel, micropatterned biomaterials. *Pure and Applied Chemistry*, *80*(11), 2479–2487. doi:10.1351/pac200880112479

[8] Teixeira, A. I., Abrams, G. a, Bertics, P. J., Murphy, C. J., & Nealey, P. F. (2003). Epithelial contact guidance on well-defined micro- and nanostructured substrates. *Journal of cell science*, *116*(Pt 10), 1881–92. doi:10.1242/jcs.00383

[9] Dalby, M. J., Riehle, M. O., Yarwood, S. J., Wilkinson, C. D. ., & Curtis, A. S. . (2003). Nucleus alignment and cell signaling in fibroblasts: response to a micro-grooved topography. *Experimental Cell Research*, *284*(2), 272–280. doi:10.1016/S0014-4827(02)00053-8

[10] Gallego, D., Ferrell, N. J., & Hansford, D. J. (2007). Fabrication of Piezoelectric Polyvinylidene Fluoride (PVDF) Microstructures by Soft Lithography for Tissue Engineering and Cell Biology Applications. *Materials Research*, *1002*.

[11] Vernekar, V. N., Cullen, D. K., Fogleman, N., Choi, Y., García, A. J., Allen, M. G., Brewer, G. J., et al. (2009). SU-8 2000 rendered cytocompatible for neuronal bioMEMS applications. *Journal of biomedical materials research. Part A*, *89*(1), 138–51. doi:10.1002/jbm.a.31839

CHAPTER 4

PVDF and PVDF-TrFE nanofibers

In this chapter, we discuss the fabrication of PVDF and PVDF-TrFE nanofibers by electrospinning techniques. The interest of these nanofibers relies on the easy and low cost fabrication, conserved piezoelectric crystalline phase of the polymer and possible application of the fibers as new scaffolds for advanced tissue engineering. Actually, there are a huge number of investigations on electrospinning techniques for the production of functional nanofibers [**1-12**] but few have been done with PVDF or PVDF-TrFE. Intuitively, PVDF and PVDF-TrFE are thermoplastic and piezoelectric materials, so that once made in aligned nanofibers, they might be used for enhanced and directed growth of cardiac or neural cells due to the charge effects. More interestingly, if one can mechanically actuate nanofibers, the resulted piezoelectric effects will affect the charge distribution or the cell response. Reversely, the electric or mechanic activity of the cells might be monitored. Therefore, we aimed at production of aligned nanofibers and demonstration of their cell-culture compatibility.

4.1 Electrospinning of aligned nanofibers with precise localization

Electrospinning is a chaotic process by nature as it relies as breaking the surface tension of a liquid with a strong electric field and the traveling of the liquid at high speed to the collector. At the end of the Taylor cone the ejected liquid forms a single liquid jet. After this zone there is a zone of rapid acceleration of the liquid (**Fig 4.1**) where the solvent evaporates while the nanofibers are formed.

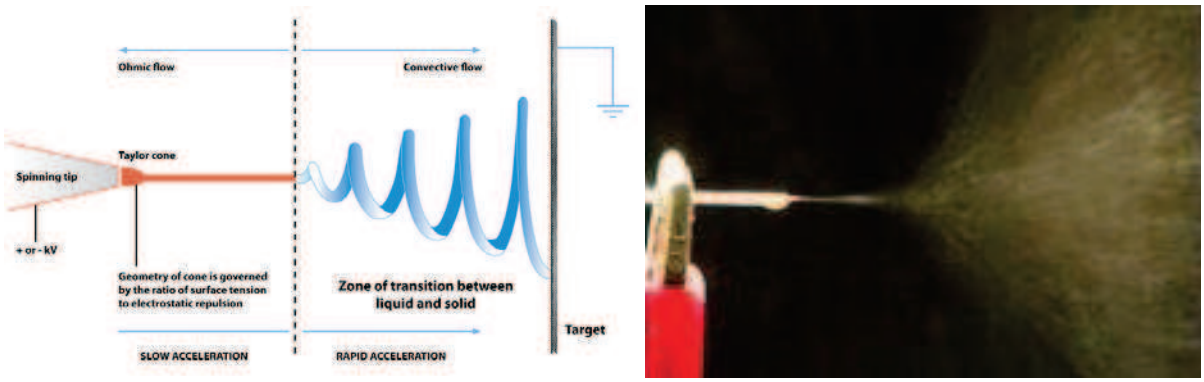

(a) (b)

Figure 4.1 Schematic (**a**) and photograph (**b**) of electrospinning of nanofibers. (From [**13-14**])

In general, the jet at the end of the Taylor cone splits in a multitude of nanofibers that are randomly deposited on the collector but aligned fibers can be obtained by controlling the flying trajectory of jet. Since the electrospinning is based on the manipulation of the liquid jet using electrical field and the fibers are preferentially deposited on the conductive part of the collector, it is relatively easy to control the fiber deposition by regulating the distribution of the electrical field on the collector.

Thus, the general approach to obtain the aligned fibers is to use a rotating drum [**15-25**].When the drum rotates with a speed high enough to generate a linear velocity in the range between 2 m/s and 186 m/s, aligned fibers can be deposed on the surface of the drum. When the velocity of the drum is too low, only random fibers can be obtained. Otherwise when the velocity of the drum is too high, most the fibers are dispersed in air. Other drum-like collectors such as conductive disks, rings, or drums with wound wires can also be used to produce aligned fibers [**26**]. Another approach is to use flat electrodes with narrow splits defined by mechanic cutting or lithography patterning [**27-33**]. Localization of nanofibers (within a 5mm spot) has been obtained by replacing the needle by a silicon tip [**34**] and reducing the collector-tip distance to 1cm. However precise localization of nanofibers within a single nanofibers resolution can only be obtained by Near Field ElectroSpinning (NFES).

4.1.1 Near Field Electrospinning

Near field electrospinning (NFES) can be used to produce aligned nanofibers with precise localization. Initially, this technique has been proposed by *Sun et al.* [**35**] to achieve single PEO (Poly Ethylene Oxide) nanofiber deposition following predefined pattern (**Fig. 4.2-4.4**).

A tungsten tip (25µm) is dipped in the PEO solution and placed above the collector (500µm-3mm) and high voltage is applied (0.6-1.6 kV). The tip is displaced over the collector to create the patterns.

Chang et al. [**36**] used this technique to achieve single nanofiber deposition made of PVDF which should be useful for piezoelectric energy generation.

In the present study, we evaluated the performance of this technique using the same fabrication protocol. First, 18 wt% PVDF was dissolved in a mixture of DMF/Acetone

(6g/4g). Then, 3 wt% Zonyl@UR (Dupont) was added in the solution. Here, Zonyl@UR is a fluorosurfactant which can lower the surface tension of the solution.

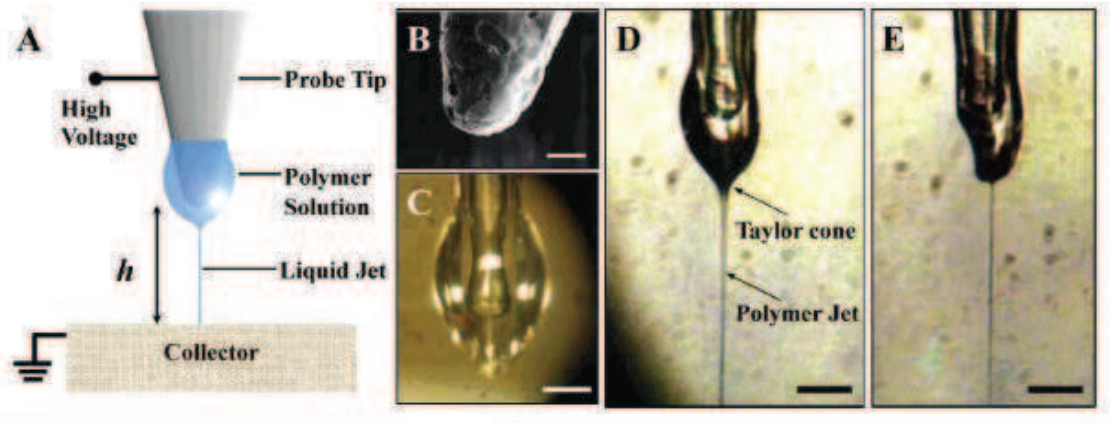

Figure 4.2 (**A**) Schematic of near field electrospinning process. (**B**) SEM picture of the tungsten tip. (Scale bar 10 µm) (**C**) Optical image of the solution droplet on the tip. (Scale bar 20 µm) (**D**) Tip with the Taylor cone during electrospinning. (Scale bar 25 µm) (**E**) Same picture when most of the solution on the tip has been electrospun (From [**35**]). (Scale bar 25 µm)

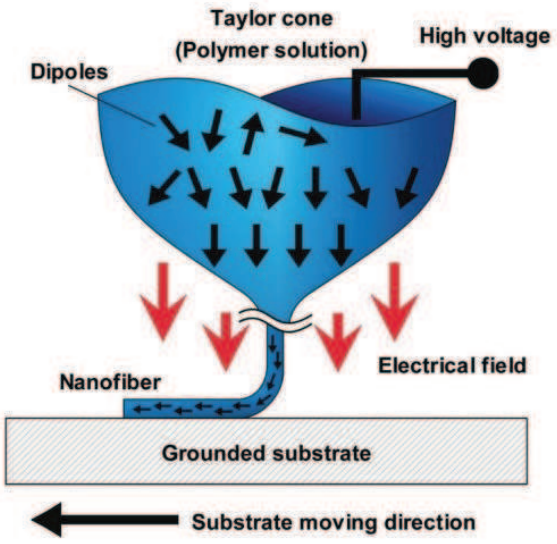

Figure 4.3 Schematic of near field electrospinning. (From [**36**])

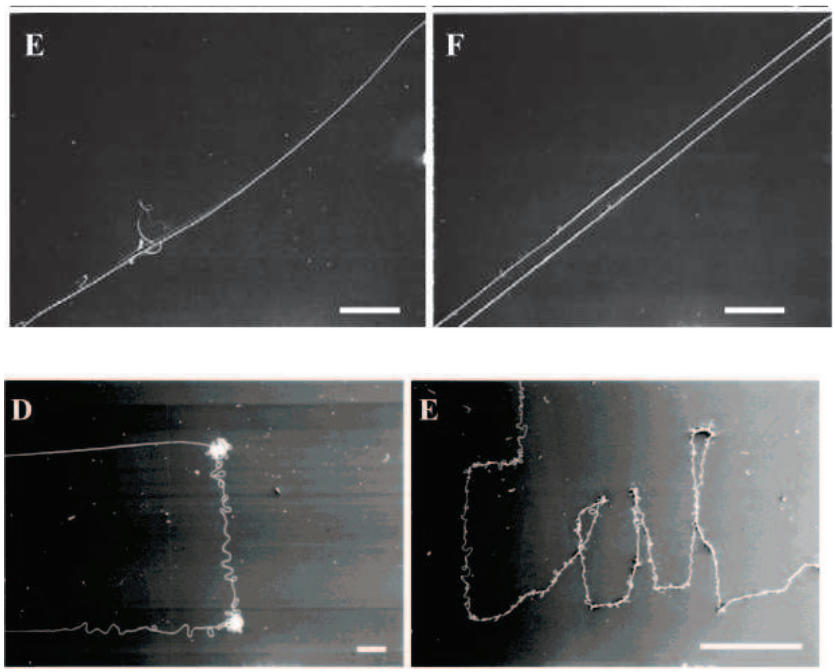

Figure 4.4 Single PEO (Poly Ethylene Oxide) nanofiber deposition achieved by near field electrospinning. (From [**35**])

Our experimental set-up is as follows: A dispensing robot (Fisnar I&J 7100) was used for the movement control of a very thin acupuncture needle close to the surface of a grounded substrate (**Fig. 4.5**). The needle itself is connected to a high voltage power supply (Heinzinger TNC 30000) (**Fig 4.5b**) and the electrospinning process is monitored with a digital microscope (Dino-Lite AM4013MT).

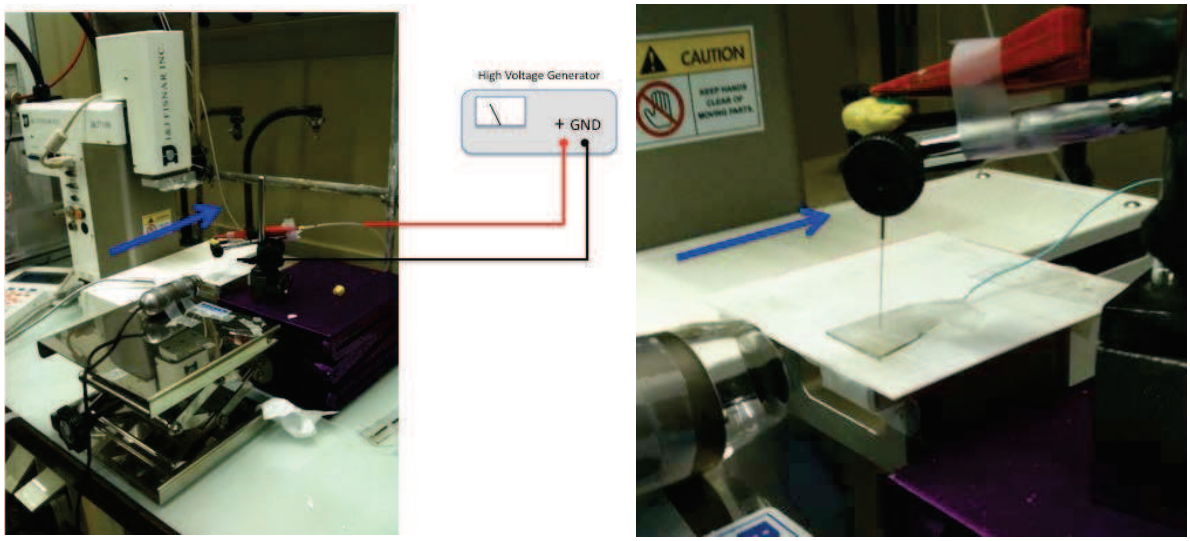

Figure 4.5 Experimental setup used in this work for near field electrospinning.

The collector is made of gold electrodes patterned on a Kapton thin film (Dupont Kapton HN) which is an electrical insulator, flexible and compatible with the microfabrication processes. The gold electrodes with a 1 mm gap were fabricated on Kapton by sputtering using a shadow mask. They were connected to the power supply after wire bonding with conductive epoxy. To ensure the flatness of the electrodes, Kapton was reversibly attached on a glass substrate.

During the electrospinning, a droplet of the polymer solution is deposited on the needle and a high voltage is applied progressively. To avoid the spark due to air break by the high electric field, the voltage should be increased step by step. When the droplet is dragged down by the electric field, the Taylor cone appears. In general, the applied voltage is around 1.5 kV with an electrode to collector distance of 1 mm. As soon as the Taylor cone is formed, the needle should be moved rapidly in order to drag the fiber in a straight line across the electrodes (**Fig. 4.6**). Due to its strong hydrophobicity, a white solid shell trends to be formed outside the PVDF droplet which makes it difficult to form PVDF nanofibers by this method. We then used a solution of 18% wt PEO (PolyEthylene Oxide) to test the same process. Nevertheless, we managed to get a single PVDF nanofiber between the electrodes.

Figure 4.7 shows SEM images of the fabricated single PVDF nanofiber which has a diameter of ~5 µm. Obviously, this diameter is much larger than that produced by conventional electrospinning (<1 µm) but it is consistent with what has been produced by *Chang et al.* [**37**]. Moreover, the deposited nanofiber showed a flat morphology, indicating that during NFES the solvent was not fully evaporated from the PVDF solution when the fiber is formed on the surface of the substrate. Accordingly, a later evaluation of the solvent resulted in a flat morphology of the fiber. Neither this flat morphology nor the large fiber diameter is desired for our application purposes, we then renounced this method and turned on more conventional approaches using patterned electrodes.

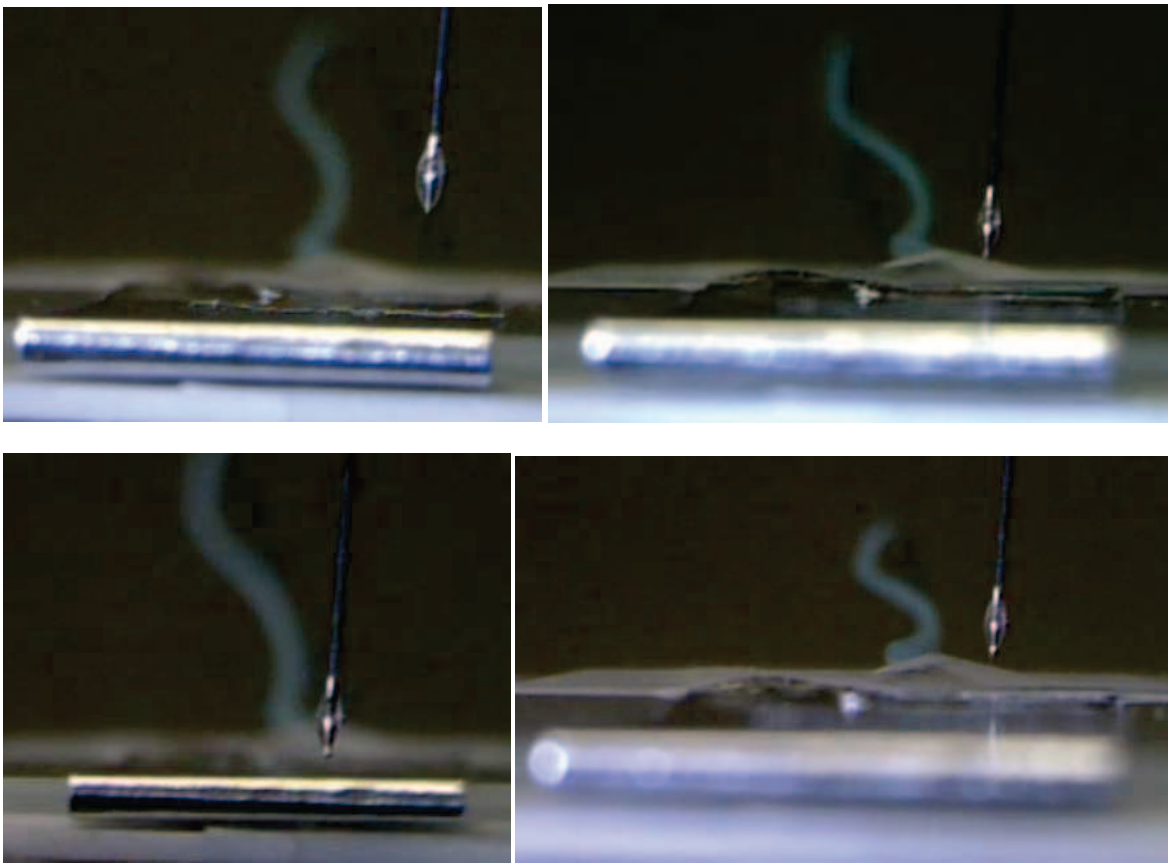

Figure 4.6 Photographs to illustrate the near field electrospinning process

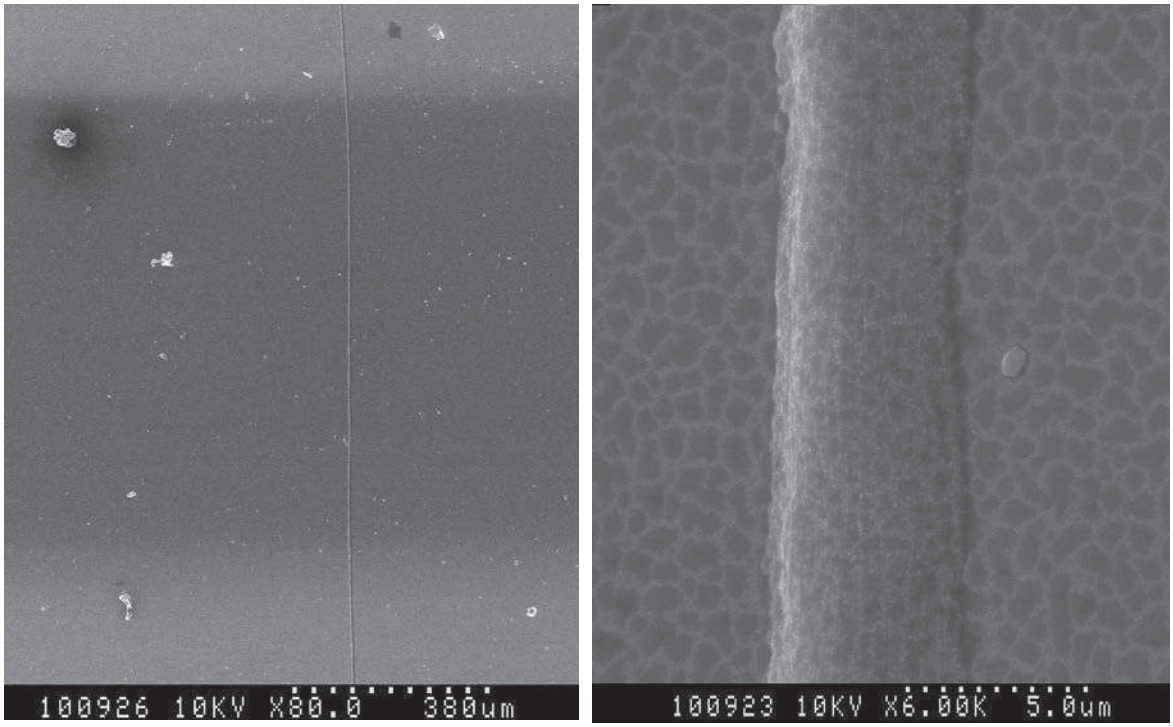

Figure 4.7 (**a-b**) SEM Images of a single PVDF nanofiber deposited between 2 gold electrodes on Kapton.

4.1.2 Aligned nanofibers on patterned electrodes

Conventional methods of electrospinning for producing aligned nanofibers are based on the use of rotating drums [**15-25**], disks [**38-45**] or metal frames assisted by electric field [**27-32**] or magnetic field [**46-48**]. Whereas the rotating drums are used to deposit nanofibers on rigid substrates, the metal frames are used to deposit suspended nanofibers. In both cases, an additional step is required to transfer the nanofibers to the final substrates. In our work, we deposited the requested nanofibers on a final substrate by using a pair of patterned electrodes. We were interested in this method mainly because the patterned electrodes could be used not only for the control of nanofiber alignment but also for the electric or piezoelectric characterization of the deposited nanofibers. Two grounded electrodes were patterned on an insulating substrate. When they are used as collector, an electrostatic force is generated which pulls the nanofibers to be deposited cross the electrodes. Initially, *Li et al.* demonstrated this method by using quartz and polystyrene substrates.

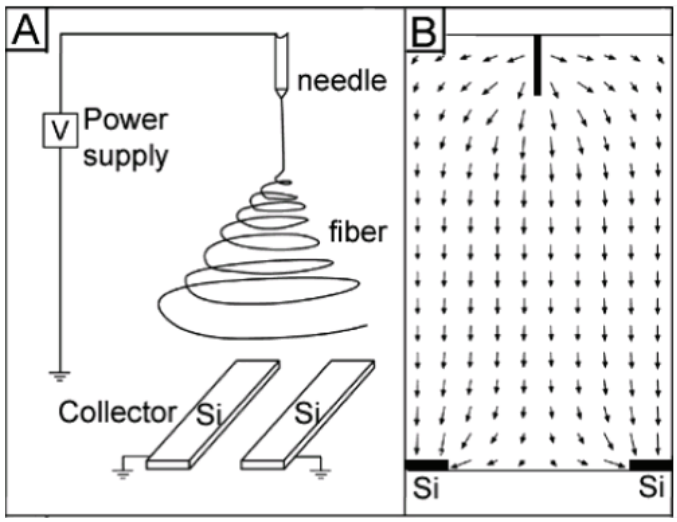

Figure 4.8 (**A**) Schematic illustration of the setup for electrospinning that we used to generate uniaxially aligned nanofibers. The collector contained two pieces of conductive silicon stripes separated by a gap. (**B**) Calculated electric field strength vectors in the region between the needle and the collector. The arrows denote the direction of the electrostatic field lines. (From [**27**])

In order to test the feasibility of cell culture on piezoelectric nanofibers, we performed in this work the same study with other types of substrates.

PVDF (Sigma-Aldrich) or PVDF-TrFE (70/30) (Piezotech) were dissolved in DMF with a concentration of 18 % (w/w). Gold electrodes have been fabricated on a substrate with different electric resistances (**Table 4.1**) including glass, Kapton and quartz using standard photolithography with different electrode configurations.

Material	**Resistivity (Ω m)**
Quartz	7.5×10^{17}
Glass	10×10^{10} to 10×10^{14}
Kapton	1.5×10^{19}
Air	1.3×10^{16} to 3.3×10^{16}

Table 4.1 Resistivity of different substrates, comparing to that of air.

We used a syringe pump (Longer pump TSC2-60) to provide a continuous flow of the polymer solution (1ml/h). The positive terminal of the high voltage power supply (Heinzinger LNC 30000) is connected to the needle of the syringe and the negative terminal is connected to the two electrodes of the connector. The gap between the needle and the grounded electrodes is about 5 cm and the applied voltage is fixed at 8 kV.

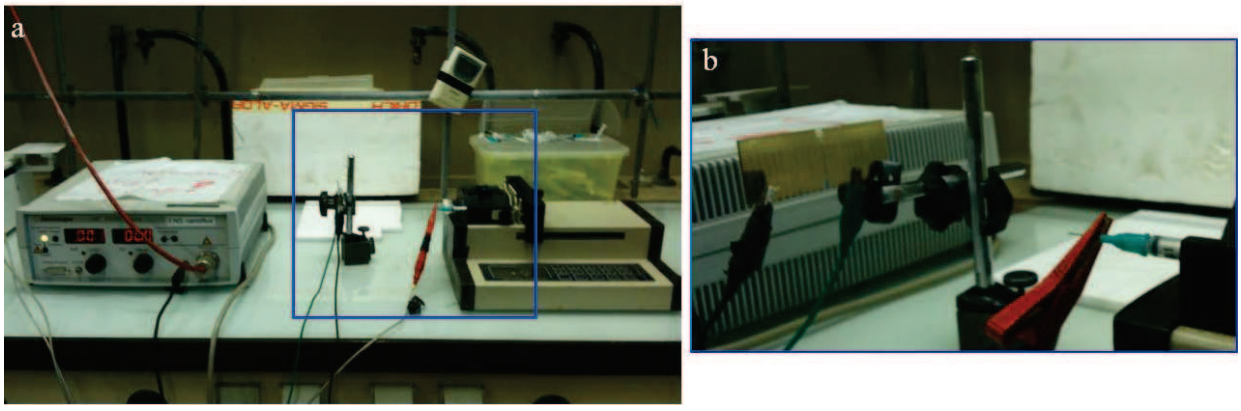

Figure 4.9 Experimental setup of electrospinning used in this work.

We first tested the feasibility of nanofiber deposition with 4 electrodes: two pairs of opposite electrodes are grounded alternatively to produce crisscrossed nanofibers patterns. When the solution arrives steadily at the end of the syringe needle, high voltage is applied for a short time (40 sec).**Figure 4.10** shows the microphotograph pictures of deposited nanofibers using a metallic frame (a), a glass substrate (b), a Kapton thin film (c), and a quartz plate (d). As can be expected, the alignment of the nanofibers is better on a substrate with a higher resistivity. However, the nanofibers produced on Kapton which has the highest resistivity (1.5 x $10^{19}\Omega$ m) shows a lower alignment rate compared to the nanofibers on quartz (7.5×10^{17}), indicating that the resistivity of the substrate is not the only parameter to influence the alignment performance. In fact, the poor alignment of the nanofibers on Kapton can be attributed to the antistatic effect of the material which may perturb the electric field distribution between electrodes. Note that the glass substrate does not support a good alignment of the fibers.

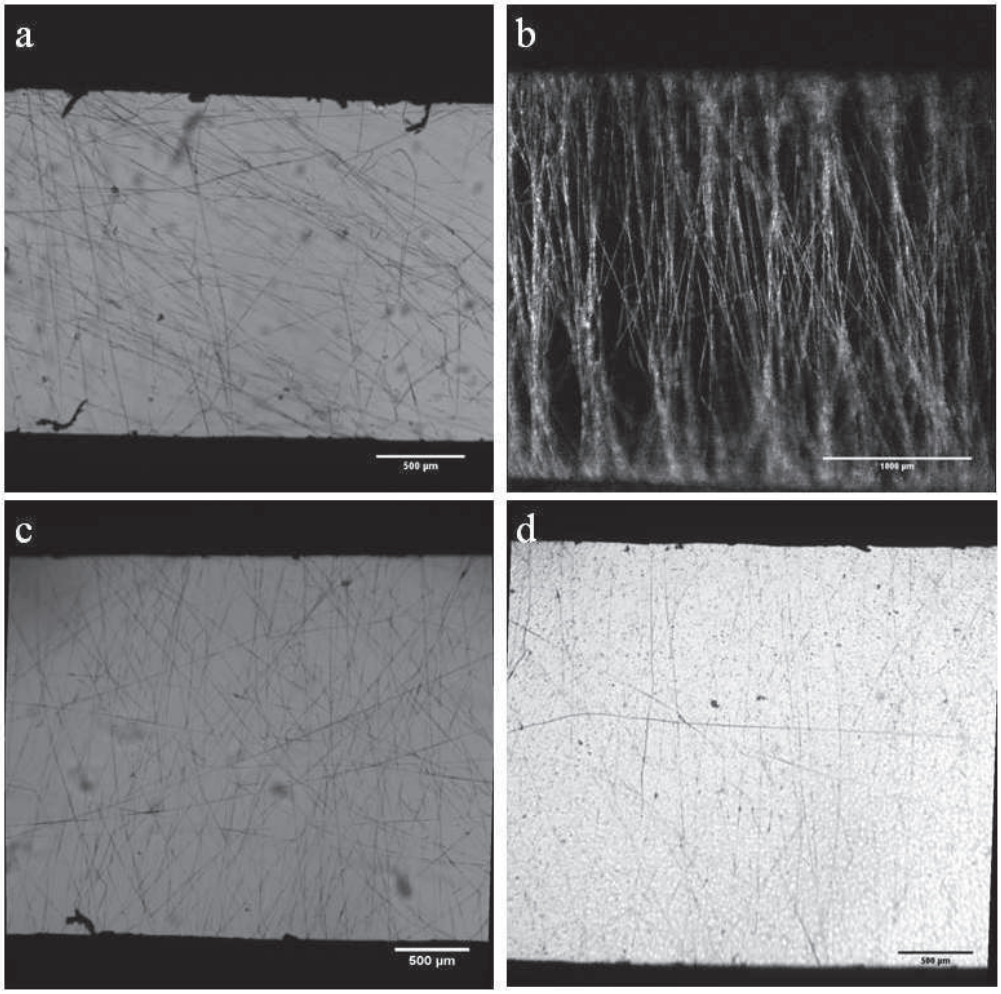

Figure 4.10 Microphotograph of electrospun nanofibers using 2 electrodes for alignment and different isolating material between those electrodes: (**a**) air, (**b**) quartz, (**c**) Kapton, (**d**) glass.

Nevertheless, by using a pair of tapered electrodes with a smaller gap (1mm) aligned nanofibers could still be obtained on a glass substrate, as shown in **Fig. 4.11**. The high magnification pictures of the gap area between the two electrodes shows that the most of nanofibers in the center part of the electrode are uniaxally aligned but the nanofibers deposited on the edge area of the electrodes followed the electric field lines which are curved.

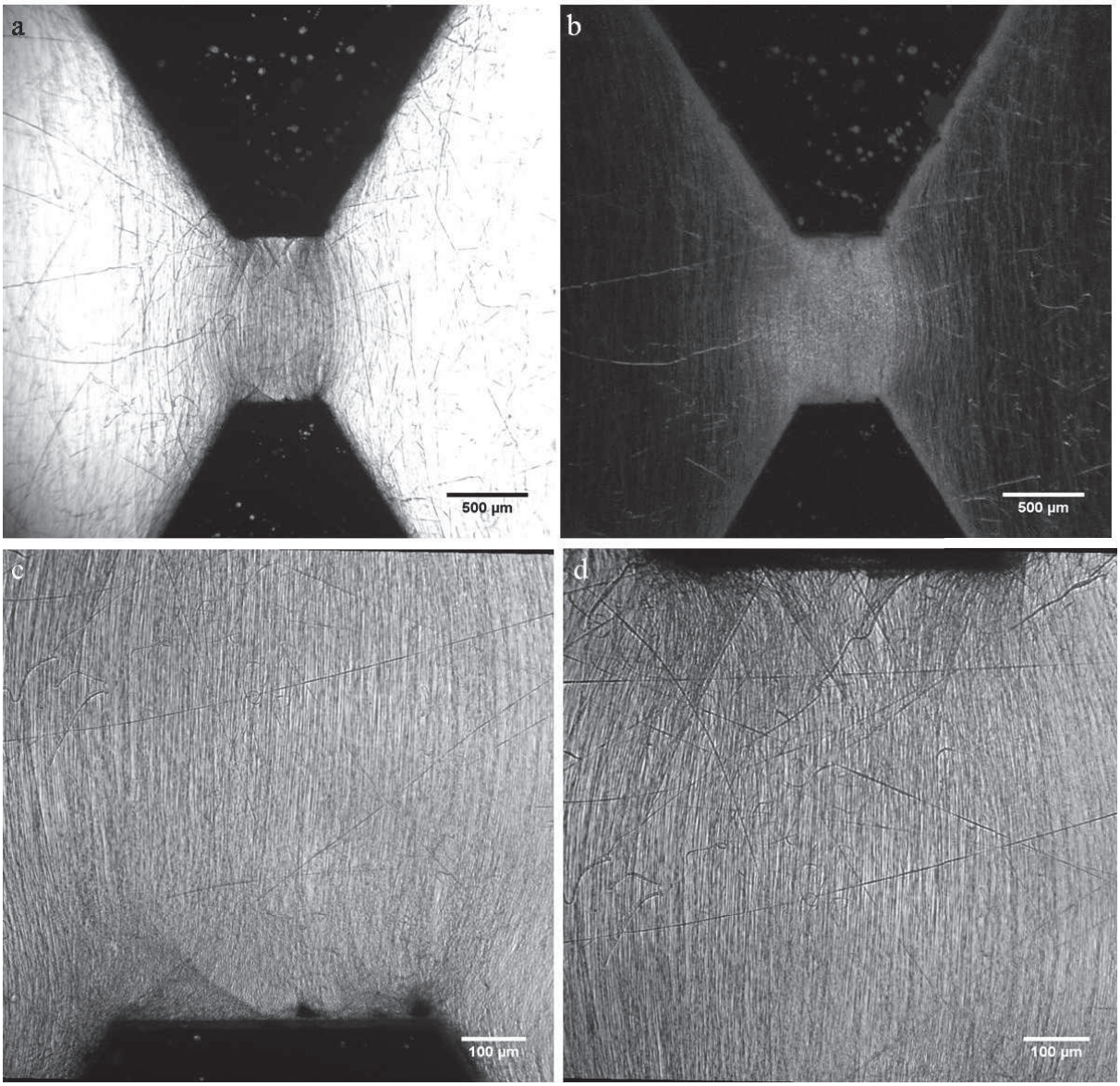

Figure 4.11 Microphotograph of PVDF-TrFE aligned between a pair of triangle shaped electrodes. (**a**) Observation using bright field. (**b**) Observation using dark field. (**c-d**) High magnification observations showing that nanofibers follows perfectly electric field lines.

In order to overcome this undesired effect, we then designed a pair of two rectangular electrodes with the same gap. The results are shown in **Fig. 4.12**. Now the area of well-aligned nanofibers can be sufficient large (1mm x 5mm). Thus, we achieved the deposition of uniaxally aligned PVDF-TrFE nanofibers on conventional glass substrates.

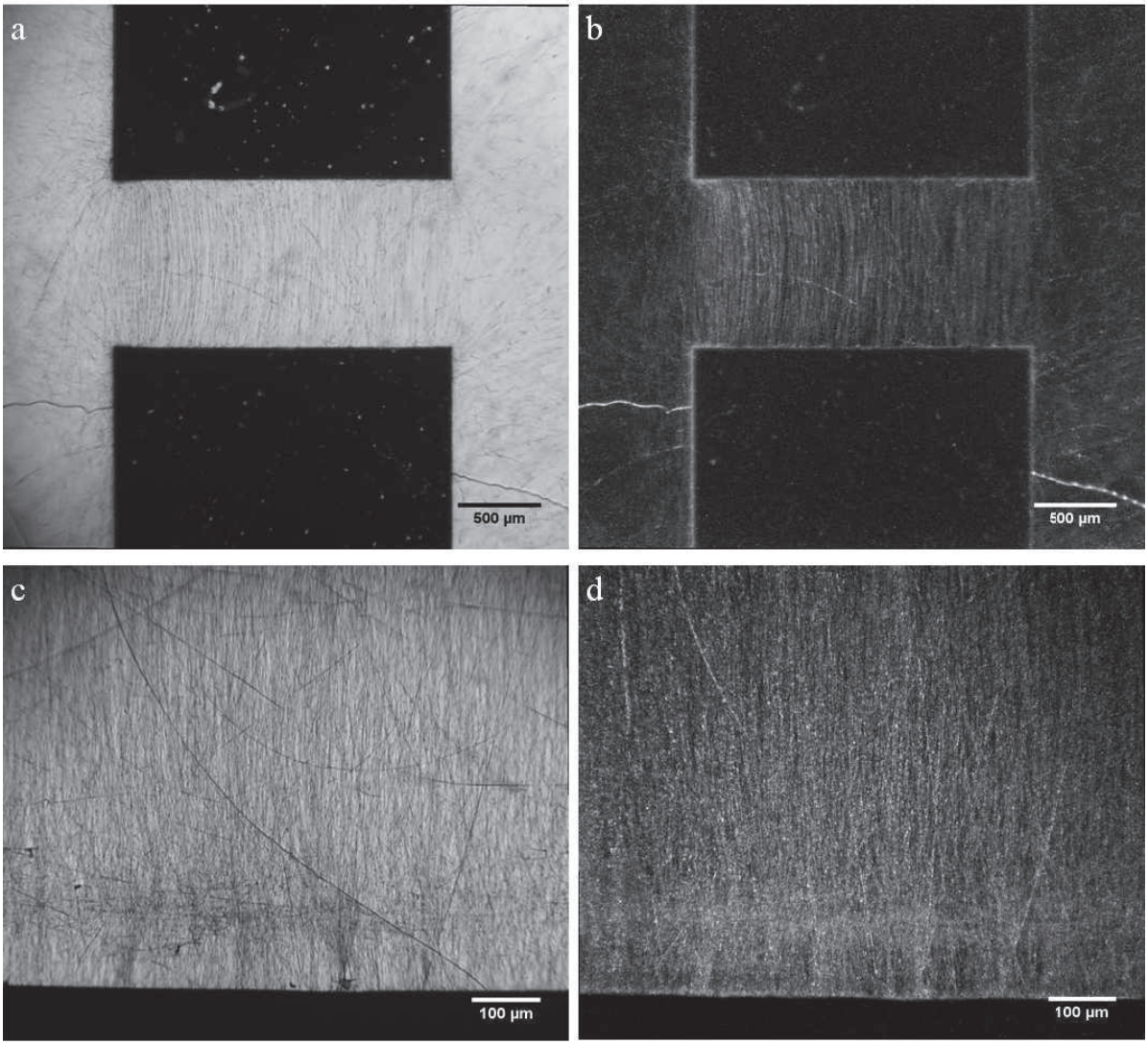

Figure 4.12 Microphotograph of PVDF-TrFE aligned between a pair of normal electrodes. (**a**) Observation using bright field. (**b**) Observation using dark field. (**c-d**) High magnification observations showing that nanofibers follows perfectly electric field lines.

By changing the electrode layout; we can control the deposition patterns of the nanofibers. After the optimization, we can now deposit the crisscrossed nanofibers based on the 4 electrodes configuration (**Fig 4.13b**). Since such types of electrodes can be easily produced on different substrates, this method should be easy and flexible for applications.

4.2 Characterization of nanofibers

Obviously, the density of the aligned nanofibers is electrospinning time dependent: Longer the electrospinning time, higher the nanofiber density. Moreover, the quality of the produced nanofibers might also be electrospinning time dependent. This can be seen by observation of PVDF-TrFE nanofibers obtained by 20 sec and 30 sec. electrospinning on glass (**Fig.4.14**). In the following, we compared their diameter, morphology and density in order to have a clear assessment,

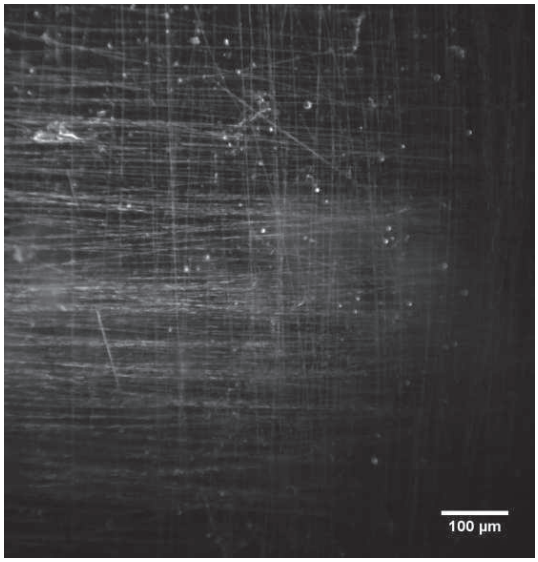

Figure 4.13 Microphotograph of crisscrossed PVDF-TrFE nanofibers obtained by using 2 pairs of electrodes grounded consecutively.

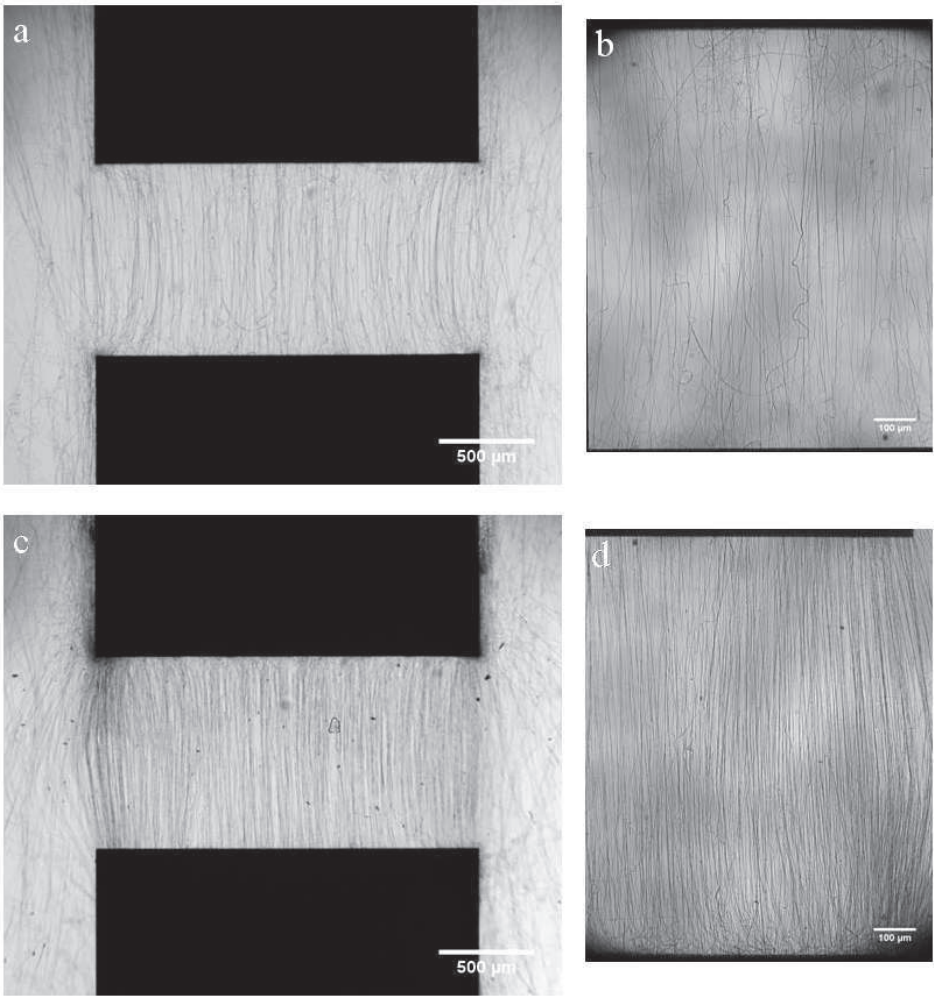

Figure 4.14 Microphotographs of aligned PVDF-TrFE nanofibers between electrodes with different electrospinning time: (**a-b**) 20 s, (**c-d**) 30 s.

4.2.1 Fiber alignment quantification

To characterize the performance of the fiber alignment, we adopted a method proposed by *Lee et al.* [**1**] and *Wang et al.* [**49**]. Samples were analyzed using SEM (Hitachi S-800). For each samples 3 SEM pictures were taken at the same magnification (600X, 150µm x 200 µm window). A line is drawn perpendicularly to the fibers direction. The angle (ø) between the fibers and this reference line were measured (**Fig 4.15**), which provides the absolute deviation value (ADV) of the measured angles from 90°.

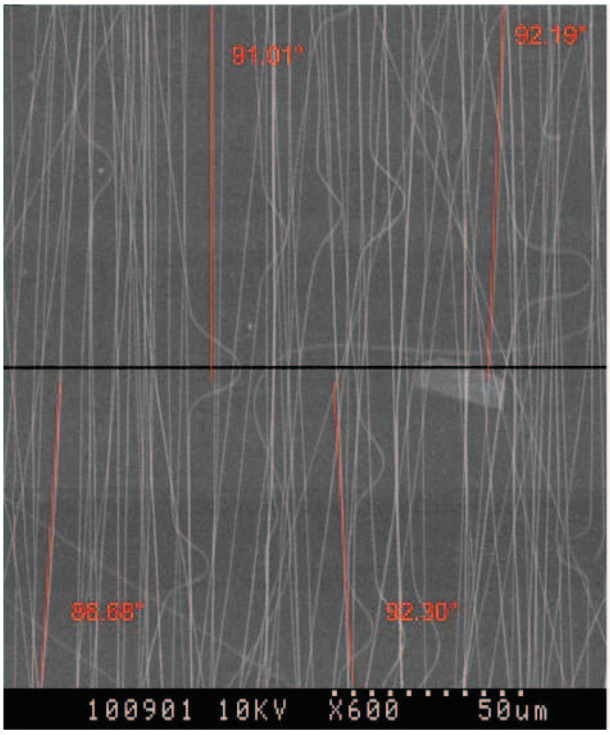

Figure 4.15 SEM picture of aligned PVDF-TrFE nanofibers for degree calculation of the fiber alignment.

For each picture 50 ADV measurement are made on 3 samples, giving a histogram of ADV distribution as shown in **Fig. 4.16**. Accordingly, we calculated the averaged absolute deviation (AAD) for each picture using:

$$AAD = \frac{\sum_{0}^{n} ADV}{n}$$

The percentage of alignments is then given by:

$$\%alignment = \frac{(90^\circ - AAD)}{90^\circ} \times 100$$

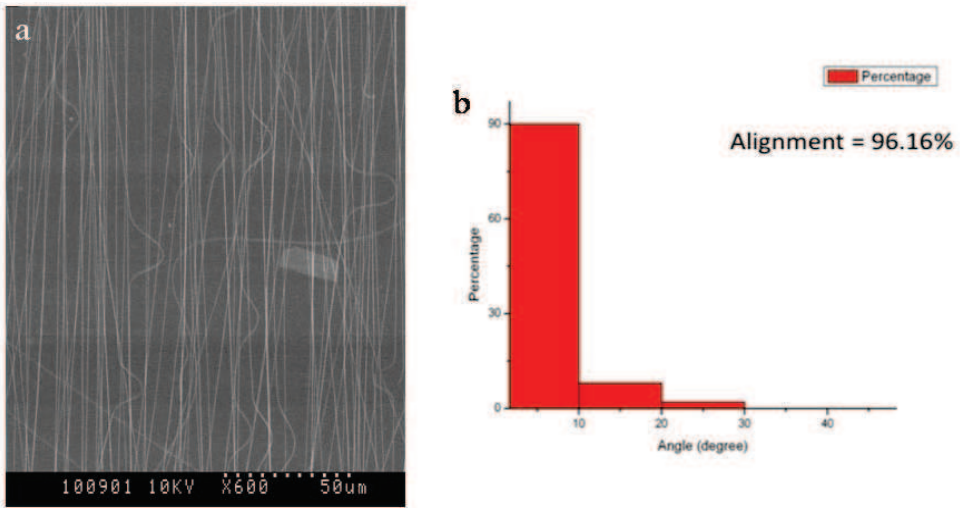

Figure 4.16 (**a**) SEM of aligned PVDF-TrFE nanofibers. (**b**) Diagram of alignment degrees.

4.2.2 Nanofibers morphology and diameter

The averaged diameter of the fibers was determined based on SEM pictures at the highest magnification. Based an analysis of 8 pictures on different samples, we deduced an averaged diameter of the fibers of 350 nm.

Figure 4.17 SEM image of PVDF-TrFE nanofibers for determination of the fibers diameters.

4.3 X-Ray diffraction measurements.

An X-Ray Diffractometer (Rigaku UltraX 18HF) has been used to determinate the crystal phase of the PVDF-TrFE nanofibers before and after annealing in order to characterize their piezoelectric properties. Annealing was performed at 135°C for 48 h, followed by ice quenching to fix crystalline phases of the polymer. As shown in **Fig. 4.18**, this annealing and quenching process is sufficiently efficient to enhance the crystalline phase of the nanofibers, where the peak at 19.75° is a characteristic of the piezoelectric β phase of the polymer. This result is significant to confirm the piezoelectric activity of the aligned PVDF-TrFE nanofibers.

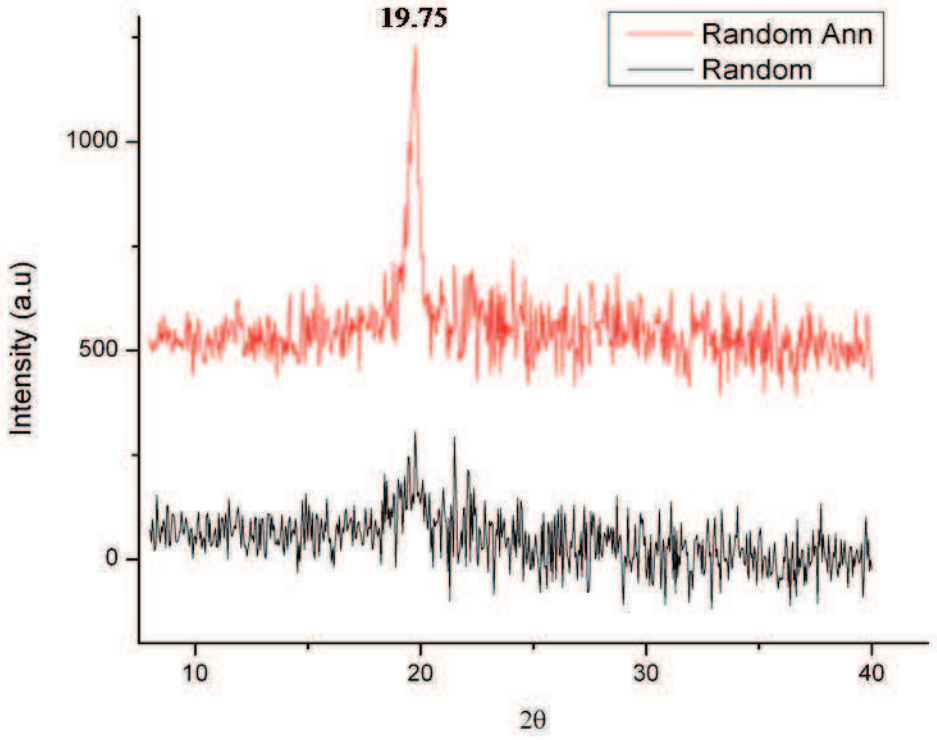

Figure 4.18 X-ray diffraction spectra of PVDf-TrFE nanofibers before (black) and after annealing (red).

4.4 Neuron culture

Neurons were isolated from E16 rat embryos. They were then cultured in an incubator at 37°C with 5 % CO2 in Dulbecco's-modified Eagle's medium (DMEM, Sigma, France) supplemented with 10 % FBS (Bioscience, France), 1 %L-glutamine, 1% Penicillin/Streptomycin (P/S) (Invitrogen, France).

Figure 4.19 shows phase contrast images of neurons after culture for 5 days on randomly deposited nanofibers with (**a,b**) or without (**c,d**) plasma treatment. As can be clearly seen, neurons cultured on nanofibers attached better on those with plasma treatment but they are not healthy on those without plasma treatment. In the former case, neural networks were well formed. In the latter case, their somas are not attached on the nanofibers and accordingly, their neuritis (axons or dendrites) are not well developed.

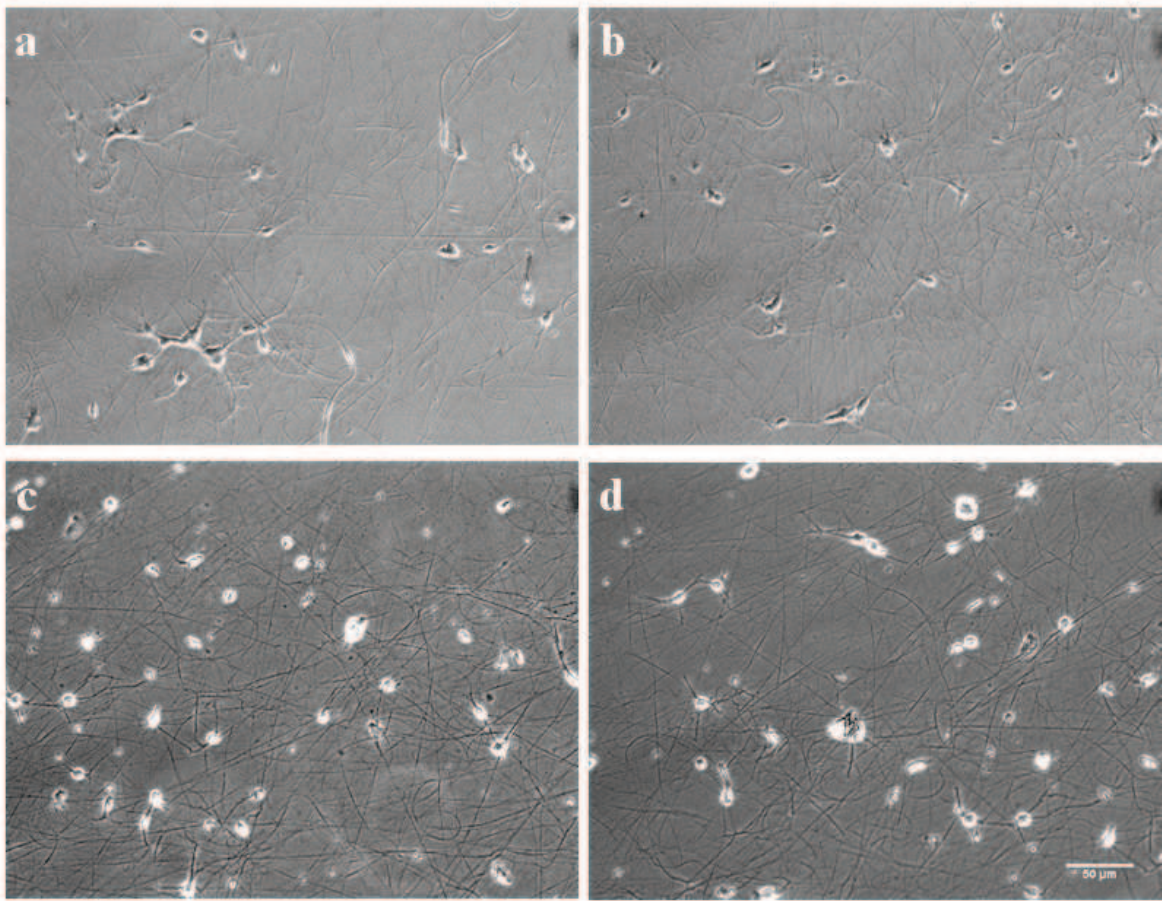

Figure 4.19 Neurons cultured on random electrospun PVDf-TrFE nanofibers with (**a-b**) and without (**c-d**) plasma treatment.

On aligned nanofibers, however, the influence of the surface treatment appears to be less important since neurons are attached and neural networks are clearly formed on both samples with **(Fig. 4.20)** or without **(Fig. 4.21)** plasma treatment. In addition, the outgrowth of neurites was remarkably influenced by the alignment of the nanofibers as the most of the dendrites follow the alignment direction of the fibers.

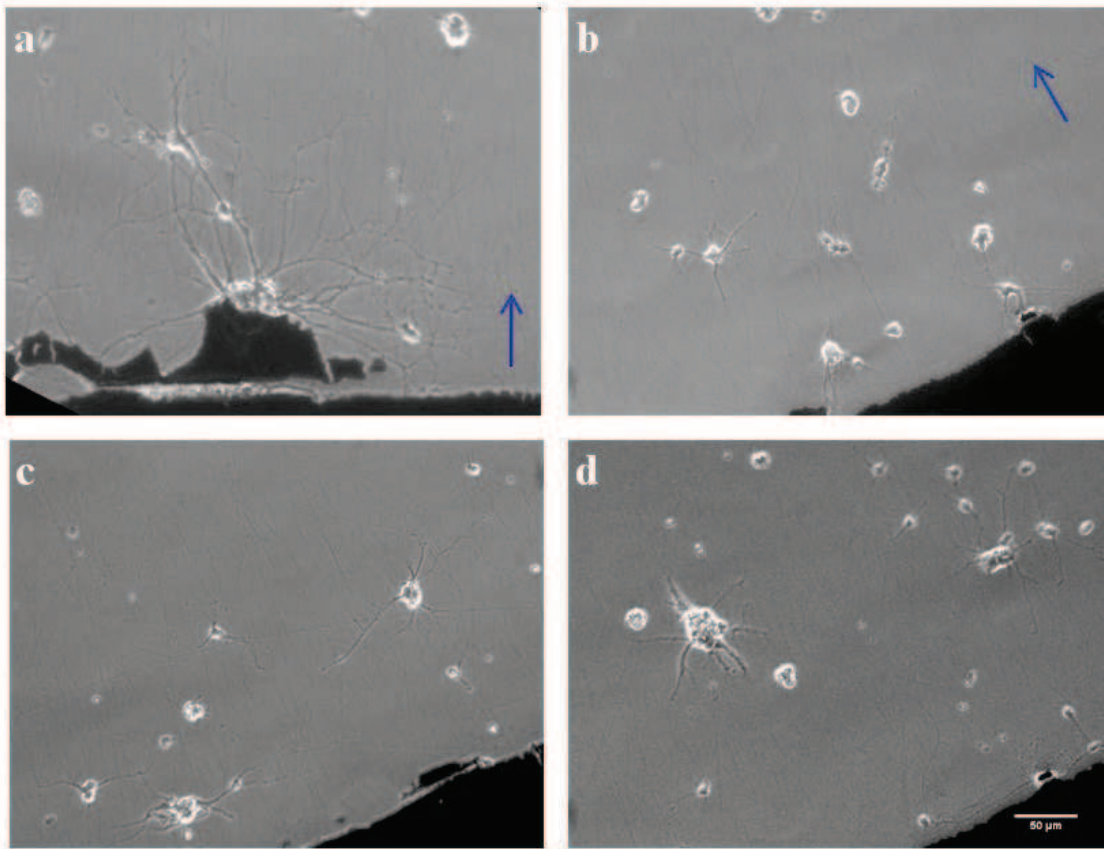

Figure 4.20 Neurons cultured on aligned PVDf-TrFE nanofibers after plasma treatment. The blue arrows indicate the nanofibers direction.

Figures 4.22 and **4.23** show more specifically the effect of aligned nanofibers on neurites orientation. Noticeably, even if the soma of a neuron is not polarized parallel to the nanofibers underneath, their neurites are guided by the aligned fibers (**Fig. 4.22b**). Moreover, the aligned nanofibers supported a better outgrowth of neurites and a better network formation compared to the one cultured on random nanofibers.

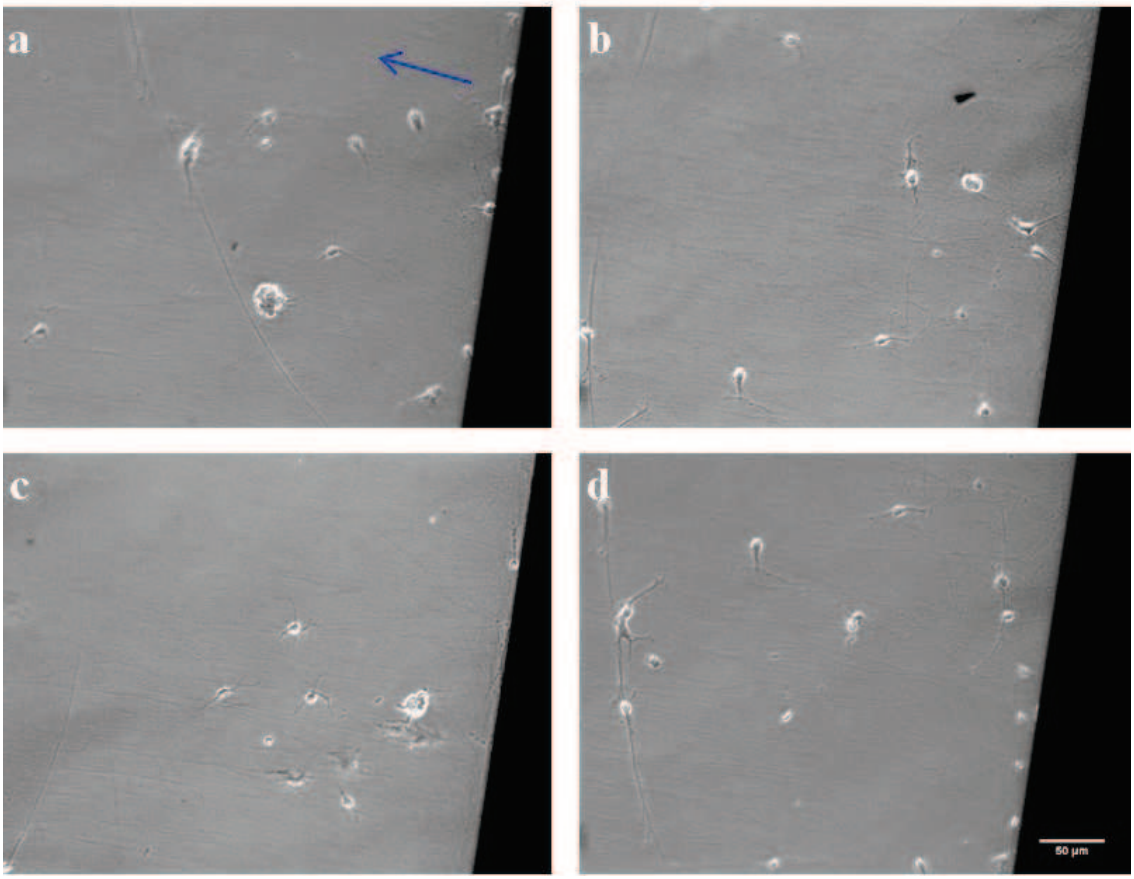

Figure 4.21 Neurons cultured on aligned PVDf-TrFE nanofibers without plasma treatment. The blue arrows indicate the nanofibers direction.

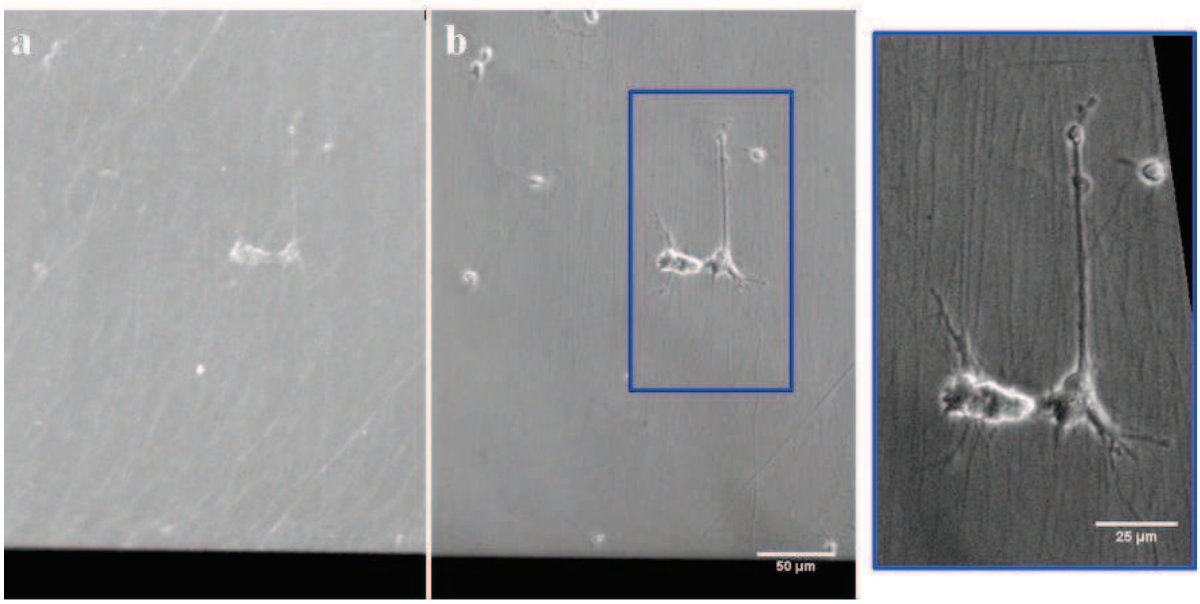

Figure 4.22 Neurons cultured on aligned PVDF-TrFE nanofibers without plasma treatment. (**a**) Focus is made on the nanofibers. (**b**) Focus is made on the neurons. (**c**) Detail of the neurons.

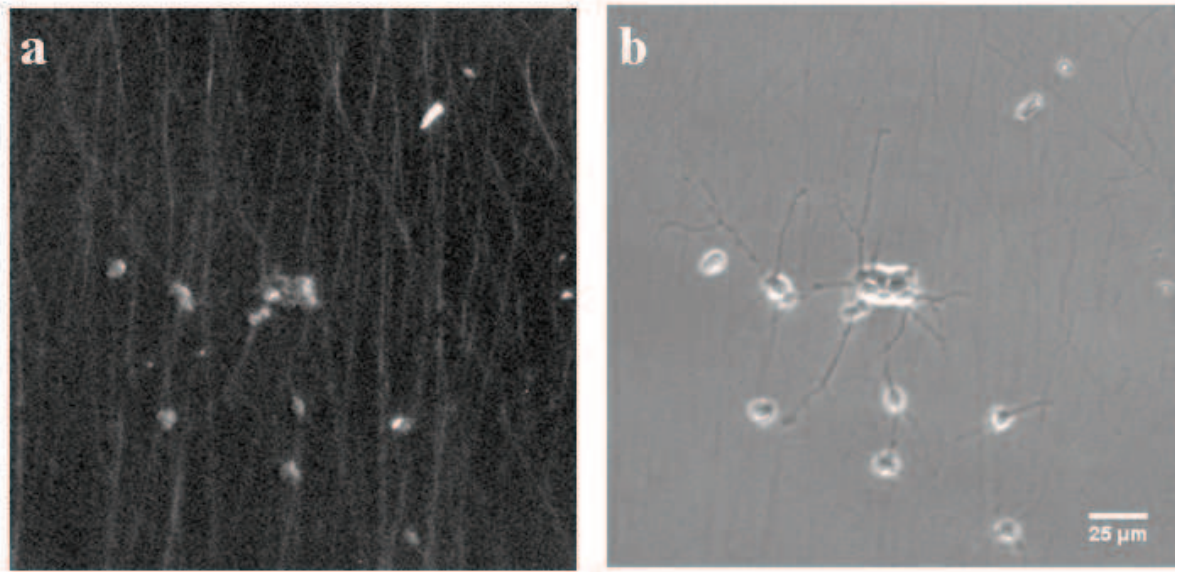

Figure 4.23 Neurons cultured on aligned PVDf-TrFE nanofibers after plasma treatment. (**a**) Focus is made on the nanofibers (**b**) Focus is made on the neurons.

4.5 Conclusion

We have developed a reliable fabrication technology to produce aligned PVDF-TrFE nanofibers on patterned electrodes. These fibers showed a conserved piezoelectric crystalline phase and a high degree of alignment (>90%). The fabricated nanofibers could then be tested for neuron culture with and without plasma surface treatment. As expected, the neurons cultured on aligned and plasma treated nanofibers showed an enhanced outgrowth of neurites comparing on that on random nanofibers or aligned fibers without plasma treatment.

References

[1] Lee, Y.-S., Collins, G., & Livingston Arinzeh, T. (2011). Neurite extension of primary neurons on electrospun piezoelectric scaffolds. Acta biomaterialia, 7(11), 3877–86. doi:10.1016/j.actbio.2011.07.013

[2] Xie, J., Willerth, S. M., Li, X., Macewan, M. R., Rader, A., Sakiyama-Elbert, S. E., & Xia, Y. (2009). The differentiation of embryonic stem cells seeded on electrospun nanofibers into neural lineages. Biomaterials, 30(3), 354–62. doi:10.1016/j.biomaterials.2008.09.046

[3] Lee, J. Y., Bashur, C. A., Goldstein, A. S., & Schmidt, C. E. (2009). Polypyrrole-coated electrospun PLGA nanofibers for neural tissue applications. *Biomaterials*, *30*(26), 4325–35.

[4] Xie, J., Macewan, M. R., Willerth, S. M., Li, X., Moran, D. W., Sakiyama-Elbert, S. E., & Xia, Y. (2009). Conductive Core-Sheath Nanofibers and Their Potential Application in Neural Tissue Engineering. *Advanced functional materials*, *19*(14), 2312–2318. doi:10.1002/adfm.200801904

[5] Li, W., Guo, Y., Wang, H., Shi, D., Liang, C., Ye, Z., Qing, F., et al. (2008). Electrospun nanofibers immobilized with collagen for neural stem cells culture. *Journal of materials science. Materials in medicine*, *19*(2), 847–54. doi:10.1007/s10856-007-3087-5

[6] Gerardo-Nava, J., Führmann, T., Klinkhammer, K., Seiler, N., Mey, J., Klee, D., Möller, M., et al. (2009). Human neural cell interactions with orientated electrospun nanofibers in vitro. *Nanomedicine (London, England)*, *4*(1), 11–30. doi:10.2217/17435889.4.1.11

[7] Liu, T., Teng, W. K., Chan, B. P., & Chew, S. Y. (2010). Photochemical crosslinked electrospun collagen nanofibers: synthesis, characterization and neural stem cell interactions. *Journal of biomedical materials research. Part A*, *95*(1), 276–82. doi:10.1002/jbm.a.32831

[8] Lam, H. J., Patel, S., Wang, A., Chu, J., & Li, S. (2010). In vitro regulation of neural differentiation and axon growth by growth factors and bioactive nanofibers. *Tissue engineering. Part A*, *16*(8), 2641–8. doi:10.1089/ten.TEA.2009.0414

[9] Wang, Y., Yao, M., Zhou, J., Zheng, W., Zhou, C., Dong, D., Liu, Y., et al. (2011). The promotion of neural progenitor cells proliferation by aligned and randomly oriented collagen nanofibers through β1 integrin/MAPK signaling pathway. *Biomaterials*, *32*(28), 6737–44. doi:10.1016/j.biomaterials.2011.05.075

[10] Subramanian, A., Krishnan, U. M., & Sethuraman, S. (2012). Axially aligned electrically conducting biodegradable nanofibers for neural regeneration. *Journal of materials science. Materials in medicine*, *23*(7), 1797–809. doi:10.1007/s10856-012-4654-y

[11] Gertz, C. C., Leach, M. K., Birrell, L. K., Martin, D. C., Feldman, E. L., & Corey, J. M. (2010). Accelerated neuritogenesis and maturation of primary spinal motor neurons in response to nanofibers. *Developmental neurobiology*, *70*(8), 589–603. doi:10.1002/dneu.20792

[12] Schnell, E., Klinkhammer, K., Balzer, S., Brook, G., Klee, D., Dalton, P., & Mey, J. (2007). Guidance of glial cell migration and axonal growth on electrospun nanofibers of poly-epsilon-caprolactone and a collagen/poly-epsilon-caprolactone blend. *Biomaterials*, *28*(19), 3012–25. doi:10.1016/j.biomaterials.2007.03.009

[13] http://en.wikipedia.org/wiki/Electrospinning

[14] http://www.nano109.com/arge.php?argecategoryId=47&argeId=166

[15] Boland, E., Wnek, G., Simpson, D., Pawlowski, K., & Bowlin, G. (2001). Tailoring tissue engineering scaffolds using electrostatic processing techniques: A study of poly(glycolic acid) electrospinning. *Journal of Macromolecular Science, Part A*, *38*(12), 1231–1243. doi:10.1081/MA-100108380

[16] Matthews, J. A., Wnek, G. E., Simpson, D. G., & Bowlin, G. L. (2002). Electrospinning of Collagen Nanofibers. *Biomacromolecules*, *3*(2), 232–238. doi:10.1021/bm015533u

[17] Katta, P., Alessandro, M., Ramsier, R. D., & Chase, G. G. (2004). Continuous Electrospinning of Aligned Polymer Nanofibers onto a Wire Drum Collector. *Nano Letters*, *4*(11), 2215–2218. doi:10.1021/nl0486158

[18] Sundaray, B., Subramanian, V., Natarajan, T. S., Xiang, R.-Z., Chang, C.-C., & Fann, W.-S. (2004). Electrospinning of continuous aligned polymer fibers. *Applied Physics Letters*, *84*(7), 1222. doi:10.1063/1.1647685

[19] SHIN, M., KIM, Y., KIM, S., LEE, H., & SPINKS, G. (2008). Enhanced conductivity of aligned PANi/PEO/MWNT nanofibers by electrospinning. *Sensors and Actuators B: Chemical*, *134*(1), 122–126. doi:10.1016/j.snb.2008.04.021

[20] Meng, Z. X., Wang, Y. S., Ma, C., Zheng, W., Li, L., & Zheng, Y. F. (2010). Electrospinning of PLGA/gelatin randomly-oriented and aligned nanofibers as potential scaffold in tissue engineering. *Materials Science and Engineering: C*, *30*(8), 1204–1210. doi:10.1016/j.msec.2010.06.018

[21] Hou, H., Ge, J. J., Zeng, J., Li, Q., Reneker, D. H., Greiner, A., & Cheng, S. Z. D. (2005). Electrospun Polyacrylonitrile Nanofibers Containing a High Concentration of Well-Aligned Multiwall Carbon Nanotubes. *Chemistry of Materials*, *17*(5), 967–973. doi:10.1021/cm0484955

[22] Tian, F., Hosseinkhani, H., Hosseinkhani, M., Khademhosseini, A., Yokoyama, Y., Estrada, G. G., & Kobayashi, H. (2008). Quantitative analysis of cell adhesion on aligned micro- and nanofibers. *Journal of biomedical materials research. Part A*, *84*(2), 291–9. doi:10.1002/jbm.a.31304

[23] Wang, C.-Y., Zhang, K.-H., Fan, C.-Y., Mo, X.-M., Ruan, H.-J., & Li, F.-F. (2011). Aligned natural-synthetic polyblend nanofibers for peripheral nerve regeneration. *Acta biomaterialia*, *7*(2), 634–43. doi:10.1016/j.actbio.2010.09.011

[24] Wan, L.-S., & Xu, Z.-K. (2009). Polymer surfaces structured with random or aligned electrospun nanofibers to promote the adhesion of blood platelets. *Journal of biomedical materials research. Part A*, *89*(1), 168–75. doi:10.1002/jbm.a.31907

[25] Wang, Y.-Y., Lü, L.-X., Feng, Z.-Q., Xiao, Z.-D., & Huang, N.-P. (2010). Cellular compatibility of RGD-modified chitosan nanofibers with aligned or random orientation. *Biomedical materials (Bristol, England)*, *5*(5), 054112. doi:10.1088/1748-6041/5/5/054112

[26] Ramakrishna, Seeram Fujihara, K., Teo, W.-E., Lim, T.-C., & Ma, Z. (2005). *An Introduction to Electrospinning and Nanofibers*. World Scientific Publishing.

[27] Li, D., Wang, Y., & Xia, Y. (2003). Electrospinning of Polymeric and Ceramic Nanofibers as Uniaxially Aligned Arrays. *Nano Letters*, *3*(8), 1167–1171. doi:10.1021/nl034425

[28] Li, D., Wang, Y., & Xia, Y. (2004). Electrospinning Nanofibers as Uniaxially Aligned Arrays and Layer-by-Layer Stacked Films. *Advanced Materials*, *16*(4), 361-366. doi:10.1002/adma.200306226

[29] Dersch, R., Liu, T., Schaper, A. K., Greiner, A., & Wendorff, J. H. (2002). Electrospun Nanofibers: Internal Structure and Intrinsic Orientation. *JOURNAL OF POLYMER SCIENCE PART A-POLYMER CHEMISTRY*, *41*(4), 545–553.

[30] Yu, J., Qiu, Y., Zha, X., Yu, M., Yu, J., Rafique, J., & Yin, J. (2008). Production of aligned helical polymer nanofibers by electrospinning. *European Polymer Journal*, *44*(9), 2838–2844. doi:10.1016/j.eurpolymj.2008.05.020

[31] Xin, Y., Huang, Z., Chen, J., Wang, C., Tong, Y., & Liu, S. (2008). Fabrication of well-aligned PPV/PVP nanofibers by electrospinning. *Materials Letters*, *62*(6-7), 991–993. doi:10.1016/j.matlet.2007.07.031

[32] Xie, J., Macewan, M. R., Ray, W. Z., Liu, W., Siewe, D. Y., & Xia, Y. (2010). Radially aligned, electrospun nanofibers as dural substitutes for wound closure and tissue regeneration applications. *ACS nano*, *4*(9), 5027–36. doi:10.1021/nn101554u

[33] Cooper, A., Jana, S., Bhattarai, N., & Zhang, M. (2010). Aligned chitosan-based nanofibers for enhanced myogenesis. *Journal of Materials Chemistry*, *20*(40), 8904. doi:10.1039/c0jm01841d

[34] Kameoka, J., Orth, R., Yang, Y., Czaplewski, D., Mathers, R., Coates, G. W., & Craighead, H. G. (2003). A scanning tip electrospinning source for deposition of oriented nanofibres. *Nanotechnology*, *14*(10), 1124

[35] Sun, D., Chang, C., Li, S., & Lin, L. (2006). Near-field electrospinning. *Nano letters*, *6*(4), 839–42. doi:10.1021/nl0602701

[36] Chang, C., Tran, V. H., Wang, J., Fuh, Y.-K., & Lin, L. (2010). Direct-write piezoelectric polymeric nanogenerator with high energy conversion efficiency. *Nano letters*, *10*(2), 726-31. doi:10.1021/nl9040719

[37] Chang, J., Dommer, M., Chang, C., & Lin, L. (2012). Piezoelectric nanofibers for energy scavenging applications. *Nano Energy*, *1*(3), 356-371. Elsevier. doi:10.1016/j.nanoen.2012.02.003

[38] Zhou, Z., Lai, C., Zhang, L., Qian, Y., Hou, H., Reneker, D. H., & Fong, H. (2009). Development of carbon nanofibers from aligned electrospun polyacrylonitrile nanofiber bundles and characterization of their microstructural, electrical, and mechanical properties. *Polymer*, *50*(13), 2999–3006. doi:10.1016/j.polymer.2009.04.058

[39] Feng, Z.-Q., Chu, X.-H., Huang, N.-P., Leach, M. K., Wang, G., Wang, Y.-C., Ding, Y.-T., et al. (2010). Rat hepatocyte aggregate formation on discrete aligned nanofibers of type-I collagen-coated poly(L-lactic acid). *Biomaterials*, *31*(13), 3604–12. doi:10.1016/j.biomaterials.2010.01.080

[40] Corey, J. M., Gertz, C. C., Wang, B.-S., Birrell, L. K., Johnson, S. L., Martin, D. C., & Feldman, E. L. (2008). The design of electrospun PLLA nanofiber scaffolds compatible with serum-free growth of primary motor and sensory neurons. *Acta biomaterialia*, *4*(4), 863–75. doi:10.1016/j.actbio.2008.02.020

[41] Lu, H., Feng, Z., Gu, Z., & Liu, C. (2009). Growth of outgrowth endothelial cells on aligned PLLA nanofibrous scaffolds. *Journal of materials science. Materials in medicine*, *20*(9), 1937–44. doi:10.1007/s10856-009-3744-y

[42] Ma, J., He, X., & Jabbari, E. (2011). Osteogenic differentiation of marrow stromal cells on random and aligned electrospun poly(L-lactide) nanofibers. *Annals of biomedical engineering*, *39*(1), 14–25. doi:10.1007/s10439-010-0106-3

[43] Feng, Z.-Q., Lu, H.-J., Leach, M. K., Huang, N.-P., Wang, Y.-C., Liu, C.-J., & Gu, Z.-Z. (2010). The influence of type-I collagen-coated PLLA aligned nanofibers on growth of blood outgrowth endothelial cells. *Biomedical materials (Bristol, England)*, *5*(6), 065011. doi:10.1088/1748-6041/5/6/065011

[44] Theron, A., Zussman, E., & Yarin, A. L. (2001). Electrostatic field-assisted alignment of electrospun nanofibres. *Nanotechnology*, *12*(3), 384–390. doi:10.1088/0957-4484/12/3/329

[45] Teo, W. E., Kotaki, M., Mo, X. M., & Ramakrishna, S. (2005). Porous tubular structures with controlled fibre orientation using a modified electrospinning method. *Nanotechnology*, *16*(6), 918–924. doi:10.1088/0957-4484/16/6/049

[46] Wang, H., Tang, H., He, J., & Wang, Q. (2009). Fabrication of aligned ferrite nanofibers by magnetic-field-assisted electrospinning coupled with oxygen plasma treatment. *Materials Research Bulletin*, *44*(8), 1676–1680. doi:10.1016/j.materresbull.2009.04.006

[47] Liu, Y., Zhang, X., Xia, Y., & Yang, H. (2010). Magnetic-field-assisted electrospinning of aligned straight and wavy polymeric nanofibers. *Advanced materials (Deerfield Beach, Fla.)*, *22*(22), 2454–7. doi:10.1002/adma.200903870

[48] Yang, D., Zhang, J., Zhang, J., & Nie, J. (2008). Aligned electrospun nanofibers induced by magnetic field. *Journal of Applied Polymer Science*, *110*(6), 3368–3372. doi:10.1002/app.28896

[49] Wang, H. B., Mullins, M. E., Cregg, J. M., Hurtado, A., Oudega, M., Trombley, M. T., & Gilbert, R. J. (2009). Creation of highly aligned electrospun poly-L-lactic acid fibers for nerve regeneration applications. *Journal of neural engineering*, *6*(1), 016001. doi:10.1088/1741-2560/6/1/016001

CHAPTER 5

Nanofibers doped with magnetic nanoparticles for remote activation

In this chapter, we study the feasibility of nanofiber inclusion of magnetic nanoparticles for remote activation. Fe_3O_4 magnetic nanoparticles have been used for inclusion into PVDF-TrFE nanofibers. Our results show that the incorporated nanoparticles are homogenously dispersed in to the fibers and that the piezoelectric crystalline phase of PVDF-TrFE nanofibers remains after the nanoparticles inclusion. We also investigated the cell culture compatibility of nanoparticles doped fibers, showing the request bio-compatibility.

5.1 Introduction

PVDF and PVDF-TrFE are both piezoelectric [**1-13]**, ferroelectric [**14-23**] and pyroelectric [**24-31**] materials. As shown in previous chapters, they can be shaped in different forms by using lithography techniques. They can also be used for electrospinning of nanofibers. In addition, surface treatments can be used to modify the physicochemical properties of the surfaces of the polymers. PVDF and PVDF-TrFE have been blended with other polymers in order to give new properties. For example the blend PVDF/PMMA is used to give better mechanical properties to PVDF as it decreases surface roughness and increase hydrophilicity **[37-37]**. However the piezoelectric and ferroelectric properties of PVDF will be reduced by this blend [**38-39**].

Doping of functional materials in PVDF and PVDF-TrFE follow the same principle as the PVDF blend but the goal is to incorporate only a few portion of a new component into PVDF to enhance its properties, in the form of ceramics, chemicals and nanoparticles. PVDF is also often doped with nano-sized ceramic in nanocomposite to enhance its dielectric properties [**40-47**], for use as electrolyte. Chemical doping has been used to enhance piezoelectric [**48-49**] and conductive [**50-51**] properties of PVDF. Nanoparticles doping has been used for a wide range of applications. Nanoparticles are generally integrated in the PVDF solution which is electrospun to make nanofibers. We can quote as examples SiO2 nanoparticles doping to make PVDF electrospun membranes superhydrophobic [**52**], Silver nanoparticles doping to make antibacterial membranes [**53**] and nanofibers doped with nickel nanoparticles for the production of hydrogen [**54**]. Some studies used nanoparticles doping to provoke crystalline phase change in order to enhance piezoelectric properties of the resulting nanofibers [**55-59**]. Magnetic nanoparticles have been incorporated in PVDF and PVDF-TrFE only in forms of nanocomposite for dielectric purposes [**60-64**].

One of the possibilities is doping super-paramagnetic nanoparticles such as Fe_2O_3 in PVDF-TrFE. When a crystalline phase of the polymer is turned on, it should be possible to use a magnetic field to bend the aligned and suspended nanofibers so that piezoelectric responses of the fibers should be measurable.

Historically, iron oxides coated with a polymer (dextran) have been used since 1960's to treat iron anemias [**65**]. Due to their large sizes, these particles were only paramagnetic (weakly sensitive to magnetic fields). Chemists then used the affinity of iron oxide with dextran to make iron oxide nanoparticles in order to enhance the efficiency of the anemia treatment (dextran magnetite). These nanoparticles are now super-paramagnetic (SPM) as they are highly sensitive to magnetic fields. *Ogushi* [**66**] discovered that due to their super-paramagnetic properties, polymer-coated iron oxide nanoparticles can be used as a magnetic resonance imaging (MRI) contrast agent. Indeed, the super-paramagnetic iron oxide nanoparticles (SPION) have been used for this purpose until recently. They were thought to be safe as SPION can be degraded very fast by macrophages but the bio-toxicity of SPION is still a debating subject [**67-69**].

The extremely small size (10 – 100 nm) of SPIONs coupled with the possibility to manipulate them remotely by applying an external magnetic field gradient makes SPION very promising for nano-medicine and biomedical applications [**70-75**]. Indeed, the possibility to adapt their size to their target (e.g. genes 2 nm) and the possibility to functionalize their surface with a wide range of molecules open the way to targeted drug delivery [**76-78**]. Principal biomedical applications of SPIONs are: cell sorting and separation [**79-80**], drug delivery [**81-90**] and hyperthermia based cancer treatments **[91-96**]. For example, magnetic nanoparticles have also been used for doping of nanofibers which could then be used for a controlled movement of neurons in culture [**97**] and for remote control of ion channels and neurons [**98**]. It has also been demonstrated that magnetic nanoparticles can induce osteo-regeneration or release growth factors. For this purpose, they can be used in design and fabrication of scaffolds in tissue engineering [**99-103**].

5.2 Fabrication of PVDF-TrFE nanofibers

5.2.1 Synthesis of Fe_3O_4 Nanoparticles

We used the protocol developed by Liu J. in our ENS laboratory [**104**] which allows easy synthesizing of Fe_3O_4 magnetic nanoparticles. Iron (II) and iron (III) were co-precipitated in alkaline solution. In atypical experimental procedure, 2.7 g of $FeCl_3$ and 1.39 g of $FeSO_4$ powder were added into 100 mL of water and mixed until homogeneous under N_2 protection. Then the solution was heated to 80◦C, followed by adding 12 mL of 25% (w/w) NH3·H2O quickly with strong magnetic stirring. The solution color changed from orange to black, leading to a black precipitate. After 5 min stirring, 2 mL of oleic acid was added until the magnetic nanoparticles aggregated together. To remove the excess oleic acid, the aggregate was rinsed several times with ethanol under an external magnetic field. The nanoparticles were dried under a vacuum pump for usage. Nanoparticles produced using this process have a size of 15 nm.

5.2.2 Preparation of PVDF-TrFE/Fe_3O_4 solution

18% (w/w) PVDF-TrFE solution was prepared by dissolving 0.9 g of PDVF-TrFE powder (Piezotech, France) in 5g of DMF (Sigma-Aldrich, France). After mixing the solution overnight at 70°C, 25 mg of Fe_20_3 nanoparticles were incorporated. Solution was then heated at 70°C to reduce its viscosity and improve the nanoparticles incorporation, followed by mixing with a vortex agitator for 10 rounds of 30 sec.

5.2.3 Electrospinning of Fe_2O_3 nanoparticles containing FVDF-TrFE nanofibers

Electrospinning was carried out using the standard far field electrospinning method: Solution was loaded into a 1 ml syringe; the needle of the syringe is connected to a high voltage generator (positive terminal); a glass slide is used as collector with a grounded crocodile clip. The distance between the needle and the collector is 5 cm for an applied voltage of 10 kV. The syringe pump was set up to deliver the solution at a rate of 1ml/h. The same setup was used to produce random nanofibers of PVDF-TrFE with or without magnetic particles.

Figure 5.1 shows images of magnetic particle containing PVDF-TrFE nanofibers. Overall, we observe rather general nanofiber morphology with no beading but some

aggregates due to the presence of magnetic nanoparticles (a). The higher resolution images show that the inclusion of the magnetic nanoparticles into the fibers is efficient (b, d). Some fibers trend to break into short segment (c) but no deformation is observed.

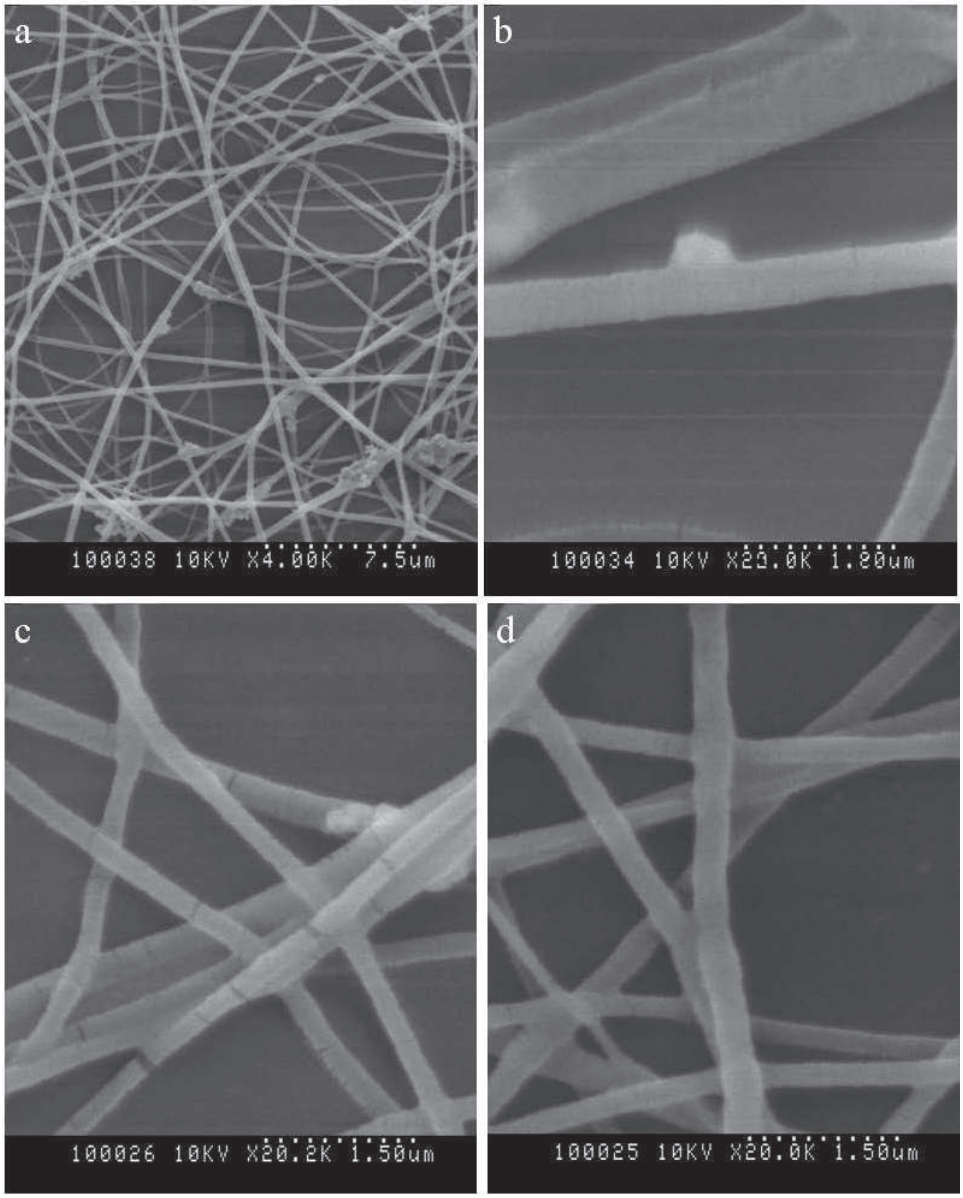

Figure 5.1 SEM images of electrospun PVDF-TrFE nanofibers containing Fe_3O_4 nanoparticles.

The average size of Fe_3O_4 nanoparticles we used is about 15 nm which makes it difficult to observe them clearly by SEM. However, when compared with PVDF-TrFE nanofibers without magnetic particle inclusion, the doping induced morphologic change of the fibers can be clearly seen (Fig. 5.2). Indeed, that the surface of PVDF-TrFE fibers without NPs is smoother than those with NPs. In contrast, some of the NPs containing nanofibers tread to break into short segments, as mentioned above (**Fig 5.2a**).

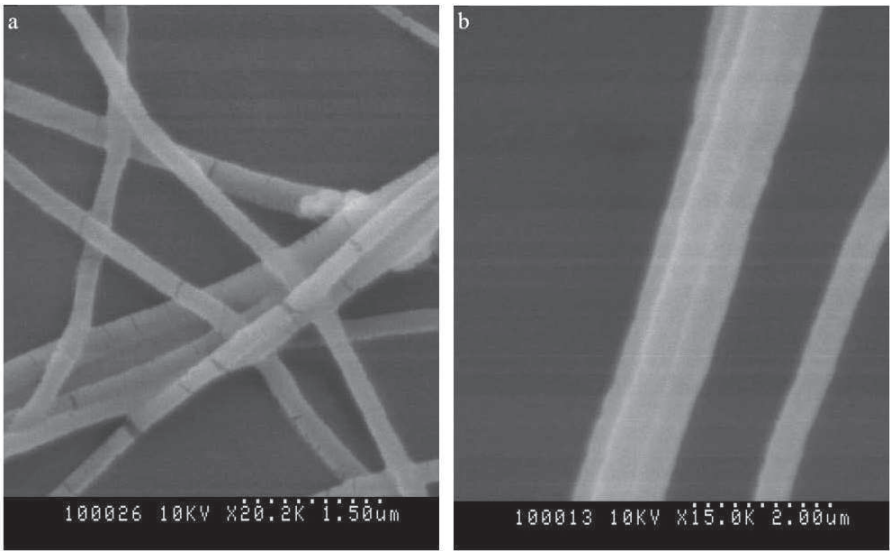

Figure 5.2 SEM images of electrospun PVDF-TrFE nanofibers with (**a**) or without (**b**) doping of Fe_3O_4 nanoparticles.

The mean diameter of the nanofibers was determined by using 8 SEM images at high magnification (>10k) and 7 measurements were performed for each of the images. Data were then analyzed using share-soft ImageJ and Origin 8, resulting in a mean diameter of 288 nm, which is comparable to that obtained by electrospinning of PVDF-TrFE nanofibers without magnetic particle containing (**Fig 5.3**).

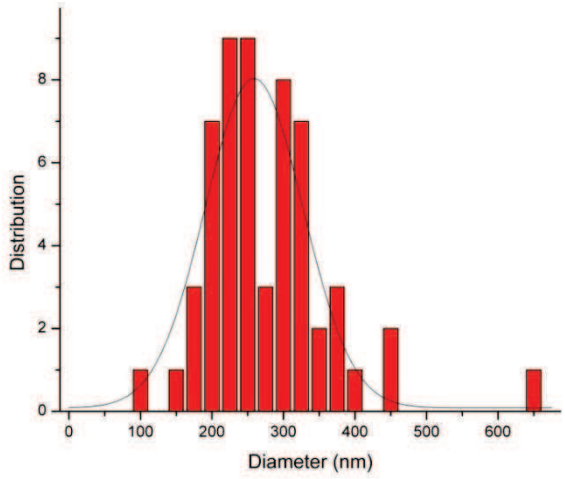

Figure 5.3 Diameter distribution of electrospun PVDf-TrFE /Fe3O4 nanofibers.

5.2.4 Annealing of the nanofibers

In order to reinforce their piezoelectric activity of the nanofibers, all fibers were annealed at 130°C 96 hours After annealing, the fibers were quenched in ice water to obtain the desired crystalline phases of the processed materials.

5.3 Characterization of the piezoelectric property of the fibers

5.3.1 XRD measurements

We used X-ray diffractometer (Rigaku ultraX 18) to characterize the crystalline phases of Fe_2O_3 nanoparticles containing PVDF-TrFE nanofibers. It is known that PVDF-TrFE has 3 major crystalline phases, i.e. α, β and γ phases, in which the β phase should have the highest piezoelectric activity. Without going into detail, we compared the results of nanofibers obtained using different parameters, i.e., random and aligned nanofibers with or without annealing (**Fig. 5.4**).

Figure 5.4 shows a comparison of the XRD spectra of the nanofibers with and without annealing. In both cases, the XRD peak is centered on 20°, indicating a piezoelectric β phase of PVDF-TrFE nanofibers. As expected, the amplitude of the XRD peak much increased after annealing due to the enhancement of the crystalline β phase.

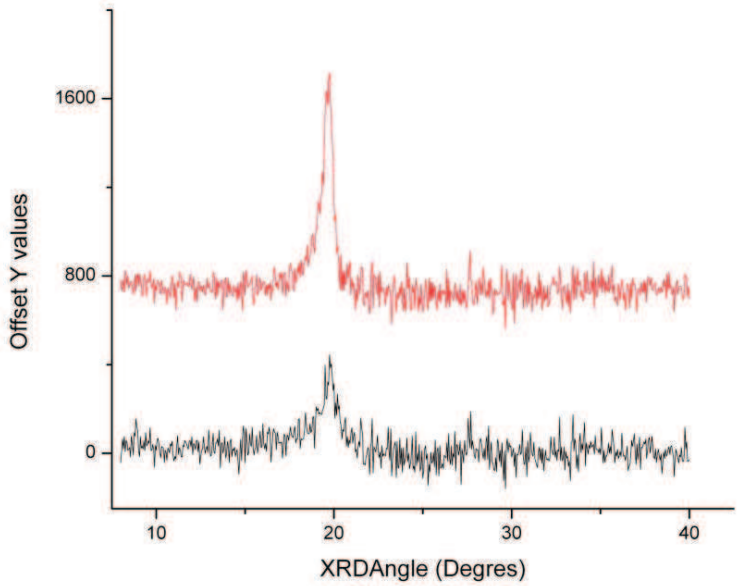

Figure 5.4 XRD diffraction spectra: before (black) and after (red) annealing.

5.3.2 FTIR measurements

The fabricated PVDF-TrFE nanofibers have also been studied using Fourier transmission infrared (FTIR) spectroscopy. **Figure 5.5** shows the measured FTIR spectra of pure (a) and magnetic particle doped (b) PVDF-TrFE nanofibers. Clearly, the characteristic peak of the piezoelectric crystalline phase of PVDF centered at 1285 cm^{-1} appears in both spectra, suggesting that the inclusion of Fe_3O_4 particles did not disturb the piezoelectric crystalline phase of PVDF.

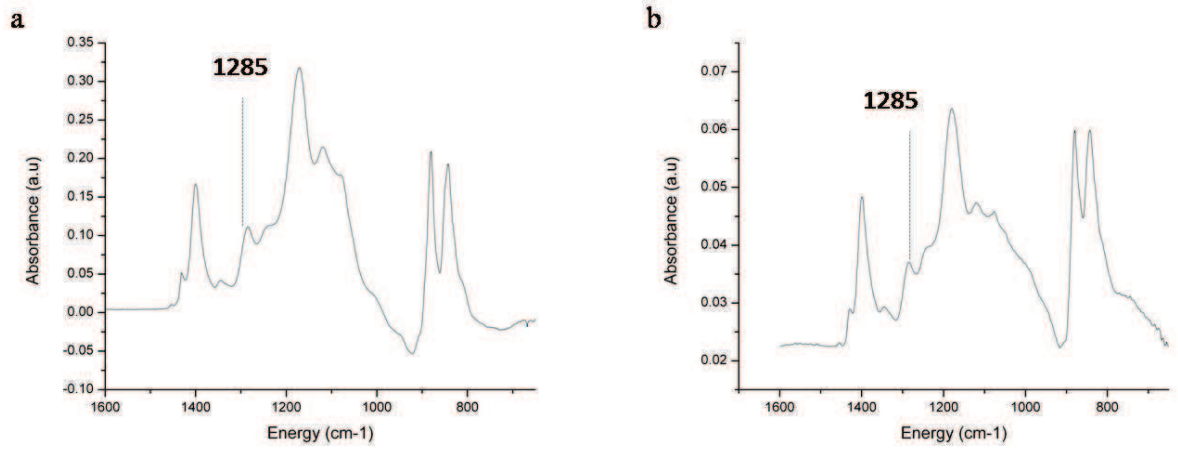

Figure 5.5 FTIR spectra of pure (**a**) and magnetic particle doped (**b**) PVDF-TrFE nanofibers.

5.4 Magnetic properties

In order to demonstrate that the fabricated nanofibers have magnetic properties we used a simple method : nanofibers were peeled off slightly from the surface with a razor blade in order to form a suspended fiber bundle (**Fig. 5.6a**). A small magnet is approached from the nanofiber bundle and we can see clearly the movement of the nanofiber bundle following the magnetic field (**Fig. 5.6b**).

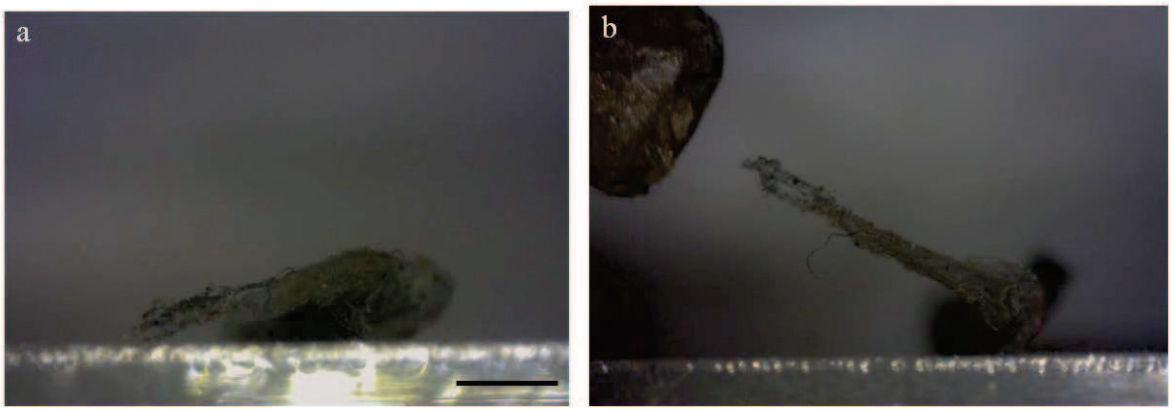

Figure 5.6 Macroscopic magnetic activation of PVDF-TrFE /Fe_3O_4 nanofibers. (**a**) Without magnetic field (**b**) With magnetic field generated by a small magnet (Scale bar is 1mm).

5.5 Cell Culture

In order to test biocompatibility of PVDF-TrFE /Fe $_3O_4$ nanofibers, cells (3T3) were cultured using the protocol described in chapter 3. For this experiment no coating or surface modification was realized before to cell seeding in order to asses intrinsic properties of the nanofibers. In addition the sterilization of substrate was realized using 70% alcohol has UV sterilization could modify nanofibers surface properties. Cells were seeded at normal density (0.3×10^6 cells/cm^{-2}).

We can see that after 1 hour (**Fig 5.7a-b**), cells begins to attach as they would o on normal uncoated cell culture substrate (e.g.; glass slide). After 12 hours (**Fig 5.7c-d**), cells are no longer visible on top of nanofibers (**Fig 5.7c)**. A zoom shows that in fact cells spread and integrate inside the nanofiber layers (**Fig 5.7d).** This type of behavior is generally a good sign of biocompatibility.

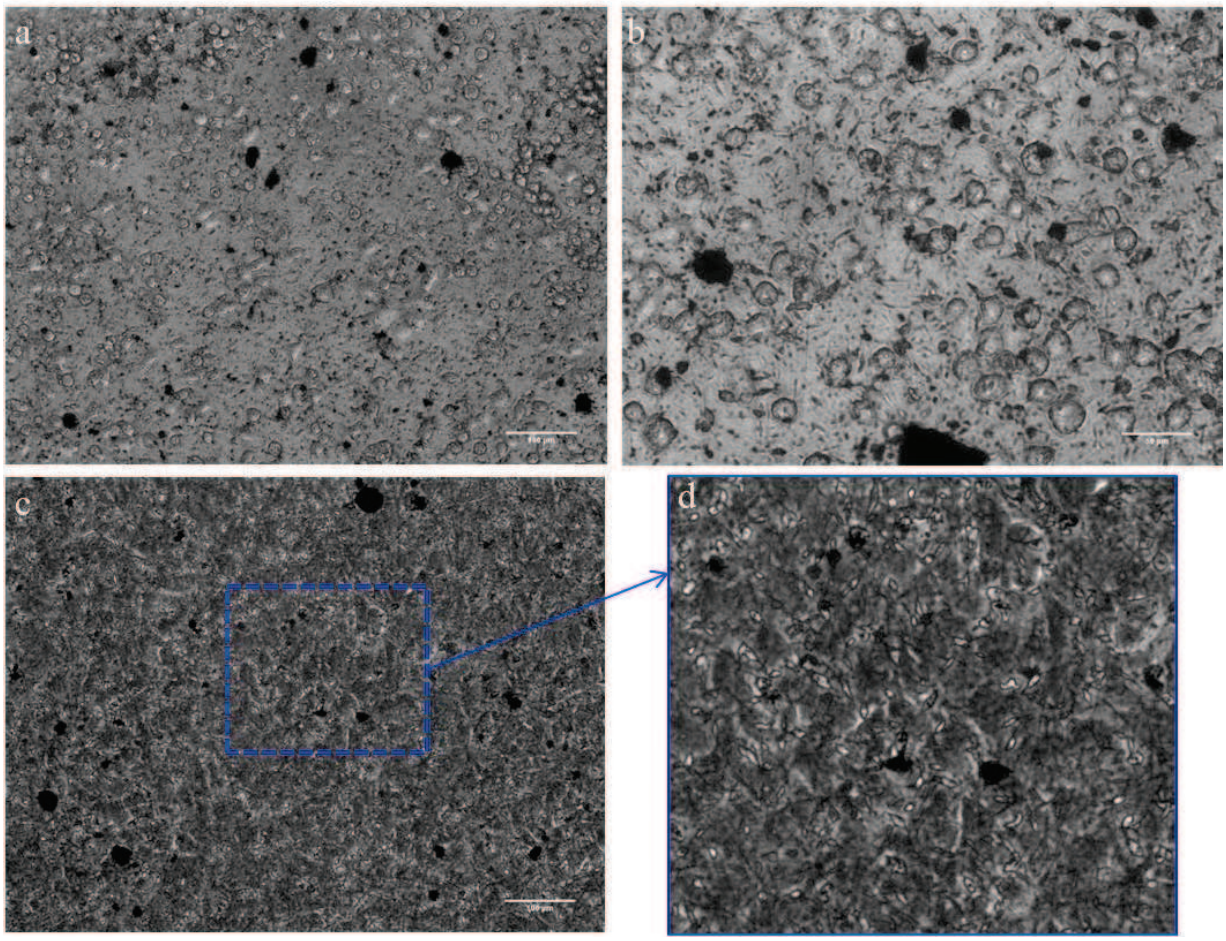

Figure 5.7 Cells (3T3) cultured on a membrane of PVDF-TrFE /Fe_3O_4 : (**a-b**) After 1 hour. (**c-d**) After 12 hours (**d**) Zoomed area from (**c**) to show cells inside the nanofibers .

After 36hours cells are still alive and spreading in the nanofibers mat (**Fig 5.8c**) and the layer of cells become more visible which mean that the cell density increased.

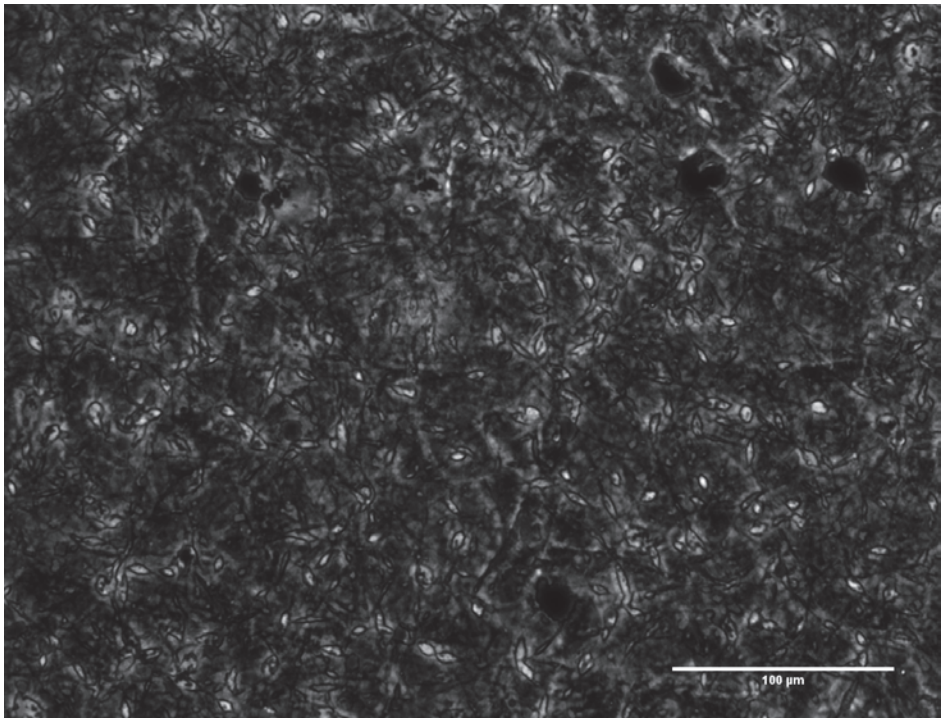

Figure 5.8 Cells (3T3) cultured a membrane of PVDF-TrFE /Fe_3O_4 after 36 hours.

5.6 Conclusion

We studied the feasibility of nanofiber inclusion of magnetic nanoparticles for remote activation with a magnetic field. Fe_3O_4 magnetic nanoparticles have been used for inclusion into PVDF-TrFE nanofibers. Under optimal conditions, the incorporated nanoparticles are homogenously dispersed in to the fibers but the piezoelectric crystalline phase of PVDF-TrFE nanofibers remained unchanged after inclusion. The results of a preliminary cell culture showed a good biocompatibility of nanoparticles doped fibers. In addition, the macroscopic response of the fiber to a magnetic field could be confirmed. Further investigations are needed to demonstrate the expected activation of cells induced by piezoelectric effects of the fibers a under alternative magnetic field.

References

[1] Kawai, H. (1969). The Piezoelectricity of Poly (vinylidene Fluoride). *Jpn. J. Appl. Phys.*, *8*(7), 975. doi:10.1143/JJAP.8.975

[2] Fukada, E., & Takashit.S. (1969). Piezoelectric Effect in Polarized Poly (vinylidene Fluoride). *Jpn. J. Appl. Phys.*, *8*(7), 960. doi:10.1143/JJAP.8.960

[3] Nakamura, K., & Wada, Y. (1971). Piezoelectricity, pyroelectricity, and the electrostriction constant of poly(vinylidene fluoride). *Journal of Polymer Science Part A-2: Polymer Physics*, *9*(1), 161–173. doi:10.1002/pol.1971.160090111

[4] Tamura, M. (1974). Piezoelectricity in uniaxially stretched poly(vinylidene fluoride). *Journal of Applied Physics*, *45*(9), 3768. doi:10.1063/1.1663857

[5] Oshiki, M., & Fukada, E. (1975). Inverse piezoelectric effect and electrostrictive effect in polarized poly(vinylidene fluoride) films. *Journal of Materials Science*, *10*(1), 1–6. doi:10.1007/BF00541025

[6] Tamura, M., Ogasawara, K., & Yoshimi, T. (1976). Piezoelectricity in uniaxially stretched poly(vinylidene fluoride) films and its applications. *Ferroelectrics*, *10*(1), 125–127. doi:10.1080/00150197608241962

[7] Tasaka, S., & Miyata, S. (1981). The origin of piezoelectricity in poly(vinylidene fluoride). *Ferroelectrics*, *32*(1), 17–23. doi:10.1080/00150198108238668

[8] Johnson, G. E., Blyler, L. L., Crane, G. R., & Gieniewski, C. (1981). Thermal piezoelectric stability of poled uniaxially-and biaxially-oriented poly(vinylidene fluoride. *Ferroelectrics*, *32*(1), 43–47. doi:10.1080/00150198108238672

[9] Tashiro, K., Tadokoro, H., & Kobayashi, M. (1981). Structure and piezoelectricity of poly(vinylidene fluoride). *Ferroelectrics*, *32*(1), 167–175. doi:10.1080/00150198108238688

[10] Fukada, E., Date, M., Neumann, H. E., & Wendorff, J. H. (1988). Nonlinear piezoelectricity in poly(vinylidene fluoride). *Journal of Applied Physics*, *63*(5), 1701. doi:10.1063/1.339905

[11] Harnischfeger, P., & Jungnickel, B.-J. (1990). Features and origin of the dynamic and the nonlinear piezoelectricity in poly (vinylidene fluoride). *Ferroelectrics*, *109*(1), 279–284. doi:10.1080/00150199008211426

[12] Stack, G. M., & Ting, R. Y. (1989). Piezoelectric properties and temperature stability of poly(vinylidene fluoride-trifluorethylene) copolymers. *IEEE transactions on ultrasonics, ferroelectrics, and frequency control*, *36*(4), 417–23. doi:10.1109/58.3177

[13] Wang, H., Zhang, Q. M., Cross, L. E., & Sykes, a. O. (1993). Piezoelectric, dielectric, and elastic properties of poly(vinylidene fluoride/trifluoroethylene). *Journal of Applied Physics*, *74*(5), 3394. doi:10.1063/1.354566

[14] Scheinbeim, J. I., Yoon, C. H., Pae, K. D., & Newman, B. A. (1980). Ferroelectric hysteresis effects in poly(vinylidene fluoride) films. *Journal of Applied Physics*, *51*(10), 5156. doi:10.1063/1.327462

[15] Herchenröder, P., Segui, Y., Horne, D., & Yoon, D. (1980). Ferroelectricity of Poly(Vinylidene Fluoride): Transition Temperature. *Physical Review Letters*, *45*(26), 2135–2137. doi:10.1103/PhysRevLett.45.2135

[16] Scheinbeim, J. I., Yoon, C. H., Pae, K. D., & Newman, B. a. (1980). Ferroelectric hysteresis effects in poly(vinylidene fluoride) films. *Journal of Applied Physics*, *51*(10), 5156. doi:10.1063/1.327462

[17] Herchenröder, P., Segui, Y., Horne, D., & Yoon, D. Y. (1980). Ferroelectricity of Poly(Vinylidene Fluoride): Transition Temperature. *Phys. Rev. Lett.*, *45*(26), 2135–2138.

[18] Kochervinski, V. V. (2003). Piezoelectricity in crystallizing ferroelectric polymers: Poly(vinylidene fluoride) and its copolymers (A review), *48*(4), 649–675.

[19] Hicks, J. C., Jones, T. E., & Logan, J. C. (1978). Ferroelectric properties of poly(vinylidene fluoride-tetrafluoroethylene). *Journal of Applied Physics*, *49*(12), 6092. doi:10.1063/1.324528

[20] Jayasuriya, A. C., & Scheinbeim, J. I. (2001). Ferroelectric behavior in solvent cast poly (vinylidene fluoride/hexafluoropropylene) copolymer films, *176*, 386–390.

[21] Xu, H. (2001). Dielectric properties and ferroelectric behavior of poly(vinylidene fluoride-trifluoroethylene) 50/50 copolymer ultrathin films. *Journal of Applied Polymer Science*, *80*(12), 2259–2266. doi:10.1002/app.1330

[22] Mai, M., Martin, B., & Kliem, H. (2011). Ferroelectric switching in Langmuir-Blodgett and spin-coated thin films of poly(vinylidene fluoride/trifluoroethylene) copolymers. *Journal of Applied Physics*, *110*(6), 064101. doi:10.1063/1.3636397

[23] Takahashi, Y., Nakagawa, Y., Miyaji, H., & Asai, K. (1987). Direct evidence for ferroelectric switching in poly(vinylidene fluoride) and poly(vinylidene fluoride-trifluoroethylene) crystals. *Journal of Polymer Science Part C: Polymer Letters*, *25*(4), 153–159. doi:10.1002/pol.1987.140250402

[24] Lee, H., Salomon, R. E., & Labes, M. M. (1978). Pyroelectricity in Polymer Blends of Poly(vinylidene fluoride). *Macromolecules*, *11*(1), 171–175. doi:10.1021/ma60061a030

[25] McKinney, J. E., Davis, G. T., & Broadhurst, M. G. (1980). Plasma poling of poly(vinylidene fluoride): Piezo- and pyroelectric response. *Journal of Applied Physics*, *51*(3), 1676. doi:10.1063/1.327775

[26] Wada, Y., & Hayakawa, R. (1981). A model theory of piezo- and pyroelectricity of poly(vinylidene fluoride) electret. *Ferroelectrics*, *32*(1), 115–118. doi:10.1080/00150198108238681

[27] Newman, B. A., Chung, K. T., Pae, K. D., & Scheinbeim, J. I. (1981). Piezoelectric and pyroelectric properties of poly(vinylidene fluoride) films at high hydrostatic pressure. *Ferroelectrics*, *32*(1), 135–140. doi:10.1080/00150198108238684

[28] Takemura, T. (1984). Piezo- and pyroelectric properties of poly(vinylidene fluoride) under high pressure. *Ferroelectrics*, *57*(1), 243–248. doi:10.1080/00150198408012766

[29] Al-Jishi, R., & Taylor, P. L. (1985). Equilibrium polarization and piezoelectric and pyroelectric coefficients in poly(vinylidene fluoride). *Journal of Applied Physics*, *57*(3), 902. doi:10.1063/1.334690

[30] Gerhard-Multhauptab, R. (1987). Poly(vinylidene fluoride): A piezo-, pyro- and ferroelectric polymer and its poling behaviour. *Ferroelectrics*, *75*(1), 385–396. doi:10.1080/00150198708008991

[31] Christie, M. C., Scheinbeim, J. I., & Newman, B. A. (1997). Ferroelectric and piezoelectric properties of a quenched poly(vinylidene fluoride-trifluoroethylene) copolymer. *Journal of Polymer Science Part B: Polymer Physics*, *35*(16), 2671–2679. doi:10.1002/(SICI)1099-0488(19971130)35:16<2671::AID-POLB10>3.0.CO;2-6

[32] Nunes, S. P., & Peinemann, K. V. (1992). Ultrafiltration membranes from PVDF/PMMA blends. *Journal of Membrane Science*, *73*(1), 25–35. doi:10.1016/0376-7388(92)80183-K

[33] Ochoa, N. (2003). Effect of hydrophilicity on fouling of an emulsified oil wastewater with PVDF/PMMA membranes. *Journal of Membrane Science*, *226*(1-2), 203–211. doi:10.1016/j.memsci.2003.09.004

[34] Kang, S. J., Park, Y. J., Bae, I., Kim, K. J., Kim, H.-C., Bauer, S., Thomas, E. L., et al. (2009). Printable Ferroelectric PVDF/PMMA Blend Films with Ultralow Roughness for Low Voltage Non-Volatile Polymer Memory. *Advanced Functional Materials*, *19*(17), 2812–2818. doi:10.1002/adfm.200900589

[35] Frensch, H., & Wendorff, J. H. (1986). Open-circuit thermally stimulated current of PVDF/PMMA blends. *Polymer*, *27*(9), 1332–1336. doi:10.1016/0032-3861(86)90030-3

[36] Nasir, M., Matsumoto, H., Minagawa, M., Tanioka, A., Danno, T., & Horibe, H. (2009). Preparation of PVDF/PMMA Blend Nanofibers by Electrospray Deposition: Effects of Blending Ratio and Humidity. *Polymer Journal*, *41*(5), 402–406. doi:10.1295/polymj.PJ2008171

[37] Morra, B. S., & Stein, R. S. (1982). Morphological studies of poly(vinylidene fluoride) and its blends with poly(methyl methacrylate). *Journal of Polymer Science: Polymer Physics Edition*, *20*(12), 2261–2275. doi:10.1002/pol.1982.180201208

[38] Domenici, C., De Rossi, D., Nannini, A., & Verni, R. (1984). Piezoelectric properties and dielectric losses in PVDF–PMMA blends. *Ferroelectrics*, *60*(1), 61–70. doi:10.1080/00150198408017510

[39] Hahn, B. R., & Wendorff, J. H. (1985). Piezo- and pyroelectricity in polymer blends of poly(vinylidene fluoride)/poly(methyl methacrylate). *Polymer*, *26*(11), 1611–1618. doi:10.1016/0032-3861(85)90272-1

[40] Raghavan, P., Zhao, X., Kim, J.-K., Manuel, J., Chauhan, G. S., Ahn, J.-H., & Nah, C. (2008). Ionic conductivity and electrochemical properties of nanocomposite polymer electrolytes based on electrospun poly(vinylidene fluoride-co-hexafluoropropylene) with nano-sized ceramic fillers. *Electrochimica Acta*, *54*(2), 228–234. doi:10.1016/j.electacta.2008.08.007

[41] Manna, S., & Nandi, A. K. (2007). Piezoelectric beta polymorph in poly(vinylidene fluoride)-functionalized multiwalled carbon nanotube nanocomposite films. *JOURNAL OF PHYSICAL CHEMISTRY C*, *111*(40), 14670–14680. doi:10.1021/jp0731021

[42] Dang, Z.-M., Xu, H.-P., & Wang, H.-Y. (2007). Significantly enhanced low-frequency dielectric permittivity in the BaTiO[sub 3]/poly(vinylidene fluoride) nanocomposite. *Applied Physics Letters*, *90*(1), 012901. doi:10.1063/1.2393150

[43] Wang, M., Zhao, F., Guo, Z., & Dong, S. (2004). Poly(vinylidene fluoride-hexafluoropropylene)/organo-montmorillonite clays nanocomposite lithium polymer electrolytes. *Electrochimica Acta*, *49*(21), 3595–3602. doi:10.1016/j.electacta.2004.03.028

[44] Liu, H. J., Hwang, J. J., & Chen-Yang, Y. W. (2002). Effects of organophilic clay on the solvent-maintaining capability, dimensional stability, and electrochemical properties of gel poly(vinylidene fluoride) nanocomposite electrolytes. *Journal of Polymer Science Part A: Polymer Chemistry*, *40*(22), 3873–3882. doi:10.1002/pola.10484

[45] Raghavan, P., Zhao, X., Manuel, J., Chauhan, G. S., Ahn, J.-H., Ryu, H.-S., Ahn, H.-J., et al. (2010). Electrochemical performance of electrospun poly(vinylidene fluoride-co-hexafluoropropylene)-based nanocomposite polymer electrolytes incorporating ceramic fillers and room temperature ionic liquid. *Electrochimica Acta*, *55*(4), 1347–1354. doi:10.1016/j.electacta.2009.05.025

[46] Wang, J., Wang, Y., Wang, F., Li, S., Xiao, J., & Shen, Q. (2009). A large enhancement in dielectric properties of poly(vinylidene fluoride) based all-organic nanocomposite. *Polymer*, *50*(2), 679–684. doi:10.1016/j.polymer.2008.11.040

[47] Guo, Y., Liu, Y., Wang, J., Withers, R. L., Chen, H., Jin, L., & Smith, P. (2010). Giant Magnetodielectric Effect in 0-3 Ni0.5Zn0.5Fe2O4-Poly(vinylidene-fluoride) Nanocomposite Films. *JOURNAL OF PHYSICAL CHEMISTRY C*, *114*(32), 13861–13866. doi:10.1021/jp103777r

[48] Xu, H., Ni, S., & Yang, C. (2002). High Polarization Levels in Poly (vinylidene fluoride – trifluoroethylene) Ferroelectric Thin Films Doped with Diethyl Phthalate.

[49] Scheinbeim, I., & Newman, B. A. (1990). Effect of Tricrecyl Phosphate Doping on the Remanent Polarization in Uniaxially Oriented Poly (viny1idene fluoride), *648*(42), 642–648.

[50] Choia, C. ., Traczb, A., Jeszkab, J. ., Boiteuxa, G., Seytrea, G., Ulańskic, J., & Kryszewskib, M. (1990). Conductive poly(vinylidene fluoride) reticulate doped with the CT complex TTF-TCNQ. *Proceedings of the 21st Europhysics Conference on Macromolecular Physics 'Electrical and Optical Active Polymers" Structure, Morphology and Properties*, *37*, 181–188. doi:10.1016/0379-6779(90)90145-B

[51] Privalko, V., Ponomarenko, S., Privalko, E., Lobkov, S., Rekhteta, N., Pud, A., Bandurenko, A., et al. (2005). Structure/Property Relationships for Poly(Vinylidene Fluoride)/Doped Polyaniline Blends. *Journal of Macromolecular Science, Part B: Physics*, *44*(5), 749–759. doi:10.1080/00222340500251394

[52] Wang, S., Li, Y., Fei, X., Sun, M., Zhang, C., Li, Y., Yang, Q., et al. (2011). Preparation of a durable superhydrophobic membrane by electrospinning poly (vinylidene fluoride) (PVDF) mixed with epoxy-siloxane modified SiO2 nanoparticles: a possible route to superhydrophobic surfaces with low water sliding angle and high water contact angle. *Journal of colloid and interface science*, *359*(2), 380–8. doi:10.1016/j.jcis.2011.04.004

[53] Yuan, J., Geng, J., Xing, Z., Shen, J., Kang, I., & Byun, H. (2009). Electrospinning of Antibacterial Poly (vinylidene fluoride) Nanofibers Containing Silver Nanoparticles, 1–5. doi:10.1002/app

[54] Sheikh, F. A., Cantu, T., Macossay, J., & Kim, H. (2011). Fabrication of Poly(vinylidene fluoride) (PVDF) Nanofibers Containing Nickel Nanoparticles as Future Energy Server Materials. *Science of Advanced Materials*, *3*(2), 216–222. doi:10.1166/sam.2011.1148

[55] Miranda, D., Sencadas, V., Sánchez-Iglesias, A., Pastoriza-Santos, I., Liz-Marzán, L. M., Ribelles, J. L. G., & Lanceros-Mendez, S. (2009). Influence of Silver Nanoparticles Concentration on the α- to β-Phase Transformation and the Physical Properties of Silver Nanoparticles Doped Poly(vinylidene fluoride) Nanocomposites. *Journal of Nanoscience and Nanotechnology*, *9*(5), 2910–2916. doi:10.1166/jnn.2009.208

[56] Mandal, D., Henkel, K., & Schmeißer, D. (2012). The electroactive β-phase formation in Poly(vinylidene fluoride) by gold nanoparticles doping. *Materials Letters*, *73*, 123–125. doi:10.1016/j.matlet.2011.11.117

[57] Mandal, D., Kim, K. J., & Lee, J. S. (2012). Simple Synthesis of Palladium Nanoparticles, β-Phase Formation, and the Control of Chain and Dipole Orientations in Palladium-Doped Poly(vinylidene fluoride) Thin Films. *Langmuir: the ACS journal of surfaces and colloids*, *28*(28), 10310–7.

[58] Martins, P., Costa, C. M., Benelmekki, M., Botelho, G., & Lanceros-Mendez, S. (2012). On the origin of the electroactive poly(vinylidene fluoride) β-phase nucleation by ferrite nanoparticles via surface electrostatic interactions. *CrystEngComm*, *14*(8), 2807. doi:10.1039/c2ce06654h

[59] Jaleh, B., Fakhri, P., Noroozi, M., & Muensit, N. (2012). Influence of Copper Nanoparticles Concentration on the Properties of Poly(vinylidene fluoride)/Cu Nanoparticles Nanocomposite Films. *Journal of Inorganic and Organometallic Polymers and Materials*, *22*(4), 878–885. doi:10.1007/s10904-012-9660-5

[60] Reich, S., & Goldberg, E. P. (1983). Poly(vinylidene fluoride)-γFe2O3 magnetic composites. *Journal of Polymer Science: Polymer Physics Edition*, *21*(6), 869–879. doi:10.1002/pol.1983.180210604

[61] Gupta, A., & Chatterjee, R. (2009). Magnetic, dielectric, magnetoelectric, and microstructural studies demonstrating improved magnetoelectric sensitivity in three-phase BaTiO[sub 3]–CoFe[sub 2]O[sub 4]–poly(vinylidene-fluoride) composite. *Journal of Applied Physics*, *106*(2), 024110. doi:10.1063/1.3181061

[62] Jing, X., Shen, X., Song, H., & Song, F. (2011). Magnetic and dielectric properties of barium ferrite fibers/poly(vinylidene fluoride) composite films. *Journal of Polymer Research*, *18*(6), 2017–2021. doi:10.1007/s10965-011-9610-x

[63] Martins, P., Costa, C. M., Botelho, G., Lanceros-Mendez, S., Barandiaran, J. M., & Gutierrez, J. (2012). Dielectric and magnetic properties of ferrite/poly(vinylidene fluoride) nanocomposites. *Materials Chemistry and Physics*, *131*(3), 698–705. doi:10.1016/j.matchemphys.2011.10.037

[64] Zhang, J. X., Dai, J. Y., So, L. C., Sun, C. L., Lo, C. Y., Or, S. W., & Chan, H. L. W. (2009). The effect of magnetic nanoparticles on the morphology, ferroelectric, and magnetoelectric behaviors of CFO/P(VDF-TrFE) 0–3 nanocomposites. *Journal of Applied Physics*, *105*(5), 054102. doi:10.1063/1.3078111

[65] Josephson, L. (2006). Magnetic Nanoparticles for MR Imaging. In L. J. Lee, Abraham P.;Lee (Ed.), *BioMEMS and Biomedical Nanotechnology* (Springer., pp. 227–237).

[66] M. Ohgushi, K. Nagayama, and A. Wada. Dextran-magnetite: a new relaxation reagent and its application to T2 measurements in gel systems. *J. Mag. Res.*, (1969–1992), 29(3):599–601, 1978.

[67] Mahmoudi, M., Laurent, S., Shokrgozar, M. a, & Hosseinkhani, M. (2011). Toxicity evaluations of superparamagnetic iron oxide nanoparticles: cell "vision" versus physicochemical properties of nanoparticles. *ACS nano*, *5*(9), 7263–76. doi:10.1021/nn2021088

[68] García, A., Espinosa, R., Delgado, L., Casals, E., González, E., Puntes, V., Barata, C., et al. (2011). Acute toxicity of cerium oxide, titanium oxide and iron oxide nanoparticles using standardized tests. *Desalination*, *269*(1-3), 136–141. doi:10.1016/j.desal.2010.10.052

[69] Singh, N., Jenkins, G. J. S., Asadi, R., & Doak, S. H. (2010). Potential toxicity of superparamagnetic iron oxide nanoparticles (SPION). *Nano reviews*, *1*, 1–15. doi:10.3402/nano.v1i0.5358

[70] Pankhurst, Q. A., Connolly, J., Jones, S. K., & Dobson, J. (2003). Applications of magnetic nanoparticles in biomedicine. *Journal of Physics D: Applied Physics*, *36*(13), R167–R181. doi:10.1088/0022-3727/36/13/201

[71] Berry, C. C., & Curtis, A. S. G. (2003). Functionalisation of magnetic nanoparticles for applications in biomedicine. *Journal of Physics D: Applied Physics*, *36*(13), R198–R206. doi:10.1088/0022-3727/36/13/203

[72] Ito, A., Shinkai, M., Honda, H., & Kobayashi, T. (2005). Medical application of functionalized magnetic nanoparticles. *Journal of bioscience and bioengineering*, *100*(1), 1–11. doi:10.1263/jbb.100.1

[73] Gao, J., Gu, H., & Xu, B. (2009). Multifunctional magnetic nanoparticles: design, synthesis, and biomedical applications. *Accounts of chemical research*, *42*(8), 1097–107. doi:10.1021/ar9000026

[74] Hao, R., Xing, R., Xu, Z., Hou, Y., Gao, S., & Sun, S. (2010). Synthesis, functionalization, and biomedical applications of multifunctional magnetic nanoparticles. *Advanced materials (Deerfield Beach, Fla.)*, *22*(25), 2729–42. doi:10.1002/adma.201000260

[75] Laurent, S., Forge, D., Port, M., Roch, A., Robic, C., Vander Elst, L., & Muller, R. N. (2008). Magnetic iron oxide nanoparticles: synthesis, stabilization, vectorization, physicochemical characterizations, and biological applications. *Chemical reviews*, *108*(6), 2064–110. doi:10.1021/cr068445e

[76] Giri, S., Trewyn, B. G., Stellmaker, M. P., & Lin, V. S.-Y. (2005). Stimuli-responsive controlled-release delivery system based on mesoporous silica nanorods capped with magnetic nanoparticles. *Angewandte Chemie (International ed. in English)*, *44*(32), 5038–44. doi:10.1002/anie.200501819

[77] Sun, C., Lee, J. S. H., & Zhang, M. (2008). Magnetic nanoparticles in MR imaging and drug delivery. *Advanced drug delivery reviews*, *60*(11), 1252–65. doi:10.1016/j.addr.2008.03.018

[78] McCarthy, J. R., & Weissleder, R. (2008). Multifunctional magnetic nanoparticles for targeted imaging and therapy. *Advanced drug delivery reviews*, *60*(11), 1241–51. doi:10.1016/j.addr.2008.03.014

[79] Park, H.-Y., Schadt, M. J., Wang, L., Lim, I.-I. S., Njoki, P. N., Kim, S. H., Jang, M.-Y., et al. (2007). Fabrication of magnetic core@shell Fe oxide@Au nanoparticles for interfacial bioactivity and bio-separation. *Langmuir: the ACS journal of surfaces and colloids*, *23*(17), 9050–6. doi:10.1021/la701305f

[80] Gu, H., Ho, P.-L., Tsang, K. W. T., Wang, L., & Xu, B. (2003). Using biofunctional magnetic nanoparticles to capture vancomycin-resistant enterococci and other gram-positive bacteria at ultralow concentration. *Journal of the American Chemical Society*, *125*(51), 15702–3. doi:10.1021/ja0359310

[81] Arruebo, M., Fernández-Pacheco, R., Ibarra, M. R., & Santamaría, J. (2007). Magnetic nanoparticles for drug delivery. *Nano Today*, *2*(3), 22–32. doi:10.1016/S1748-0132(07)70084-1

[82] Dobson, J. (2006). Magnetic nanoparticles for drug delivery. *Drug Development Research*, *67*(1), 55–60. doi:10.1002/ddr.20067

[83] McBain, S. C., Yiu, H. H. P., & Dobson, J. (2008). Magnetic nanoparticles for gene and drug delivery. *INTERNATIONAL JOURNAL OF NANOMEDICINE*, *3*, 169–180.

[84] Alexiou, C., Jurgons, R., Schmid, R., Hilpert, A., Bergemann, C., Parak, F., & Iro, H. (2005). In vitro and in vivo investigations of targeted chemotherapy with magnetic nanoparticles. *Journal of Magnetism and Magnetic Materials*, *293*(1), 389–393. doi:10.1016/j.jmmm.2005.02.036

[85] Jurgons, R., Seliger, C., Hilpert, A., Trahms, L., Odenbach, S., & Alexiou, C. (2006). Drug loaded magnetic nanoparticles for cancer therapy. *Journal of Physics: Condensed Matter*, *18*(38), S2893–S2902. doi:10.1088/0953-8984/18/38/S24

[86] Alexiou, C., Schmid, R. J., Jurgons, R., Kremer, M., Wanner, G., Bergemann, C., Huenges, E., et al. (2006). Targeting cancer cells: magnetic nanoparticles as drug carriers. *European biophysics journal : EBJ*, *35*(5), 446–50. doi:10.1007/s00249-006-0042-1

[87] Shubayev, V. I., Pisanic, T. R., & Jin, S. (2009). Magnetic nanoparticles for theragnostics. *Advanced drug delivery reviews*, *61*(6), 467–77. doi:10.1016/j.addr.2009.03.007

[88] Yoon, T.-J., Kim, J. S., Kim, B. G., Yu, K. N., Cho, M.-H., & Lee, J.-K. (2005). Multifunctional nanoparticles possessing a "magnetic motor effect" for drug or gene delivery. *Angewandte Chemie (International ed. in English)*, *44*(7), 1068–71. doi:10.1002/anie.200461910

[89] Kumari, S., & Singh, R. P. (2012). Glycolic acid-g-chitosan-Pt-Fe3O4 nanoparticles nanohybrid scaffold for tissue engineering and drug delivery. *International journal of biological macromolecules*, *51*(1-2), 76–82. doi:10.1016/j.ijbiomac.2012.01.040

[90] Huang, C., Zhou, Y., Tang, Z., Guo, X., Qian, Z., & Zhou, S. (2011). Synthesis of multifunctional Fe3O4 core/hydroxyapatite shell nanocomposites by biomineralization. *Dalton transactions (Cambridge, England: 2003)*, *40*(18), 5026–31. doi:10.1039/c0dt01824d

[91] Lin, T.-C., Lin, F.-H., & Lin, J.-C. (2012). In vitro feasibility study of the use of a magnetic electrospun chitosan nanofiber composite for hyperthermia treatment of tumor cells. *Acta biomaterialia*, *8*(7), 2704–11. doi:10.1016/j.actbio.2012.03.045

[92] Jordan, A., Scholz, R., Wust, P., & Fähling, H. (1999). Magnetic fluid hyperthermia (MFH): Cancer treatment with AC magnetic field induced excitation of biocompatible superparamagnetic nanoparticles. *Journal of Magnetism and Magnetic Materials*, *201*(1-3), 413–419. doi:10.1016/S0304-8853(99)00088-8

[93] Johannsen, M., Gneveckow, U., Eckelt, L., Feussner, A., WaldÖFner, N., Scholz, R., Deger, S., et al. (2005). Clinical hyperthermia of prostate cancer using magnetic nanoparticles: Presentation of a new interstitial technique. *International Journal of Hyperthermia*, *21*(7), 637–647. doi:10.1080/02656730500158360

[94] Jordan, A., Scholz, R., Maier-Hauff, K., van Landeghem, F. K. H., Waldoefner, N., Teichgraeber, U., Pinkernelle, J., et al. (2006). The effect of thermotherapy using magnetic nanoparticles on rat malignant glioma. *Journal of neuro-oncology*, *78*(1), 7–14. doi:10.1007/s11060-005-9059-z

[95] Thiesen, B., & Jordan, A. (2008). Clinical applications of magnetic nanoparticles for hyperthermia. International journal of hyperthermia: the official journal of European Society for Hyperthermic Oncology, North American Hyperthermia Group, 24(6), 467–74. doi:10.1080/02656730802104757

[96] Fortin, J.-P., Gazeau, F., & Wilhelm, C. (2008). Intracellular heating of living cells through Néel relaxation of magnetic nanoparticles. *European biophysics journal : EBJ*, *37*(2), 223–8. doi:10.1007/s00249-007-0197-4

[97] Kriha, O., Becker, M., Lehmann, M., Kriha, D., Krieglstein, J., Yosef, M., Schlecht, S., et al. (2007). Connection of Hippocampal Neurons by Magnetically Controlled Movement of Short Electrospun Polymer Fibers—A Route to Magnetic Micromanipulators. Advanced Materials, 19(18), 2483–2485. doi:10.1002/adma.200601937

[98] Huang, H., Delikanli, S., Zeng, H., Ferkey, D. M., & Pralle, A. (2010). Remote control of ion channels and neurons through magnetic-field heating of nanoparticles. *Nature nanotechnology*, *5*(8), 602–6. doi:10.1038/nnano.2010.125

[99] Panseri, S., Cunha, C., D'Alessandro, T., Sandri, M., Russo, A., Giavaresi, G., Marcacci, M., et al. (2012). Magnetic hydroxyapatite bone substitutes to enhance tissue regeneration: evaluation in vitro using osteoblast-like cells and in vivo in a bone defect. *PloS one*, *7*(6), e38710. doi:10.1371/journal.pone.0038710

[100] Panseri, S., Russo, A., Cunha, C., Bondi, A., Di Martino, A., Patella, S., & Kon, E. (2012). Osteochondral tissue engineering approaches for articular cartilage and subchondral bone regeneration. *Knee surgery, sports traumatology, arthroscopy*, *20*(6), 1182–91. doi:10.1007/s00167-011-1655-1

[101] Panseri, S., Russo, a, Giavaresi, G., Sartori, M., Veronesi, F., Fini, M., Salter, D. M., et al. (2012). Innovative magnetic scaffolds for orthopedic tissue engineering. *Journal of biomedical materials research. Part A*, *100*(9), 2278–86. doi:10.1002/jbm.a.34167

[102] Wei, Y., Zhang, X., Song, Y., Han, B., Hu, X., Wang, X., Lin, Y., et al. (2011). Magnetic biodegradable Fe3O4/CS/PVA nanofibrous membranes for bone regeneration. *Biomedical materials)*, *6*(5), 055008. doi:10.1088/1748-6041/6/5/055008

[103] Ziv-Polat, O., Skaat, H., Shahar, A., & Margel, S. (2012). Novel magnetic fibrin hydrogel scaffolds containing thrombin and growth factors conjugated iron oxide nanoparticles for tissue engineering. *International journal of nanomedicine*, *7*, 1259–74. doi:10.2147/IJN.S26533

[104] Liu, J., Shi, J., Jiang, L., Zhang, F., Wang, L., Yamamoto, S., Takano, M., et al. (2012). Segmented magnetic nanofibers for single cell manipulation. *Applied Surface Science*, *258*(19), 7530–7535. doi:10.1016/j.apsusc.2012.04.077

Conclusion and perspectives

The main objective of this thesis was to fabricate PVDF micropatterns and nanofibers and to study their usefulness in tissue engineering.

PVDF is a highly non-reactive, piezoelectric, and thermoplastic fluoro-polymer. Intrinsically, PVDF is neither cytophilic nor cytotoxic but its piezoelectric characteristic is interesting for advanced applications in cell biology and tissue engineering such as piezoelectric sensing and actuation of cellular activities. Previously, only a few of preliminary investigations have been done on the micro-processing ability of PVDF and their biocompatibility. Therefore, we proposed to apply different microfabrication techniques, including micro-photolithography, soft-lithography, micro-contact printing, electrospinning and a variety of surface treatments, to the realization of topographic features of PVDF as well as the physicochemical properties of their surfaces. The fabricated PVDF structures were systematically evaluated by spectroscopic characterization and cell culture tests, thereby providing preliminary assessments as clear as possible.

Firstly, we studied several patterning techniques for the easy fabrication of PVDF microstructures. It turns out, however, that the conventional photolithography techniques are not applicable to PVDF due to the process incompatibility such as solvent not selectivity.

PVDF is a thermoplastic polymer with a relative low glass transition temperature so that hot embossing can be easily applied to deform a thin layer for PVDF deposited on a glass substrate. However, it is difficult to achieve a clear pattern without residual in the recessed area. Although some interesting effects could be observed such as growth confinement and edge dominated contact guidance, cell culture on such patterns did not allow clear assessments. In fact, due to repulsion of both patterned lines and not well-defined residual features fibroblasts trended to assembly in 3-D like fibrous structures.

Capillary assisted hot embossing was then used to achieve a better microstructure patterning of PVDF. Now, a PVDF solution is deposited on ta PDMS mold and partially evaporated after spinning. After covering with a flat substrate, the liquid PVDF penetrates into the recessed part of the PDMS mold. Due to capillary force enhanced by heating, PVDF

microstructures could be formed nicely without noticeable residuals in the contact area of PDMS-substrate. As results, we obtained 10 μm to 100 μm line-and-space gratings of 2 μm height and 100 pitch pillars of 7 μm height. Spectroscopic characterizations (XRD, FTIR) of the samples showed that PVDF after the hot embossing still have a γ phase which can be converted to piezoelectric β phase by poling. Now, fibroblasts cultured of on these nicely patterned PVDF were spread in the trenches to form well defined 2D cell sheets between lines.

We have also used micro-contact printing to define cytophilic areas a flat PVDF surface. Our results showed that a fibronectin patterned surface was excellent for cell growth with high pattern selectivity: No cells adhere outside of the printed area defined by fibronectin. As PVDF commonly used in western-blot works for all types of proteins, our method should be applicable to many other types of proteins.

More generally, the wetting property of PVDF can be tuned from hydrophobic to hydrophilic by oxygen plasma or oxygen containing RIE techniques. Our results showed that the treated PVDF surfaces were stable in time and suited for cell culture. However, the SF_6 containing RIE turned the PVDF surface into super-hydrophobic, which is also stable in time. Moreover, neither oxygen plasma nor RIE surface treatment does modify the crystalline phase of PVDF, which is important to preserve the piezoelectric and ferroelectric properties of the material.

In this work, we also worked on the fabrication PVDF based nanofibers. PVDF-TrFE copolymer was chosen because of its native piezoelectric β phase. We were particularly interested in cell interaction with aligned piezoelectric nanofibers. In order to obtain PVDF-TrFE nanofibers with precise positioning which are required for later electric wiring using patterned electrodes, we first used the near field electrospinning but could not achieve our objective. In fact, only flat fibers with large dimensions could be obtained which were less defined comparing to those produced by standard microfabrication techniques. Then, we used electric-field assisted far field electrospinning to produce aligned PVDF-TrFE nanofibers between two electrodes. As results, we obtained nanofibers of a typical diameter of about 350 nm and a typical alignment ratio larger that 90%. By using a four electrodes configuration, we also fabricated crisscrossed nanofiber patterns. The results of surface characterization (XRD, FTIR) showed that these nanofibers still have the piezoelectric β phase but it could be enhanced by annealing and ice quenching. Neuronal cell culture on aligned PVDF-TrFE

nanofibers showed a clear enhancement of neurites outgrowth compared to those cultured on random nanofiber mats.

Finally, we embedded magnetic nanoparticles made in Fe_2O_3 in electrospun PVDF-TrFE nanofibers to test the feasibility of magnetic activation of piezoelectric nanofibers. If successful, this activation should be measured by either optical imaging or electric monitoring. The scanning electron microscopic observation confirmed that the magnetic nanoparticles have been successfully integrated into the polymer blend and that the produced nanofibers have the same dimension (350 nm) as normal PVDF-TrFE nanofibers. The surface characterization showed that the incorporation of magnetic nanoparticles into the polymer does not modify significantly the crystalline piezoelectric β phase. By using a macroscopic magnet, we also confirmed the possibility of remote manipulation of the fibers with a magnetic field. Preliminary culture tests showed the expected cell adhesion and spreading but the magnetic field induced piezoelectric activation of cell activities is still to be investigated.

Up to date, piezoelectric properties of PVDF should impact on the neuronal outgrowth but this has not been properly demonstrated. The possibility of using a magnetic field to mechanically activate the magnetic nanoparticles containing fibers should allow modulating the surface charges, thereby providing a way to address this interesting question. Further studies can be directed to the coupling between magnetic activation and surface charge effect at tissue levels.

As conclusion, PVDF and PVDF based copolymers are promising for biological and biomedical applications. These materials can be easily processed to obtain either well-defined micropatterns or nanofibers, which can then be used for cell culture study and tissue engineering. The wetting properties of the PVDF surfaces can be turned from hydrophobic to hydrophilic or super-hydrophobic. In particular, microcontact printing of PVDF allows defining cytophilic zone on a flat cytophobic surface with a very high selectivity. Taking into account the fact that PVDF is now under intensive investigation for piezoelectric sensors and actuators, we believe that PVDF based biomedical devices could be developed for many important applications.

Appendix A:

High Density Plasmon Sensor

Microelectronic Engineering 88 (2011) 2474–2477

Contents lists available at ScienceDirect

Microelectronic Engineering

journal homepage: www.elsevier.com/locate/mee

Fabrication of high density gold nanoparticle arrays on glass for high sensitivity bio-detection

Kevin Lhoste [a], Laurent Malaquin [b], Laurent Billot [c], Anne Marie Haghiri-Gosnet [c], Yong Chen [a,d,*]

[a] Ecole Normale Supérieure, CNRS-ENS-UPMC UMR 8640, 24 rue Lhomond, 75231 Paris, France
[b] Institut Curie/CNRS/UPMC UMR168, 26 rue d'Ulm, 75005 Paris, France
[c] Laboratoire de Photonique et de Nanostructures, CNRS, Route de Nozay, 91460 Marcoussis, France
[d] Institute for Integrated Cell-Material Sciences, Kyoto University, 606-8507 Kyoto, Japan

ARTICLE INFO

Article history:
Available online 30 November 2010

Keywords:
Nanofabrication
Self assembly
Nanoparticles
Bio-sensors

ABSTRACT

We report a nanofabrication process to produce high density arrays of self-assembled gold nanoparticle on glass substrates which can be used for surface plasmon based bio-sensing. Capillary assisted particle assembly (CAPA) has been used to trap gold particles of 80–150 nm diameters into arrays of holes of 90–160 nm diameters made of polydimethylsiloxane (PDMS). A thermal assisted micro-contact printing technique was developed to transfer the assembled gold nanoparticles on the surface of a glass substrate using a spin coated thin layer thermoplastic polymer for adhesion. Our results showed that it is possible to obtain homogenous gold particle assembly with a pitch size down of 160 nm. The fabricated samples were used for optical determination of refractive indices of chemical solutions based on surface plasmon bio-sensing.

1. Introduction

Nanoparticles are now widely used in chemical and biochemical processing such as biological imaging, cell capture, solid phase syntheses, etc. [1–3]. Besides, they can be manipulated by different physical and chemical means such as optical tweezers, magnetic, electric or dielectric forces as well as micro flows [4–6]. Moreover, nanoparticles can be used in colloid lithography where particles are closely packed to form mono-layer of periodic structure on a substrate which can be then transferred by etching, lift-off and other techniques [7,8]. In some cases, the assembled particles can be used as active medium for such as electromagnetic wave tailoring [9,10]. One of the remaining main challenges in the development of devices that utilize micro- and nanoparticles is particle organization and integration on surfaces. Indeed, some of the most interesting electronic, optical or biological properties only appear in well-ordered particle arrays. Self-assembly is an intriguing method to order large numbers of small particles on large surfaces efficiently. In order to obtain arbitrary patterns, nanoparticles can first be self assembled on a lithography defined template and then be transferred onto a substrate. Such a printing strategy has been recently proven to be efficient to produce patterns of gold nanoparticles with a single particle resolution [11]. In this work, we show that this technique can also be applied to obtain high density nanoparticles arrays in a controllable way. We used capillary assisted assembly to create well controlled arrangements of particles [12].

When a drop of particle solution is dried slowly on a flat surface, the particles aggregate at the rim of the droplet because of the combination of convective flows that appears upon evaporation and attractive capillary forces that arises between particles when the water film thickness is in the dimension of the particle diameter. On a patterned surface, it is possible to direct the assembly of particles by inducing a geometrical confinement into holes or close to the edge of a pattern. By correlating the particle and hole sizes, localized immobilization of single particles can be achieved. With a template of high density hole arrays, we were able to fill homogeneously the template with gold nanoparticles and then to print them on the surface of a substrate. In order to understand the detail of the filling mechanism and to evaluate the performance of such a method, a systematic investigation has been developed by using a template of holes of different sizes and periods.

2. Experimental

The template for particle assembling used in this work was obtained by casting polydimethylsiloxane (PDMS) on patterned silicon masters using the methods and materials reported previously [13,14]. Silicon molds were fabricated by electron beam lithography and reactive ion etching techniques. Prior to their use, trichloromethylsiloxane (TMCS) was evaporated on the surface of the

* Corresponding author at: Ecole Normale Supérieure, CNRS-ENS-UPMC UMR 8640, 24 rue Lhomond, 75231 Paris, France.
E-mail address: yong.chen@ens.fr (Y. Chen).

0167-9317/$ - see front matter © 2010 Elsevier B.V. All rights reserved.
doi:10.1016/j.mee.2010.11.053

molds for facilitating the mold separation. Then, patterns were transferred into PDMS by casting, resulting in arrays of holes of diameters ranging from 90 to 160 nm and period ranging between 140 and 320 nm, whereas the depth of holes was kept the same (0.2 μm). In order to control the wettability of the colloidal suspension and to facilitate capillary assembly ($30° < \theta < 60°$), we added an aqueous 0.1 wt.% emulsion of Triton X-45 (Fluka) mixed with a 10 mM aqueous solution of sodiumdodecylsulphonate (Fluka) in the colloidal solution (water).

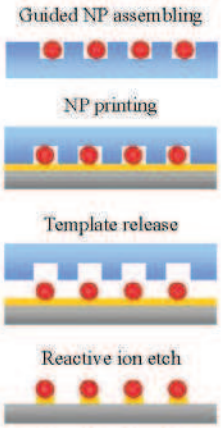

Fig. 1. Schematic fabrication flow chart of thermal micro-contact printing based pattern transfer.

The printing technique applicable to the nanoparticle transfer is shown in Fig. 1. We used a thin layer (~50 nm) of polymethylmethacrylate (PMMA) spin-coated on a glass plate as substrate for particle transfer. The transfer was then achieved by micro-contact printing at 120 °C with a pressure of ~10 kg for 20 min. Such a thermal transfer makes the PMMA layer soft enough for the gold nanoparticle adhesion but hard enough for their immobilization after cooling down to the room temperature.

To illustrate the application potential, the patterned high density gold particles were used for bio-sensing. A simple apparatus has been used to measure absorption spectra of the gold particles submerged in a bio-solution with or without drying. For the measurements without drying, a droplet of biomolecule solution is contained in the reservoir on the top of the nanoparticle arrays. Then, the chip was placed on an inverted microscope and illuminated with a collimated white light beam coming from the top side. An optical

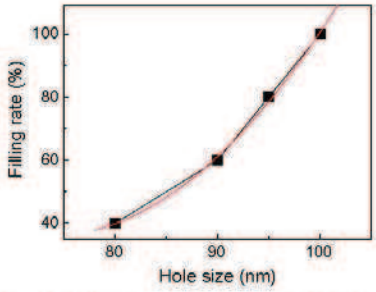

Fig. 4. Template hole filling rate as a function of hole size for 80 nm diameter particles.

Fig. 2. Optical images of nanoparticles assembled with templates of the same hole diameter (80 nm) but different spacing: (a) 120 nm, (b) 90 nm and (c) 50 nm, showing different assembling situations (pattern size: 0.2 × 0.2 mm^2).

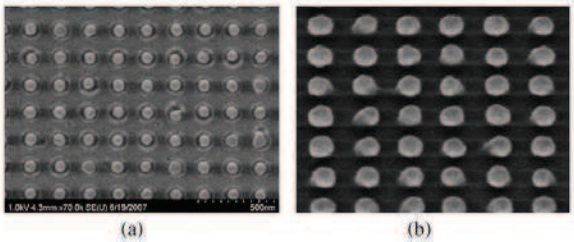

Fig. 3. SEM images of 80 nm gold nanoparticles before (a) and after (b) transfer from a PDMS stamp to a glass slide.

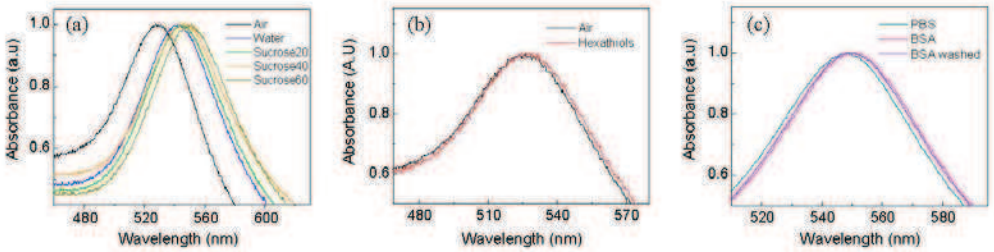

Fig. 5. Absorption spectra of 80 nm diameter-and-spacing gold particle array recorded in different situations: (a) in air, water, and sucrose solutions (20%, 40%, and 60%), (b) in air with and without adsorption of hexadecanethiols, and (c) in PBS solution, BSA and BSA after PBS washing.

fiber on the bottom is linked to a spectrometer (ocean optics USB2000) which records the absorption spectrum of the system. Similarly, the remaining biomolecules on gold particles after drying could also be detected by absorption measurements.

3. Results and discussion

Several processing parameters affect the quality of the particle assembly: the diameter of holes in the PDMS template (D), the diameter of nanoparticles (d), the contact angle of the colloidal solution over the PDMS template (θ^*), the speed (v) and the temperature (T) of the moving stage in capillary assisted particle assembly (CAPA).

It was found that the nanoparticles trapping efficiency increases with the template hole diameter as well as the contact angle of the colloidal solution. We also found a strong dependency between the hole diameter and the contact angle. Indeed both the diameter of the structure and their period influences the surface roughness and thus the wettability of the surface. As demonstrated in previous works [12,15], we found an optimum of the efficiency of the capillary assisted assembly method between 30° and 60°.

Fig. 2 shows microphotographs of three typical cases of nanoparticle assembling with templates of the same hole diameter (80 nm) but different spacing ranging from 50 to 120 nm. To understand the observed phenomena, the well-known Wenzel equation can be used, i.e., con $\theta^* = r \cos\theta$, where θ is the contact angle of the material (PDMS), r is the surface rugosity, and θ^*, the contact angle of patterned surface. At a given surfactant (Triton X100-SDS) concentration (20% v/v), the higher the hole density or the smaller the hole spacing, the smaller the contact angle. When the contact angle is too high (low hole density or low surfactant concentration), the capillary force might be not efficient to bring particles enter into the holes (Fig. 2a). Otherwise, when the contact angle is too small (low hole density), the "stick–slip" patterns can be produced (Fig. 2c) and unspecific deposition occurs. For the intermediate hole density (Fig. 2b), the contact angle is 46° with a surfactant concentration of 20% (v/v) and a filling rate of 99% could be reached. Similar arguments could also be developed to interpret the results obtained with the same hole density but different values of surfactant concentrations (not shown here).

Fig. 3 shows scanning electron micrographs (SEM) of the assembled 80 nm diameter gold particles in holes of diameter 100 nm before (a) and after (b) transfer onto the surface of a glass substrate with a 50 nm thick PMMA layer. A slight penetration of the gold particles into the thin layer PMMA could be noticed. As expected, all holes are filled with particles and all assembled particles could be transferred. The PMMA thin layer can be replaced by other types of thin layer. In particular, the transfer can also be done with the help of a water droplet [16].

In general, if the particle concentration of the solution is sufficiently high, it is possible to fill all template holes. In practice, the filling probability decreases with the hole size of the template. These experimental data obtained in this work are fitted with a parabolic curve, as shown in Fig. 4. This can be understood by considering the fact that the probability of filling a hole of diameter D with a particle size d is proportional to $(D-d)^2$. On the other hand, if the hole size of the template is too large, the particle location would not be accurate. Therefore, the optimized condition would be 100 nm for 80 nm particles.

The fabrication of high density gold nanoparticle arrays is interesting for the fabrication of surface plasmon based bio-sensors. To reduce the signal to noise ratio of the detection, it is important to increase the number of particles per unit area in the weak coupling limit. All data were obtained by using 80 nm particles with 8 nm inter-particle distance. Optical spectra were recorded for the detection of sucrose, bovine serum albumin (BSA), phosphate-buffered saline (PBS) and hexadecanethiols of different concentrations. Plasmon resonance peaks could be identified with the centre-wavelength depending on the sample solution. Increasing the refractive index of the solution or the biomolecule concentration leads to a red shift of the resonance peak. Fig. 5 shows the absorption spectra of the 80 nm gold particle arrays in air, water and sucrose 20%, 40% and 60% (a), in air with and without hexadecanethiols coating (b), and in PBS and 0.1 wt.% BSA incubated in PBS for 100 min before and after PBS washing (c). A red shift of 1.75 nm induced by small molecule (2 nm) coating could be determined. From our data, we obtained device sensitivity ($\Delta\lambda/\Delta n$) of 60–92 nm/RIU (Refractive Index Unit).

4. Conclusion

We successfully demonstrated the feasibility of patterning high density gold nanoparticles on a glass surface and using them as high sensitivity bio-sensors, thus extending the application capability of capillary assisted particle assembly method. Because it is low cost and high throughput and can be potential applied at a large range of particle materials, this method also holds potential for other applications in optics, and electronics or sensing applications in biology.

Acknowledgment

This work was supported by European Commission through project contract CP-FP 214566-2 (Nanoscales) and French National Research Agency through project contract ANR-09-PIRI-0030-03 (PAGDEG).

References

[1] M.T. Blom, E. Chmela, R.E. Oosterbroek, R. Tijssen, A. Van den Berg, Anal. Chem. 75 (2003) 6761.

[2] B. Dubertret, P. Skourides, D.J. Norris, V. Noireaux, A.H. Brivanlou, A. Libchaber, Science 298 (2002) 1759.
[3] V. Studer, R. Jameson, E. Pellereau, A. Pépin, Y. Chen, Microelectron. Eng. 73–74 (2004) 852.
[4] S. Gaugiran, S. Getin, J.M. Fedeli, H. El-Shimy, T. Fukuda, Opt. Express 13 (18) (2005) 6956.
[5] S.S. Guo, C.C. Zuo, W.H. Huang, Y. Chen, Microelectron. Eng. 83 (2006) 1655.
[6] M. Suzuki, T. Yasukawa, Y. Mase, D. Shiku, T. Matsue, Langmuir 20 (2004) 11005.
[7] Y.D. Yin, Y. Lu, B. Gates, Y.N. Xia, J. Am. Chem. Soc. 123 (2001) 8718.
[8] C.L. Cheung, R.J. Nikolic, C.E. Reinhardt, T.F. Wang, Nanotechnology 17 (2006) 1339.
[9] Y.N. Xia, B. Gates, Y.D. Yin, Y. Lu, Adv. Mater. 12 (2000) 693.
[10] S.A. Maier, M.L. Brongersma, P.G. Kik, et al., Adv. Mater. 13 (2001) 1501.
[11] T. Kraus, L. Malaquin, H. Schmid, W. Riess, N.D. Spencer, H. Wolf, Nat. Nanotechnol. 2 (2007) 570.
[12] L. Malaquin, T. Kraus, H. Schmid, H. Wolf, Langmuir 23 (2007) 11513.
[13] J. Shi, C. Peroz, D. Perade, J. Salary, M. Belotti, W.H. Huang, Y. Chen, Microelectron. Eng. 83 (2006) 1664.
[14] M. Geissler, H. Wolf, R. Stutz, E. Delamarche, U.W. Grummt, B. Michel, Langmuir 19 (2003) 6301.
[15] D. Peyrade, M. Gordon, G. Hyvert, K. Berton, J. Tallal, Microelectron. Eng. 83 (2006) 1521.
[16] C. Vieu, A. Cerf, Colloids Surf. A 342 (2009) 136.

Appendix B:

Microfluidic Patch clamp

Introduction

The classic patch clamp technique is considered as the most sensitive technique to study membrane ionic channels within single channel sensitivity. In addition, this technique is used to study neuronal network behaviour with high precision of the measured neuron. We want to study in which extend we can implement this technique in microfluidics to study neurons at different scales: cell and network levels with microfluidic patch clamp on cells and ionic channel level with microfluidic patch clamp on bilayers.

Background

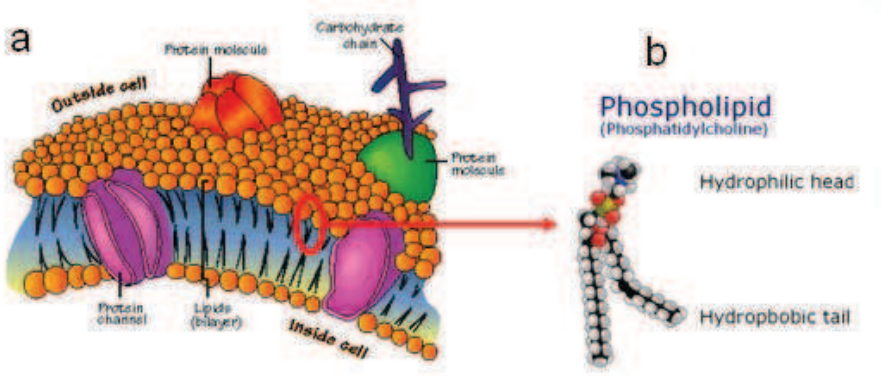

Figure 0.1 (**a**) Cell membrane(from [**1**]).(**b**) Cell membrane Phospholipid. From [**2**].

Cell membrane and Ion Channels

The cell membrane is composed of a thin lipid bilayer (~5nm) of phospholipids: Phosphatidylcholine. The hydrophobic tails are all oriented towards inside of the membrane and the hydrophilic head (polar) are oriented outside making an impermeable barrier between the inside and the outside of the cell. This barrier is impermeable because water molecules cannot cross directly the hydrophobic layer. Transmembrane proteins are specialized in the transport of ions and water soluble organic molecules between inside and outside of the cell. Those proteins are called ions channels.

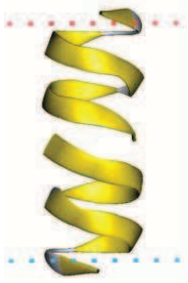

Figure 0.2 Gramicidin A Ionic Channel. From [**3**].

The gating of an ion channel is its way of opening and closing.

We can order ion channels by their gating type or by the ions they let passing through.

Concerning the gating type there is 3 main categories:

- Voltage gated channels
- Ligand gated channels
- Other gating (Inward-rectifier potassium channel, calcium-activated potassium channels, light gated channels, etc…)

Concerning the ions species there is :

- Chloride channels
- Potassium channels
- Sodium channels
- Calcium channels
- Proton channels

Ionic channels are very important for the physiology of the cell and ionic channels malfunctions due to genetic mutations lead to many diseases [4] such as muscles disorders (e.g.: Hyperkalemic periodic paralysis, myotonia, …), neuronal disorders (e.g., epilepsy, migraine,…),some kidney disorders, cystic fibrosis, heart diseases.

Ionic channels are also responsible of electric signal propagation along nerves including neuronal action potential.

The Patch clamp technique

The Patch clamp technique has been invented in by Neher and sakmann in 1976 [**5**]. They have been awarded with the Nobel price in medicine in 1991.

A very thin glass pipette (1-2um aperture) filled with electrolyte and connected to an electrode is placed near the cell. Then a small aspiration is realised in order to make a gigaohm seal between the membrane and the pipette opening.

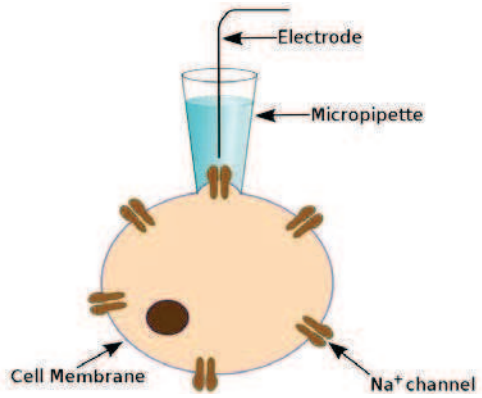

Figure 0.3 Principle of the patch clamp technique (from [**6**])

This technique allow to measure the activity to of single ion channels

The problem of this technique is its lack of automation : the experimenter needs to be well trained to realised a patch clamp efficiently and in one day he cannot realize more than 10 or 20 patch clamp which is a lock for high throughput screening of drugs targeting ion channels.

It is very interesting to implement this technique in microfluidic in order to get the benefits from automation, miniaturization and integration of other component into the device.

1. Patch-Clamp on cells

At the cell and network level the goal is to design a microfluidic device capable of handling cells and performing automated patch clamp on it. At the ionic channel scale the goal is to perform patch clamp on bilayer membrane or artifical cells in order

1.1 Overview of actual microfluidic patch clamp

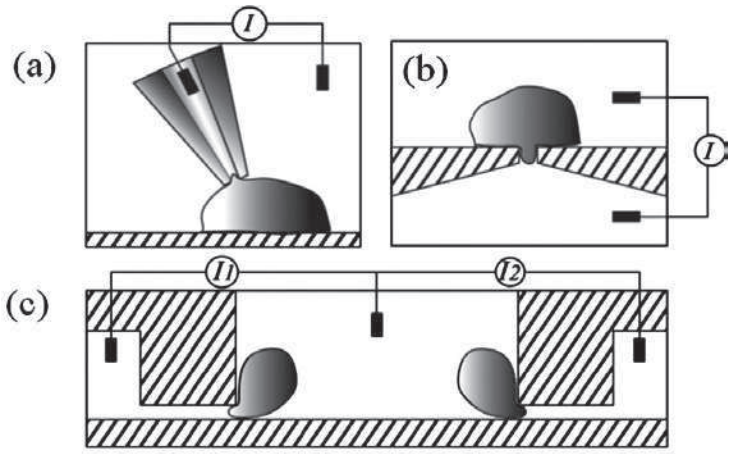

Figure 1.1 Comparison between (**a**) "classic" patch clamp based on glass micropipette. (**b**) Planar patch clamp (c) Lateral patch clamp From [**7**].

There are 2 main families of microfluidic patch clamp:

Planar patch clamp (figure 1.1 b): Cells are aspirated through a small aperture (1-2um) in a membrane. The membrane can be in glass (figure 1.2) patterned with microfabrication techniques. This technique is interesting because it uses classical microfabrication techniques and can be used on glass which is the ideal material for patch clamp: it is an electric isolator and has a small surface roughness which make the cells attach more easily.

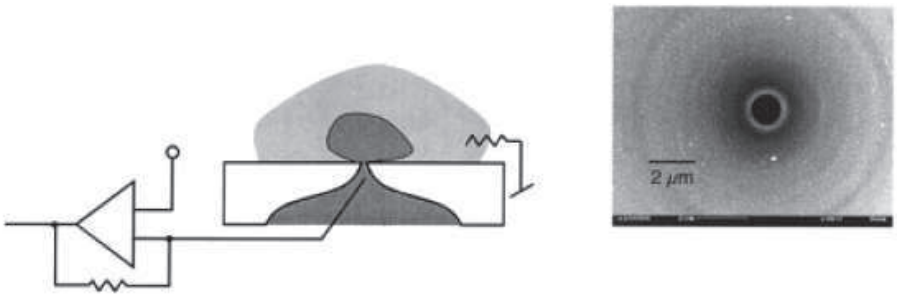

Figure 1.2 Whole Cell Planar patch clamp on an aperture etched in glass (from [**8**])

Some channels can also be made in glass in order to manipulate cells, to bring them on the patch sites (figure 1.3) and to avoid membrane fragments to block patch apertures.

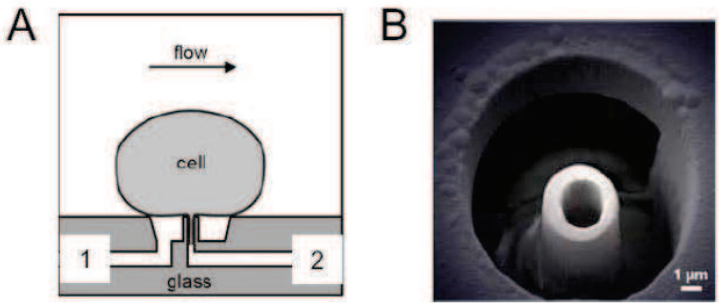

Figure 1.3 The CytoPatchTM chip. (**A**). Cross section. A cell is trapped by suction applied to the large port 1 of the device. Subsequent suction on the central port 2 forms a seal, and currents are recorded through port 2. (**B**). Scanning electron microscope (SEM) image of the device from above. From [**9**].

Some groups [**10**] realised patch clamp aperture in PDMS. The advantage is that it is easier to fabricate and disposable but the success rate of the patch clamp is less good than with glass. The other advantage of planar patch clamp is that it is easy to integrate with microeletrode arrays to realise multiple recordings.

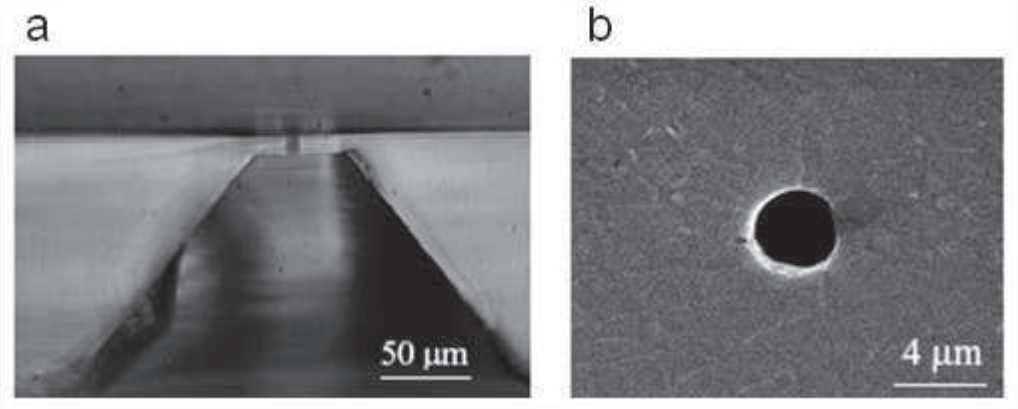

Figure 1.4 PDMS Patch-Clamp aperture (**a**) side view of a sliced partition (**b**) SEM picture of a molded aperture .From [**10**].

Lateral Patch clamp (figure 1.1 c): Cells pass through a main channel and are trapped by smaller channels (2-3um) perpendicular to the main one. This kind of device is entirely made in PDMS. The advantage are multiple : It is easy to fabricate and disposable; The measure can be multiplexed in order to record many patch clamp experiment in the same time; it is possible to monitor optically the patch clamp process and we can incorporate classical microfluidic elements such as mixer, gradients etc… in order to build a complete lab-on-chip device. The main disadvantage is that the PDMS is not ideal for making gigaseals because of the surface roughness.

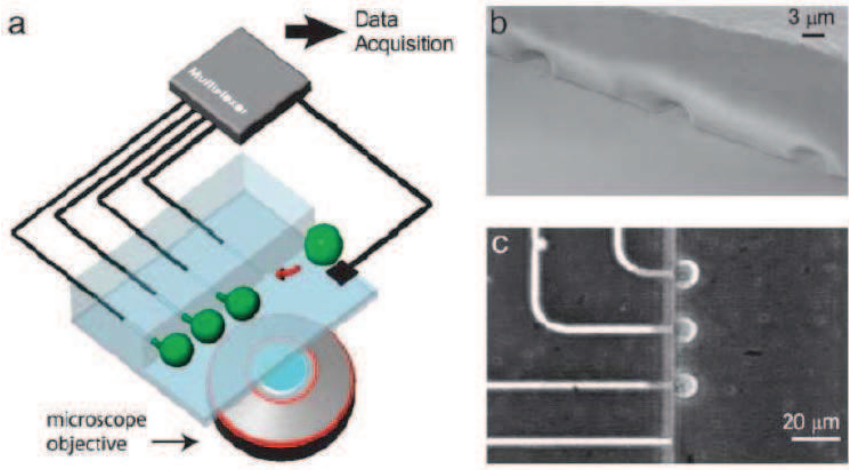

Figure 1.5 Side trapped patch-clamp array on a microfluidic platform. (**A**) Cell trapping is achieved by applying negative pressure to recording capillaries, which open into a main chamber containing cells in suspension. Patch clamp recordings are obtained by placing AgCl electrodes in each of the capillaries, as well as in the main chamber. The device is bonded to a glass coverslip for optical monitoring. (**B**) Scanning electron micrograph of three recording capillary orifices as seen from the main chamber. (**C**) Darkfield optical microscope image of cells trapped at three capillary orifices. From [**7**].

We choose to study how to implement the lateral patch clamp because of its simplicity and the possibility to use classical inverted microscope to monitor in real time progression of the patch clamp as well as checking viability of the cell culture.

1.2 Work of the first year

1.2.1 Chip fabrication

In order to do a prototype of the device before doing an optical mask, a prototype as been designed using existing masks. The layout is the following:

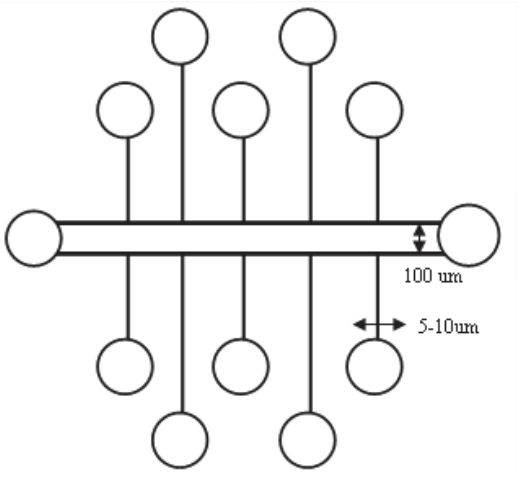

Figure 1.6 Layout of the cell patch clamp chip V1.0

The device is constituted of 2 layers of channels: one layer is the main channel which is 100um wide and will receive the cells in the buffer solution. The other layer of channels is for trapping cells by aspiration and doing the patch clamp.

We used the following process

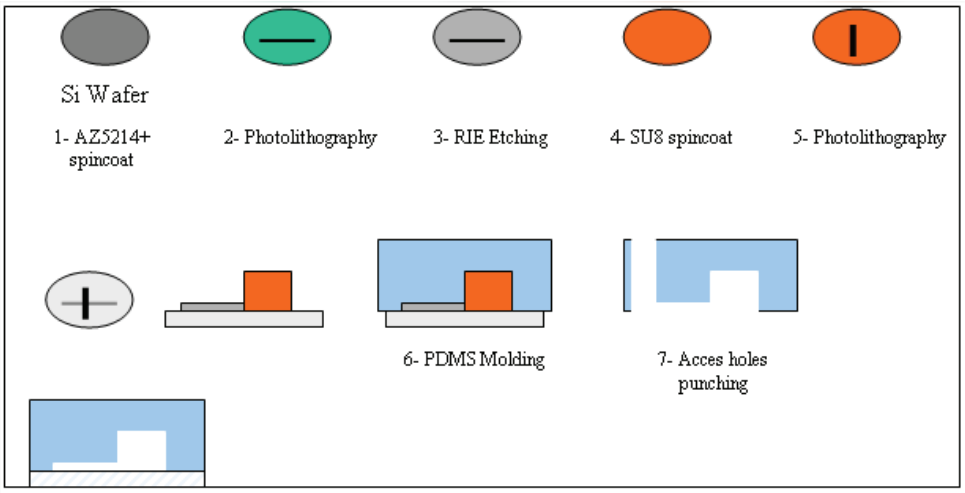

Figure 1.7 Process of device fabrication

For the first layer (patch channels) a photolithography is realised with AZ5214 to obtain 1um layer. We use this layer as a protection for RIE etching in order to reach a thickness of 5um. The second layer is realised in SU8 2050 to get a channel thickness of 20um. After surface treatment avoid PDMS to stick to the mold (TMCS 3'),PDMS (5:1) is casted. We used 5:1 mixing ratio in order to avoid possible collapse of smallest channels. After baking overnight, the device is unmolded and access holes are punched. The device is bonded on a glass slide.

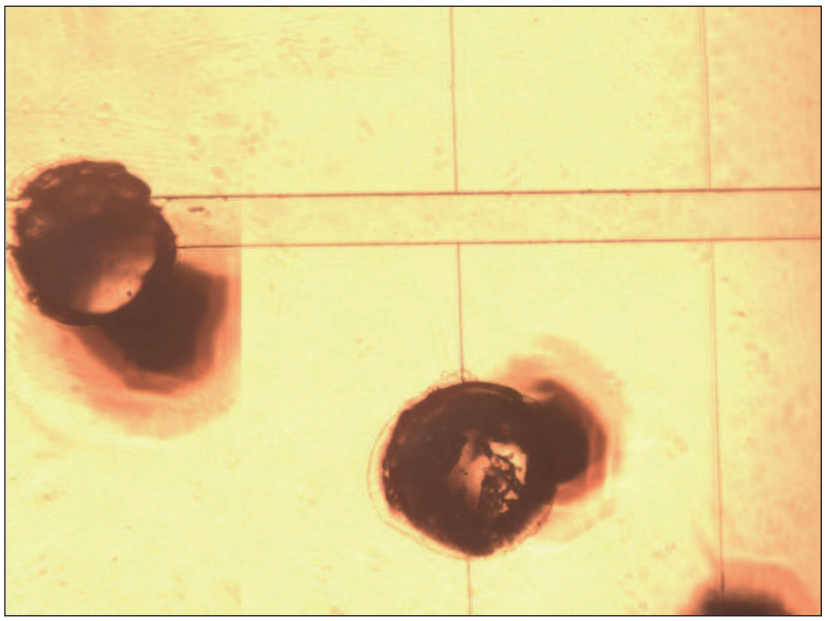

Figure 1.8 Picture of the device

1.2.2 Results

The setup is the following:

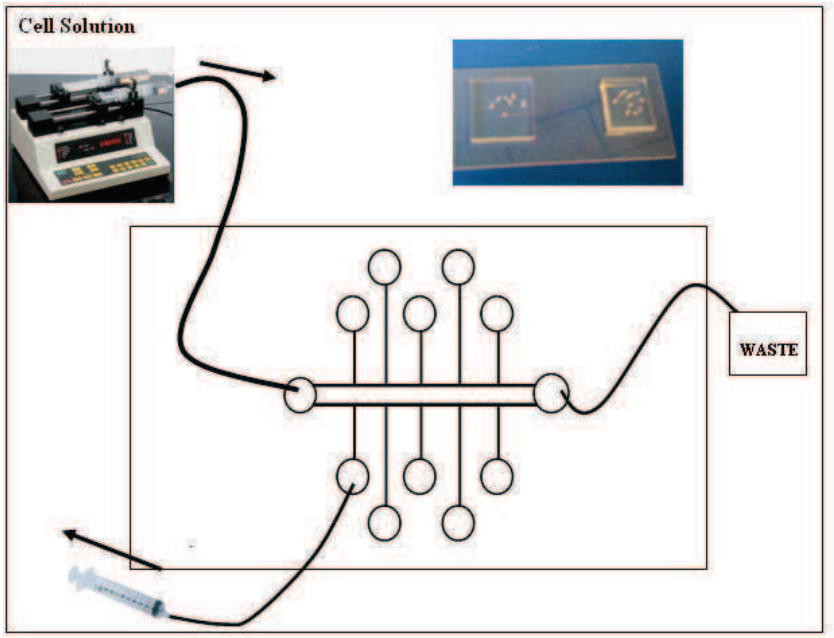

Figure 1.9 Experimental setup

The cells suspension (K562-RPMI 1640 with 10% serum) is injected in the device with a syringe pump (Harvard apparatus) with the lowest flow possible (1uL/h). The outlet is connected to a waste collector. A syringe is connected to the patch channel in order to realise cell aspiration by applying negative pressure. We can also push on the syringe to release cells from the aspiration site. The whole process is monitored in real time with an Olympus inverted microscope.

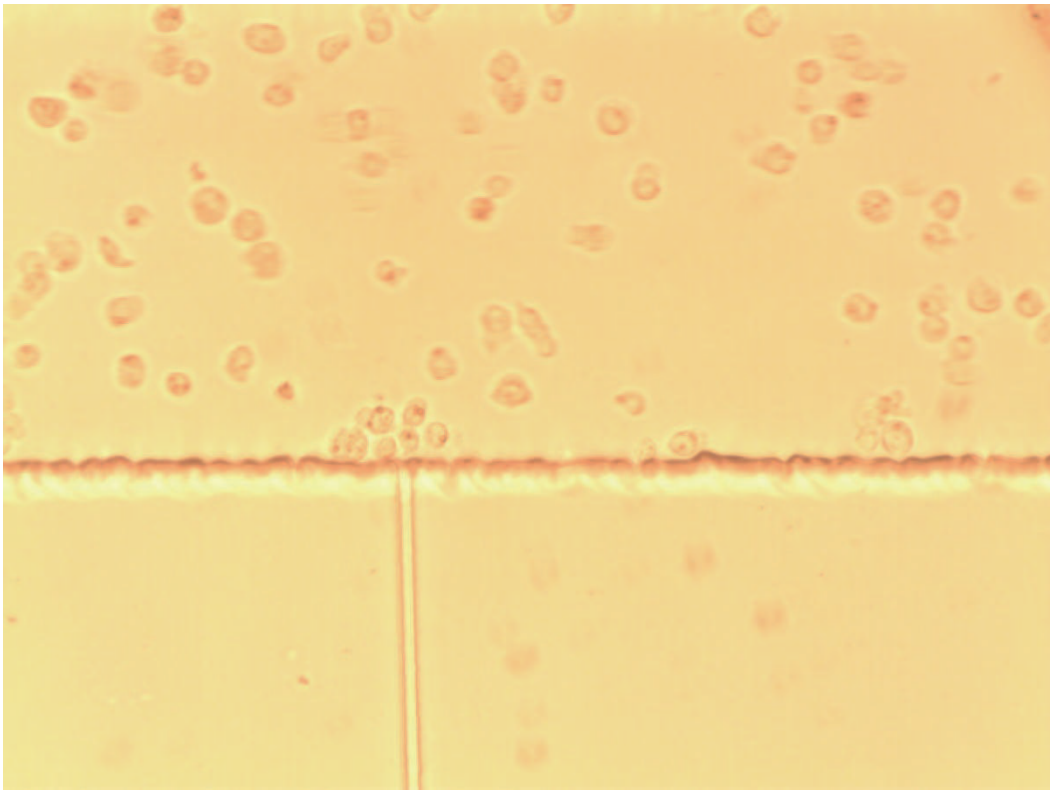

Figure 1.10 Aspiration of cells with the patch channel.

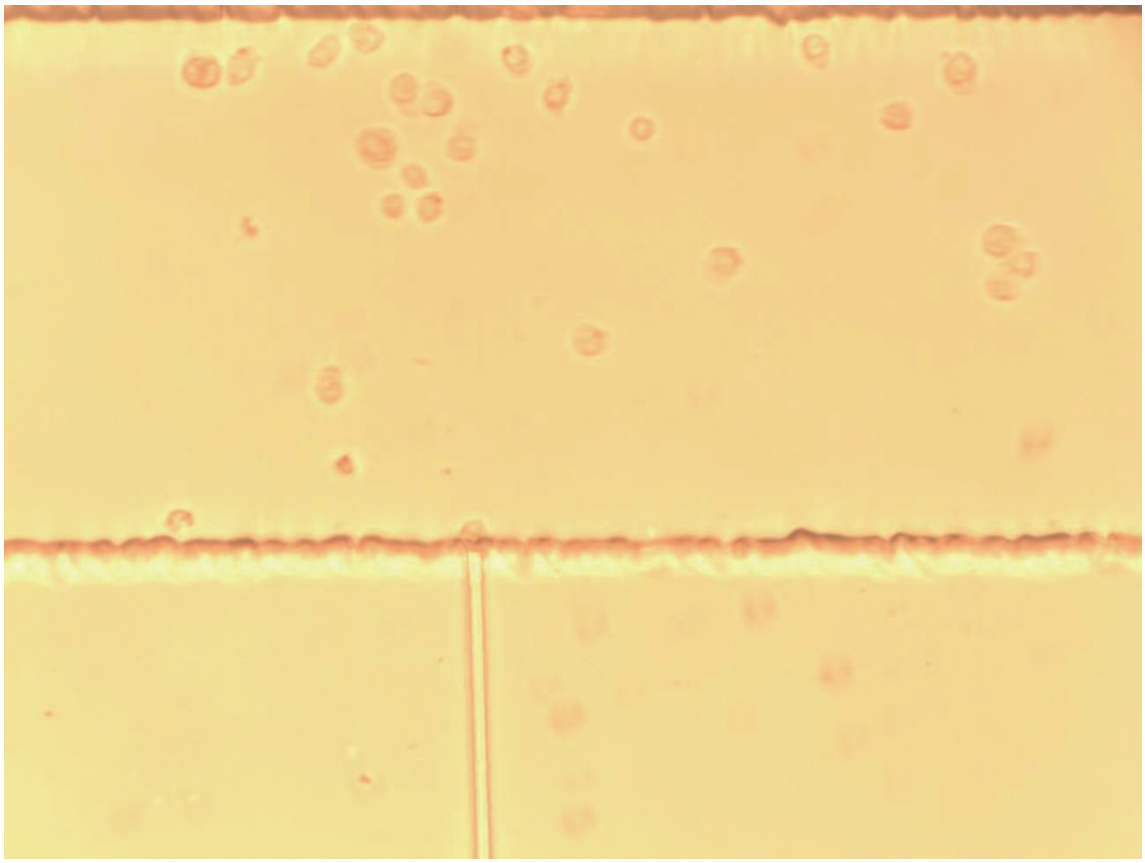

Figure 1.11 Aspiration of a single cell with the patch channel

We managed to “trap” single cells at the opening of the patch channel (Fig. 1.11). When the cell suspension flow is very low it is easy to target visually the cell we want and to trap it by applying negative pressure and then, release it by applying positive pressure. We can also apply positive pressure in order to avoid unwanted cells to be trapped.

1.2.3 Evaluation and Improvements

This prototype validates the design of lateral patch clamp. The next step is to incorporate electrodes in order to get an accurate evaluation of the design in terms of patch clamp performance (% of successful patch clamp/nb of test).

The Ag/AgCl electrodes have been designed and fabricated (cf. Project 2) but the missing point was the bonding between electrode passivation layer (SU8) and PDMS of the channels. This blocking point can be passed by replacing SU8 passivation layer by PhotoPDMS (cf. process in annex) or SiO2 or Spin On Glass.

The next version of the design will incorporate smaller size patch channels (2um).

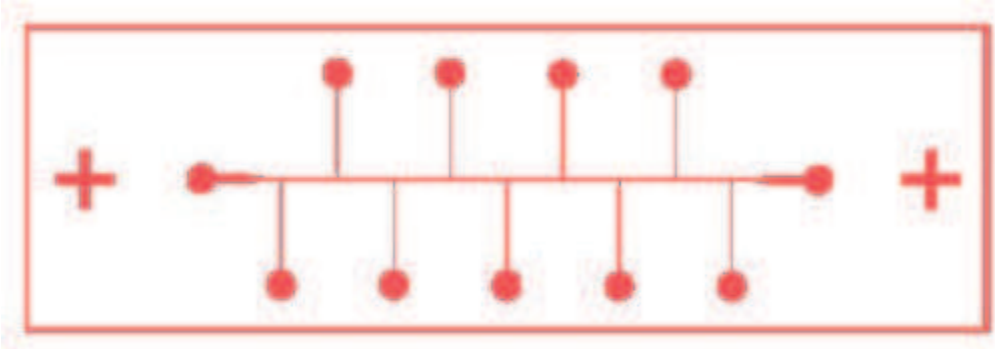

Figure 1.12 Layout of the patch clamp device V1.1

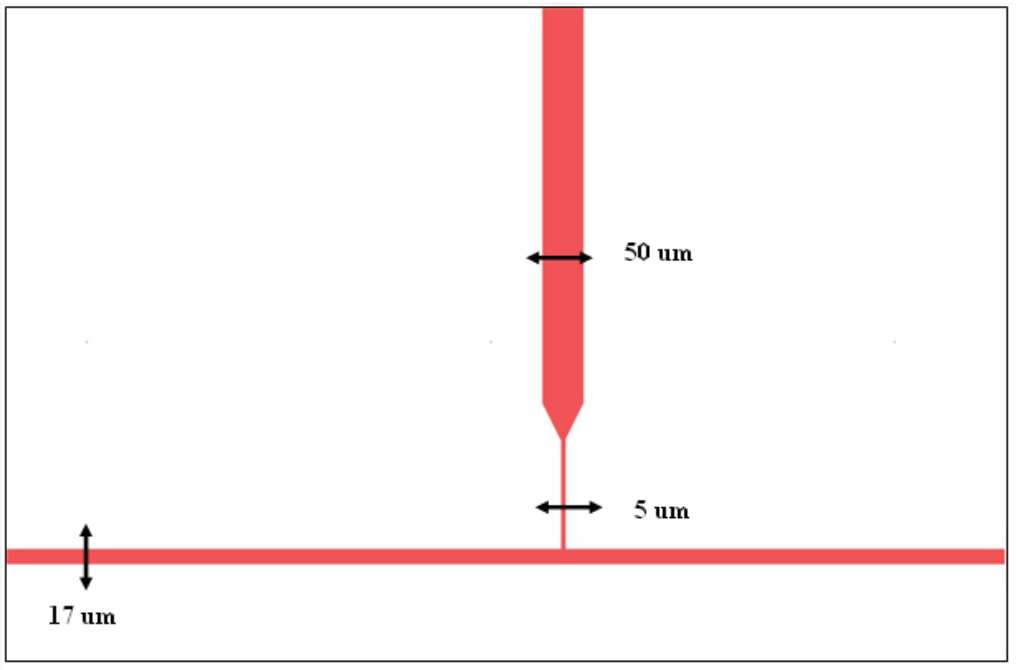

Figure 1.13 Layout of the patch clamp device V1.1

After the validation of this design and the incorporation of electrodes, we will design channels to manipulate cells in the channel in order choose precisely the moment when we want the cell to be aspirated by the patch channel and in order to avoid fragment of cells to collapse the patch channels. We will also study different channel geometries and incorporate other microfluidic component components.

In a longer term we will try to use this device on growing neurons. The challenge will be to be able to sustain neuron growth until they are able to emit action potentials and without creating flows that kill neurons.

1.3 Conclusion

We managed to realise the first steps before being able to do a real lateral patch clamp. This technique seems to be promising and from our knowledge has never been used for analysing neuronal growth in real time.

2. Patch clamp on Bilayer Lipid Membranes (BLM)

After discussions with Prof. Loic Auvray we decided first to realise membrane formation in "macro" environment with commercial apparatus by using the conventional "painting" technique (Figure 2.1a). The membrane formation is not so complicated but only when all the equipment is well set up and the good parameters found. We choose also to make this experiment in macro in order to have a way to compare performance and sensitivity of the microfluidic device we intend to design.

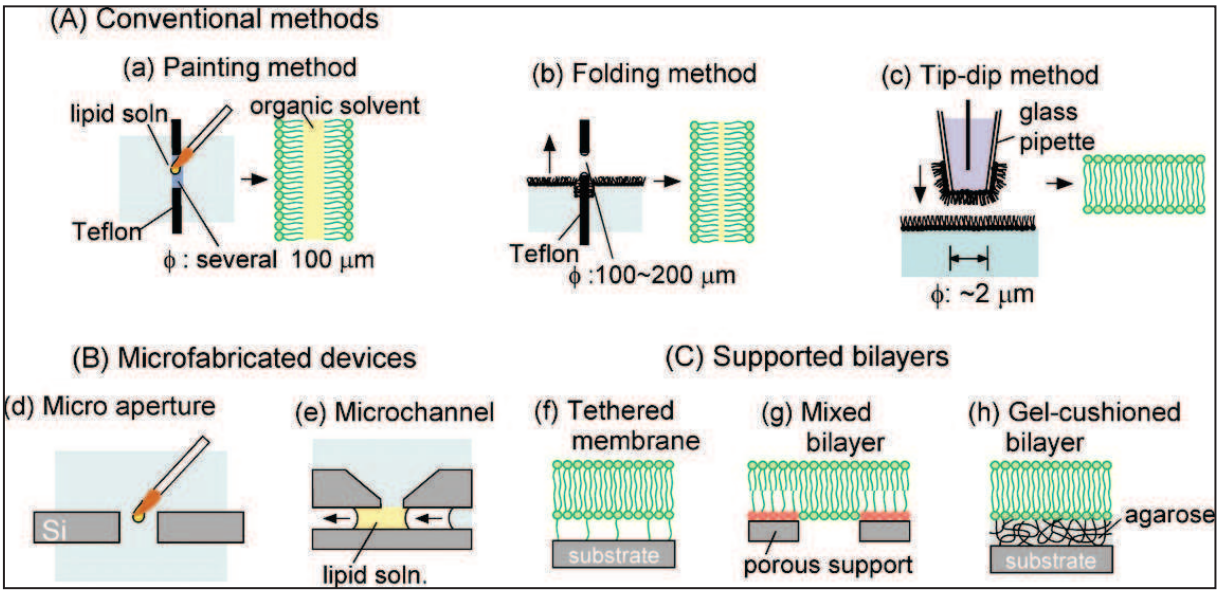

Figure 2.1 Conventional and microfabricated methods for preparing lipid bilayers. From [11].

The more conventional techniques for BLM formation are the painting method (Figure 2.1 a) and the folding method (Figure 2.1 b). The painting method is easier to realise but BLMs formed by this technique contains solvent that make the BLM thickness decrease during experiment. The folding method is solventless because all the solvent is evaporated before contacting the two monolayers. We choose to use first the painting technique to learn how to make BLMs and characterise them.

2.1 Formation of a Bilayer Lipid Membrane using the "painting" technique

We bought a bilayer chamber (Warner instruments BCH-22A) and a Teflon cuvette with a 250um aperture (**Figure 2.2**).

Figure 2.2 Bilayer Chamber and cuvette

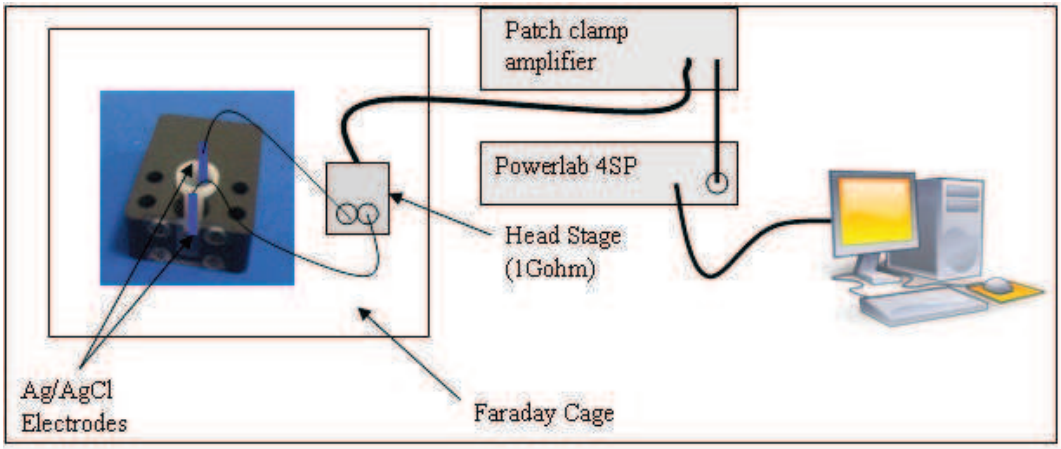

Figure 2.3 Setup of the Bilayer station

The Bilayer chamber and cuvette are in a faraday cage to avoid electromagnetic noise. The 2 Ag/AgCl electrodes are connected to the head stage of the patch clamp amplifier (Biologic BLM-120) which is interfaced to a computer through an analogic to digital converter (ADInstrument Powerlab 4SP). The 2 Ag/AgCl electrodes are made from pure silver wire dipped into sodium hypochlorite NaClO (from household bleach : chlorox 2%) for few minutes in order to generate a thick layer of AgCl.

2.1.1 Process of Bilayer formation.

We followed the process made by Abdelghani Oukhaled (Université Evry) in his PhD thesis [**12**]:

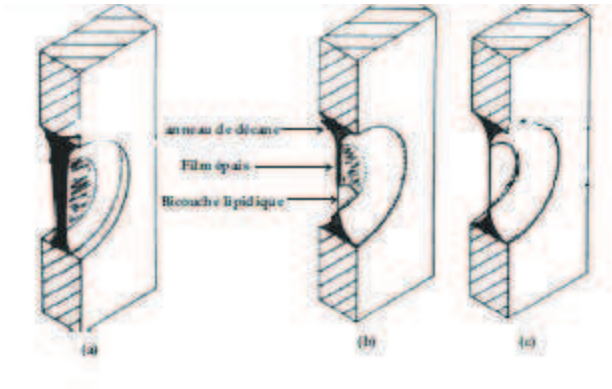

Figure 2.4 Process of Bilayer formation with the Mueller and Rodin technique. From [**12**].

First the cuvette is well cleaned (acetone, isopropanol) and dried under azote flow. The measurement apparatus is turned on at the time in order make it stable but input is not enable in order to avoid overload.

Then, we "precoat" the aperture with a small droplet of lipid solution (DPhPC 0.025%, Avanti Polar) and wait 30minutes for the solvent to evaporate. This step is essential for stability of the bilayer.

We place the electrodes connected to the measurement apparatus to the 2 partitions and we fill the 2 partitions with KCl solution (1M). The input is turned on it should "overload" that means that too much current is flowing between the two electrodes and so that there is no bilayer yet.

A pipette is loaded and unloaded with a small volume of lipids in order to put the smallest amount of lipids inside. An air bubble is formed in the chamber near the aperture and should pass on the aperture in order to form the bilayer.

If the bilayer is well formed the current is blocked, there no more overload and the current flowing between electrodes should be of the order of few pA (**figure 2.4**).

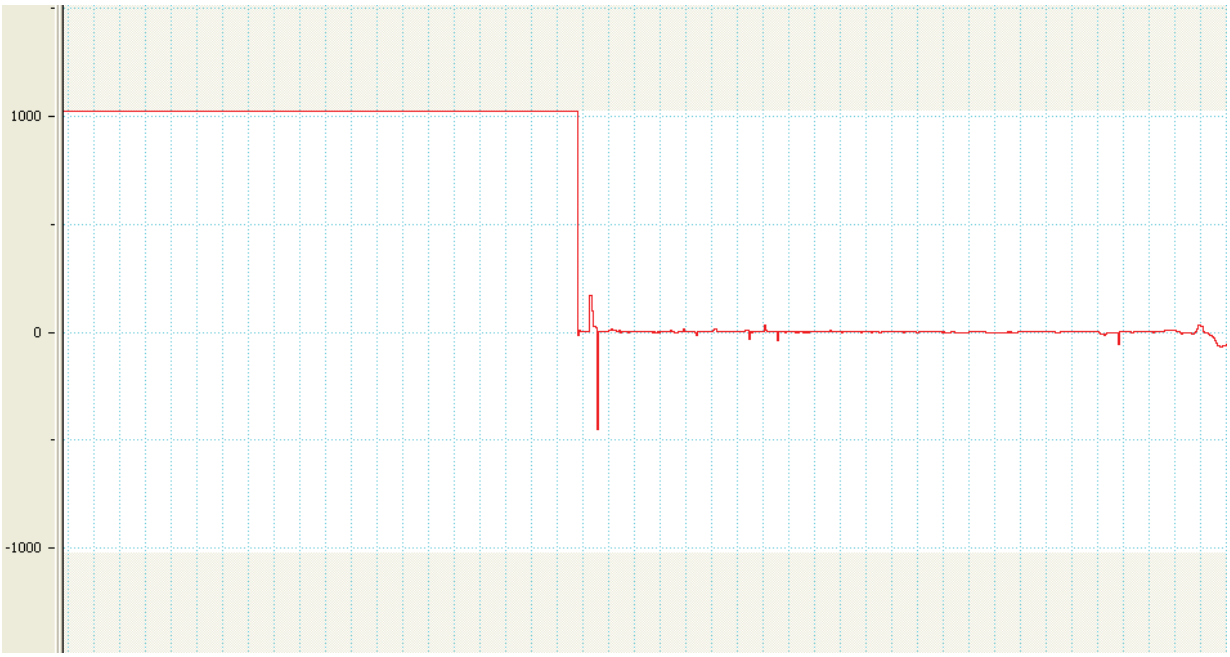

Figure 2.5 Recording of the current blockage when the bilayer is formed

We can monitor bilayers's thickness in real time by measuring its capacitance. The capacitance will increase with time because of the solvent evaporation. We can measure capacitance directly on the patch clamp amplifier.

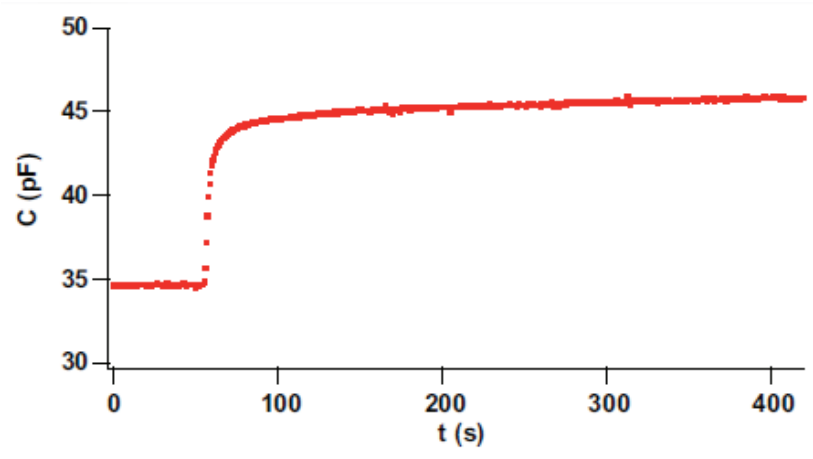

Figure 2.6 Evolution of capacitance of a Bilayer in time. From [12]

It means that the membrane become thinner. At the beginning the capacitance is 34pF, it correspond to a 9.2 nm thick bilayer. After 400 seconds it reach 45pF which correspond to a 6.8nm thick bilayer. At the maximum the capacitance can be around 85pF.

We can also apply a differential potential in order to realise an electroconstriction of the bilayer and so to make it thinner.

2.1.2 Incorporation of nanopores (alpha-hemolysin)

The solution of alpha–hemolysin (sigma Aldrich) is prepared with a concentration of 0.1mg of alpha-hemolysin for each ml of HEPES buffer.

This solution is stored in the freezer (-20°C) and should be bring at room temperature just prior to experiment to avoid protein denaturation.

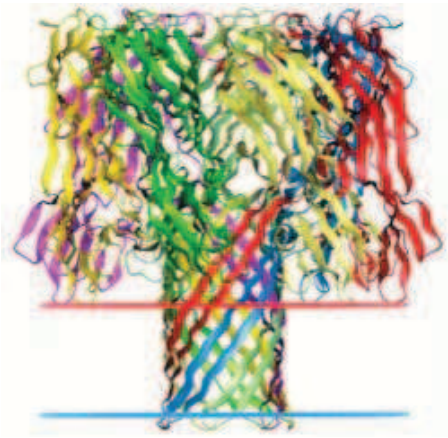

Figure 2.7 Structure of the Alpha –Hemolysin nanopore. From [13].

When the bilayer is thin enough (45pF-85pF/7-5nm) 10ul of alpha-hemolysin solution is injected into one of the partition of the chamber. A potential is applied between the two electrodes (100mV) the negative electrode should be the one in the partition with alpha-hemolysin. It is important to wait until the bilayer is very thin otherwise the ionic channels cannot incorporate into the membrane.

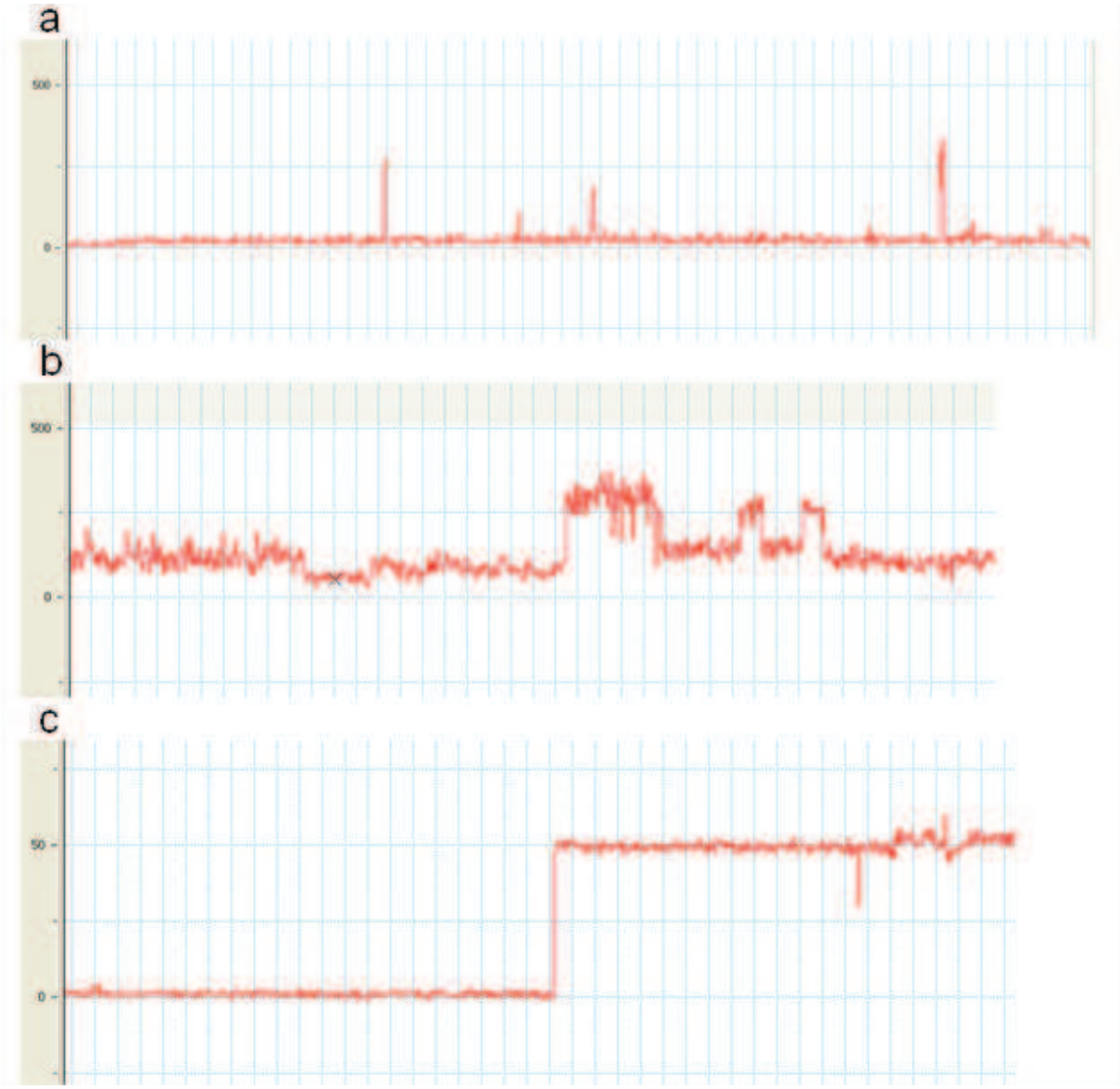

Figure 2.8 Recording of the current after incorporation of alpha-hemolysin (unit pA)

We observe some plateau corresponding to different number of nanopore in the membrane.

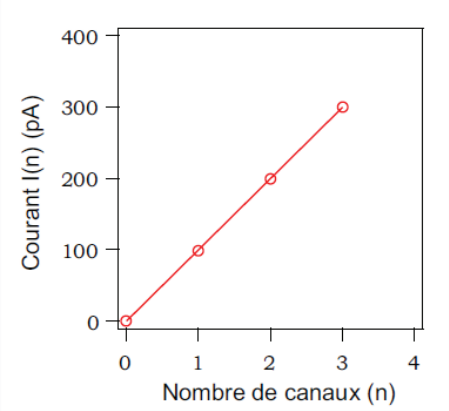

Figure 2.9 Curve representing the current in function of the number of alpha-hemolysin nanopore inserted in the membrane. From [**12**]

2.2 Overview of BLM formation microfluidic channels

The main technique of bilayer formation in microfluidics is the formation of a bilayer through a micro-aperture in silicon or glass.

There is few publications on formation of bilayers in microchannels. We wanted to study what can be the simplest system to form bilayers in microchannels.

Funakoshi et al. in 2006 demonstrated that it is possible to form bilayer in microfluidics by contacting 2 monolayers of lipids.

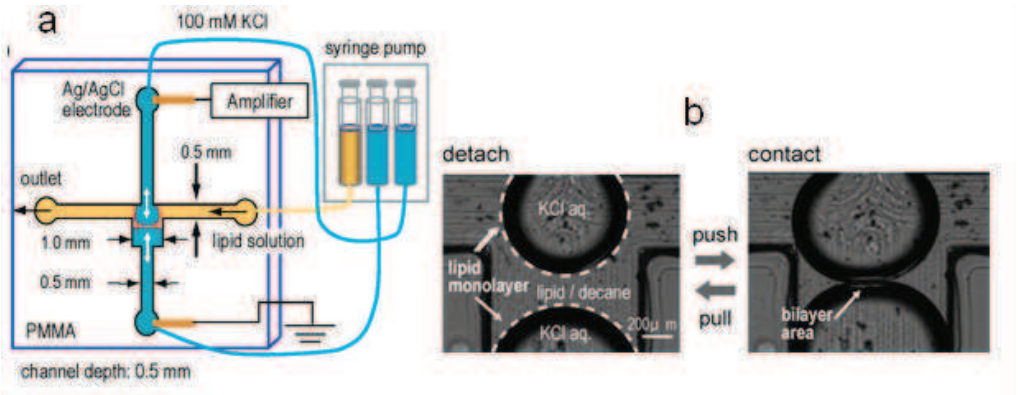

Figure 2.10 Formation of bilayer in microchannels by contacting 2 monolayer. From [**14**]

Their design is very interesting because it is very simple: a cross channel and 3 syringe pump. The device is made in PMMA in order to avoid solvent leakage because PDMS permeability to solvents. Two monolayers of KCl are put in contact at the intersection with lipids. At each

interface KCl/lipid there is a monolayer of lipid and when the 2 monolayer are contacted it make a stable bilayer

Malmstadt et al. [**15**] have an interesting approach : they use PDMS but instead of trying to avoid solvent leakage, they use PDMS solvent permeability to form solventless bilayer which increase reproducibility and sensitivity of measurements.

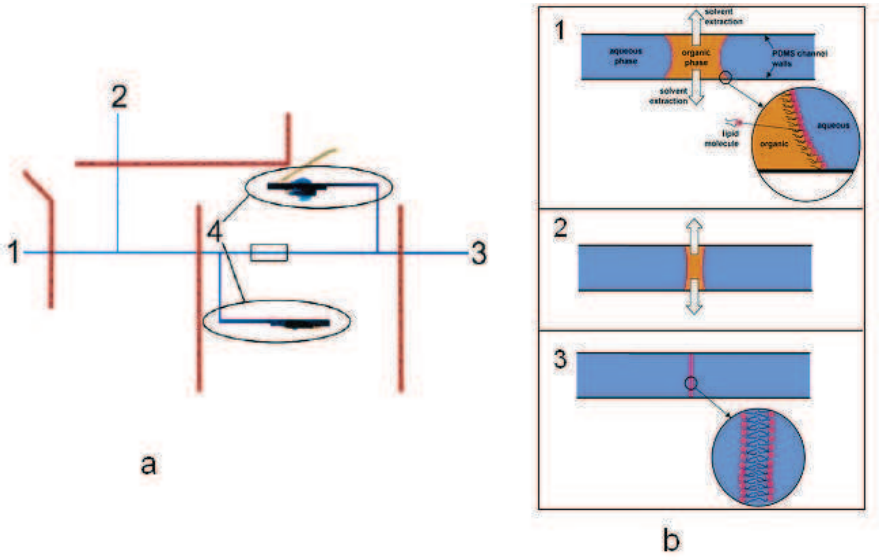

Figure 2.11 (**a**) Layout of the device (**b**) Principle of solvent extraction.From [**15**].

The device is constituted of a simple T channel, two inputs, two electrodes and valves to isolate each part of the device. A droplet of lipids is sent in water to the middle of the 2 electrodes, the valves are closed and the solvent begin to evaporate (figure 2.11b).After few minutes all the solvent is evaporated and the bilayer still isolate the two electrodes.

2.3 Design a microfluidic bilayer formation device

2.3.1 BLM V1.0

We choose first to try to redo the experiment made by *Funakoshi et al.* [**14**] to have a very easy bilayer formation device.

Fabrication of the channels:

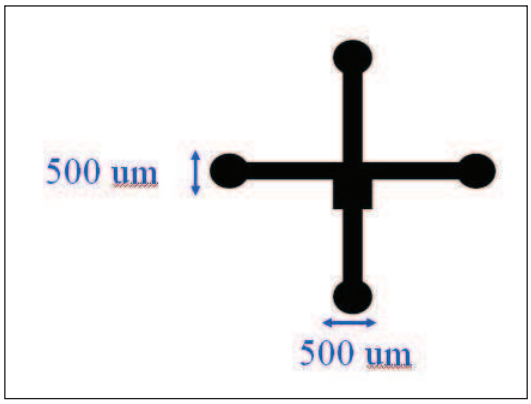

Figure 2.12 Layout of the BLM Chip V1.0

Results

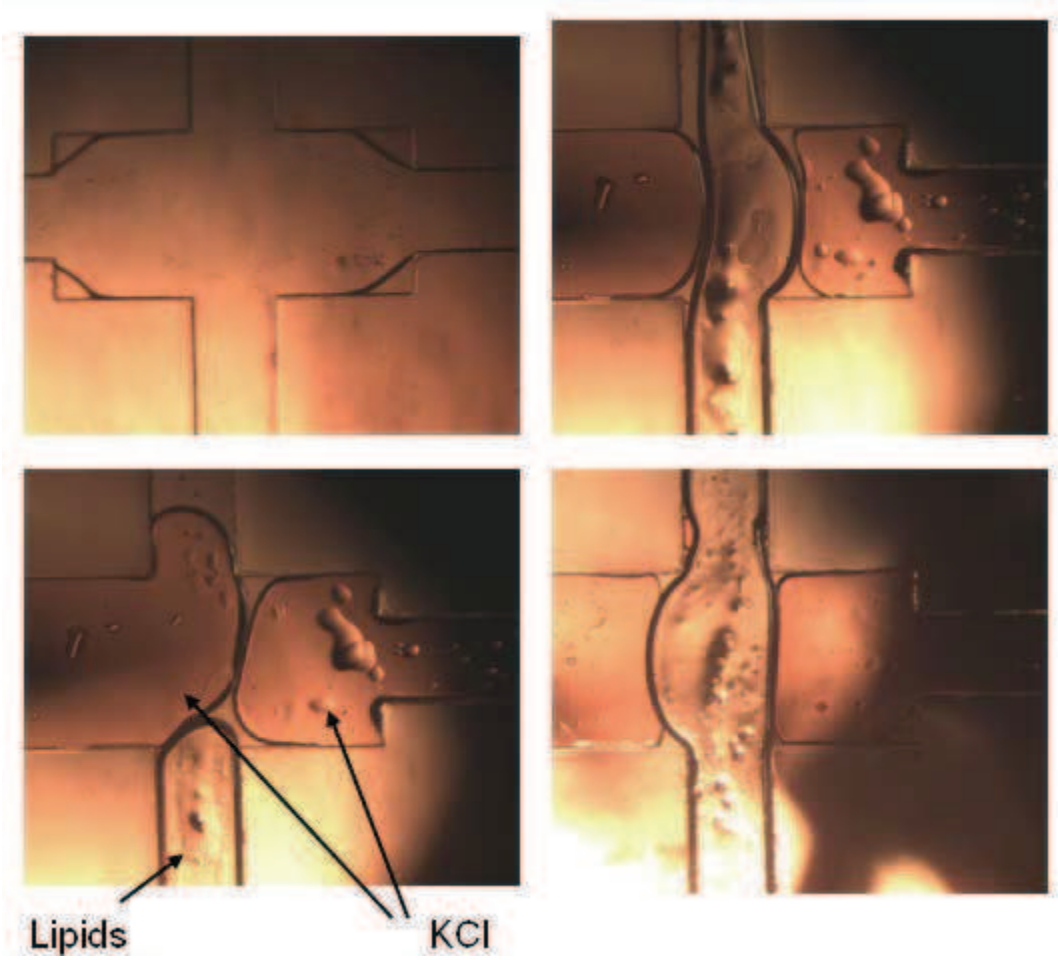

Figure 2.13 Attempts to form a bilayer from contacting monolayers of lipids

Conclusion

It was too difficult to control precisely the formation of the bilayer because the interface between lipids and KCl is very unstable. In addition the main benefits of doing microfluidics is reduction of volume of solutions and so reduction of the cost of operation but this design uses 1mL of high concentrated lipid solution which is very expensive.

For the next version of the device we will change the design for a more stable one.

2.3.2 Fabrication of the Ag/AgCl electrodes:

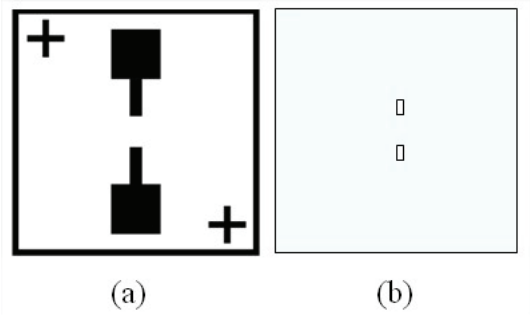

Figure 2.14 Layout of the Ag/AgCl electrodes (**a**) and of the dielectric layer (**b**).

We choose to make Silver-Silver Chloride electrodes because it is the most common electrode used in electrophysiology, it is easy to make and regenerate. Ag/AgCl electrode has also small impedance which makes them suitable for measuring small current.

We need also a dielectric (**b**) which let the solution contact only the area where there is silver chloride.

Fabrication of the electrodes

Glass slide is cleaned and patterned with reversible photoresist (AZ5214). After exposure and development of the photoresist, silver is deposited by e-beam and the resist remaining is lift-off in acetone overnight.

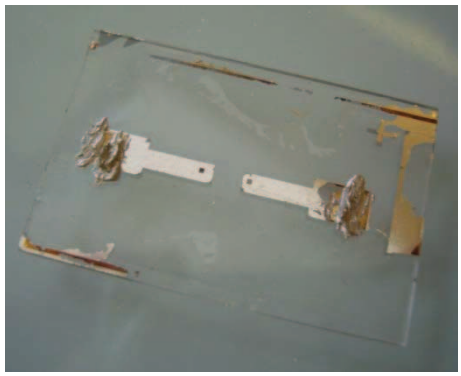

Figure 2.15 Picture of the Ag electrodes

Test of different dielectric layers

SU-8 (2050) photoresist is spin coat on the electrode and the photolithography is realised. After development it let appear silver only for contact pads and the active area of the electrodes.

Figure 2.16 SU-8 Passivation layer on Ag electrode

A droplet of NaClO is put on the silver of the active areas for 5 minutes. We can see clearly the AgCl formed on those areas.

The wires are stuck to the contact pads with conductive glue and the device is put in plasma cleaner for bonding with fluidic channels.

Result

The SU8 photoresist does not bond with PDMS and so the device is leaking.

In order to solve this problem we developed the same process by replacing SU8 by photosensitive PDMS (c.f. process in annex).

Figure 2.17 Test of the photoPDMS

The bonding is better but only if we use a different formulation of PDMS between passivation layer and channels (for example the photoPDMS is 5:1 and the channels are 10:1).

The best solution would be a deposition of SiO2 but the equipment we have in the lab cannot allow us to deposit the 1um layer of SiO2. An alternative can be a spin coating of spin-on-glass polymer followed by high temperature backing but it require a high temperature furnace..

Characterisation of the electrodes

A small current (5nA) is passed thought the electrodes to see when the potential drift occurs. The potential of the electrodes remained 0 for at least 24h the KCl solution evaporated before we could find any change of potential. It means the Ag/AgCl we made are stable in time.

2.3.3 BLM V2.0

For the second version of the device we choose to test the design from Malmstadt et al. [**15**].

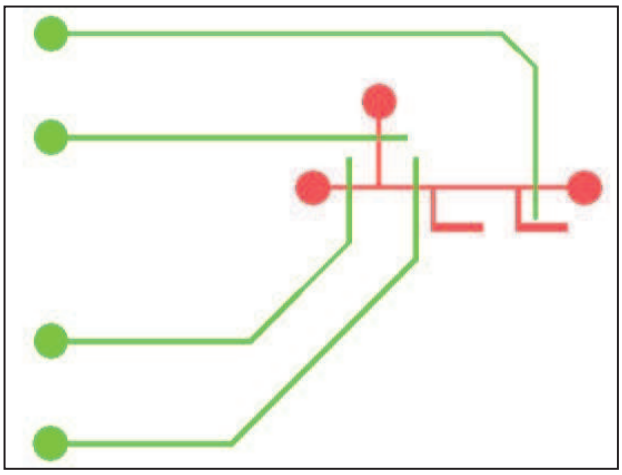

Figure 2.18 Layout of the BLM Chip Channels V2.0

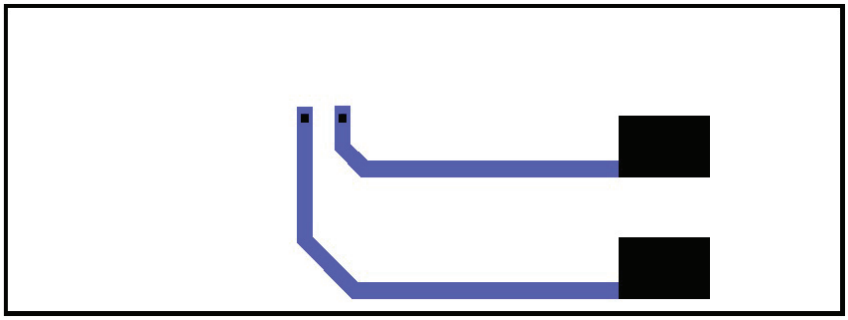

Figure 2.19 Layout of the BLM Chip electrodes V2.0

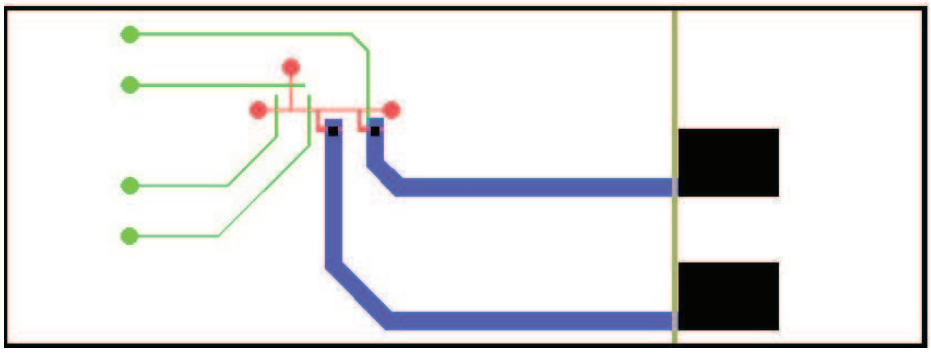

Figure 2.20 Layout of the BLM Chip V2.0

The device is constituted by three layers : A layer of electrodes(**figure 2.20** blue part), a passivation layer (**figure 2.20** black parts), a layer of fluidic channel (figure 2.18 red channels) and a layer of valves **fig 2.18** green channels).

Before to realise this device, we had to find the good process of valve fabrication.

Fabrication of valves

Quake's research group at Stanford University has been the first group to use elastomeric properties of PDMS to realize pneumatically actuated valves [**16, 17**]**.**

They use a cross channel architecture composed of two levels: an actuation channel that will contain air to apply pressure on the fluidic layer to close it (**figure 2.21 c**) and a fluidic layer where the liquid flows. There is two main configuration : the push-down configuration (**figure 2.21 a**) where the actuation layer is on the top of the fluidic layer and the push-up (**figure 2.21 b**) where the fluidic layer is on the top of the actuation layer.

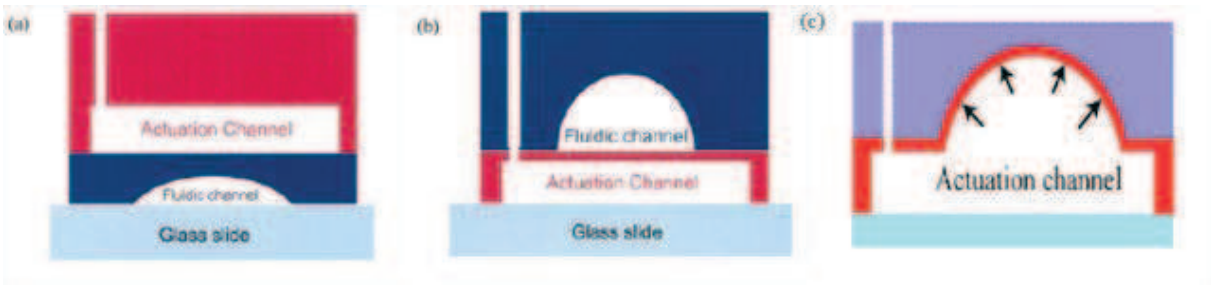

Figure 2.21 Pneumatically actuated valves (**a**) Push down configuration (**b**) Push-up configuration (**c**) Push-up valve activated. From [**17**].

The principle of fabrication is a 2 step soft lithography: the membrane layer is spin coated in order to get a thin layer and the other layer is molded. The two layer are bonded together by plasma and baked overnight before unmolding (**figure 2.22**).

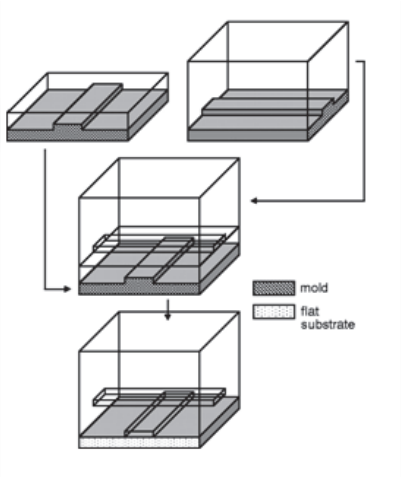

Figure 2.22.Principle of multilayer soft lithography. From [**16**].

The key of the success for the bonding between the two layers of PDMS is the difference of PDMS formulation between the two layers: one layer is in PDMS 5A:1B (for push-down configuration the actuation layer) and the other in PDMS 10:1 (for the push-down configuration the fluidic layer). In the 10A:1B PDMS there is excess of vinyl groups that will diffuse at the bonding interface to the other layer (5A:1B) where there is excess of Si-H groups. The result is an excellent bonding between the two layers.

We choose to use the push-down configuration as it is less sensitive in terms of membrane thickness and easier to realise. We followed the process 1 based on photolithography parameters and valve fabrication process of M. Lounaci [**17**].

The key of the success for valves fabrication is to get round fluidic channels to make it close completely. This is done by baking photoresist after its vitreous transition temperature in order to make it “reflow” and get round features. We get this by using AZ9260 photoresist and baking it at 140°C for 5 minutes.

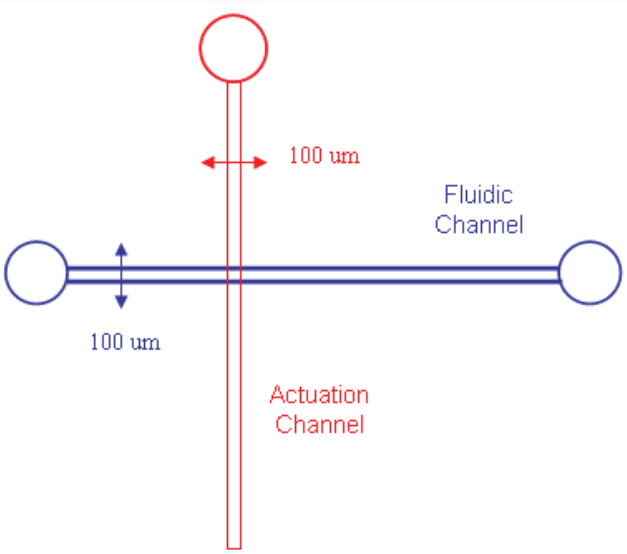

Figure 2.23 Design of the valve

Results

Those pictures are made with an inverted microscope.

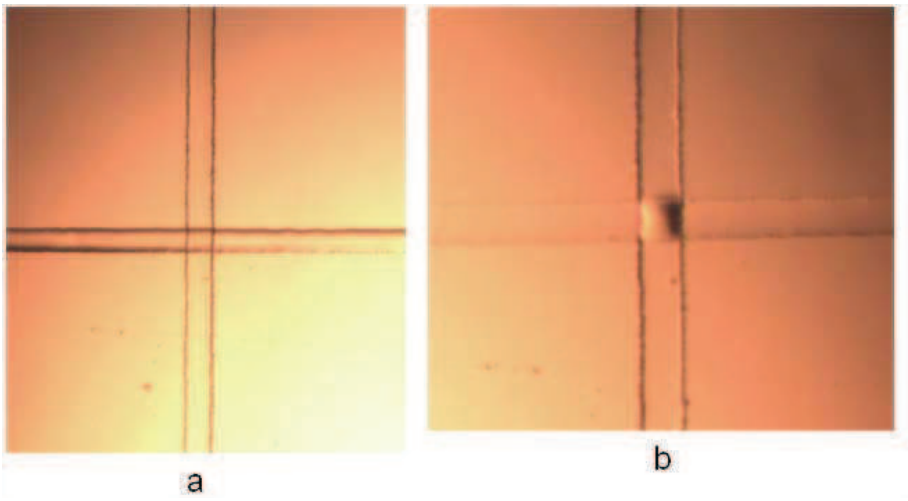

Figure 2.24 Overview of device (**a**) opened (**b**) closed without water in the main channel

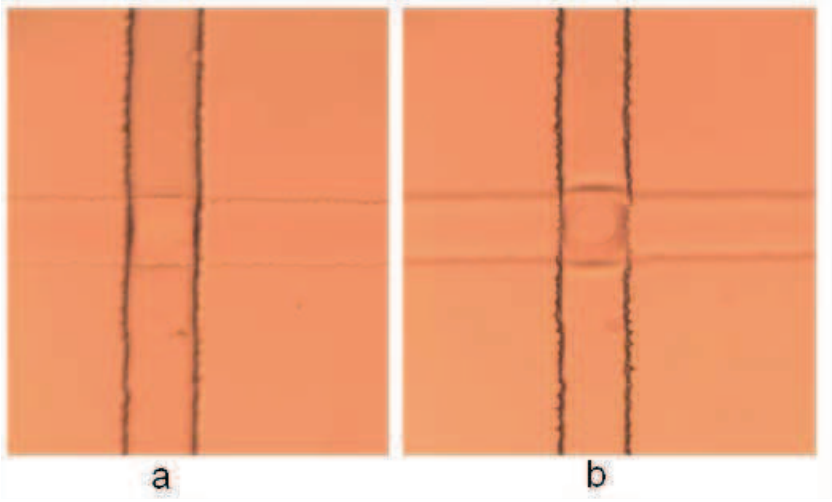

Figure 2.25 Valve operation (**a**) opened (**b**) closed

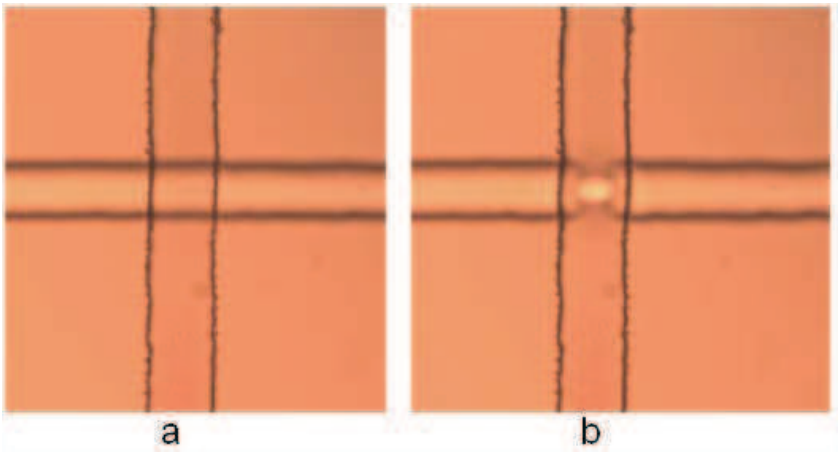

Figure 2.26 Valve operation (**a**) opened (**b**) closed

We flow water in the fluidic channel with a syringe. The valve is operated with air pressure. When we inject air to the actuation layer, the fluidic channel on the bottom is deformed the valve is closed.

The valve is opening and closing well and there is no more flow in the fluidic channel. It means that the membrane is thin enough to be deformed by the air flow (around 2 P.S.I).

2.4 Conclusion

The process of valves is working well and integrated with BLM V2.0 it should lead to a functional device. We had problems to equilibrate pressure in the BLM V1.0 design of channels. This will be solved by the integration of valves that will isolate Bilayer formation zone.

3. References

[1] http://library.thinkquest.org/C004535/cell_membranes.html

[2] http://en.wikipedia.org/wiki/Cell_membrane

[3] http://opm.phar.umich.edu/protein.php?pdbid=1grm

[4] B. Dworakowska and K. Dolowy: Ion channels-related diseases. Acta biochimica botanica, Vol. 47 No. 3/2000**,** 2000.

[5] E. Neher, and B. Sakmann: Single-Channel Currents Recorded from Membrane of Denervated Frog Muscle-Fibers. *Nature* 260(5554):799-802, 1976.

[6] http://en.wikipedia.org/wiki/Patch-clamp

[7] J. Seo, C. Ionescu-Zanetti, J. Diamond, R. Lal and L.P. Lee : Integrated multiple patch-clamp array chip via lateral cell trapping junctions. *Applied Physics Letters* 84(11):1973-1975, 2004.

[8] N. Fertig, R.H. Blick, and J.C. Behrends: Whole cell patch clamp recording performed on a planar glass chip. Biophysical Journal 82(6):3056-3062,2002.

[9] P. van Stiphout, , T. Knott, T. Danker, and A. Stett: 3D Microfluidic Chip for Automated Patch-Clamping. In VDE Mikrosystemtechnik-Kongress. Technik VVdEEIeVaVVI, (VDI/VDE-IT):435-438,2005.

[10] X. Li: Microfluidic System for Planar Patch-Clamp Electrode Arrays, PhD Thesis Yale University, 2006.

[11] A. Hirano-Iwata, M. Niwano, M. Sugawara: The design of molecular sensing interfaces with lipid-bilayer assemblies, Trends in Analytical Chemistry, Vol. 27, No. 6, 2008

[12] A. Oukhaled : Transport de macromolécules à travers un pore nanométrique unique, PhD Thesis, Université Evry, 2006.

[13] http://opm.phar.umich.edu/protein.php?pdbid=7ahl

[14] K. Funakoshi, H. Suzuki and S. Takeuchi: Lipid Bilayer Formation by Contacting Monolayers in a Microfluidic Device for Membrane Protein Analysis, Anal. Chem. 2006, 78, 8169-8174,2006.

[15] N. Malmstadt, M. A. Nash, R. F. Purnell and J. J. Schmidt : Automated Formation of Lipid-Bilayer Membranes in a Microfluidic Device, *Nano Lett.*, 2006, 6 (9), 1961-1965, 2006.

[16] M. A. Unger, H.-P. Chou, T. Thorsen, A. Scherer, and S. Quake: Monolithic Microfabricated Valves and Pumps by Multilayer Soft Lithography,Science, vol. 288, no. 7, pp. 113-116, April 2000.

[17] V. Studer, V., G. Hang, A. Pandolfi, M. Ortiz, W.F. Anderson, and S.R. Quake: Scaling properties of a low-actuation pressure microfluidic valve. Journal of Applied Physics 95(1):393-398,2004.

[18] M. Lounaci: Systèmes microfluidiques pour la cristallisation des proteins : Apports technologiques à la comprehension du processus et influence de la hauteur des canaux, PhD Thesis, 2009.

[19] P. Allain : PVDF-based piezoelectric sensor for interfacial force study in microfluidics, Master's degree internship report,2009.

[20] A. Asgar, S. Bhagat, P.Jothimuthu and I. Papautsky: Photodefinable polydimethylsiloxane (PDMS) for rapid lab-on-a-chip prototyping, Lab on a Chip,June 2007.

Appendix C:

Protocols

Protocol 1: Immunostaining

Immunostaining: Actin and Nuclei

This protocol is for the fluorescent labeling of Actin, DNA/nuclei, and another protein (triple stain) in cells. This is written with the assumption that cells are plated onto glass coverslips that are suitable for high-NA optical microscopy (No. 1-2 glass coverslips, which can be spin coated with PDMS). It also assumes that cells are kept in either 35 mm petri dishes or wells of a 6-well plate. In order to see the labeled cells, you will need an Epifluorescent or laser confocal microscope with the appropriate filters for the selected fluorophores. In our laboratory, DAPI is visualized with the 'A' Filter cube set from Leica, Alexa 488 with the 'GFP' filter cube, and tetramethyl rhodamine with the 'N3' filter cube.

The basic principle is that you use chemicals that specifically bind to a desired cellular component. For the Actin and DNA stains, these chemicals are either auto-fluorescent or chemically modified to have an attached fluorophore. For the protein, you use an antibody that binds to the protein of interest- this is called a primary antibody. You then incubate the cells with a secondary antibody that is directed against the primary antibody, and this secondary antibody has a fluorphore attached to it.

DAPI is a fluorescent molecule that, when bound to DNA and excited with UV light, fluoresces a blue color. Phallodin is a toxin that is derived from the 'death cap' toadstool *Amanita phalloides*- it is a chemical that binds specifically to actin filaments. In this case, the toxin has been chemically modified with a fluorophore called 'Alexa488', which is excited by blue light and fluoresces green. It is similar to Fluorescein (commonly called 'FITC'), but is more stable to degradation. For this protocol, the secondary antibody has a tetramethlyrhodamine fluorophore attached to it. Every time a fluorophore is exposed to excitatory light, it is degraded and fades the longer it is exposed. As these fluorophores respond to light in the visible spectrum, it is advised that you keep them in the dark as much as possible to prevent degradation. When doing microscopy, it is advised that you keep your exposure times short and at low intensity.

This protocol involves direct handling of coverslips with fine-tipped forceps. The fine tipped forces can transfer all of the strength of your hand to a 1 mm^2 area on a 17 µm-thick piece of glass. If you are careful breakages should be rare. However they do occur. If you crack or break a coverslip during this procedure, you can still continue to stain the cells on the remaining glass provided that it is large enough to mount (see final step in the protocol).

This method of labeling requires that you kill the cells by briefly crosslinking them with a highly reactive aldehyde, which is toxic to both the cells and the scientist. Note that these toxins can target reproductive organs, and can be more toxic to females. Please exercise caution when handling aldehyde solutions, and strictly follow the safety measures outlined in this protocol.

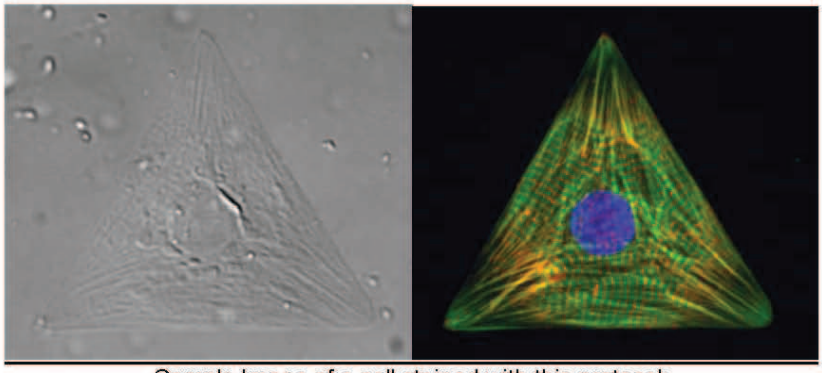

Sample Image of a cell stained with this protocol:
Left: DIC image of a triangular patterned cell. *Right:* Same cell, stained for the Nucleus (DAPI, blue), actin (phalloidin, green), and α-actinin (monoclonal α-actinin, red secondary).

Reagents

Fixative:

4% Paraformadehyde + TX-100 in PBS (Stock solution)

Preparation:
Take one 10 mL ampule of 16% PFA (Electron Microscopy sciences #15710) and dilute with 30 mL of PBS. Final diluted stock solution should be in a glass receptacle, and protected from light. Do all of your PFA work with gloves, lab coat, and eye protection in the chemical hood. All materials that come in contact with PFA are toxic and are NOT to be rinsed or disposed of in either the biological or regular waste. Store unused fixative in a chemical refrigerator, protected from light.

When you are ready to stain, for each coverslip that you intend to fix, take 2 mL of PFA stock solution (4% in PBS) and place into a 15 mL centrifuge tube. Label the tube, wrap it in foil, and label it again. The label should include the word 'TOXIC'. For each 2 mL of PFA that you have isolated, add 1 µL of Triton-X 100. The TX-100 will gel, so add it dropwise to the solution and gently agitate the tube after addition. Since you are adding such a small volume of TX-100, it would be a good idea to remove 10-20 mL from the large TX-100 bottle and use that as your source of TX-100, to prevent contamination of the stock bottle.

Stains:

DAPI: DNA staining reagent
4',6-diamidino-2-phenylindole, dihydrochloride (molecular probes, product #D1306) is shipped as a 10 mg solid in a small brown bottle. It does not dissolve well in PBS. Dissolve the entire 10 mg solid in 2.0 mL of dH_2O. Store in freezer, protected from light (shelf life – minimum 6 months). Before use, remove from freezer and allow to thaw while the bottle is held upright. I recommend aliquoting this to prevent freeze-thaw.

Phalloidin: actin Binding agent
Use AlexaFluor 488 Phalloidin, shipped as a 300 U solid (Molecular Probes/Invitrogen #A123-79). Make stock by dissolving 300 U solid with 1.5 mL Methanol (I use HPLC grade MeOH for this). Store in freezer.

Primary Antibody: Various

Secondary Antibody: Depends on Primary used.

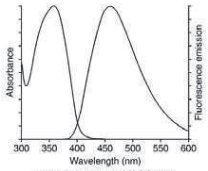

Excitation-Emission Spectrum for DAPI

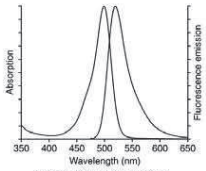

Excitation-Emission Spectrum for Alexa 488

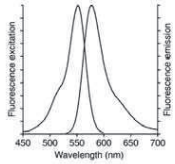

Excitation-Emission Spectrum for Tetramethylrhodamine

Preservative:

SlowFade Light anti-fade kit (Molecular Probes/Invitrogen #S7461). *NOTE: we have 2 types of kits in our lab, one with DAPI included, one without. Use ONLY the one without DAPI. The kits that contain DAPI are clearly labeled as such.* There are 3 bottles in the kit. Use 'Component A antifade reagent in glycerol buffer', the mid-sized dropper bottle.

Other materials:

Fine-tipped forceps, PBS, Glass slides, pipettes, eppendorf tubes, slide box.

Immunostaining Disease Biophysics Group

PROTOCOL

Fix your cells

1. Place your PFA aliquot and PBS into a warm water bath (37°C), let them get to temperature.
2. Once the solutions are warmed, remove your cells from the incubator and transfer them to the chemical hood. Rise the cells 3X in warm PBS.
3. After your 3rd PBS wash, aspirate the PBS and replace with 2 mL of 4% PFA solution per coverslip. Your cells must sit in the fixative for no longer than 15 minutes. Note, when using different antibodies this is a variable you can play around with.

Wash 1

1. After the fixation period, aspirate PFA solution and dispose appropriately.
2. Immediately add 3-4 mL of PBS to the coverslips, and swirl gently to rinse. Let stand for 5-10 min.
3. Aspirate PBS and repeat step #2.
4. Repeat step #3, leaving the coverslips in PBS. Note, at this point you can leave your coverslips in PBS at 4°C for several days, although it is advisable to stain as soon as possible.

Stain

Note: Once you add a fluorescent stain, you should protect your coverslips from light.

1. Prepare your staining agent by mixing 1 µL of your DAPI stock and 1 µL of your phalloidin stock with 198 µL of PBS for each of your coverslips. Mix well and protect from light.
2. To this mixture, add an appropriate amount of your antibody. For monoclonal anti-sarcomeric α-actinin (clone EA-53 from sigma), monoclonal anti-vinculin (HVIN-1 from sigma), polyclonal anti-Connexin-43 (#C-6319 from Sigma), 1 µL into the mixture from step 1 per coverslip works well.
3. Take a large Petri dish and place 200 µL drops of the staining agent on its surface. There should be one 200 µL drop per coverslip that you are staining.
4. Remove the glass coverslips from the final PBS wash solution. Do not aspirate the PBS- use fine-tip forceps to gently remove the coverslips from the wells.
5. Dry the coverslip. This is done by carefully holding the coverslip perpendicular to the lab bench. Once a bead of liquid builds up at the bottom of the coverslip, press the edge of the coverslip against a Kim Wipe to wick away the excess moisture. The goal is NOT to completely dry the coverslip- simply remove excess PBS from the glass surface.
6. Once dry, place the coverslip face down on the 200 µL drop of fixative solution (similar to the manual PDMS coating procedure for coverslips).

7. Cover with aluminum foil. Incubate at room temperature for 1-2 hours.

Wash 2

1. During the incubation, rinse the receptacle that the coverslips came in with PBS.
2. Add 3-4 mL of PBS to the receptacle.
3. After the incubation period, move coverslips into the PBS and swirl gently to rinse. NOTE: if you are having problems with background staining, I suggest you let the coverslips sit in the PBS for 5-10 minutes before washing again.
4. Aspirate PBS and repeat step #3.
5. Repeat step #4, leaving the coverslips in PBS.

Secondary Stain

1. For each coverslip, prepare 200 µL of a secondary stain.
2. The secondary stain should be composed of 199 µL PBS and 1 µL of the secondary antibody
    a. If you used a monoclonal primary antibody, use an anti-mouse secondary antibody
        i. I use Goat-anti-mouse IgG (H+L) Tetramethylrhodamine (Invitrogen Product # T2762). Note that you can use whichever fluorophore you want, as long as you have the correct filter cube and that it does not have the same excitation/emission characteristics of DAPI or Alexa-488.
    b. If you used a rabbit polyclonal primary antibody, use an anti-rabbit secondary antibody
        i. I use Goat-anti-rabbit IgG (H+L) Tetramethylrhodamine (Invitrogen Product # T2769). Note that you can use whichever fluorophore you want, as long as you have the correct filter cube and that it does not have the same excitation/emission characteristics of DAPI or Alexa-488.
3. incubate the secondary antibody for 1-2 hours at room temperature.

Wash 3

1. During the incubation, rinse the receptacle that the coverslips came in with PBS.
2. Add 3-4 mL of PBS to the receptacle.
3. After the 1 hour incubation period, move coverslips into the PBS and swirl gently to rinse. NOTE: if you are having problems with hbackground staining, I suggest you let the coverslips sit in the PBS for 5-10 minutes before washing again.
4. Aspirate PBS and repeat step #3.
5. Repeat step #4, leaving the coverslips in PBS.

Mount

1. Prepare one glass slide for each coverslip. Label the glass slide. If your slide is dusty, blow dry with compressed air or clean with 70% ethanol and dry.
2. Using the small dropper bottle in the preservative solution kit, drop one SMALL drop onto the center of your glass slide.
3. Remove the rinsed coverslip from the PBS and dry, using the same technique outlined in step 4 of the staining procedure. Use the fine-point forceps.
4. Drop the coverslip face down onto the preservative drop. I recommend that you first hold the coverslip at a 45° angle (cell side down) against the coverslip, and touch the edge of the drop with the edge of the coverslip. Then release the coverslip and allow it to fall onto the preservative. Gently place a kimwipe over the coverslip and gently press it against the glass slide. Small amounts of preservative will get squeezed out along the coverslip edges, which will be absorbed by the wipe.
5. Examine the preservative for bubbles. If there are large bubbles, you will most likely be able to eliminate them by gently squeezing the coverslip with your forceps. If there are several bubbles, slide the coverslip off of the glass slide and try again.
6. Once you are satisfied with the coverslip and preservative, gently remove excess preservative from the exposed coverslip and glass slide.
7. Paint around the edges of the coverslip with nail polish. I recommend using a clear nail polish or nail hardener. Let dry.
8. Once dry, your coverslips are ready for microscopy. If you do not have immediate access to the microscope, store in a slide box or a dark box, in the freezer. Slides will keep for several months but deteriorate over time.

End protocol.

Protocol 2: Fabrication of photosensitive PDMS

1- Make 10 : 1 PDMS

2- Dissolve Benzophenone (**3% in weight** compared to the weight of PDMS) in m-Xylene. Quantity of m-Xylene has to be enough to dissolve completely Benzophenone crystals.

3- Mix Benzophenone with PDMS for 15 minutes

4- Spincoat of the photoPDMS

5- Exposure: This photoPDMS is positive : UV will react with Benzophenone creating radicals which will prevent exposed photoPDMS from curing. I try different time exposure from 10 seconds to 10 minutes. The optimum appeared to be **5 minutes**. The gap between the mask and the sample should small. In order to do this you can pile 2 glass slide on each side of the sample and put the sample on it.

6- Post exposure bake : **110°C for 40 seconds** (this step is critical if PEB is too long everything will be cured)

7- Let the sample cool down few seconds

8- Reveal in Toluene (Be careful Toluene is very volatile and bad for else always work under the solvent hood!) for few seconds (10~30).

9-Rinse under water